CRANFIELD UNIVERSITY

VALERIY GORNYAKOV

EFFICIENT MODELLING AND EVALUATION OF ROLLING FOR MITIGATION OF RESIDUAL STRESS AND DISTORTION IN WIRE ARC ADDITIVE MANUFACTURING

SCHOOL OF AEROSPACE, TRANSPORT AND MANUFACTURING
Welding Engineering and Laser Processing Centre

PhD
Academic Year: 2011 - 2021

Supervisor: Jialuo Ding
Associate Supervisor: Yongle Sun
August 2021

CRANFIELD UNIVERSITY

SCHOOL OF AEROSPACE, TRANSPORT AND MANUFACTURING
Welding Engineering and Laser Processing Centre

PhD

Academic Year 2011 - 2021

VALERIY GORNYAKOV

Efficient modelling and evaluation of rolling for mitigation of residual stress and distortion in wire arc additive manufacturing

Supervisor: Jialuo Ding
Associate Supervisor: Yongle Sun
August 2021

This thesis is submitted in partial fulfilment of the requirements for the degree of Doctor of Philosophy
(NB. This section can be removed if the award of the degree is based solely on examination of the thesis)

ABSTRACT

Wire and Arc Additive Manufacturing (WAAM) is a promising technology for manufacturing large-scale parts with low costs and short lead time. One of the main challenges in applying WAAM in industry is the effective control of residual stress and distortion. It has been found that high-pressure inter-layer rolling can effectively mitigate the residual stress and distortion of WAAM components. However, the mechanism behind the mitigation efficacy is of a complex nature and has not been well understood. Finite element analysis (FEA) has proven to be a reliable and accurate method for simulating the thermo-mechanical process. The FEA simulation of large-scale inter-layer rolling is challenging due to the high computational cost and complicated coupling between WAAM and rolling.

This research is based on efficient models for simulating WAAM deposition and rolling processes, and their combination for large-scale structures. The efficient modelling method is developed using a reduced-size model to determine the steady-state solution, and then mapping the solution to a full-size structure for further analysis. This method is successfully applied to study the evolution of residual stress and plastic strain during the post-build and inter-layer rolling of WAAM deposited walls. The numerical predictions are verified with experimental results.

Cyclic formation of tensile residual stress occurs during the WAAM deposition, whereas inter-layer rolling counteracts the development of the residual stress. The effectiveness of roller designs is studied for reducing residual stress of the WAAM process. Compared with a flat roller, a slotted roller can induce greater longitudinal plastic strains and more effectively reduce the tensile residual stress in the WAAM wall. Removal of the clamps only results in a slight redistribution of residual stress in the post-build and inter-layer rolled WAAM components, since the rolling mitigates most of the tensile residual stresses caused by WAAM. To enhance the manufacturing efficiency, stacked-layers rolling can replace inter-layer rolling for RS and distortion mitigation in tall WAAM parts. Influences of main process parameters, such as rolling load and roller-to-component friction, on mitigation of RS and distortion are also studied. Finally, based on the

understanding gained through the simulations, recommendation of an optimal rolling strategy is made for future industrial application.

Keywords: wire and arc additive manufacturing, efficient FE model, residual stress, plastic strain, distortion, post-build rolling, in-process rolling, large-scale part, process optimisation

ACKNOWLEDGEMENTS

The PhD study was one of my greatest passions in the last ten years. I was growing two beautiful kids during my research, working long months offshore away from civilisation, building a family house, and was on infinite COVID-19 quarantines…

Therefore, I want to acknowledge people who made this long and prosperous journey possible, my supervisors Dr Paul Colegrove, Dr Jialuo Ding and Dr Stewart Williams, for their patience, support, technical and scientific guidance. I want to express my gratitude to associate supervisor Dr Yongle Sun, who guided me during the study's final part and taught me to write papers. I want to thank my friend Dr Stephan Egerland for manuscripts proofreading and help with academic language, and Dr Daniel Cozzolino, who brought me to the world of numerical modelling. I would like to acknowledge financial support from WAAMMat and NEWAM (EPSRC grant EP/R027218/1) programs.

I want to thank my dear wife and parents for the indispensable support, motivation, and inspiration in minutes of doubts.

LIST OF PUBLICATIONS

Journals

- Gornyakov V., Sun Y., Ding J., Williams S. Computationally Efficient Models of High Pressure Rolling for Wire Arc Additively Manufactured Components. Applied Sciences. 4 January 2021; 11(1): 402. Available at: DOI:10.3390/app11010402
- Gornyakov V., Sun Y., Ding J., Williams S. Efficient determination and evaluation of steady-state thermal-mechanical variables generated by wire arc additive manufacturing and high pressure rolling. Accepted for publication in Modelling and Simulation in Materials Science and Engineering (Manuscript ID: MSMSE-105517.R2).
- Gornyakov V., Ding J., Sun Y., Williams S., Understanding and designing post-build rolling for mitigation of residual stress and distortion in wire arc additively manufactured components. Submitted to Materials & Design in Elsevier (Manuscript ID: JMADE-D-21-02630) for Publication.
- Gornyakov V., Sun Y., Ding J., Williams S., Modelling and optimising hybrid process of wire arc additive manufacturing and high pressure rolling. To be submitted soon to Additive Manufacturing in Elsevier (Manuscript ID: TBA) for Publication.

Conference

- Sun Y., Gornyakov V., Ding J., Williams S. Finite element analysis of post-build and inter-layer rolling for large-scale components deposited by wire arc additive manufacturing. NWC21. October 2021, Salzburg, Austria. (abstract and presentation to be published)

TABLE OF CONTENTS

LIST OF FIGURES

LIST OF TABLES

LIST OF EQUATIONS

LIST OF ABBREVIATIONS

10L	rolled every 10 layers
2D	two-dimensional
3D	three-dimensional
4L	rolled every 4 layers
AM	additive manufacturing
BTF	buy-to-fly ratio
CAD	computer-aided design
CMT	cold metal transfer
CPU	central processing unit
DC GMAW	direct current gas metal arc welding
DED	direct energy deposition
EPS	equivalent plastic strain
FE	finite element
FEA	finite element analysis
FEM	finite element method
GTAW	gas tungsten arc welding
HPC	high performance computing
IL	inter-layer
IS	in situ
L	layer
LL	last layer
MAG	metal active gas
MIG	metal inert gas
NEWAM	new wire additive manufacturing
PAW	plasma arc welding
PB	post-build
PBF	powder bed fusion
PDE	partial differential equation
P-GMAW	pulse gas metal arc welding
PS	plastic strain
RS	residual stress
S	stress

SAW	submerged arc welding
TIG	tungsten inert gas
TP	thermocouple
WELPC	welding engineering and laser processing centre
WAAM	wire arc additive manufacturing

1 INTRODUCTION

1.1. Research background

Wire and Arc Additive Manufacturing (WAAM) is an emerging technology, which has gained popularity in the last decade thanks to its high deposition rate, low costs associated with equipment and consumable, good structural integrity of produced components and low material wastage. WAAM allows the near-net-shape manufacture of medium to large-scale components with variable wall thickness and various metallic materials.

One of the main technical challenges limiting the wider adoption of this manufacturing process in the industry is residual stress (RS), which is mainly caused by thermally induced uneven plastic deformation between different regions of deposit. RS is the main cause of cracks and distortion in the deposited component, which often leads to damage or waste of substandard product. Various techniques have been proposed to manage the residual stresses and distortion in WAAM components during the manufacturing stage, such as symmetrical and back-to-back building, and to optimise deposition parameters. The application of these techniques usually allows to minimise distortion. However, the remaining RS may still negatively affect the fatigue performance and the corrosion resistance of the component and may reduce the service life. Post-build heat treatment can largely eliminate RS, but it could be costly and detrimental to the mechanical properties of the produced part.

Researchers in WELPC at Cranfield University found that high-pressure inter-layer rolling can mitigate the RS and distortion and improve the microstructure of the WAAM built parts. In these previous experimental studies, the roller was positioned on the top surface of the deposited layer and a vertical rolling load was applied. However, the experimental results did not reveal the underlying mechanism that controls the RS and deformation during inter-layer rolling, because it is difficult to obtain enough information from the experiment to establish the understanding.

Finite element simulations of WAAM deposition have been remarkably helpful for gaining insights into the WAAM-induced RS and distortion. Unfortunately, the literature still lacks modelling study of high pressure rolling for mitigation of the RS and distortion induced by the WAAM deposition. Rolling simulations are needed for analyses and evaluation of the RS and plastic strain during combined WAAM deposition and high pressure rolling. The modelling will help establish a fundamental understanding of the key phenomenon, such as evolution of RS and plastic strain, that occur during the alternating deposition and rolling in the layer-by-layer manufacturing process. In previous studies, numerical simulations have been attempted to investigate the post-build rolling of WAAM components. However, due to substantial computational cost, numerical models were normally limited to simulate only one layer rolling in relatively short WAAM parts. There is no report on the inter-layer rolling model for large-scale WAAM components. Therefore, an efficient modelling method for high-pressure rolling simulation of large-scale WAAM components is needed.

Despite all the advantages, the application of inter-layer rolling can significantly increase manufacturing time. Therefore, optimising the rolling strategy is important to enhance the manufacturing efficiency. It is straightforward to apply post-build rolling or stacked-layers rolling, instead of inter-layer rolling, for reduction of rolling operations and hence manufacturing time. However, such rolling strategy should be verified with respect to the intended efficacy of mitigation of RS and distortion. In addition, the rolling effectiveness could be improved through novel design of rollers, which also needs a systematic study.

1.2. Research gap

A literature survey (Chapter 3) of relevant research areas is conducted, and the following research gaps are summarised:

1. Previous models on rolling process are not efficient to be applied for analysing inter-layer rolling of large-scale WAAM parts.
2. A fundamental understanding of plastic strain evolution and stress development during WAAM deposition and inter-layer rolling is absent.

3. Previous experiments have demonstrated that post-build rolling and stacked-layers rolling can be used to control WAAM distortions; however, for these rolling processes, the mechanism responsible for the mitigation of WAAM-induced RS and distortion is yet to be thoroughly understood.
4. There is a lack of rational-based optimisation strategy for the integrated rolling to provide sufficient control of RS and distortion using the fewest rolling operations during WAAM deposition.

1.3. Aim and objectives

The present PhD research aims to develop better understanding of the mechanisms enabling the high-pressure rolling to mitigate RS and distortion in large-scale WAAM parts, and furthermore to optimise the rolling process for enhancing mitigation effectiveness and manufacturing efficiency.

The objectives are listed below:

1. To develop an efficient FE model to investigate the strain and stress evolution during the complex thermal and mechanical response to the WAAM deposition and rolling.
2. To understand the mechanism about how the deposition process and rolling process interact and change the strain and stress distributions.
3. To study the influences of roller design and rolling parameters on the effectiveness of the rolling process for mitigating WAAM-induced RS and distortion.
4. To develop an optimisation strategy for the in-process rolling during WAAM deposition, based on the comprehensive understanding and efficient prediction of the thermomechanical response to the hybrid process of WAAM and rolling.

1.4. Thesis structure

The thesis contains eight chapters, which are listed below:

Chapter 1. This chapter presents the research background, research gaps, aims and objectives and structure of the thesis.

Chapter 2. This chapter presents the research methodology used for current PhD research.

Chapter 3. This chapter presents an overall literature review of theoretical background, methods and the state-of-the-art.

Chapter 4. This chapter presents the development of efficient high-pressure rolling models for WAAM components.

Chapter 5. This chapter presents the development and validation of efficient modelling method for simulation of WAAM and rolling using short efficient models with the subsequent transfer of steady-state solution to the large model to determine RS and distortion in large-scale WAAM parts before and after removal of clamps.

Chapter 6. This chapter presents a study of post-build rolling of WAAM components. The change of RS and plastic strain distribution before and after rolling is explained. Influences of roller design, rolling load and friction coefficient on the efficacy of the rolling process to mitigate RS and distortion are studied. The necessity of incorporation of WAAM model solution in the rolling simulation is also examined.

Chapter 7. This chapter presents a study on hybrid process of WAAM deposition and rolling. Coupled WAAM + rolling models are developed and validated. The evolution of RS and plastic strain during alternating WAAM deposition and rolling is studied. Optimisation of the rolling process is also conducted for reduction of manufacturing time. The mechanism of RS mitigation by inter-layer rolling and stacked-layers rolling are investigated and the mitigation effectiveness is assessed. The effect of the rolling on the distortion of the WAAM component after removal of clamps is also studied.

Chapter 8. This chapter presents the summary of research, contribution to knowledge and recommendations for future work.

2 Research methodology

2.1 Literature review

A literature review was conducted to introduce the theoretical background, latest research and methods in the investigated field, and to identify research gaps. The following procedure was implemented for literature review:

1. Identification of keywords. Following keywords were selected for searching of books and papers: additive manufacturing, wire and arc additive manufacturing, residual stress, distortion, mitigation, post-build rolling, inter-layer rolling, numerical model, heat source, thermal-mechanical model, and rolling model.
2. The search of papers. Papers were searched in the Scopus database and obtained from reference lists of downloaded papers. Google search engine was used to find technical reports and papers.
3. Analysis of papers. Abstract and conclusions sections of downloaded articles were read first and figures were briefly reviewed. The papers that are assessed as relevant to the investigated topic were read thoroughly. The obtained data were analysed and summarised for identification of research gaps. References of collected papers were managed with the Zotero application.

2.2 Modelling methods

2.2.1 Development of an efficient rolling model for WAAM

At the initial stage of the research, the efficient rolling model for WAAM parts was developed to provide an efficient tool for studying post-build rolling and inter-layer rolling. During the development of the efficient rolling model, the applicability of the efficient modelling techniques reported in the literature was assessed. Efficient rolling models were created, and their computational cost and accuracy were compared. The most suitable method was down selected to be used for the subsequent studies of this project.

2.2.2 Development and validation of efficient thermal-mechanical model and steady-state solution mapping technique

The pre-rolling RS and PS distributions generated by the WAAM process are required to accurately simulate high-pressure rolling. To provide initial conditions for the rolling analysis, development of an efficient thermal-mechanical WAAM model was conducted. The reported efficient modelling techniques for simulation of thermal field and residual stress generation were tested for efficient simulation of WAAM. The reduced length transient thermal-mechanical model was found to be the most appropriate for accurate and efficient simulations. However, the model was not able to predict residual stress in unclamped large-scale WAAM part due to the dependence of constraint on length.

A RS reconstruction technique for scaling steady-state solution from short models to large-scale models was developed. Then, the efficient modelling technique was employed for analyses of WAAM and rolling. Numerical predictions were compared with experimental results to validate the developed efficient modelling technique.

2.2.3 Investigation of the post-build rolling for WAAM

Post-build rolling models were created with the use of the efficient modelling method. The RS and PS distributions generated by the short thermal-mechanical WAAM model were used as the initial conditions for the post-rolling models for the clamped component. The effects of various roller designs, rolling loads and friction coefficients were investigated. The influence of post-build rolling on the RS and distortion in the long WAAM component after removal of clamps was also studied.

2.2.4 Investigation and optimisation of the in-process rolling for WAAM

WAAM deposition and inter-layer rolling models were created based on the developed “base” efficient models. The temperature field predicted by the short thermal model was incorporated in the mechanical model for the coupled WAAM deposition and rolling simulations. The obtained results were analysed to reveal

the evolution of plastic strain and RS during the hybrid process of WAAM and rolling, and to understand the RS and distortion mitigation mechanisms. To validate the models, the numerical predictions were compared with previous experimental measurements. Moreover, additional simulations were conducted to investigate the performance of staked-layers rolling as a replacement for inter-layer rolling to reduce manufacturing time. With the help of the efficient modelling method, the influences of different rolling strategies on the RS and distortion in the large WAAM parts were studied.

2.3 Research route

The research route implemented in this PhD project is schematically presented in Figure 2-1. Literature survey demonstrated that large-scale FE models, as required to investigate the WAAM deposition and inter-layer rolling, are not available for the scientific community mainly due to enormous computational cost. The assessment of available modelling techniques demonstrated that reduced length models are most efficient and accurate compared to conventional large-scale models of WAAM deposition and rolling. Instead of developing the large-scale coupled WAAM deposition and rolling model, the new development of efficient models was divided to the following sub-categories:

- Development of reduced length efficient rolling model
- Development of reduced length thermal-mechanical WAAM model
- Development of the modelling technique for transferring the steady-state solution from efficient reduced-length models to the full-length model for further analysis

To prove the accuracy of each developed model, and modelling approach was validated against experimental results. In conjunction, the developed models were used to obtain key physical variables for revealing mechanisms of the high-pressure rolling to mitigate WAAM tensile RS and vertical distortion. Process optimisation study was also conducted to improve mitigation efficacy and reduce the in-process rolling manufacturing time. The obtained results were collected, analysed and presented in this thesis.

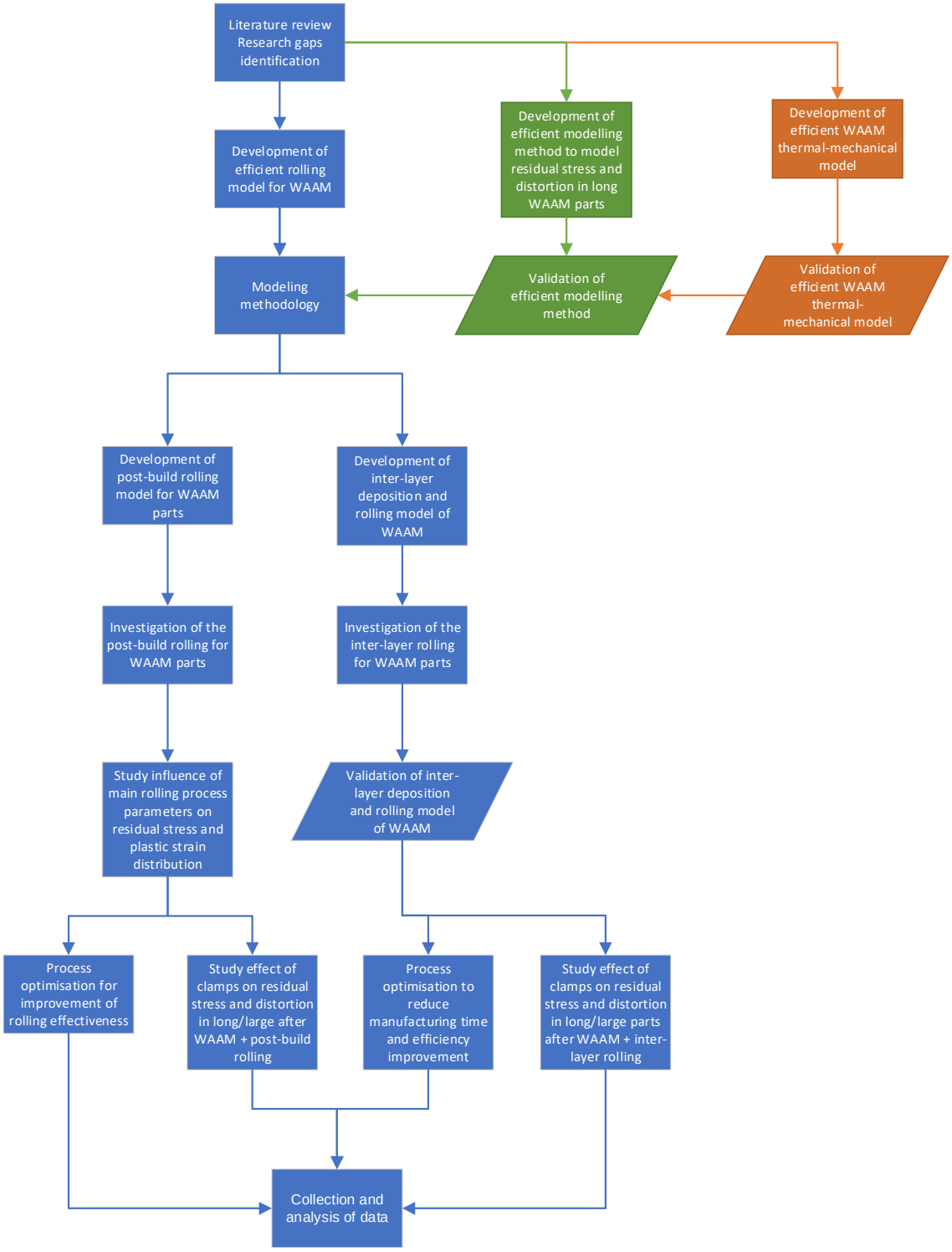

Figure 2-1 Research route diagram.

3 Literature review

This thesis is written in paper format, and each paper contains a comprehensive introduction section. However, due to the limitation of paper size, the Introduction sections of the chapters do not include a review of fundamental knowledge and all the relevant research conducted in the investigated field. This chapter on literature review aims to provide an overview of theoretical background, methodology and latest research related to mitigation of RS and distortion in conventional welds and WAAM. The focus made here is on FEA simulation of thermal field, RS generation and post-build rolling (no inter-layer simulation was reported in the literature).

3.1 Additive Manufacturing

3.1.1 Overview of the technology

Several traditional technologies are used for the manufacture of complex components in modern mechanical engineering. Components that are manufactured by forging processes have remarkable mechanical properties, but their production is limited by the size and complexity of the components. Parts that are made with the investment casting may have more complex structures, larger sizes and require less or no machining (near-net-shape) [1]. However, the cost and time of making using this technology are significant [1]. Also, the resultant mechanical properties, comparable to wrought materials, can only be achieved using complex heat treatments [1]. Production of components from wrought blocks of material is connected with significant machining (milling) and subsequent disposal of a large amount of unused material.

The aforementioned drawbacks of the traditional manufacturing technology are particularly relevant to the manufacture of small batches of complex profile components of expensive metals and/or difficult-to-process metals [2]. Additive Manufacturing technologies (AM) were developed to overcome these difficulties and to accelerate production. AM technologies usually rely on fusing successive layers using various welding processes and powder or wire feedstock materials [3–5].

The AM technologies provide fabrication of 3D near-net-shape complex metallic [6] and intermetallic components [4,7] with mechanical properties comparable to wrought material [8–11]. Thanks to AM technology, a phase of extensive machining can be prevented, which in turn has a positive impact on the economic aspect of production and reduces the environmental impact [5,9,12].

Powder bed fusion (PBF) and direct energy deposition (DED) are the main forms of the metal AM [13]. PBF method relies on selective sintering/melting of material within powder bed using laser or electron beam in a controlled atmosphere or vacuum chamber [14]. PBF method is suitable for mass production of small, high resolution and complex parts [15]. Their build rates are slow and the dimensions of produced parts are limited by the size of the powder bed [15]. Post-processing may be required for surface and mechanical properties improvement of sintered parts [16]. During DED AM, thermal deposition occurs by melting the powder or the wire fed to the focal point of laser/ electron beam or plasma of arc [15,17].

DED systems use higher energy density for melting of material than PBF, leading to increased build rates, but results in higher surface roughness, which may require post-machining [18]. DED systems are often attached to 4- or 5- axis robotic devices and can be used to repair or deposition large and complex components without support structures [19]. Build rates of PBF systems are significantly lower compared to wire-based DED systems [20]. Re-use of the powder leads to the incorporation of oxygen in its composition and, consequently, in the deposition [21]. The powders are also fairly complex in manufacture and storage [22]. Spraying the powder also leads to environmental pollution and potential danger for an operator. As well, wire feedstock is approximately ten times cheaper than powder [23].

3.1.2 Wire plus Arc Additive Manufacturing

Wire plus Arc Additive Manufacturing (WAAM) [24,25] is a DED AM process in which the energy of the electric arc is used for melting the wire (TIG/PAW and MIG/MAG). TIG/PAW or MIG/MAG torches are mounted on a robot manipulator or gantry system and the robot repeats the form of a CAD model while fusion occurs in a layer-by-layer manner [14,24]. Metallic substrates used to support the

deposition can be incorporated into a final component or removed by machining [14].

The Cold Metal Transfer (CMT) process (a variant of the MIG/MAG process) is a popular choice for the manufacture of aluminium [14] and steel [24] WAAM components, while TIG/PAW is more suitably used for the deposition of titanium alloys [26,27]. WAAM is also used for the deposition of components from tungsten [28], tantalum [29], nickel superalloys [30]; in addition, functionally graded materials [31] were created using WAAM. The WAAM deposition allows the manufacture of complex multi-thickness components like wing spar, external landing gear assembly and wing rib [14].

The main advantages of WAAM over other AM technologies are high deposition rate (up to 9.5 kg/h for martensitic steel [32], but most practically, 1-4 kg/h [14] for steel and aluminium) and low cost of equipment and consumables [14]. The size of WAAM components is not limited by dimensions of the building table and chamber, which is essential for powder-based AM processes [12,14,25]. WAAM processes have considerably lower material wastage rates than powder-based systems, which scatter and discard up to 70-90% of consumables [4,14]. The low average Buy-To-Fly ratio (BTF) (ratio between the weight of purchased material and weight of material incorporated in produced component) of WAAM makes the technology a promising candidate for replacing current manufacturing methods such as forgings and billets [14]. BTF of current manufacturing methods can be as high as 20-25 [33], while typically for WAAM the BTF is 1.2 – 12 [14].

However, WAAM-built component's dimensional precision and surface finish may be worse than those produced by PBF AM processes [12,14]. WAAM-built parts also suffer from RS and distortion [24]. This limits the application of WAAM technologies in the industry.

3.2 Residual stress and distortion

Residual stress is self-equilibrating stress that remains in a component in the absence of external thermal or mechanical loads [34]. As a result of a thermal cycle during material deposition, WAAM parts can suffer from significant RS and

distortion [24]. RS is the major contributor to the formation of distortion in components produced with AM. Excessive distortion leads to wastage of substandard products [35–40]. RS can also be responsible for crack formation or part detachment during building [41,42]. The presence of RS reduces fatigue resistance and impair mechanical properties of an AM component [38,41], causing anisotropic behaviour of the produced deposit [41]. In analogy with conventional welding, tensile RS can significantly reduce the stress corrosion performance of a component [43]. RS can also cause brittle fracture of the component [44] and can increase susceptibility to hydrogen embrittlement [45]. Understanding RS formation mechanisms is essential to minimise RS in WAAM components and to control distortion.

In the last several decades, the formation of RS in conventional welds was extensively investigated. Unfortunately, not many studies were conducted explaining RS in WAAM. The main principles of RS formation are similar for conventional welding and WAAM. However, RS distribution in WAAM walls is different compared to conventional joints due to different heat flow and restraint in butt or corner joints. Nevertheless, the main principles of RS formation will be investigated based on large amount of literature available for conventional welding and will be followed by the investigation of RS in WAAM.

The main reason for RS formation is a "misfit" in original shape between different parts or regions of component [45]. Steep thermal gradients develop, due to localised heating and cooling, in the weld zone and its close vicinity, which causes the formation of RS in the weld and adjacent parent material [45]. RS generation in the weld can be described by using the 3-rod model [46–48]; refer to Figure 3-1. The middle rod is heated until 600 °C and then cooled to the initial temperature. Due to heating, the middle rod experiences elastic compression along curve A – B and outer rods elastically expand. Compressive stresses in the middle rode raise until point B. In the point B, the stress exceeds the yield point and the rod plastically deforms along the B – C line, due to reduction of yield strength at elevated temperature. At point C cooling begins and the rod shrinks. Along curve D – E the rod does experience plastic tensile deformation, because

yield stress at that temperature is exceeded and the middle rod is constrained by the outer rods. The outer rods exhibit compressive stresses during this stage. When the system reaches point E and the final temperature equals initial temperature, in the middle rod tensile RS arises, and in outer rods compressive RS remains. If heating is stopped after point B, but before point C (for example, in point B'), the same RS will form in the middle rod as in case of heating to 600 °C**.** Similarly to this, RS forms in conventional welds and WAAM.

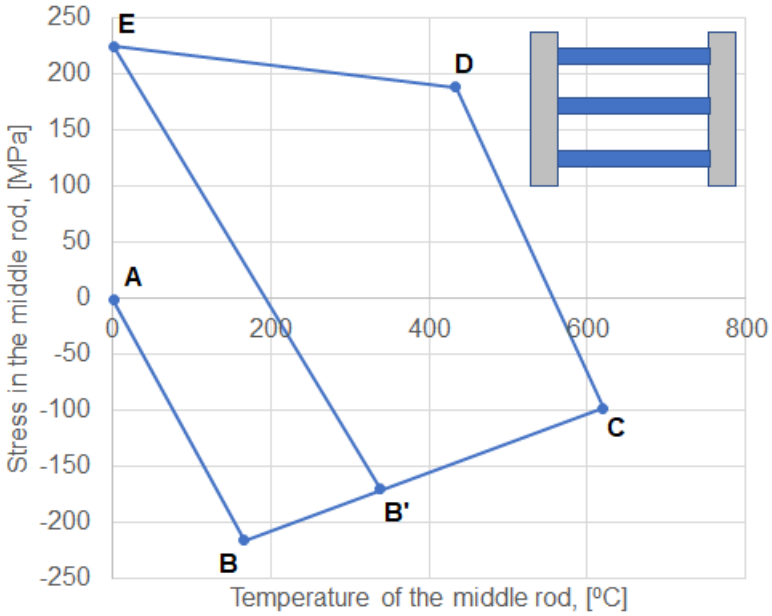

Figure 3-1 RS generation in constrained middle rod due to thermal load [48].

In addition, another mechanism of RS formation is present in AM as well. Contraction of the hot deposited layer on top of a cold constrained layer creates shear forces between the layers due to inherent thermal mismatch, resulting in RS generation.

3.2.1 Main contributors to RS formation

Process and material properties have a significant impact on RS generation. The heat input has a significant influence on RS formation and distribution [49,50]. Colegrove et al. [49] compared RS generated by six processes (SAW, DC GMAW, P-GMAW, CMT, autogenous Laser and Hybrid Laser). Distributions of RSs produced by various processes are shown in Figure 3-2. Despite a high

range of heat inputs, from relatively low value for autogenous laser and hybrid laser to high value for SAW, the magnitude of produced RS was similar. As can be seen from Figure 3-2, peaks of RS have identical magnitude, but the distribution width varies with heat input. Larger heat input promotes a wider peak RS region. Larger heat input generates larger fusion zone and heat affected zone, this causes creation of wider "misfit" region and as a result wider region affected by RS [49].

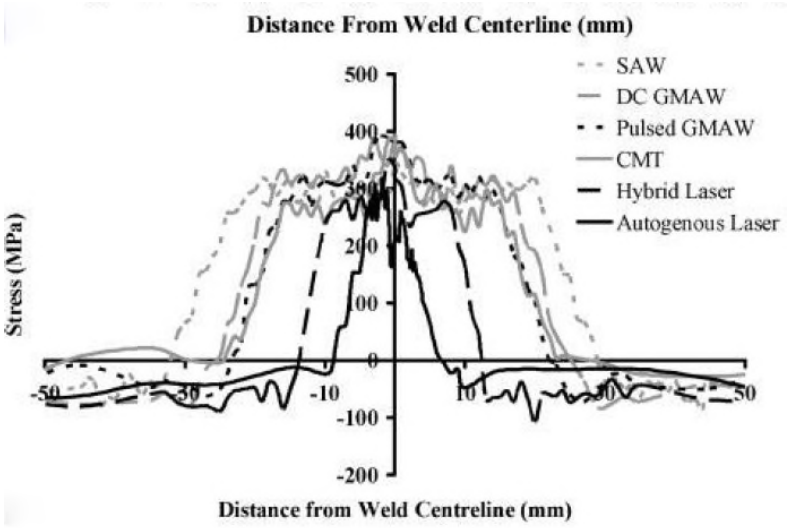

Figure 3-2 RS distribution produced by various processes [49].

In many cases, the magnitude of tensile RS in welds equals the yield stress of either deposit or parent material. However, this is true only for materials whose thermal contraction strain during cooling after welding is more significant than their yield strain [51]. The following Equation (3-1) [51] can describe this condition:

$$\alpha(T_s - T_0) \geq \sigma_\gamma / E \qquad \textbf{(3-1)}$$

where α is the coefficient of thermal expansion, T_s is the softening temperature (the temperature at which the yield strength of the material reduces by 10 % compared to yield strength at ambient temperature), T_0 is preheat or ambient temperature, σ_γ is the yield strength at preheat or ambient temperature, E is Young's modulus.

The thermal strain of C-Mn steels is 5 times greater than their yield strain, so usually, tensile RS after welding does have the same magnitude as the yield strength of the C-Mn steel. However, the thermal contraction strain of Ti-6Al-4V is low, compared to yield strain, so the resulting tensile RS has a lower magnitude than the yield strength [51].

The phase change of materials during cooling is a significant contributor to the occurrence of RS as well. The largest effect takes place in materials where phase change occurs at low temperatures during cooling [52]. 9Cr1Mo and 2.25Cr11Mo steels demonstrate phase change effects between 600 and 300 °C, the range of temperatures at which phase change occurs sensitively to cooling rate. During cooling through that range, the crystal lattice expands and as a result, tensile residual stresses relax to lower values, but after completion of phase changes, the values of residual stress grow again rapidly on cooling to room temperature, reaching yield stress in 2.25Cr11Mo specimen and lower than yield stress in 9Cr1Mo specimen [52].

3.2.2 Formation of RS in AM built components

The formation of RS in linear wall AM components is similar to conventional welds, but the main difference is an absence of constraining effects by the parent material, for example, inside a bevel/groove in butt and fillet joints. Results of numerical studies were used to explain RS formation in AM built components, because experimental studies provided only measurements of the final state of RS after deposition.

During sequential deposition of layers on the substrate, the heat generated by laser or arc expands the deposited material and creates compressive plastic strain in front of the moving puddle. When the deposited layer cools down, it shrinks and forms tensile RS in deposition (longitudinal) direction. Deposition of new layers also causes re-heating and compressive plastic flow in layers below, and the following shrinkage during cooling results in tensile RS. After deposition of multiple layers, the component is attached to the substrate and clamped, similar values of tensile longitudinal stress forms in each deposited layer. This leads to almost uniform distribution of resultant longitudinal tensile residual stress

in the WAAM wall. As a result, counterbalancing compressive longitudinal RS forms in the substrate [35]. Like in conventional welds, RS in WAAM reaches the largest values in the longitudinal direction (deposition direction) and the lowest in transversal and normal directions where the constraining effect is minimal [35,42].

Value of RS in the deposit reaches value of yield strength of the material [38,53]. In general, RS in arc deposited components is more significant than that deposited with laser due to larger fusion zones during deposition by arc [35].

RSs in WAAM built wall components were studied using FEA by Ding et al. [54] and experimentally by Colegrove et al. [24], Ding et al. [54] and Hönnige et al. [55]. It was found that in clamped component longitudinal RS has the largest magnitude. The deposition process produces tensile RS in the wall and counterbalancing compressive RS in the bottom of substrate. In the deposited wall, tensile RS distribution is uniform in longitudinal direction, regardless of the number of layers deposited [54], while the substrate is clamped [24,54,55], Figure 3-3. After removal of the clamps, RS causes the WAAM component to distort. Due to the large longitudinal tensile RS in the wall, the upper part of the wall contracts and the bottom expands. So, the distorted component takes a concave shape. As a result, RS redistributes, and the net bending moment across the section becomes zero. Tensile RS in the wall reduces [54] or even becomes compressive in the upper part [24], but RS turns to be tensile at the bottom of the substrate. Tensile RS remains at maximum in the interface between the substrate and the wall [24,54,55], refer to Figure 3-3, Figure 3-4 and **Error! Reference source not found.**Figure 3-5 Control plot.

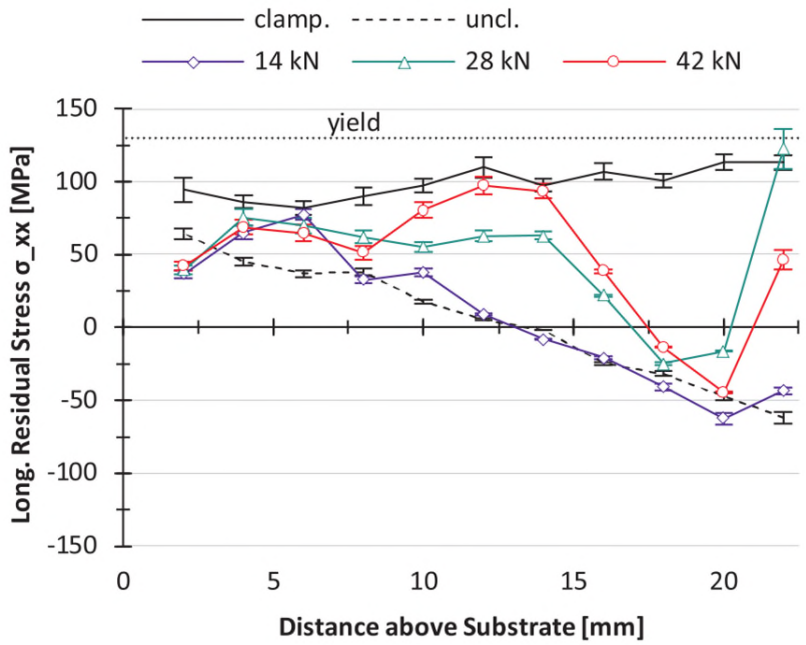

Figure 3-3 Longitudinal RS in as-built clamped and unclamped, and rolled at 14 kN, 28 kN and 42 kN aluminium WAAM component, as measured by experiments [55].

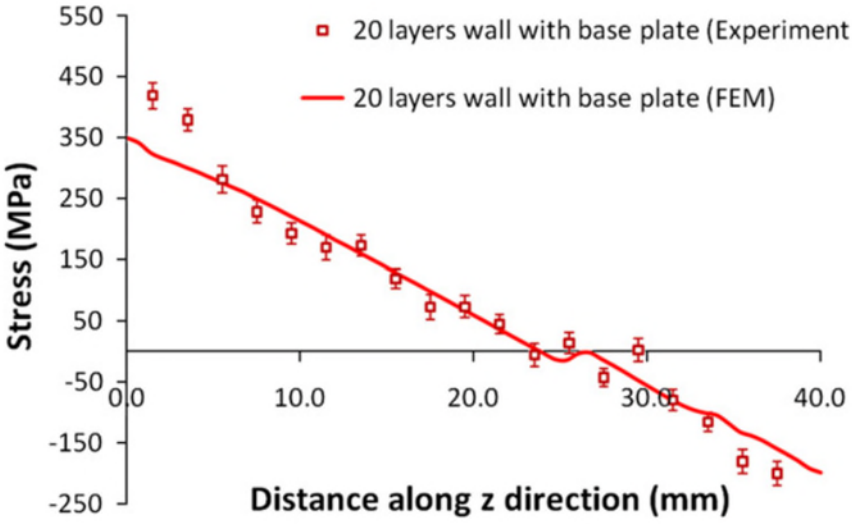

Figure 3-4 Longitudinal RS measured experimentally and predicted by numerical model in 20 layers WAAM steel wall after clamps removal [54].

3.2.3 Mitigation of RS and distortion

RS in welds arises from a "misfit" between different regions of the weld upon uneven heating and cooling [45]. The accommodation or release of RS can cause

distortion. WAAM resembles multi-pass welding, and many mechanisms revealed for welds, thanks to decades of research, are also valid to WAAM. Common methods to control distortion in conventional fabrication welding are known for many years, including reducing weld size, application of stiffeners, or weld sequencing [56]. The application of these methods indeed reduces distortion, but RS in the weld remains unchanged or even increases. Heat treatment is an effective method to eliminate RS even in thick joints [57], and it works through evenly heating the component, thereby reducing yield strength and relaxing RS gradually. However, unfortunately, this method is expensive and difficult to apply for large components.

Stress engineering methods were developed to modify/mitigate RS and as a result, to eliminate distortion. Two main techniques are used for the alleviation of RS: thermal and mechanical tensioning techniques. Tensioning techniques are transient or steady-state, applied before or during welding. Steady-state thermal tensioning is preheating or/and cooling before and during welding. Preheating the component reduces steep thermal gradients and minimises plastic strain causing RS [58]. Transient thermal tensioning applies hot or cold spots, following the heat source in front or behind. Thermal steady-state and transient techniques [59–68] were extensively investigated. However, thermal tensioning techniques have limitations. The application of heat to large components can be difficult, and the local heat sink method can contaminate the weld. In addition, thermal tensioning techniques have multiple parameters, which are difficult to control during practical application. Practical implementation of this technique requires a lot of trials to find optimal parameters.

Mechanical tensioning to reduce RS and distortion were developed to overcome the limitations of thermal methods. Steady-state mechanical tensioning is an effective method to reduce RS and distortion in relatively thin and linear parts [69], but application of this technique to thick and large welds or complex shaped geometries could be problematic.

Localised roller tensioning is a versatile and cheap method for modification of RS in the welds [70]. The first reported research was conducted in Russia by Kurkin

et al. [71,72]. Researchers found that rolling is an effective way to reduce RS and distortion in welds. Kurkin et al. [72] compared in-situ rolling and post-weld rolling and demonstrated that the latter reduces distortion much more efficiently. Contrarily, in-situ rolling was found effective to eliminate RS in thin plates in the research by Yang and Dong [61]. Altenkirch et al. [70] conducted experiments and Wen et al. performed numerical simulations [73] and they all found that the efficacy of RS reduction is proportional to the rolling load. Sule et al. [74] evaluated the efficacy of post-weld rolling to reduce RS in thick multi-layer welded AISI Type 304L austenitic stainless steel joint. Post-weld rolling significantly reduces the tensile RS caused by the weld thermal cycle, and the RS converts to be compressive in the roller contact area. As a result, the material deforms and RS relieves in whole thickness of the weld. Coules et al. [75] investigated the effect of post-weld rolling with various roller designs on RS in 6 mm thick single pass weld. High pressure rolling (150 kN) was conducted after cooling of weld to ambient temperature. Two types of rollers were used in the research: rollers that applied load to the weld seam and rollers applied the load in the vicinity of the weld (sides of the weld seam). Due to high rolling loads, both rollers induce extensive plastic deformation, but the roller design do not influence the distribution of RS.

The stress engineering techniques for mitigation of RS and distortion in the conventional welding field can be considered for the WAAM components' application because the same arc deposition processes are utilised, causing similar heat inputs. However, in conventional welds, the heat flow/conduction and mechanical restraint is larger due to joint members' influence. This leads to a different distribution of RS.

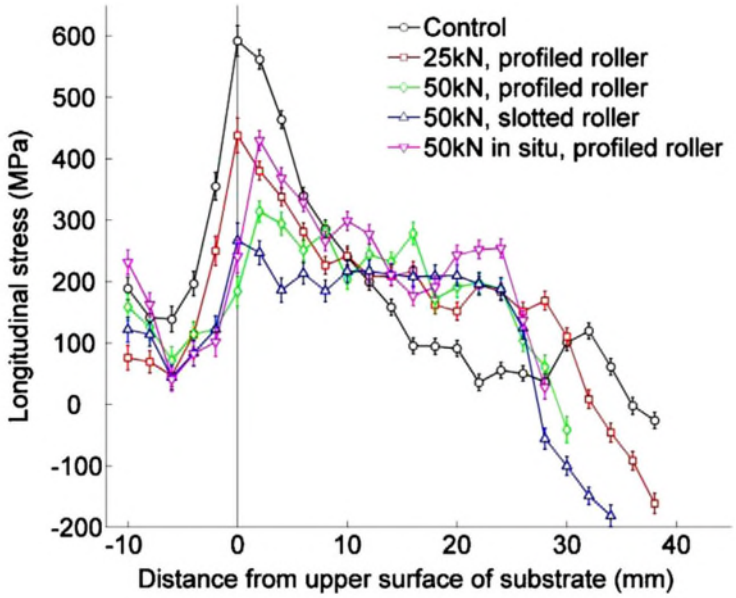

Figure 3-5 Longitudinal RS in the steel WAAM wall; as-built (control plot), inter-pass and in-situ rolled with profiled and slotted rollers at 25 kN and 50 kN loads. Measurement was conducted in unclamped condition, starting from bottom of substrate by neutron diffraction method [24].

In the last decade, localised rolling is widely implemented to alleviate RS and distortion in WAAM experiments. Colegrove et al. [24] used profiled (roller with a concave surface) and slotted rollers with loads ranging from 25 kN to 75 kN to reduce RS and distortion in mild steel WAAM components. The slotted roller was developed to create lateral restraint during rolling and to promote more significant deformation in the longitudinal direction. Several rolling strategies were investigated: rolling after every layer deposition, rolling after deposition of every four layers and rolling of the last layer only (post-build rolling). In-situ rolling, as carried out during deposition of each layer, was investigated as well. Normally, the samples were firmly clamped during the WAAM deposition and rolling. The RS and distortion were measured after removal of clamps. All rolling strategies, apart from in-situ rolling, demonstrated a large reduction of tensile longitudinal RS at the border between substrate and wall, Figure 3-5**Error! Reference source not found.**. The largest RS reduction from 650 MPa to 250 MPa was observed in samples using slotted rollers, refer to Figure 3-5**Error! Reference**

source not found.. Equipment for WAAM deposition and rolling are shown in Figure 3-6**Error! Reference source not found.**.

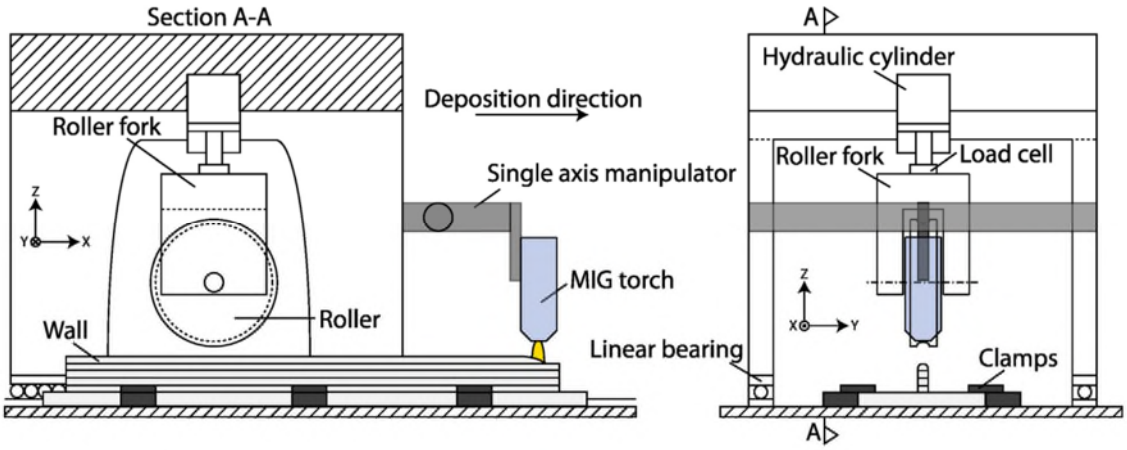

Figure 3-6 Schematic representation of equipment for WAAM deposition and rolling [24].

The results of profiled rollers demonstrated the trend that the final distortion was reduced with increase of rolling load. Slotted rollers were found even more effective to reduce distortion, Figure 3-7. Interestingly, the sample that was post-build rolled with profiled roller had a similar distortion to the inter-layer rolled sample (Figure 3-7, 50 kN roller force, profiled roller LL and profiled roller).

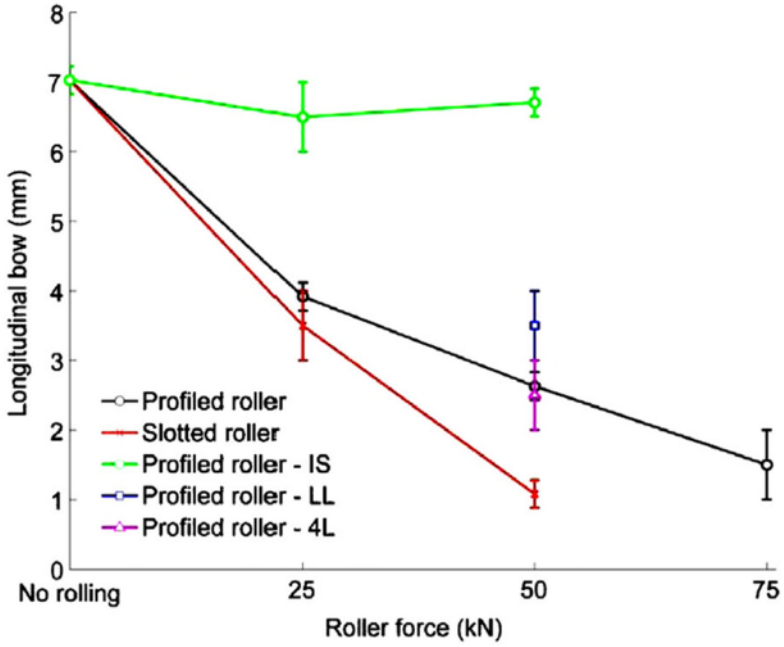

Figure 3-7 Maximum out-of-plane distortion after rolling with profiled and slotted rollers versus rolling load (IS – in situ rolled, LL – rolled last layer only, 4L – rolled every 4 layers) [24].

Colegrove et al. [76] and Martina et al. [77] investigated inter-layer rolling with flat and profiled rollers of Ti-6Al-4V WAAM components. For both rollers, distortion decreases with an increase of rolling load, but similar to steel components [24] the distortion was not eliminated completely.

Vertical rolling applied to WAAM is found less effective to reduce RS and distortion, compared to conventional welds. In conventional welds, due to restraining effects caused by the parent material, rolling load caused large deformation in the deposition direction. In WAAM components, due to the absence of side restraint, rolling load caused significant deformation in transversal direction. To overcome this side effect of vertical rolling, Hönnige et al. [78] developed a side rolling technique. After deposition, the clamped WAAM wall turned horizontally and was rolled from one side. During side rolling, the plastic deformation in transversal direction was limited by adjacent deposited layers, causing large strain in longitudinal direction. In Ti-6Al-4V WAAM side rolling mitigates RS and completely eliminates distortion. In a further study, Hönnige et al. [79] compared the efficiency of side rolling with vertical inter-layer

rolling. Measurements with neutron diffraction demonstrated significantly larger reduction of RS in side rolled samples compared to vertical rolled ones. Side rolled samples were found virtually unchanged in wall dimensions and showed decreased waviness. However, they found that side rolling is not practical for real applications. This technique can be applied only to flat or round-shaped WAAM walls.

3.3 Numerical models of WAAM deposition and rolling

Finite Element Analysis (FEA) is popular for simulation of complex material interactions, which occur during manufacturing processes. FEA is proven a robust method for thermal-mechanical simulation of WAAM process [80–88]. Plasticity theories are implemented in FEA, including strain rate dependence, elasto-plastic constitutive behaviour and thermal effects to allow simulation of material deformation during rolling, predicting distribution of RS and strains evolving under the roller [89,90]. Thermal-mechanical modelling of WAAM deposition and post-build rolling would reduce the experimental effort, the time required for process development, and the equipment cost involved in experiments.

3.3.1 Simulation of welding process

As it was discussed earlier, the thermal deposition cycle is the main reason for the development of RS in AM. Therefore, realistic simulation of the welding process is a necessary condition for accurate prediction of RS distribution. Two main mathematical approaches exist for solution of the welding process simulation: Analytical and Numerical approaches. In general, analytical and numerical approaches are different ways to solve the same governing differential equation of heat conduction, which are presented in Equation (3-2) [91]:

$$\rho C_p \frac{\partial T}{\partial \tau} = \frac{\partial}{\partial x}\left(k\frac{\partial T}{\partial x}\right) + \frac{\partial}{\partial y}\left(k\frac{\partial T}{\partial y}\right) + \frac{\partial}{\partial z}\left(k\frac{\partial T}{\partial z}\right) + \dot{q} \qquad \textbf{(3-2)}$$

where k is thermal conductivity, c_p is specific heat, ρ is density, T is the temperature and $\dot{q}$ is the heat source term.

The solution is called analytical when at least one solution can be expressed in "closed form" in terms of known constants, functions, etc. Analytical solution of heat conduction PDE, Equation (3-2), is usually obtained with use of Green's function [92]. The result of analytical calculation is the exact solution of the differential equation, which exists only for simple geometries, idealised heat sources and temperature-independent material properties due to simplification made in the analysis [92]. The method offers very low computational time required for obtaining a solution [93].

The numerical method allows the solution of a PDE, which describes welding phenomena approximately. The simulated object shall be discretised into elements, with a defined shape, number of nodes and shape function. When implementing Equation (3-2), a series of algebraic equations are developed for solving the transient heat diffusion problem [92]. Finite Element Analysis (FEA) has higher flexibility than the analytical method, but the output of analysis are approximated solutions, which depend on the type of element used and mesh density. Selection of correct element type requires extensive experience. FEA provides more accurate results when the mesh is refined sufficiently, especially in area of heat source application. However, mesh refinement increases the computational time significantly [92]. Nonlinearities like temperature dependent thermo-physical properties of materials and "complex" geometries can be solved with FEA. Transient state thermo-mechanical simulations can be conducted as well. This makes FEA highly suitable for the simulation of welding processes [92,94].

For analytical solution, Rosenthal [94,95] adopted the heat conduction equation for welding simulation. Equation (3-3) [96] gives an analytical solution for the temperature distribution produced by steady-state moving point heat source during welding of infinitely thin plates. The temperature field, generated by the point heat source can be obtained by:

$$T - T_0 = \frac{q}{2\pi kR} e^{-\frac{v(w+R)}{2a}} \quad \textbf{(3-3)}$$

where T is temperature, T_0 is initial temperature, k is thermal conductivity, R is distance to the center of the arc, q is net heat input per unit time (power), v is travel speed, w is distance in x direction in a moving coordinate of speed v and a is thermal diffusivity.

Rosenthal's point heat source assumption is imperfect due to the singularity of temperature at the heat source centre and steady-state assumption. As a result, there is a significant discrepancy between computed and experimental results, particularly in the fusion and heat affected zones [97].

Heat distribution for the first time was proposed by Pavelic et al. [98], who proposed a Gaussian distribution of heat flux on the surface. The Gaussian heat distribution model provided more accurate prediction of the thermal field in the heat affected zone and fusion zone [99,100]. Gaussian distribution is defined by the following Equation (3-4) [98]

$$q(r) = q(0)e^{-Cr^2} \tag{3-4}$$

where $q(r)$ is the surface flux at radius r (W/m^2), $q(0)$ is the maximum flux at the center of the heat source (W/m^2), C is the concentration coefficient (m^{-2}) and r is the radial distance from the centre of the heat source (m). Gaussian heat distribution source of Pavelic et al. [98] is represented in Figure 3-8.

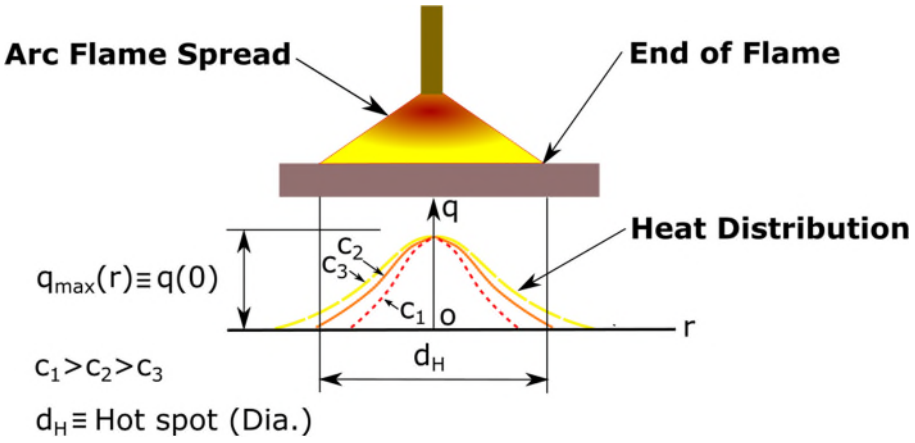

Figure 3-8 Gaussian heat distribution model of Pavelic et al. [98] (adapted from Ref. [97]).

Gaussian distribution heat source model demonstrates higher accuracy than Rosenthal's solution-based model, but it is still unsuitable for simulation of deep penetration fusion welding processes. Computed results have significant error compared to those experimentally obtained. Such inaccuracy can be explained by the fact that Gaussian distribution thermal model applies flux to the surface only and does not simulate heat distribution volumetrically throughout the weld puddle [97].

The first three-dimensional volumetric heat source model with a Gaussian distribution of heat flux in a volume of the molten zone was developed by Goldak et al. [97]. The model allowed the simulation of deep and shallow penetration welds. The shape of the heat source is double-ellipsoidal. This assumption allows taking into account the three-dimensional shape of a real molten pool. The double-ellipsoidal heat source model allows to simulate very steep temperature gradients at the front of the arc and lower gradient at the rear edge of the arc. The front half of the ellipsoid is the heat source for simulation of the leading edge of the arc and the rear half is the heat source for simulation of the trailing edge of the arc.

The double-ellipsoidal heat source developed by Goldak et al. [97] is described with Equation (3-5) and Equation (3-6), which define the power density for front and rear ellipsoids of the model separately.

$$q_f = \frac{6\sqrt{3}\, f_f Q}{\pi\sqrt{\pi} bc a_f} e^{\left[-3\left(\frac{x^2}{a_f^2}+\frac{y^2}{b^2}+\frac{z^2}{c^2}\right)\right]} \quad \textbf{(3-5)}$$

$$q_r = \frac{6\sqrt{3}\, f_r Q}{\pi\sqrt{\pi} bc a_r} e^{\left[-3\left(\frac{x^2}{a_r^2}+\frac{y^2}{b^2}+\frac{z^2}{c^2}\right)\right]} \quad \textbf{(3-6)}$$

$$f_f + f_r = 2$$

where f_f and f_r is heat in the front and rear ellipsoidal portions, Q is energy input (absorption efficiency is considered), a, b, c are independent geometrical parameters of the heat source shape. a_f and a_r represent the length of the front

and rear portions of the ellipsoid, b is width and c is the depth of the heat source, see Figure 3-9.

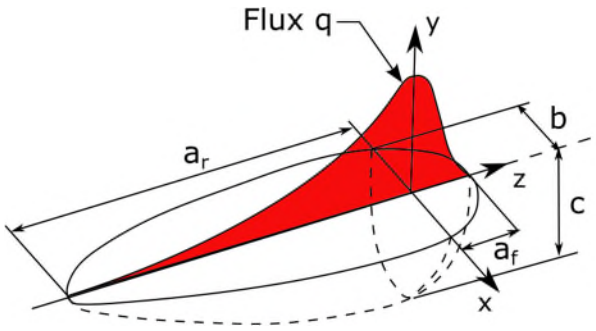

Figure 3-9 Double-ellipsoidal heat source model. Definition of geometrical parameters (adapted from Ref. [97]).

Goldak et al. [97] compared the simulation results of double-ellipsoidal heat source with Gaussian distribution model [100]. It was found that double-ellipsoidal heat source model more accurately predicts the temperature distribution field. Goldak's heat source model is used extensively in WAAM models to simulate deposition with Cold Metal Transfer (CMT) [54], Gas Metal Arc Welding (GMAW) [81,83]; in other AM models with Gas Tungsten Arc Welding (GTAW) [88], GMAW [80] and laser deposition [101]. Temperature fields predicted by these models accurately conforms with experimentally obtained results. Accurate selection of heat source model parameters is crucial. Goldak et al. [97] suggest to take dimensions from cross-sections of the weld and solidified weld pool. Transient temperature distribution predicted by thermal model of WAAM with Goldak's heat source [88] is shown in Figure 3-10.

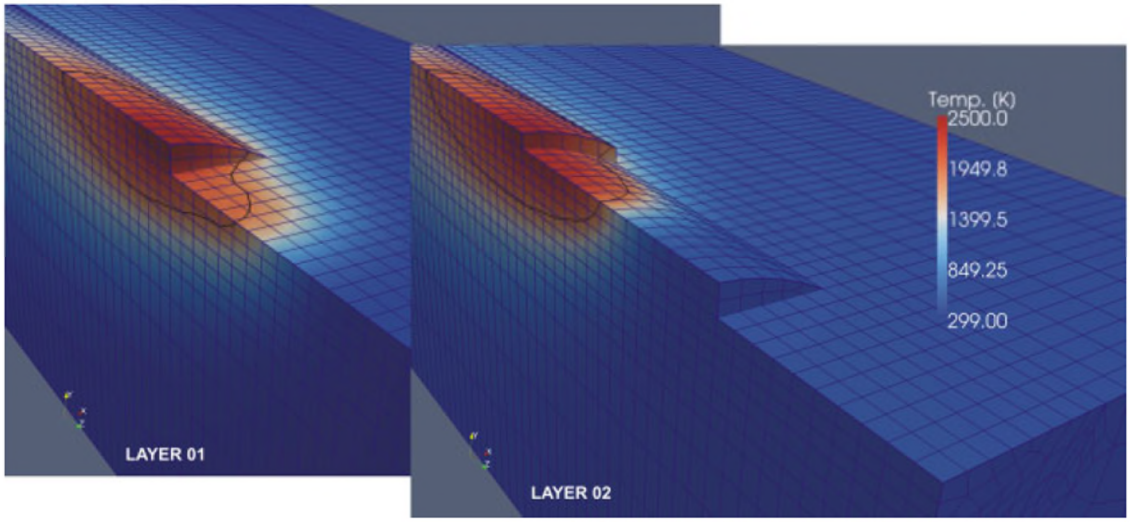

Figure 3-10 Transient temperature distribution and addition of material by element "birth" technique during WAAM deposition [88].

3.3.2 Simulation of material addition

Simulation of material deposition during multi-layer AM can be conducted in several ways. Mughal et al. [102] developed a two dimensional model of a solid free form fabrication process, which specified negligible material properties to elements that were not yet "deposited" to the substrate. This is called the "quiet" material addition method. This method introduces errors in solution and makes intricate selection of such spurious properties. Ding et al. [54], Anca et al. [88] and Xiong et al. [81] utilised element "birth" in their three-dimensional AM deposition models, and this method is similar to the "inactive" element addition approach of Lindgren et al. [103]. In Ding et al.'s model, elements are activated sequentially in front of the traveling heat source, but an even more accurate approach was proposed in Anca's model. A mesh generator activated elements, when their temperature was reaching liquidus (Figure 3-10). However, Ding et al. [82] found that simultaneous activation of the whole layer instead of sequential activation, insignificantly impaired the accuracy of the solution. The same modelling approach was used by Denlinger et al. [101]. Lindgren et al. [103] compared the accuracy of "quiet" and "inactive" element addition techniques. Both techniques have similar accuracy, but the inactive technique requires less computational resources for the model to be solved.

3.3.3 Simulation of RS generation

The mechanical model's response is caused by expansion and contraction of the material during the thermal deposition cycle and restricting effect of boundary conditions. As was found by Ding et al. [54] and Colegrove et al. [24], accurate selection of boundary conditions (simulation of work clamps/constraints) is essential for obtaining accurate RS distribution. The formulation of mechanical models can be different and depends on the material simulated. Cao et al. [104] and Ding et al. [54] created mechanical models for mild steel with only elastic-plastic behaviour without consideration of phase transformation. Predicted longitudinal RS distributions in the WAAM component before and after clamps removal are shown in Figure 3-11 and Figure 3-12.

In Chiumenti et al.'s model [84] for the deposition of Nickel superalloy 718, in addition to elastic-plastic behaviour, the solid-state phase transformation and strain hardening effect, annealing effect, viscous and mushy state behaviour at temperatures close to melting temperature are included in the mechanical analysis.

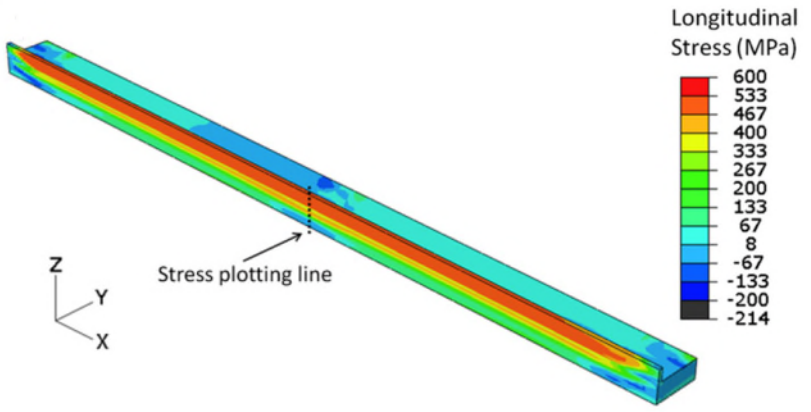

Figure 3-11 Predicted longitudinal RS in the clamped WAAM component [54].

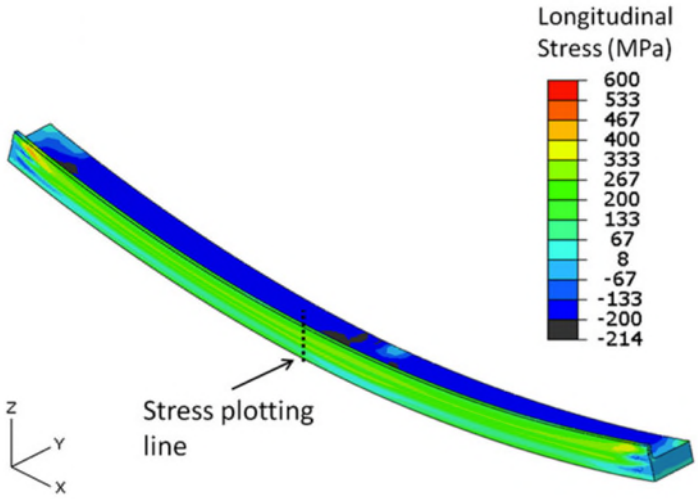

Figure 3-12 Predicted longitudinal RS in the WAAM component after removal of clamps [54].

3.3.4 Simulation of the rolling process

Simulation of the rolling process is intricate and requires careful selection of rolling model's parameters. A limited number of publications were found in the literature related to the post-build rolling simulations of WAAM components [105,106]. Multiple researches investigated numerically burnishing [107–110], deep rolling [111–114], hot and cold manufacturing rolling processes [115,116] and rolling of weld seams [117,118]. Similar to post build-rolling of WAAM, all these processes rely on the introduction of plastic deformation in the rolled components. Consequently, all reported models of rolling tackled some challenges in common.

3.3.4.1 Finite elements for rolling simulation

Rolling is a highly nonlinear contact problem that usually includes large deformations and requires a fine mesh for model convergence [111,112,117] and obtaining accurate simulation results [119]. The current tendency in 3D rolling modelling is to use hexahedral elements (Figure 3-13) instead of tetrahedral to improve the accuracy of obtained results [105,112,115–118,120–123]. As suggested by Benzley et al. [124] and Abaqus FEA Analysis User's Guide [119], hexahedral elements perform better than tetrahedral because of obtaining better

convergence rate and computational efficiency [125]. Still, tetrahedral elements are less sensitive to initial shape, but distorted hexahedral elements have lower accuracy [119].

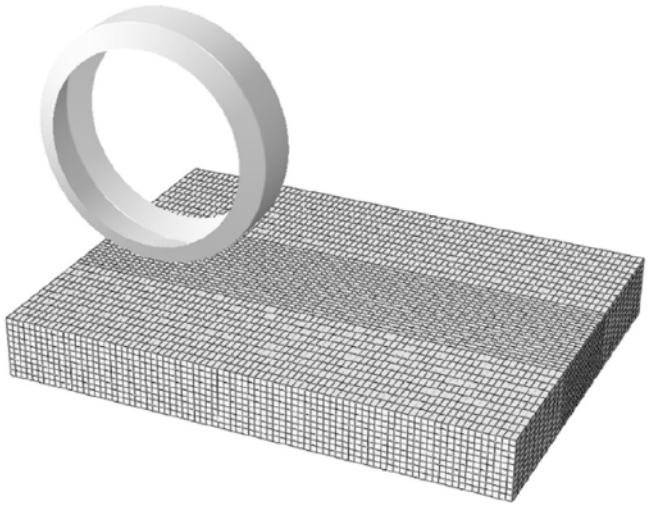

Figure 3-13 Hexahedral elements and rigid roller in rolling model for thick plate [118].

3.3.4.2 Roller simulation

In most of the reported models, the rollers are simulated as rigid/non deformable [111–113,115,116,118,120,122,123], Figure 3-13. Such modelling assumption can be made, because during experimental work rollers/tools made from materials that are much harder (tungsten carbide [111] or H13 steel [123]), than the material to be rolled. Analytically a rigid surface is a geometric surface, described by straight or curved lines and discretisation of the surface is not required. In the numerical implementation, a rigid surface provides lower contact noise and better approximation to physical interaction where FEA contact algorithms are applied [119,126]. The expected deformation of the elastic roller was found negligible and did not affect the accuracy of the solution [112] significantly. Abbaszadeh et al. [105] modelled rollers as elastically deformable to increase the accuracy of predicted results; nevertheless, differences in RS and force predictions were just detectable but insignificant at large deformations [105].

3.3.4.3 Contact interaction simulation

Basically, the Coulomb friction model is widely used for simulation of contact interaction [105,114,116–118,120,122,123]. The extended Coulomb friction model was developed to simulate slip-stick effect, which occurs during deep rolling at high loads [113]. Nevertheless, it was found that that the predicted RS distribution is not sensitive to the friction coefficient between roller and component [105,117,118], and the differences become noticeable only at high rolling loads (150 kN) [117]. A friction coefficient of 0.1 for simulation of lubricated contact between roller and component was suggested by Stolarski and Tobe [127]. This value was adopted by many researchers for simulation of lubricated contact [114,116,123]. A friction coefficient of 0.5 for unlubricated contact between steel and aluminium was suggested by Hutchings and Shipway [128], by Marks [129] and used in many rolling models [117,118].

3.3.4.4 Material plasticity models for rolling simulation

Correct selection of material plasticity models, used to characterise material behaviour, is important for accurate simulation of the rolling process. RS distributions, predicted by elastic-plastic models, are sensitive to the chosen plasticity model [122,130,131]. In general, for simulation of rolling/ burnishing processes two types of plasticity models are used: isotropic and kinematic hardening models. Isotropic hardening models imply that increases in equivalent yield stress in both tension and compression during cyclic loading, while kinematic hardening models imply that yielding in one direction reduces yield stress in the other directions [119]. Isotropic hardening models are used for general cases, where gross straining of material is involved [119]. The hardening effect was assumed isotropic in the models by Hassani-Gangaraj et al. [112], Cozzolino et al. [117], Balland et al. [120] and Pan et al. [123]. Kinematic hardening models are used to simulate cyclic loading of metals, which takes place during high-pressure rolling [117,122]. Kinematic hardening material formulation was used in the models by Bijak- Żochovski et al. [132] and Beghini et al. [111]. In the models developed by Perenda et al. [114] and Trauth et al. [113], the material behaviour is characterised by combining nonlinear kinematic and

isotropic hardening to simulate the Bauschinger effect. Coules et al. [118] modelled material using the nonlinear kinematic Chaboche hardening law [133,134]. Lan et al. [116] compared combined nonlinear isotropic/kinematic hardening and isotropic hardening models during plastic analysis of cold rolling of bearing race. Combined nonlinear isotropic/ kinematic hardening models more accurately predicted surface tangential RS, but the underestimated axial RS. Elasticity is usually modelled applying Hooke's law [105,115,117,120,122].

3.3.4.5 Clamping

During experimental and numerical modelling studies of RS generation in WAAM components it was found that the accuracy of predicted RS significantly depends on the accurate simulation of the clamping system used experimentally [24,86]. In analogy, it is natural to assume that the accuracy of predicted rolling model RS distribution will also depend on the clamping system simulated. As circular deformable component of the deep rolling models is short, a reasonable assumption is that the bottom of the component is constrained in all direction [112,113]. For an accurate rolling simulation of long parts like weld seams and WAAM walls more complex arrangements are required. Cozzolino et al. [117] developed a relatively long (465 mm) weld seam rolling model, in which the friction contact interaction was simulated between the bottom of the substrate and the worktable. To accurately simulate vacuum clamps used during the experiments, 1 atm pressure was applied to the bottom of the substrate in worktable direction. Still, due to the shortness (100 mm) of the deformable component in the WAAM rolling model of Abbaszadeh et al. [105], the bottom of the substrate was constrained for movement in all directions. However, their model was not verified against experimental studies and hence the influence of clamp simplification on the accuracy of results was left unknown.

3.3.4.6 Solution method

Implicit analysis was designed for efficient simulation of smooth nonlinear problems and used successfully for solving contact problems during rolling simulations [105,117]. Transient longitudinal PS distribution and longitudinal RS distribution at various rolling loads, as predicted by weld bead rolling model with

implicit solver, are shown in Figure 3-14 and Figure 3-15. However, implicit solvers can encounter convergence issues, where analysis involves highly nonlinear plasticity or contact problems with large deformation of elements [135].

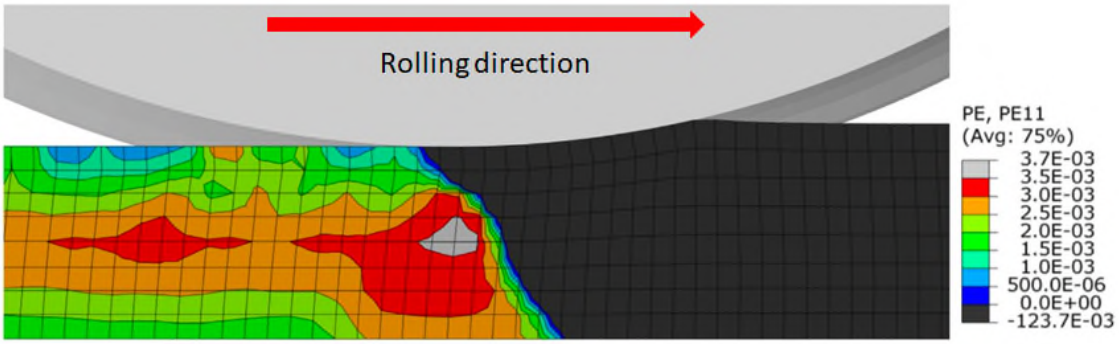

Figure 3-14 Predicted longitudinal plastic strain distribution during localised rolling of a weld bead [117].

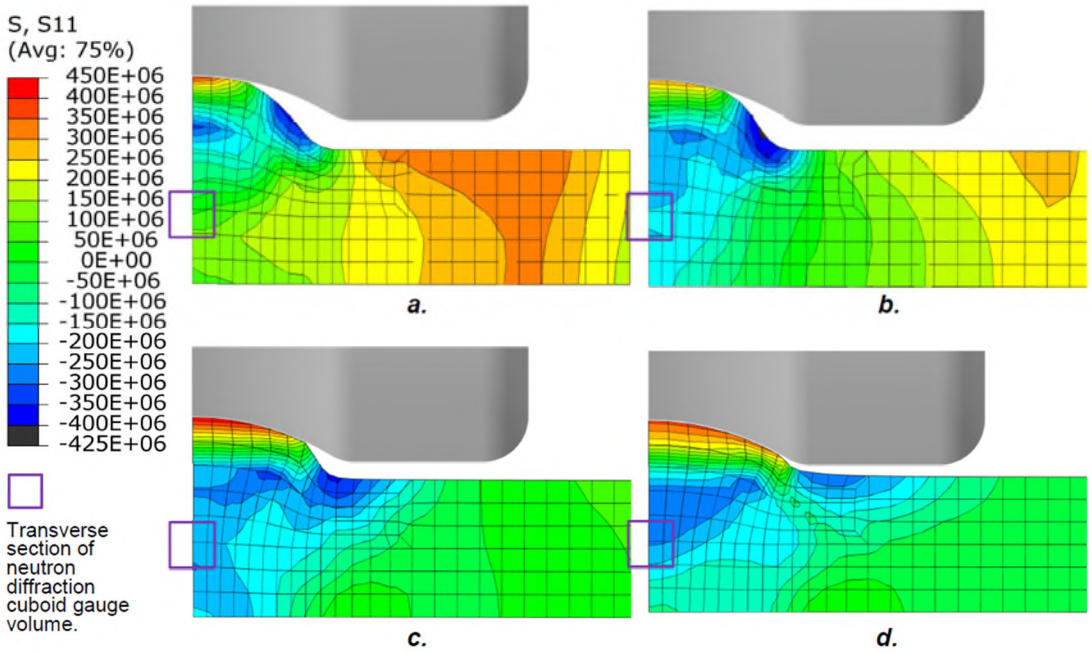

Figure 3-15 Predicted longitudinal RS in a weld bead rolled at a) 25kN, b) 50 kN, c) 100 kN and d) 150 kN rolling loads [117].

Explicit analysis method was designed to solve dynamic problems like impact or blast. It was found highly suitable for solving complex contact interactions between deformable bodies or where large material deformation is involved. The method demonstrates increased robustness/convergence and greater suitability

for parallel calculations using multiple processors [135]. Nevertheless, Harewood et al. [135] found that for simple loading conditions with rigid bodies involved in contact simulation, the implicit analysis solver requires less computational time than the explicit analysis solver. Oliver et al. [136] suggested that the implicit method is more accurate and efficient, although less robust than the explicit method. Explicit method was utilised for the simulation of deep rolling of railway axles [112] and turbine blades [113], as well as for hot [126] and cold rolling [116].

Eulerian analysis is another method for efficient simulation of large deformations. In traditional Lagrangian analysis, the material becomes closely associated with elements; hence, the material moves with elements deformation. In case of large deformation, distorted Lagrangian elements lose accuracy. Contrarily to that, in Eulerian analysis the material flows through the boundaries of non-deformable elements, which remain stationary. Element quality, which is inherent to deformable elements, is not associated with Eulerian analysis. Due to this the Eulerian analysis is efficient for solving large deformation problems [119]. During rolling simulation, using Eulerian analysis, the mesh is attached to the rotating roller and the material is deformed by the roller's action and is drawn through a non-deformable mesh. The top of the component is pre-shaped for contact with the roller and approximately corresponds to the region geometry for the steady state, which will be achieved at the end of the analysis [137]. Maniatty at al. [138] presented an Eulerian analysis method to solve large strain rate problems for simulations of rolling and extrusion processes. Mixed Eulerian-Lagrangian method was used for hot rolling process simulation by Synka et al. [139] and further development of this method was conducted by Vetyukov et al. [140].

3.3.5 State of the art: post-build rolling simulation for WAAM components

Two studies reported simulation of post-build rolling for WAAM components. Abbaszadeh et al. [105] investigated the influence of rolling load and radius of an inverted roller (convex roller) on RS and plastic strain (PS) distributions in WAAM deposited components with S355JR steel, Ti-6Al-4V titanium and AA2319 aluminium alloys. Tangestani et al. [106] studied the effects of profiled roller

(concave roller) and slotted roller design and rollers' penetration (associated with rolling load) on RS distribution in S355JR steel WAAM components. Reduced-size models were employed in both studies; refer to Figure 3-16. Roller penetration to the WAAM walls was simulated through displacement-controlled loading. Abbaszadeh et al. [105] used elastically deformable rollers, while Tangestani et al. [106] assumed rigid rollers. The models are discretised with 8 node linear hexahedral elements. The fine mesh was used in the region under the roller, where deformation was expected to be concentrated, and coarser mesh in the substrate. "Initial stress" approach was used to represent RS generated by WAAM deposition. However, Abbaszadeh et al. [105] used experimentally measured RS, whereas Tangestani et al. [106] used a validated thermo-mechanical WAAM model to generate RS.

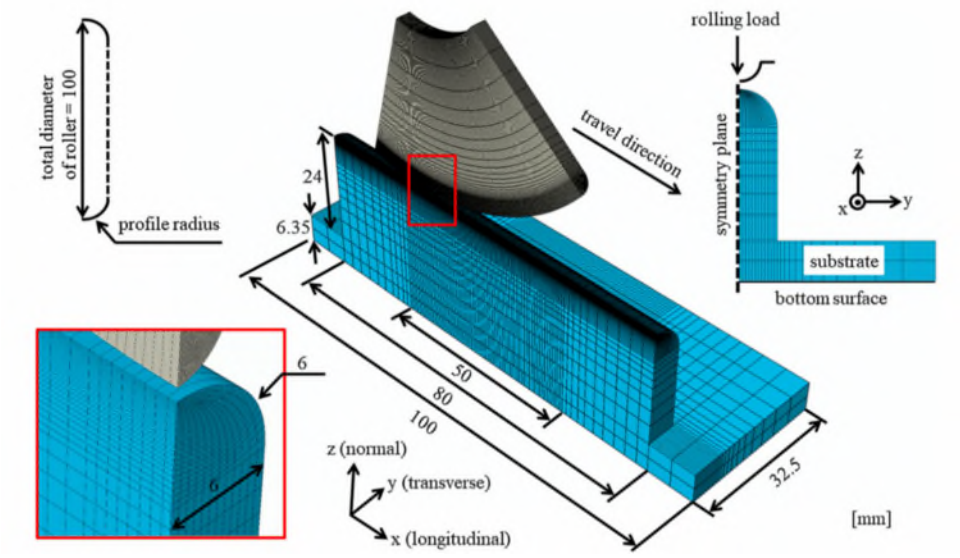

Figure 3-16 Schematic representation of the post-build rolling model for WAAM components [105].

The studies demonstrated large influence of rolling load / rolling depth on RS and PS distributions in the WAAM wall. Higher rolling load or deeper roller's penetration caused increase in the depth of compressive RS region [105,106], Figure 3-17. Interestingly, rolling with all types of rollers and at all rolling loads induced tensile RS under the rolled surface [105,106]. The increase of the rolling load also increases the magnitude and depth of induced PS [105]. Variation of

rollers' profile radius has minor influence on RS distribution [105,106], but PS changed only 2 mm below the rolled surface [105].

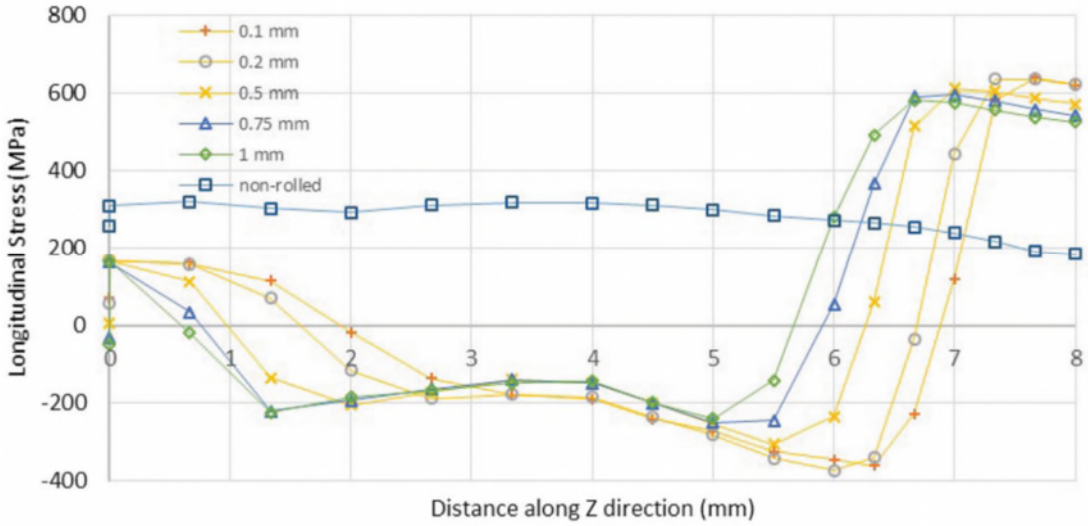

Figure 3-17 Variation of longitudinal RS distribution with increase of roller's penetration [106].

Tangestani et al. [106] found that slotted rollers are most effective for RS mitigation compared to profiled rollers. Slotted roller induces a larger magnitude of longitudinal compressive RS to a greater depth and does not cause any lateral deformation, in contrast to what predicted after rolling with profiled rollers.

However, these previous models did not simulate accurately rolling process, as the PS distribution caused by WAAM deposition was not included in the models' initial conditions. Initial PS in the WAAM wall could affect strain hardening during rolling and, as a result, final RS distribution could change. The effect of the rolling parameters and roller design on final RS and PS distributions was presented in these previous models, but the mechanism of the predicted influence was not investigated. To gain a better understanding of RS mitigation mechanism in WAAM, the impact of rolling parameters needs to be comprehensively studied and explained.

3.4 Summary

The literature review summarised RS formation's main contributors and mechanisms in welds and AM produced components, as well as the RS and distortion mitigation methods. Main numerical methods for simulation of thermal deposition, RS generation and rolling process were summarised and discussed. This knowledge is used as a background for the development of new numerical models and analysis of the obtained data. However, the survey of published experimental and numerical studies on high-pressure rolling for WAAM parts demonstrated some gaps in research and knowledge, as highlighted in Section 1.2.

3.5 References

1. Klepeisz J., Veeck S. The production of large structural titanium castings. JOM Journal of the Minerals, Metals and Materials Society. Springer Boston; 1997. 18–20 p. Available at: DOI:10.1007/s11837-997-0006-7

2. Baufeld B., Van Der Biest O. Mechanical properties of Ti-6Al-4V specimens produced by shaped metal deposition. Science and Technology of Advanced Materials. 2009; 10(1). Available at: http://www.scopus.com/inward/record.url?eid=2-s2.0-79551694565&partnerID=40&md5=3c94495f9285e7508af54e2a6987335f

3. Mok SH., Bi G., Folkes J., Pashby I. Deposition of Ti-6Al-4V using a high power diode laser and wire, Part I: Investigation on the process characteristics. Surface and Coatings Technology. 2008; 202(16): 3933–3939. Available at: DOI:10.1016/j.surfcoat.2008.02.008

4. Wang F., Mei J., Jiang H., Wu X. Laser fabrication of Ti6Al4V/TiC composites using simultaneous powder and wire feed. Materials Science and Engineering: A. 2007; 445–446(0): 461–466. Available at: DOI:10.1016/j.msea.2006.09.093

5. Al-Bermani S., Blackmore M., Zhang W., Todd I. The origin of microstructural diversity, texture, and mechanical properties in electron beam

melted Ti-6Al-4V. Metallurgical and Materials Transactions A. Springer Boston; 2010. 3422–3434 p. Available at: DOI:10.1007/s11661-010-0397-x

6. Mok SH., Bi G., Folkes J., Pashby I., Segal J. Deposition of Ti-6Al-4V using a high power diode laser and wire, Part II: Investigation on the mechanical properties. Surface and Coatings Technology. 2008; 202(19): 4613–4619. Available at: DOI:10.1016/j.surfcoat.2008.03.028

7. Katou M., Oh J., Miyamoto Y., Matsuura K., Kudoh M. Freeform fabrication of titanium metal and intermetallic alloys by three-dimensional micro welding. Materials & Design. 2007; 28(7): 2093–2098. Available at: DOI:10.1016/j.matdes.2006.05.024

8. Baufeld B., Brandl E., Van Der Biest O. Wire based additive layer manufacturing: Comparison of microstructure and mechanical properties of Ti-6Al-4V components fabricated by laser-beam deposition and shaped metal deposition. Journal of Materials Processing Technology. 2011; 211(6): 1146–1158.

9. Baufeld B., der Biest OV., Gault R. Additive manufacturing of Ti-6Al-4V components by shaped metal deposition: Microstructure and mechanical properties. Advanced Component Manufacture from Light Materials International Conference on Materials for Advanced Technologies 2009. 2010; 31, Supple(0): S106–S111. Available at: DOI:http://dx.doi.org/10.1016/j.matdes.2009.11.032

10. Tan Zhi'En E., Pang JHL., Kaminski J. Directed energy deposition build process control effects on microstructure and tensile failure behaviour. Journal of Materials Processing Technology. August 2021; 294: 117139. Available at: DOI:10.1016/j.jmatprotec.2021.117139

11. Wang J., Chew YX., Wu WJ., Jing W., Tan X., Liu E., Bi G., Tor SB., Tan SYJ., Lee YH., Merchant A., Weng F., Liu Y. Microstructure and mechanical properties of ASTM A131 EH36 steel fabricated by laser aided additive manufacturing. Materials Characterization. April 2021; 174: 110949. Available at: DOI:10.1016/j.matchar.2021.110949

12. Karayel E., Bozkurt Y. Additive manufacturing method and different welding applications. Journal of Materials Research and Technology. September 2020; 9(5): 11424–11438. Available at: DOI:10.1016/j.jmrt.2020.08.039

13. Liu J., Xu Y., Ge Y., Hou Z., Chen S. Wire and arc additive manufacturing of metal components: a review of recent research developments. The International Journal of Advanced Manufacturing Technology. November 2020; 111(1–2): 149–198. Available at: DOI:10.1007/s00170-020-05966-8

14. Williams SW., Martina F., Addison AC., Ding J., Pardal G., Colegrove P. Wire + Arc Additive Manufacturing. Materials Science and Technology. 2 May 2016; 32(7): 641–647. Available at: DOI:10.1179/1743284715Y.0000000073

15. Sing SL., An J., Yeong WY., Wiria FE. Laser and electron-beam powder-bed additive manufacturing of metallic implants: A review on processes, materials and designs: Laser and electron-beam additive manufacturing of metallic implants. Journal of Orthopaedic Research. March 2016; 34(3): 369–385. Available at: DOI:10.1002/jor.23075

16. Kumar S. Selective laser sintering: A qualitative and objective approach. The Journal of The Minerals, Metals & Materials Society (TMS). October 2003; 55(10): 43–47. Available at: DOI:10.1007/s11837-003-0175-y

17. Gao W., Zhang Y., Ramanujan D., Ramani K., Chen Y., Williams CB., et al. The status, challenges, and future of additive manufacturing in engineering. Computer-Aided Design. December 2015; 69: 65–89. Available at: DOI:10.1016/j.cad.2015.04.001

18. Yusuf SM., Gao N. Influence of energy density on metallurgy and properties in metal additive manufacturing. Materials Science and Technology. 24 July 2017; 33(11): 1269–1289. Available at: DOI:10.1080/02670836.2017.1289444

19. Zhang J., Jung Y-G. (eds.) Additive manufacturing: materials, processes, quantifications and applications. Cambridge, MA: Butterworth-Heinemann; 2018. 352 p.

20. Liu R., Wang Z., Sparks T., Liou F., Newkirk J. Aerospace applications of laser additive manufacturing. Laser Additive Manufacturing. Elsevier; 2017. pp. 351–371. Available at: DOI:10.1016/B978-0-08-100433-3.00013-0 (Accessed: 28 April 2021)

21. Ader C., Brosemer M., Freyer C., Fricke H., Hennings D., Klocke F., Kühne V., Meiners W., Over C., Pleteit H., Stührmann S., Wirth I., Wirtz T., Wissenbach K. Research on layer manufacturing techniques at Fraunhofer. Solid Freeform Fabrication Symposium (SFF). University of Texas, Austin; 2004. pp. 26–37.

22. Brandl E., Palm F., Michailov V., Viehweger B., Leyens C. Mechanical properties of additive manufactured titanium (Ti-6Al-4V) blocks deposited by a solid-state laser and wire. Materials & Design. 2011; 32(10): 4665–4675. Available at: DOI:10.1016/j.matdes.2011.06.062

23. Frazier WE. Metal Additive Manufacturing: A Review. Journal of Materials Engineering and Performance. June 2014; 23(6): 1917–1928. Available at: DOI:10.1007/s11665-014-0958-z

24. Colegrove PA., Coules HE., Fairman J., Martina F., Kashoob T., Mamash H., et al. Microstructure and residual stress improvement in wire and arc additively manufactured parts through high-pressure rolling. Journal of Materials Processing Technology. 2013; 213(10): 1782–1791. Available at: DOI:http://dx.doi.org/10.1016/j.jmatprotec.2013.04.012

25. Williams S. Metal Additive Layer Manufacture Technology for a Sustainable Future. Cranfield University, Lectures; 2012.

26. Wang F., Williams S., Colegrove P., Antonysamy AA. Microstructure and mechanical properties of wire and arc additive manufactured Ti-6Al-4V. Metallurgical and Materials Transactions A: Physical Metallurgy and Materials Science. 2013; 44(2): 968–977.

27. Martina F., Mehnen J., Williams SW., Colegrove P., Wang F. Investigation of the benefits of plasma deposition for the additive layer manufacture of Ti–6Al–

4V. Journal of Materials Processing Technology. June 2012; 212(6): 1377–1386. Available at: DOI:10.1016/j.jmatprotec.2012.02.002

28. Marinelli G., Martina F., Ganguly S., Williams S. Development of Wire + Arc additive manufacture for the production of large-scale unalloyed tungsten components. International Journal of Refractory Metals and Hard Materials. August 2019; 82: 329–335. Available at: DOI:10.1016/j.ijrmhm.2019.05.009

29. Marinelli G., Martina F., Ganguly S., Williams S. Grain refinement in an unalloyed tantalum structure by combining Wire+Arc additive manufacturing and vertical cold rolling. Additive Manufacturing. March 2020; 32: 101009. Available at: DOI:10.1016/j.addma.2019.101009

30. Asala G., Khan AK., Andersson J., Ojo OA. Microstructural Analyses of ATI 718Plus® Produced by Wire-ARC Additive Manufacturing Process. Metallurgical and Materials Transactions A. September 2017; 48(9): 4211–4228. Available at: DOI:10.1007/s11661-017-4162-2

31. Shen C., Pan Z., Cuiuri D., Roberts J., Li H. Fabrication of Fe-FeAl Functionally Graded Material Using the Wire-Arc Additive Manufacturing Process. Metallurgical and Materials Transactions B. February 2016; 47(1): 763–772. Available at: DOI:10.1007/s11663-015-0509-5

32. Martina F., Ding J., Williams S., Caballero A., Pardal G., Quintino L. Tandem metal inert gas process for high productivity wire arc additive manufacturing in stainless steel. Additive Manufacturing. January 2019; 25: 545–550. Available at: DOI:10.1016/j.addma.2018.11.022

33. Allen, J. An Investigation into the Comparative Costs of Additive Manufacture vs. Machine from Solid for Aero Engine Parts. Manufacturing Technology Rolls-Royce plc; 2006. Available at: https://www.google.com/url?sa=t&rct=j&q=&esrc=s&source=web&cd=&ved=2ahUKEwjEyLimi9TqAhWGFxQKHfBqD58QFjABegQIAxAB&url=https%3A%2F%2Fwww.sto.nato.int%2Fpublications%2FSTO%2520Meeting%2520Proceedings%2FRTO-MP-AVT-139%2FMP-AVT-139-17.pdf&usg=AOvVaw36a3Bt35OUgOYEMrnLk5UM (Accessed: 17 July 2020)

34. What is Residual Stress? TWI. Available at: https://www.twi-global.com/technical-knowledge/faqs/residual-stress (Accessed: 4 September 2021)

35. Szost BA., Terzi S., Martina F., Boisselier D., Prytuliak A., Pirling T., Hofmann M., Jarvis DJ. A comparative study of additive manufacturing techniques: Residual stress and microstructural analysis of CLAD and WAAM printed Ti-6Al-4V components. Materials and Design. 2016; 89: 559–567. Available at: DOI:10.1016/j.matdes.2015.09.115

36. Dai K., Shaw L. Distortion minimization of laser-processed components through control of laser scanning patterns. Rapid Prototyping Journal. 2002; 8(5): 270–276. Available at: DOI:10.1108/13552540210451732

37. Bai X., Zhang H., Wang G. Modeling of the moving induction heating used as secondary heat source in weld-based additive manufacturing. The International Journal of Advanced Manufacturing Technology. 2015; 77(1): 717–727. Available at: DOI:10.1007/s00170-014-6475-2

38. Mercelis P., Kruth J. Residual stresses in selective laser sintering and selective laser melting. Rapid Prototyping Journal. Emerald; 2006; 12(5): 254–265. Available at: DOI:10.1108/13552540610707013

39. Ding D., Pan Z., Cuiuri D., Li H. Wire-feed additive manufacturing of metal components: technologies, developments and future interests. The International Journal of Advanced Manufacturing Technology. 2015; 81(1): 465–481. Available at: DOI:10.1007/s00170-015-7077-3

40. Cheng B., Shrestha S., Chou K. Stress and deformation evaluations of scanning strategy effect in selective laser melting. Additive Manufacturing. Elsevier B.V.; 2016; Available at: DOI:10.1016/j.addma.2016.05.007

41. Vrancken B., Cain V., Knutsen R., Van Humbeeck J. Residual stress via the contour method in compact tension specimens produced via selective laser melting. Scripta Materialia. September 2014; 87: 29–32. Available at: DOI:10.1016/j.scriptamat.2014.05.016

42. Parry L., Ashcroft IA., Wildman RD. Understanding the effect of laser scan strategy on residual stress in selective laser melting through thermo-mechanical simulation. Additive Manufacturing. Elsevier B.V.; 2016; 12: 1–15. Available at: DOI:10.1016/j.addma.2016.05.014

43. Mochizuki M. Control of welding residual stress for ensuring integrity against fatigue and stress corrosion cracking. Nuclear Engineering and Design. 2007; 237(2): 107–123. Available at: DOI:http://dx.doi.org/10.1016/j.nucengdes.2006.05.006

44. Gao H., Dutta RK., Huizenga RM., Amirthalingam M., Hermans MJM., Buslaps T., et al. Pass-by-pass stress evolution in multipass welds. Science and Technology of Welding and Joining. 2014; 19(3): 256–264.

45. Withers PJ., Bhadeshia HKDH. Residual stress part 2 - Nature and origins. Materials Science and Technology. 2001; 17(4): 366–375.

46. Williams S. Lectures, Welding Distortion and Residual Stress. Cranfield University; 2011.

47. Wilson WM., Hao C-C. Residual stresses in welded structures. Illinois, USA: Elsevier; 1946.

48. Ueda Y., Murakawa H., Ma N. Introduction to welding mechanics. Welding deformation and residual stress prevention.

49. Colegrove P., Ikeagu C., Thistlethwaite A., Williams S., Nagy T., Suder W., et al. Welding process impact on residual stress and distortion. Science and Technology of Welding and Joining. 2009; 14(8): 717–725.

50. Woo W., An GB., Kingston EJ., Dewald AT., Smith DJ., Hill MR. Through-thickness distributions of residual stresses in two extreme heat-input thick welds: A neutron diffraction, contour method and deep hole drilling study. Acta Materialia. 2013; 61(10): 3564–3574.

51. Leggatt RH. Residual stresses in welded structures. International Journal of Pressure Vessels and Piping. 2008; 85(3): 144–151.

52. Jones W., Alberry P. A model for stress accumulation in steels during welding. Residual stresses in welded construction and their effects, proceedings of the international conference. London; 1978. pp. 15–26.

53. Rangaswamy P., Griffith ML., Prime MB., Holden TM., Rogge RB., Edwards JM., et al. Residual stresses in LENS® components using neutron diffraction and contour method. Materials Science and Engineering: A. 2005; 399(1): 72–83. Available at: DOI:10.1016/j.msea.2005.02.019

54. Ding J., Colegrove P., Mehnen J., Ganguly S., Sequeira Almeida PM., Wang F., et al. Thermo-mechanical analysis of Wire and Arc Additive Layer Manufacturing process on large multi-layer parts. Computational Materials Science. 2011; 50(12): 3315–3322. Available at: DOI:http://dx.doi.org/10.1016/j.commatsci.2011.06.023

55. Hönnige JR., Colegrove PA., Ganguly S., Eimer E., Kabra S., Williams S. Control of residual stress and distortion in aluminium wire + arc additive manufacture with rolling. Additive Manufacturing. August 2018; 22: 775–783. Available at: DOI:10.1016/j.addma.2018.06.015

56. Conrardy C., Dull R. Control of Distortion in Thin Ship Panels. SNAME-JSP-1997-13-2-83. 1 May 1997; 13(02): 83–92.

57. Cho JR., Lee BY., Moon YH., Van Tyne CJ. Investigation of residual stress and post weld heat treatment of multi-pass welds by finite element method and experiments. Journal of Materials Processing Technology. November 2004; 155–156: 1690–1695. Available at: DOI:10.1016/j.jmatprotec.2004.04.325

58. ASM handbook Welding, brazing and soldering. Materials Park, OH, ASM; 2001. pp. 1094–1103.

59. Huang TD., Conrardy C., Dong P., Keene P., Kvidahl L., DeCan L. Engineering and production technology for lightweight ship structures, Part ii: Distortion mitigation technique and implementation. 2007; 23(02): 82–93. Available at: DOI:https://doi.org/10.5957/jsp.2007.23.2.82

60. Li J., Guan Q., Shi YW., Guo DL. Stress and distortion mitigation technique for welding titanium alloy thin sheet. Science and Technology of Welding and Joining. October 2004; 9(5): 451–458. Available at: DOI:10.1179/136217104225021643

61. Yang YP., Dong P. Buckling Distortions and Mitigation Techniques for Thin-Section Structures. Journal of Materials Engineering and Performance. February 2012; 21(2): 153–160. Available at: DOI:10.1007/s11665-011-9928-x

62. Gabzdyl J., Johnson A., Williams S., Price D. Laser weld distortion control by cryogenic cooling. In: Miyamoto I, Kobayashi KF, Sugioka K, Poprawe R, Helvajian H (eds.) Osaka, Japan; 2003. p. 269. Available at: DOI:10.1117/12.486497 (Accessed: 18 February 2020)

63. Guo, SQ, Li, XH, Xu, WL, Liu, XS, Wan, X, Tian, XT Welding distortion control of thin Al alloy plate by static thermal tensioning. Journal of Materials Science & Technology. January 2001; 17(1): 163–164.

64. van der Aa EM., Hermans MJM., Richardson IM. Conceptual model for stress and strain development during welding with trailing heat sink. Science and Technology of Welding and Joining. 1 July 2006; 11(4): 488–495. Available at: DOI:10.1179/174329306X120714

65. Ilman MN., Kusmono, Muslih MR., Subeki N., Wibowo H. Mitigating distortion and residual stress by static thermal tensioning to improve fatigue crack growth performance of MIG AA5083 welds. Materials & Design. June 2016; 99: 273–283. Available at: DOI:10.1016/j.matdes.2016.03.049

66. Burak Y., Bisijina LP., Romanjuk Y., Kazimirov AA., Morgun VP. Controlling the longitudinal plastic shrinkage of metal during welding. Avtom. Svarka. 1977; 288(3): 27–29.

67. Burak Y., Romanjuk Y., Kazimirov AA., Morgun VP. Selection of the optimum fields for preheating plates before welding. Avtom. Svarka. 1979; 314(5): 5–9.

68. Deo MV., Michaleris P. Mitigation of welding induced buckling distortion using transient thermal tensioning. Science and Technology of Welding and Joining. 1 February 2003; 8(1): 49–54. Available at: DOI:10.1179/136217103225008919

69. Richards DG., Prangnell PB., Williams SW., Withers PJ. Global mechanical tensioning for the management of residual stresses in welds. Materials Science and Engineering: A. August 2008; 489(1–2): 351–362. Available at: DOI:10.1016/j.msea.2007.12.042

70. Altenkirch J., Steuwer A., Withers PJ., Williams SW., Poad M., Wen SW. Residual stress engineering in friction stir welds by roller tensioning. Science and Technology of Welding and Joining. February 2009; 14(2): 185–192. Available at: DOI:10.1179/136217108X388624

71. Kurkin SA., Anufriev VI., Milekhin ES. Improving the mechanical properties of welded joints in the AMg6 alloy by plastic deformation during arc welding. Svarochnoe Proizvodstvo. 1980; (27): 20–24.

72. Kurkin SA., Anufriev VI. Preventing distortion of welded thin-walled members of AlMg6 and 1201 aluminum alloys by rolling the weld with a roller behind the welding arc. Svarochnoe Proizvodstvo. 1984; (31): 52–55.

73. Wen SW., Colegrove PA., Williams SW., Morgan SA., Wescott A., Poad M. Rolling to control residual stress and distortion in friction stir welds. Science and Technology of Welding and Joining. August 2010; 15(6): 440–447. Available at: DOI:10.1179/136217110X12785889549787

74. Sule J., Ganguly S., Coules H., Pirling T. Application of local mechanical tensioning and laser processing to refine microstructure and modify residual stress state of a multi-pass 304L austenitic steels welds. Journal of Manufacturing Processes. April 2015; 18: 141–150. Available at: DOI:10.1016/j.jmapro.2015.03.003

75. Coules HE., Colegrove P., Cozzolino LD., Wen SW., Kelleher JF. High pressure rolling of low carbon steel weld seams: Part 2 – Roller geometry and

residual stress. Science and Technology of Welding and Joining. January 2013; 18(1): 84–90. Available at: DOI:10.1179/1362171812Y.0000000080

76. Colegrove PA., Martina F., Roy MJ., Szost BA., Terzi S., Williams SW., et al. High Pressure Interpass Rolling of Wire + Arc Additively Manufactured Titanium Components. Advanced Materials Research. August 2014; 996: 694–700. Available at: DOI:10.4028/www.scientific.net/AMR.996.694

77. Martina F., Roy MJ., Szost BA., Terzi S., Colegrove PA., Williams SW., et al. Residual stress of as-deposited and rolled wire+arc additive manufacturing Ti–6Al–4V components. Materials Science and Technology. 21 September 2016; 32(14): 1439–1448. Available at: DOI:10.1080/02670836.2016.1142704

78. Williams SW., Colegrove PA., Ganguly S. Residual stress characterization and control in the additive manufacture of large scale metal structures. Sydney, Australia; 2016. pp. 455–460. Available at: DOI:10.21741/9781945291173-77 (Accessed: 3 March 2020)

79. Hönnige JR., Colegrove PA., Ganguly S., Eimer E., Kabra S., Williams S. Control of residual stress and distortion in aluminium wire + arc additive manufacture with rolling. Additive Manufacturing. August 2018; 22: 775–783. Available at: DOI:10.1016/j.addma.2018.06.015

80. Zhao H., Zhang G., Yin Z., Wu L. A 3D dynamic analysis of thermal behavior during single-pass multi-layer weld-based rapid prototyping. Journal of Materials Processing Technology. March 2011; 211(3): 488–495. Available at: DOI:10.1016/j.jmatprotec.2010.11.002

81. Xiong J., Lei Y., Li R. Finite element analysis and experimental validation of thermal behavior for thin-walled parts in GMAW-based additive manufacturing with various substrate preheating temperatures. Applied Thermal Engineering. November 2017; 126: 43–52. Available at: DOI:10.1016/j.applthermaleng.2017.07.168

82. Ding J., Colegrove P., Mehnen J., Williams S., Wang F., Almeida PS. A computationally efficient finite element model of wire and arc additive

manufacture. The International Journal of Advanced Manufacturing Technology. 2014; (70): 227–236. Available at: DOI:10.1007/s00170-013-5261-x

83. Montevecchi F., Venturini G., Grossi N., Scippa A., Campatelli G. Finite Element mesh coarsening for effective distortion prediction in Wire Arc Additive Manufacturing. Additive Manufacturing. December 2017; 18: 145–155. Available at: DOI:10.1016/j.addma.2017.10.010

84. Chiumenti M., Cervera M., Salmi A., Agelet de Saracibar C., Dialami N., Matsui K. Finite element modeling of multi-pass welding and shaped metal deposition processes. Computer Methods in Applied Mechanics and Engineering. August 2010; 199(37–40): 2343–2359. Available at: DOI:10.1016/j.cma.2010.02.018

85. Montevecchi F., Venturini G., Scippa A., Campatelli G. Finite Element Modelling of Wire-arc-additive-manufacturing Process. Procedia CIRP. 2016; 55: 109–114. Available at: DOI:10.1016/j.procir.2016.08.024

86. Ding J. Thermo-mechanical Analysis of Wire and Arc Additive Manufacturing Process. PhD Thesis. Cranfield University; 2012.

87. Graf M., Hälsig A., Höfer K., Awiszus B., Mayr P. Thermo-Mechanical Modelling of Wire-Arc Additive Manufacturing (WAAM) of Semi-Finished Products. Metals. 1 December 2018; 8(12): 1009. Available at: DOI:10.3390/met8121009

88. Anca A., Fachinotti VD., Escobar-Palafox G., Cardona A. Computational modelling of shaped metal deposition. International Journal for Numerical Methods in Engineering. 7 January 2011; 85(1): 84–106. Available at: DOI:10.1002/nme.2959

89. Lee CH., Kobayashi S. New solutions to rigid-plastic deformation problems using a matrix method. Journal of Engineering for Industry. 1 August 1973; 95(3): 865–873. Available at: DOI:10.1115/1.3438238

90. Hwang SM., Kobayashi S. Preform design in plane-strain rolling by the finite-element method. International Journal of Machine Tool Design and

Research. January 1984; 24(4): 253–266. Available at: DOI:10.1016/0020-7357(84)90060-X

91. Yan Z., Liu W., Tang Z., Liu X., Zhang N., Li M., et al. Review on thermal analysis in laser-based additive manufacturing. Optics & Laser Technology. October 2018; 106: 427–441. Available at: DOI:10.1016/j.optlastec.2018.04.034

92. Perret W., Schwenk C., Rethmeier M. Comparison of analytical and numerical welding temperature field calculation. Computational Materials Science. February 2010; 47(4): 1005–1015. Available at: DOI:10.1016/j.commatsci.2009.11.032

93. Pittner A., Weiß D., Schwenk C., Rethmeier M. Methodology to improve applicability of welding simulation. Science and Technology of Welding and Joining. September 2008; 13(6): 496–508. Available at: DOI:10.1179/136217108X329322

94. Rosenthal D. The theory of moving sources of heat and its application to metal treatments. Transactions of the ASME. November 1946; 68(8): 849–866.

95. Rosenthal, D., Schmerber, R. Thermal study of arc welding. Welding Journal. 1938; 17(4): 2–8.

96. Eagar TW., Tsai NS. Temperature fields produced by traveling distributed heat sources. Welding Journal (Miami, Fla). December 1983; 62(12): 346–355.

97. Goldak J., Chakravarti A., Bibby M. A new finite element model for welding heat sources. Metallurgical Transactions B. June 1984; 15(2): 299–305. Available at: DOI:10.1007/BF02667333

98. Pavelic V., Tanbakuchi R., Uyehara O., Myers P. Experimental and computed temperature histories in gas tungsten arc welding of thin plates. Welding Journal Research Supplement. 1969; 48: 296–305.

99. Friedman, E. Analysis of weld puddle distortion and its effect on penetration. 1978; 57: 161.

100. Krutz, G. W., Segerlind, L. J. Finite element analysis of welded structures. Welding Research Supplement. 1978; 57: 211.

101. Denlinger ER., Michaleris P. Effect of stress relaxation on distortion in additive manufacturing process modeling. Additive Manufacturing. October 2016; 12: 51–59. Available at: DOI:10.1016/j.addma.2016.06.011

102. Mughal MP., Fawad H., Mufti RA., Siddique M. Deformation modelling in layered manufacturing of metallic parts using gas metal arc welding: effect of process parameters. Modelling and Simulation in Materials Science and Engineering. September 2005; 13(7): 1187–1204. Available at: DOI:10.1088/0965-0393/13/7/013

103. Lindgren L-E., Runnemalm H., Näsström MO. Simulation of multipass welding of a thick plate. International Journal for Numerical Methods in Engineering. 1999; 44(9): 1301–1316. Available at: DOI:10.1002/(SICI)1097-0207(19990330)44:9<1301::AID-NME479>3.0.CO;2-K

104. Cao J., Gharghouri MA., Nash P. Finite-element analysis and experimental validation of thermal residual stress and distortion in electron beam additive manufactured Ti-6Al-4V build plates. Journal of Materials Processing Technology. November 2016; 237: 409–419. Available at: DOI:10.1016/j.jmatprotec.2016.06.032

105. Abbaszadeh M., Hönnige JR., Martina F., Neto L., Kashaev N., Colegrove P., et al. Numerical Investigation of the Effect of Rolling on the Localized Stress and Strain Induction for Wire + Arc Additive Manufactured Structures. Journal of Materials Engineering and Performance. August 2019; 28(8): 4931–4942. Available at: DOI:10.1007/s11665-019-04249-y

106. Tangestani R., Farrahi GH., Shishegar M., Aghchehkandi BP., Ganguly S., Mehmanparast A. Effects of Vertical and Pinch Rolling on Residual Stress Distributions in Wire and Arc Additively Manufactured Components. Journal of Materials Engineering and Performance. April 2020; 29(4): 2073–2084. Available at: DOI:10.1007/s11665-020-04767-0

107. Röttger K. Walzen hartgedrehter Oberflächen. PhD Thesis. Aachen: RWTH; 2003.

108. Yen YC., Sartkulvanich P., Altan T. Finite Element Modeling of Roller Burnishing Process. CIRP Annals. 2005; 54(1): 237–240. Available at: DOI:10.1016/S0007-8506(07)60092-4

109. Balland P., Tabourot L., Degre F., Moreau V. An investigation of the mechanics of roller burnishing through finite element simulation and experiments. International Journal of Machine Tools and Manufacture. February 2013; 65: 29–36. Available at: DOI:10.1016/j.ijmachtools.2012.09.002

110. Manouchehrifar, A., Alasvand, K. Finite Element Simulation of Deep Rolling and Evaluate the Influence of Parameters on Residual Stress Recent Researches in Applied Mechanics. WSEAS Press, Athens. : 121–127.

111. Beghini M., Bertini L., Monelli BD., Santus C., Bandini M. Experimental parameter sensitivity analysis of residual stresses induced by deep rolling on 7075-T6 aluminium alloy. Surface and Coatings Technology. September 2014; 254: 175–186. Available at: DOI:10.1016/j.surfcoat.2014.06.008

112. Hassani-Gangaraj SM., Carboni M., Guagliano M. Finite element approach toward an advanced understanding of deep rolling induced residual stresses, and an application to railway axles. Materials & Design. October 2015; 83: 689–703. Available at: DOI:10.1016/j.matdes.2015.06.026

113. Trauth D., Klocke F., Mattfeld P., Klink A. Time-efficient Prediction of the Surface Layer State after Deep Rolling using Similarity Mechanics Approach. Procedia CIRP. 2013; 9: 29–34. Available at: DOI:10.1016/j.procir.2013.06.163

114. Perenda J., Trajkovski J., Žerovnik A., Prebil I. Residual stresses after deep rolling of a torsion bar made from high strength steel. Journal of Materials Processing Technology. April 2015; 218: 89–98. Available at: DOI:10.1016/j.jmatprotec.2014.11.042

115. Mehner T., Bauer A., Härtel S., Awiszus B., Lampke T. Residual-stress evolution of cold-rolled DC04 steel sheets for different initial stress states. Finite

Elements in Analysis and Design. May 2018; 144: 76–83. Available at: DOI:10.1016/j.finel.2017.11.006

116. Lan J., Feng S., Hua L. The residual stress of the cold rolled bearing race. Procedia Engineering. 2017; 207: 1254–1259. Available at: DOI:10.1016/j.proeng.2017.10.879

117. Cozzolino LD., Coules HE., Colegrove PA., Wen S. Investigation of post-weld rolling methods to reduce residual stress and distortion. Journal of Materials Processing Technology. September 2017; 247: 243–256. Available at: DOI:10.1016/j.jmatprotec.2017.04.018

118. Coules HE., Horne GCM., Kabra S., Colegrove P., Smith DJ. Three-dimensional mapping of the residual stress field in a locally rolled aluminium alloy specimen. Journal of Manufacturing Processes. April 2017; 26: 240–251. Available at: DOI:10.1016/j.jmapro.2017.02.010

119. Abaqus FEA Software. Version 6.14 - 4. User manual; Theory Guide.

120. Balland P., Tabourot L., Degre F., Moreau V. Mechanics of the burnishing process. Precision Engineering. January 2013; 37(1): 129–134. Available at: DOI:10.1016/j.precisioneng.2012.07.008

121. Bouzid Saï W., Saï K. Finite element modeling of burnishing of AISI 1042 steel. The International Journal of Advanced Manufacturing Technology. March 2005; 25(5–6): 460–465. Available at: DOI:10.1007/s00170-003-1993-3

122. L. D. Cozzolino Finite element analysis of localised rolling to reduce residual stress and distortion. PhD Thesis. Cranfield University; 2013.

123. Pan R., Pirling T., Zheng J., Lin J., Davies CM. Quantification of thermal residual stresses relaxation in AA7xxx aluminium alloy through cold rolling. Journal of Materials Processing Technology. February 2019; 264: 454–468. Available at: DOI:10.1016/j.jmatprotec.2018.09.034

124. Benzley S., Perry E., Merkley K., Clark B., Sjaardema G. A comparison of all hexagonal and all tetrahedral finite element meshes for elastic and elasto-

plastic analysis. Proceedings, 4th International Meshing Roundtable. 1 January 1995; 17.

125. Tanner DA., Robinson JS. Time transient validation of residual stress prediction models for aluminium alloy quenching. Materials Science and Technology. 21 September 2016; 32(14): 1533–1543. Available at: DOI:10.1080/02670836.2016.1195122

126. Wang M., Yang H., Sun Z., Guo L., Ou X. Dynamic explicit FE modeling of hot ring rolling process. Transactions of Nonferrous Metals Society of China. December 2006; 16(6): 1274–1280. Available at: DOI:10.1016/S1003-6326(07)60006-5

127. Stolarski TA., Tobe S. Rolling Contacts. Chichester, UK: John Wiley & Sons, Ltd; 2000. Available at: DOI:10.1002/9781118903001 (Accessed: 23 April 2020)

128. Hutchings IM., Shipway P. Tribology: Friction and wear of engineering materials. 2nd edn. Elsevier Ltd.; 2017.

129. Marks LS. Marks' standard handbook for mechanical engineers. Eleventh editon, [90. anniversary edition]. Avallone EA, Baumeister T, Sadegh AM (eds.) New York: McGraw-Hill; 2007.

130. Andersen L.F. Residual stresses and deformations in steel structures. PhD Thesis. Department of Naval Architecture and Offshore Engineering, Technical University of Denmark; 2000.

131. Smith MC., Smith AC., Wimpory R., Ohms C. A review of the NeT Task Group 1 residual stress measurement and analysis round robin on a single weld bead-on-plate specimen. International Journal of Pressure Vessels and Piping. August 2014; 120–121: 93–140. Available at: DOI:10.1016/j.ijpvp.2014.05.002

132. Bijak-Żochowski M., Marek P. Residual stress in some elasto-plastic problems of rolling contact with friction. International Journal of Mechanical Sciences. January 1997; 39(1): 15–32. Available at: DOI:10.1016/0020-7403(96)00018-5

133. Chaboche JL. Constitutive equations for cyclic plasticity and cyclic viscoplasticity. International Journal of Plasticity. January 1989; 5(3): 247–302. Available at: DOI:10.1016/0749-6419(89)90015-6

134. Chaboche JL. Time-independent constitutive theories for cyclic plasticity. International Journal of Plasticity. January 1986; 2(2): 149–188. Available at: DOI:10.1016/0749-6419(86)90010-0

135. Harewood FJ., McHugh PE. Comparison of the implicit and explicit finite element methods using crystal plasticity. Computational Materials Science. April 2007; 39(2): 481–494. Available at: DOI:10.1016/j.commatsci.2006.08.002

136. Oliver J., Huespe AE., Cante JC. An implicit/explicit integration scheme to increase computability of non-linear material and contact/friction problems. Computer Methods in Applied Mechanics and Engineering. April 2008; 197(21–24): 1865–1889. Available at: DOI:10.1016/j.cma.2007.11.027

137. Abaqus FEA Software. Version 6.14 - 4. User manual; Example Problems Guide.

138. Maniatty AM., Dawson PR., Weber GG. An Eulerian elasto-viscoplastic formulation for steady-state forming processes. International Journal of Mechanical Sciences. January 1991; 33(5): 361–377. Available at: DOI:10.1016/0020-7403(91)90075-E

139. Synka J., Kainz A. A novel mixed Eulerian–Lagrangian finite-element method for steady-state hot rolling processes. International Journal of Mechanical Sciences. December 2003; 45(12): 2043–2060. Available at: DOI:10.1016/j.ijmecsci.2003.12.008

140. Vetyukov Yu., Gruber PG., Krommer M., Gerstmayr J., Gafur I., Winter G. Mixed Eulerian-Lagrangian description in materials processing: deformation of a metal sheet in a rolling mill: Mixed Eulerian-Lagrangian description in materials processing: deformation of a metal sheet in a rolling mill. International Journal for Numerical Methods in Engineering. 9 March 2017; 109(10): 1371–1390. Available at: DOI:10.1002/nme.5314

4 Computationally efficient models of high pressure rolling for wire arc additively manufactured components

This chapter is based on the following publication:

Gornyakov V., Sun Y., Ding J., Williams S. Computationally Efficient Models of High Pressure Rolling for Wire Arc Additively Manufactured Components. Applied Sciences. 4 January 2021; 11(1): 402. Available at: DOI:10.3390/app11010402

The conventional full-scale single run rolling model of the WAAM component developed in Cranfield University is highly computationally inefficient. This restrained the further development of inter-layer rolling models for investigation and optimisation of the hybrid WAMM + rolling process widely studied in previous experimental research This Chapter presents four efficient single run rolling models. Their efficiency and accuracy were compared to the conventional full-scale rolling model. The influences of deformable elastic roller and boundary conditions on model efficiency and accuracy were investigated.

Abstract: High pressure inter-layer rolling is an effective method to reduce residual stress and distortion in metallic components built by wire arc additive manufacturing (WAAM). However, the mechanisms of the reduction in residual stress and distortion during inter-layer rolling are not well understood. Conventional finite element models for rolling are highly inefficient, hindering the simulation of inter-layer rolling for a large WAAM components. This study aims to identify the most suitable modelling technique for finite element analysis of large WAAM component rolling. Four efficient rolling models were developed, and their efficiency and accuracy were compared with reference to a conventional large-scale rolling model (i.e., control model) for a WAAM built wall. A short-length transient model with fewer nodes than the control model was developed to reduce computational time. Accurate predictions of stress and strain and a reduction in computational time by 96.5% were achieved using the short-length model when an implicit method for numerical solution was employed, while similar efficiency but less accurate prediction was obtained when an explicit solution method was

adopted. A Eulerian steady-state model was also developed, which was slightly less efficient (95.91% reduction in computational time) but was much less accurate due to unrealistic representation of rolling process. The applicability of a 2D rolling model was also examined and it was found that the 2D model is highly efficient (99.52% time reduction) but less predictive due to the 2D simplification. This study also shows that the rigid roller adopted in the models is beneficial for improving efficiency without sacrificing accuracy.

Keywords: wire + arc additive manufacturing; computationally efficient rolling model; implicit analysis; explicit analysis; Eulerian analysis; 2D plane stress model

4.1 Introduction

Wire arc additive manufacturing (WAAM) is an emerging technology that is particularly suited to building large components through adding multiple layers of materials with the aid of an arc heat source, robotic manipulator and computer control. WAAM allows production of large components with medium resolution and surface quality [1], using a wide range of materials, such as steel [2,3], titanium alloy [4], nickel superalloy [5], aluminium [6], tantalum [7,8] and tungsten [9,10]. It was used for building a variety of components, from relatively simple walls [3] and cylindrical structures [11] to complex components with variable wall thicknesses, e.g., demo parts of turbine blades, wing spar and landing gear structures [11]. WAAM utilises off-the-shelf industrial robots, conventional welding power sources and cheap welding wire consumables that are readily available in the market, thereby reducing initial investments, build up and operational costs [12–15]. WAAM is also more environmentally friendly compared to powder based additive manufacturing processes [16]. In comparison with traditional manufacturing techniques, WAAM can substantially reduce material usage, manufacturing costs and lead time, and hence it has attracted great interest for applications in aerospace, transport and energy industries.

During WAAM deposition the concentrated heating by the electric arc causes local material expansion. The material with low yield strength at elevated temperature deforms in compression during heating due to the constraint

imposed by the surrounding material. After the arc passes, the deformed material cools down and tends to shrink [17]. The heating-cooling cycle results in thermal stresses and plastic strains (PSs) in the deposited layers and the substrate (usually restrained by clamps, fixtures, etc.). After deposition, residual stress (RS) arises in the built part, which can lead to distortion after removal of the external restraint [3,18,19]. RS is usually detrimental to performance, since it can adversely affect fatigue life, increase probability of brittle fracture and reduce corrosion resistance [20–23].

High pressure rolling was found effective in reducing RS and distortion in WAAM built components [3,4,24], since it induces tensile PS in the built part and substrate, which compensates for the compressive PS caused by the thermal deposition cycle. The rolling can be implemented in different ways. For instance, inter-pass rolling after WAAM deposition of each layer was demonstrated as effective in reducing RS and distortion [3,4]; rolling every four deposited layers and rolling solely on the last layer of a WAAM built component were found effective as well [3]. Effective rolling should commence when the WAAM component is cooled to ambient temperature (below 50 °C), because in situ rolling (i.e., roller follows welding torch) has a negligible effect on distortion [3]. Experiments showed that an increase in rolling load is beneficial for the mitigation of RS and distortion [3,4]. Regarding the effect of roller geometry, the use of a slotted roller instead of a flat or profiled roller (i.e., roller with a groove) can significantly improve the efficacy of rolling, since the lateral restraint of the slotted roller promotes larger longitudinal deformation in the rolled material [3]. High pressure rolling has been successfully applied to WAAM deposited walls [3,4] and intersections [25,26], using materials such as mild steel [3] and titanium alloy [4,24,25]. The rolling also can improve fatigue life and mechanical properties [27,28], refine microstructure [3,24–26,29] and reduce porosity [6,30]. However, detailed mechanisms of the reduction in RS and distortion during high pressure rolling of WAAM are not well understood.

The finite element method (FEM) is widely used in simulations of rolling [31,32], which can reduce experimental effort, time and cost. However, current FEM

simulations of rolling in WAAM are highly inefficient, especially for large components. For instance, high performance computing (HPC) facility was required to simulate rolling in a 456 mm long part, and the computational time was up to 95 h [33]. When multi-layer rolling is used in WAAM [3,4,24], the computational demands are further exacerbated, and the simulation of rolling in a typical 20-layer WAAM part could take weeks. This makes multi-layer rolling simulation impractical. Therefore, efficient modelling techniques are needed to reduce computational time while still ensuring accuracy.

In current literature only two publications were found to address rolling simulation of WAAM built components [34,35]. For similar problems, the modelling research relevant to WAAM rolling includes the simulations of burnishing [36–39], deep rolling processes [40–43], hot and cold manufacture rolling processes [44,45], and rolling for reducing RS in quenched block [46] and weld seams [33,47]. All of these aforementioned rolling processes are technically similar to high pressure rolling in WAAM, i.e., additional plastic deformation is introduced in the component to impose a desired effect. Thus, the development of efficient rolling models for WAAM will be mainly based on a literature survey of the allied fields. The available efficient modelling techniques are summarised as follows.

4.1.1 Non-uniform mesh density

The time required to solve an FEM model largely depends on the number of nodes involved in analysis. Rolling is a highly nonlinear contact problem, which usually involves large deformation and requires fine mesh for numerical convergence [33,40,41] and accurate prediction [48]. Non-uniform mesh density, actively used in most of the FEM simulations of rolling, keeps the dense mesh in the contact region and the coarse mesh in other regions far from the roller, thereby reducing the total number of nodes with minimum impact on accuracy. The creation of non-uniform mesh density does not require special techniques or algorithms and can be done using standard Finite Element Analysis (FEA) software tools. Such a strategy to generate efficient models has been widely adopted in 2D [40,49,50] and 3D [33,34,38,41–43,45–47] simulations of rolling and burnishing.

4.1.2 Reduced length of modelled component

Reducing the length of the modelled component is also effective for improving efficiency, since it can reduce the number of nodes in the FEM model. However, it is questioned whether a short model can represent the behaviour of a large full-scale model. An early study by Bijak-Żochovski et al. [49] examined rolling contact with friction, and it was found that short models are sufficient to “stabilise analysed quantities” [49] and “further wheel travel does not effectively change the pictures of stresses and strain in tested area” [49]; in other words, the reduced length is sufficient for the model to reach a steady-state of rolling.

Cozzolino et al. [33] used an FEM model with significantly shorter length (465 mm) compared to the actual workpiece (750 mm) that was rolled during experiments, so as to reduce computational time, and the short model predicted similar results to the full-scale model. For rolling in a WAAM component, Abbaszadeh et al. [34] developed a model with a length of deformable component 100 mm, which was rolled along the minimal length under steady-state, and they found that a further increase of the rolling distance in analysis did not make any marked difference in the result. Short models have also been used in other rolling scenarios. For instance, Trauth et al. [42] and Perenda et al. [43] used short segments for simulations of deep rolling of a circular component. Pan et al. [46] developed a 62 mm long model for rolling simulation of quenched aluminium blocks. Hassani-Gangaraj et al. [41] and Balland et al. [51] employed short models for deep rolling and burnishing.

The main criterion to determine the shortest length for the rolled component is that the shortened component should be able to reach a steady-state of rolling. The manual of the FEM analysis software, Abaqus, suggests that the equivalent plastic strain, rolling force and torque should be used as the norms for steady-state detection. Steady-state rolling is reached when the reaction force and moment are stabilised, while the equivalent plastic strain in the rolled material becomes constant or fluctuates around a certain value [52].

4.1.3 Rigid roller

Normally, roller material (e.g., tungsten carbide [40] and H13 steel [46]) is much harder than rolled material. The elastic deformation of the roller is insignificant and barely affects the solution accuracy [41]. Therefore, rollers in most of the rolling models are assumed to be rigid and are defined as analytic surfaces, preventing discretisation of the roller and hence reducing the total number of nodes. In addition, compared to the discretised elastic or rigid surface that is represented by element faces, a smooth analytic surface allows lower contact noise and better approximation in contact formulation to improve computational efficiency [48,53]. A rigid roller or tool was adopted in the deep rolling and burnishing models by Perenda et al. [43] and Manouchehrifar et al. [39] and the weld rolling model by Cozzolino et al. [33], among many other models [40–42,44–47,51]. However, Hassani-Gangaraj et al. [41] found that their deep rolling model underestimated compressive RS in a depth of 0.2 mm below the rolled surface, and they attributed the error to the use of a rigid roller in their model. To eliminate potential errors, Abbaszadeh et al. [34] considered elastic deformation of the roller in their rolling model.

4.1.4 2D Rolling model

Rolling simulation for a simple component (e.g., single wall) can be simplified as a 2D problem, particularly when the material response to rolling is similar in the out-of-plane direction. Compared to 3D models, a 2D model can dramatically reduce the number of nodes and degrees of freedom and hence significantly improve the computational efficiency. 2D models in structural analysis are usually based on plane stress and plane strain theories. Rodríguez et al. [50] demonstrated that the predictions of a 2D burnishing model are close to those of a 3D model, and the modelling results are correlated well with experimental results. Röttger [36] created a 2D plane strain model of burnishing, which underestimated the penetration depth of the spherical rolling tool as a result of the overestimated contact surface area due to plane strain assumption. Similar research was conducted by Yen et al. [37], who used a 3D model to accurately predict tool penetration.

4.1.5 Explicit analysis for contact problems in rolling

Numerical methods used by FEM software to solve contact problems can influence the computational time and simulation accuracy. As suggested by the Abaqus manual, explicit dynamics solution techniques can be more computationally efficient and reliable than implicit methods for 3D rolling models with complex geometries, nonlinear material properties and discontinuous effects such as contact and friction [52]. However, Harewood et al. [54] found that for simple loading conditions with rigid bodies involved in contact simulation, implicit analysis solver requires less computational time than explicit analysis solver. The explicit method was found preferable for complex contact interactions, for example, between deformable bodies or where large deformation is involved. The explicit method demonstrates increased robustness/convergence and greater suitability for parallel calculations using multiple processors [54]. In contrast, Oliver et al. [55] suggested that the implicit method is more accurate and efficient, although less robust than the explicit method.

To accelerate explicit analysis for quasi-static problems, material density can be artificially increased (i.e., using mass scaling method) [52]. However, with aggressive mass scaling, inertia starts to play a significant role in the solution and will affect the result [48]. To restrict the artificial inertia effect, it is recommended by Chin et al. [56] and Abaqus Analysis User's Guide [48] that the ratio between kinetic and internal energies of the model should be maintained at no larger than 5%.

Specifically for rolling, the problem can be treated as quasi-static and solved by the explicit method for FEM analysis. For instance, Hassani-Gangaraj et al. [41] investigated RS in railway axles that experienced multi-run parallel deep rolling. Trauth et al. [42] created a model to optimise the deep rolling process for IN718 turbine blades and 42CrMo4 crankshafts, in which a mass scaling factor of 250 was used and a reduction in CPU time by two-thirds was achieved without impairing the accuracy. Lan et al. [45] developed a rolling model to predict the RS in a rolled bearing race, and a mass scaling factor of 400 was adopted to reduce computational time.

4.1.6 Eulerian analysis for contact problems in rolling

Eulerian analysis is a computationally efficient way to model large deformation [48]. Based on the Eulerian method, the rolling is simulated via material flow through the mesh in the space instead of moving the roller, such that mesh refinement is needed only near a “stationary” roller and the number of nodes can be greatly reduced [48]. The “mass scaling” option is also available for Eulerian explicit analysis to increase the stable time increment and reduce computational time for quasi-static analysis. The steady state detection option of Eulerian explicit analysis halts simulation as soon as steady state is detected [52]. The Eulerian method was used by Maniatty et al. [57] to simulate steady-state rolling and extrusion processes. The mixed Eulerian–Lagrangian method for steady-state modelling of the hot rolling process was developed by Synka et al. [58] and refined by Vetyukov et al. [59].

The literature survey summarised above shows that efficient models for simulation of high pressure rolling for WAAM components have not been reported. The conventional WAAM rolling model is computationally inefficient. The research pertinent to rolling simulations was conducted mainly in the allied fields of high-pressure weld seam rolling, deep rolling and burnishing. This limits the development of an inter-layer WAAM rolling model, which still faces practical challenges of high computational cost.

In general, a WAAM rolling model differs from the aforementioned relevant rolling models in a number of aspects, such as the unique WAAM process, component geometry, constraints and cyclic deformations involved in inter-layer rolling. In this paper, the potential efficient modelling techniques for rolling processes are investigated for application specifically in the rolling of a WAAM component. Four efficient rolling models for a WAAM deposited wall are proposed, and their computational efficiency and solution accuracy are examined relative to a large-scale rolling model [35]. The large-scale model is considered as a control model, as it most accurately represents the dimensions and the rolling process of the WAAM component built in the experiment [35]. The most efficient WAAM rolling model is employed for future analysis of inter-layer WAAM rolling.

4.2 Material and methods

S355 steel was used to build a wall in a previous WAAM experiment [35]. Twenty layers were deposited on a S355 steel base plate with chemical composition in accordance with BS EN 10225:2009. The height, width and length of each layer were approximately 2 mm, 5 mm and 500 mm, respectively. The wire feeding speed, deposition rate and weld torch travelling speed were 10 m/min, 2.352 kg/h and 0.5 m/min, respectively.

The WAAM built wall was selected for modelling in this study. The material model for the wall and substrate was based on the continuum elasticity and Mises plasticity theories, and isotropic strain hardening was assumed after initial yielding. Models in this study are purely rolling and do not include thermal effects related to WAAM deposition. The elastic–plastic material properties reported by Michaleris and DeBiccari [60] for 20 C° were adopted in this study (Table 4-1).

Table 4-1 The elastic-plastic material properties from Ref [60] for 20 C°.

Young's modulus [GPa]	Poisson's ratio	Yield stress, [MPa]	
		Plastic strain 0	Plastic strain 0.01
206	0.29	450	520

For the roller, rigid body assumption was adopted unless otherwise stated. General purpose FEM analysis software, Abaqus, was used for the modelling. For simplicity and focusing on computational efficiency, the RS in the WAAM component was not considered in the rolling simulation. The rolling models developed here were used mainly to identify the most suitable modelling technique for large WAAM components. Nevertheless, a technique for including WAAM deposition RS in the rolling model has also been developed and will be presented in the following Chapter 5.

4.2.1 Large scale implicit transient load-controlled model

A large-scale transient load-controlled rolling model was developed, following the work by Kashoob [35]. The term of transient model for mechanical analysis in the context of this research means that the solution of the model is time dependent (i.e., equilibrium at different moments), but does not involve any inertial effects.

The large-scale model simulated the rolling on the last layer of a full-size (500 mm in length) wall built using the WAAM process [35]. In the 3D model, the wall and substrate were modelled as a deformable body, while the roller was idealised as an analytical rigid shell. The model was solved using Abaqus/Standard (Static, General), based on implicit numerical algorithm. The dimensions of the model are depicted in Figure 4-1.

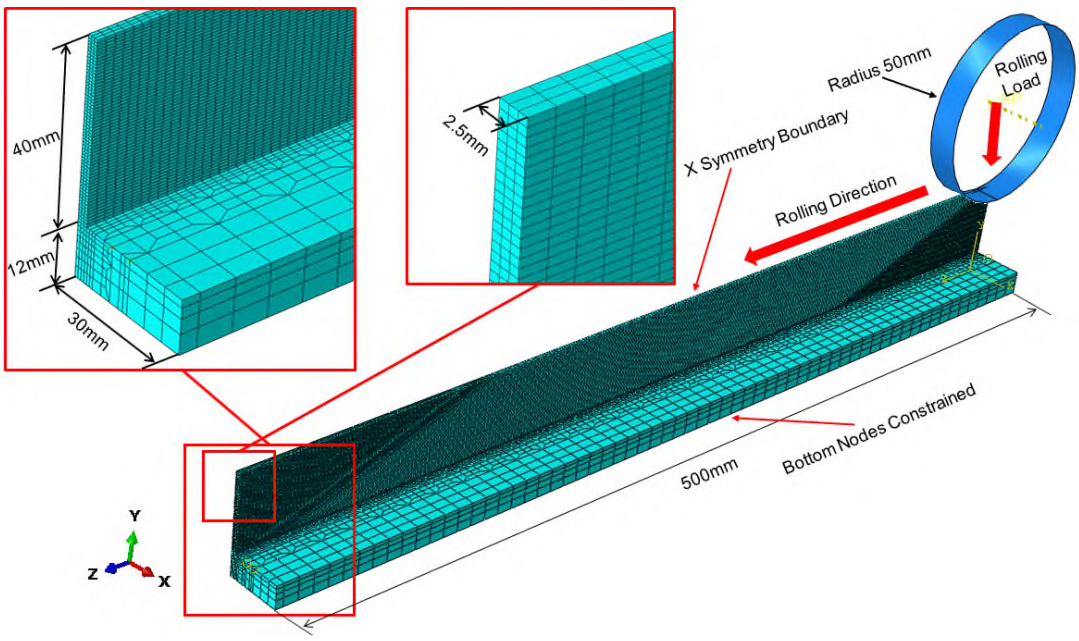

Figure 4-1 Large scale transient load-controlled model for a wire arc additive manufacturing (WAAM) component built in a previous experiment [35].

Simulating the actual rolling process, the model comprises the steps of placement, loading, rolling, unloading and removal of the roller. During rolling, a 50 kN vertical load was maintained (load-controlled mode), while no torque was applied. The roller was moved via imposing a horizontal displacement, and it also rotated due to friction between the roller and the wall. Only half of the wall and substrate was considered due to symmetry, and the out-of-plane displacement was constrained on the symmetry plane. To take account of the clamping of the substrate to the work table during the rolling process, the displacements of all nodes on the bottom surface were constrained in vertical direction. The model consisted of 63008 C3D8R (8-node, linear brick, reduced integration, hourglass control) elements. Graded mesh was employed for the model discretisation

(Figure 4-1). The element sizes were 8 × 5 × 4.521 mm and 2 × 0.833 × 0.667 mm for the regions far from and near to the roller, respectively. The model consisted of 82021 nodes. Surface-to-surface contact interaction was used in the model. The outer surface of the roller and the top surface of the wall were treated as master and slave surfaces, respectively. Finite sliding was allowed between the contact surfaces. Isotropic friction ($\mu = 0.3$) was specified for the contact interaction. Coules et al. [47] and Abbaszadeh et al. [34] suggested that a friction coefficient of 0.3 is representative for non-lubricated contact between the metallic roller and components. It was also found that the predicted RS distribution was not sensitive to the friction coefficient between the roller and component [33,34,47]. As per Cozzolino et al. [33] the difference became considerable only at high rolling loads (150 kN and higher).

4.2.2 Short implicit transient displacement-controlled model

A short implicit transient displacement-controlled model was developed (Figure 4-2) as a simplified counterpart to the large-scale transient model (Figure 4-1). To increase computational efficiency, the length of the deformable component was reduced from 500 mm to 72 mm. The 72 mm length was selected after a preliminary parametric study, and this length ensured that steady-state could be reached in the rolling simulation. This meant that the short model was sufficient to obtain a stable and consistent solution, which was not affected by the transient states at the beginning and termination of the rolling simulation. Due to the short length of the model, there was no place for the precise simulation of the rolling process sequence. To overcome this limitation, displacement-controlled penetration of the roller was used, which allowed for the simplification of analysis steps while using the same rolling load as applied in the large-scale load-controlled model. The displacement-controlled penetration enhanced computational efficiency and avoided numerical problems related to establishment of initial contact. In all the efficient models developed here, the roller penetration was controlled by displacement, which was obtained from the results of the large-scale transient model and was equivalent to a 50 kN rolling

load. The displacement-controlled roller penetration modelling technique was also used in the WAAM rolling simulation by Abbaszadeh et al. [34].

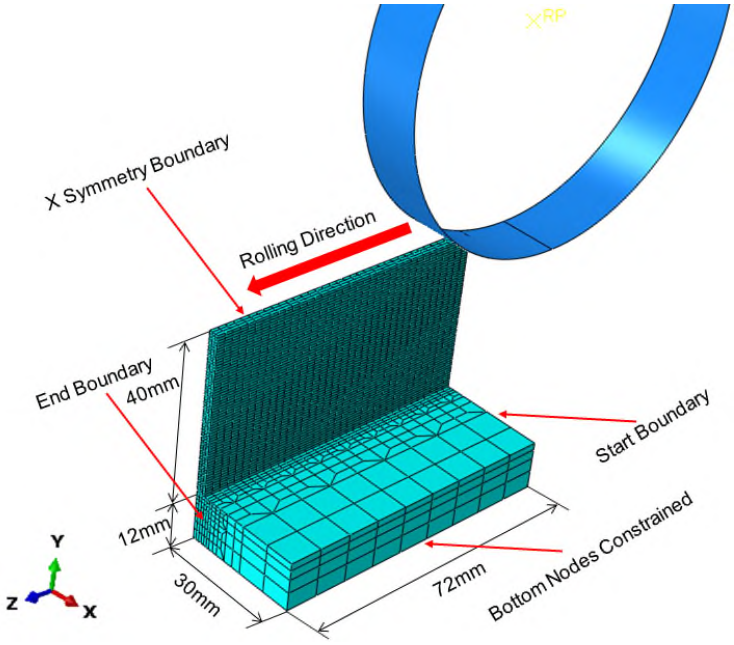

Figure 4-2 Short transient displacement-controlled model.

Another problem associated with the short length of the efficient model is the lack of stiffness in the rolling direction. During rolling of long WAAM component longitudinal plastic deformation in front and behind of the roller partially reduced/compensated by elastic deformation of the long wall. In the short component without restricted start and stop boundary conditions, absence of sufficient amount of material in front and behind of the roller to reduce/compensate plastic deformation elastically, caused the short wall unrealistically deform in rolling direction (as compared to long wall). In order to prevent unrealistic deformation in the rolling direction, a boundary condition of zero displacement was applied in the longitudinal direction at the Start and End boundaries of the short model.

To simulate clamping, nodes at the bottom of the model were constrained from movement in all directions. Element type and mesh topology were the same as those for the large-scale transient model. Smooth step amplitude was used in order to prevent instantaneous movement of the roller at the beginning of analysis. The model was solved using Abaqus/Standard (Static, General).

4.2.3 Short explicit transient displacement-controlled model

A short explicit transient model was also developed, which was identical to the short implicit transient model (Figure 4-2), except that a different solver was used. Mass scaling was used to improve the computational efficiency of the explicit analysis model, and a scaling factor of 6000 was selected after a parametric study. It should be mentioned that this scaling factor restricted the kinetic energy to less than 5% total energy, although it was significantly larger than the values (250 to 400) reported in the literature [42,43,53].

4.2.4 Eulerian steady-state model

A 3D Eulerian steady-state model was also developed based on the short length simplification, as shown in Figure 4-3. In the Eulerian short model, the material was drawn into the inflow border, underwent deformation, passed through the fixed mesh, and finally was pushed away through the outflow border. The Eulerian model comprised a 50 mm long fixed mesh (Figure 4-3 a), through which material flowed over a 500 mm distance during the rolling analysis. The Eulerian boundary conditions regulated the material flow at the inflow and outflow borders, where adaptive mesh constraints were applied to specify the material velocity perpendicular to the borders, as shown in Figure 4-3b. The model consisted of 27600 C3D8R elements (8-node linear brick, reduced integration, hourglass control) and the element dimensions were 1.881 × 0.625 × 0.667 mm. An adaptive mesh domain was specified near the roller to improve mesh quality for large deformation. The model consisted of 32007 nodes.

The interface between the roller and the wall was specified as the Eulerian sliding surface. On the bottom surface, the nodal displacement was constrained in the vertical direction to represent the clamping, while on the inflow and outflow borders, all the nodal displacements were fixed. The rolling load of 50 kN was imposed by prescribing a vertical displacement of the roller. Translation of the roller was constrained in all directions, while rotation was allowed only around the X axis. An angular velocity boundary condition was applied to the roller around of the spinning axis in order to provide the rolling torque. A predefined field of translational velocity was applied to the wall and substrate, as required to initiate

contact and minimise the transient effect of instantaneous movement at the beginning of analysis. The model was solved using Abaqus/Explicit, and the steady-state detection option was used in the model. The steady-state detection plane was positioned perpendicular to the rolling direction and behind the last point of contact (Figure 4-3 a). As soon as a constant deformed shape was achieved on the steady-state detection plane, it was considered that the rolling had reached the steady-state and the analysis was terminated.

To improve computational efficiency, rolling speed was artificially increased, i.e., the analysis step time was approximately 1% of the actual rolling time, which did not affect the result under the steady-state. In addition, a fixed mass scaling factor of 2750 was used in the analysis, close to the maximum value recommended by Abaqus Example Problems Guide [52] for similar problems. This scaling factor was deemed optimal as a result of iterative trials to minimise the computational time and the potential adverse effect of mass scaling on the accuracy.

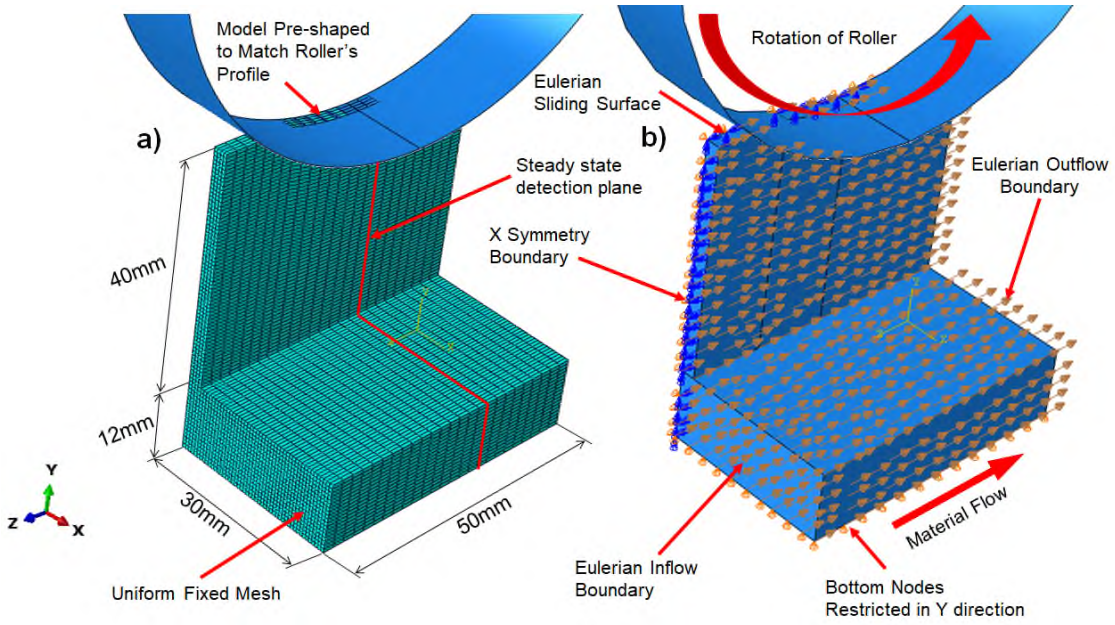

Figure 4-3 Short Eulerian steady-state model: a) dimensions and mesh, b) material flow and boundary conditions.

4.2.5 2D short implicit transient displacement-controlled model

The plane stress theory was utilised for the creation of a 2D model. The symmetry plane in the 3D model (Figure 4-2) was used to define the 2D model geometry,

as shown in Figure 4-4a, since the WAAM deposited wall is thin and flat and the RS and PS distributions in the rolling direction are of major interest in this study. The 2D model consisted of 2516 CPS4R elements (4-node, bilinear, plane stress, quadrilateral, reduced integration) and its mesh topology was similar to that for the symmetry plane of the 3D short implicit transient model. The model consisted of 2623 nodes.

The 2D and 3D short models also had similar boundary conditions and loading process, and they were both solved using Abaqus/Standard (Static, General).

To assess the potential influence of the deformable elastic roller on simulation results, an additional model with a roller made of H13 steel (Young's modulus of 230 GPa and Poisson's ratio of 0.3 [34]) was generated, as shown in Figure 4-4b. The mesh density of the elastic roller was selected to be the same as that of the WAAM wall. As a result, the roller was discretised using 3611 linear quadrilateral CPS4R elements and 157 linear triangular CPS3 elements. The number of nodes is 6391.

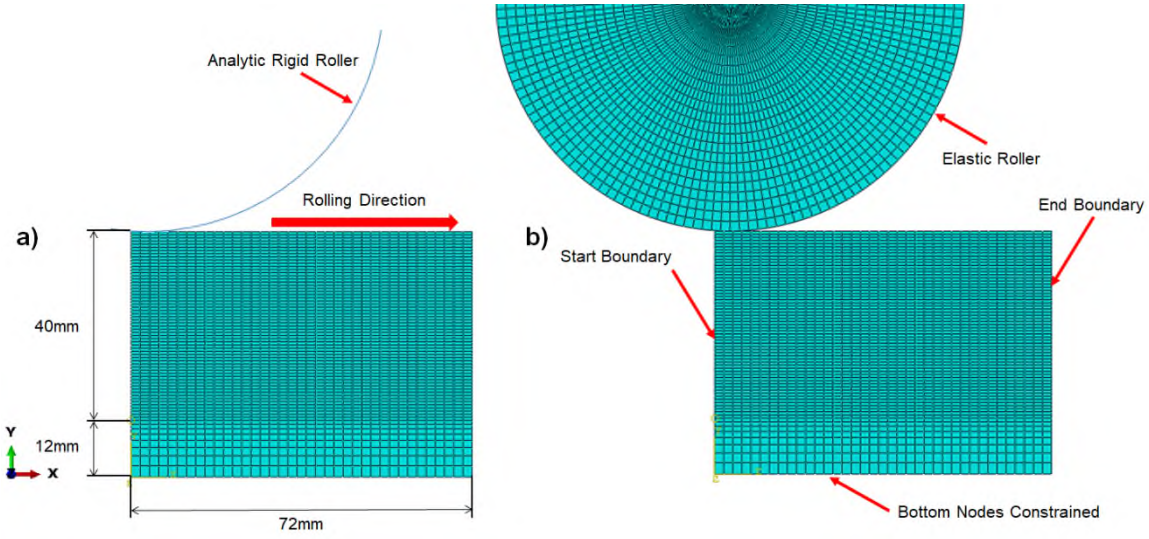

Figure 4-4 2D short transient displacement-controlled model: a) with analytic rigid roller, b) with elastic roller.

4.2.6 Inspection planes for comparison between different models

The accuracy of different efficient models was evaluated by comparison with the control model. The results for the comparison were extracted from an inspection

plane corresponding to the steady-state rolling. In the control model (3D large scale transient model), the inspection was performed in the mid-length plane. In the 3D short implicit transient, 3D short explicit transient and 2D short implicit transient models, the inspection plane was located in the x-y plane, 48 mm away from the start position of the rolling. In the Eulerian steady-state model, the inspection plane coincided with the steady-state detection plane, which was 20 mm away from the material outflow border.

4.3 Results

4.3.1 Computational efficiency

The computational efficiency was compared between different rolling models, and the total time savings for each model with reference to the control model was calculated, as shown in Table 4-2.

Table 4-2 Comparison of computational efficiency between different models.

Model	Number of nodes	Degrees of freedom	Wall clock time with 4 CPUs used (sec)	Estimated memory required to minimise I/O (MB)	Total time saving, %
3D large scale implicit transient model (control model)	82021	6	64,002	765	N/A
3D short implicit transient model	12064	6	2238	290	96.50%
3D short explicit transient model	12064	6	2355	17.6 ##	96.32%
3D Eulerian steady-state model	32007	6	2613 #	72.7 ##	95.91%
2D short implicit transient model with analytic rigid roller	2623	3	302	33	99.52%
2D short implicit transient model with elastic roller	6391	3	588	46	99.08%

Single CPU was used, since the Eulerian model using Abaqus/Explicit is restricted to serial computation.

Explicit analysis does not support swapping of memory to hard disk.

The wall clock time, i.e., the actual time required to obtain a solution, was used for the evaluation of the computational efficiency. All the models were solved using 4 Intel CPUs with 2 GB RAM available for each CPU, except the Eulerian model, which was solved using a single CPU since multiple CPUs are not supported for analysis with steady-state detection. Provided memory was sufficient for all models to avoid possible delays caused by I/O of data from virtual memory on the hard disk.

It was found that the 2D short implicit transient model with analytic rigid roller was most efficient, which saved 99.52% time relative to the control model, while the Eulerian steady-state model was least efficient, despite 95.91% time saved.

4.3.2 Steady-state rolling

Equivalent plastic strain (EPS) was used to detect the steady-state rolling. The rolling in the large scale implicit transient model (i.e., control model) reached steady state in a range of distance between 40 mm and 470 mm along the rolling direction, while this range was between 20 mm and 60 mm for the short transient models. In the steady-state rolling range, the EPS remained constant or fluctuated around a constant value, as shown in Figure 4-5.

The EPS predicted by the short implicit transient model demonstrated slightly larger fluctuation than other short models, and the fluctuation became negligible in the distance range from 40 mm to 50 mm. Based on the EPS distributions, the inspection plane of the short models was selected with a location at 48 mm from the rolling start position. The Eulerian model reached steady state after 7 sec rolling, and then the analysis halted, which was equivalent to a rolling distance of 58 mm.

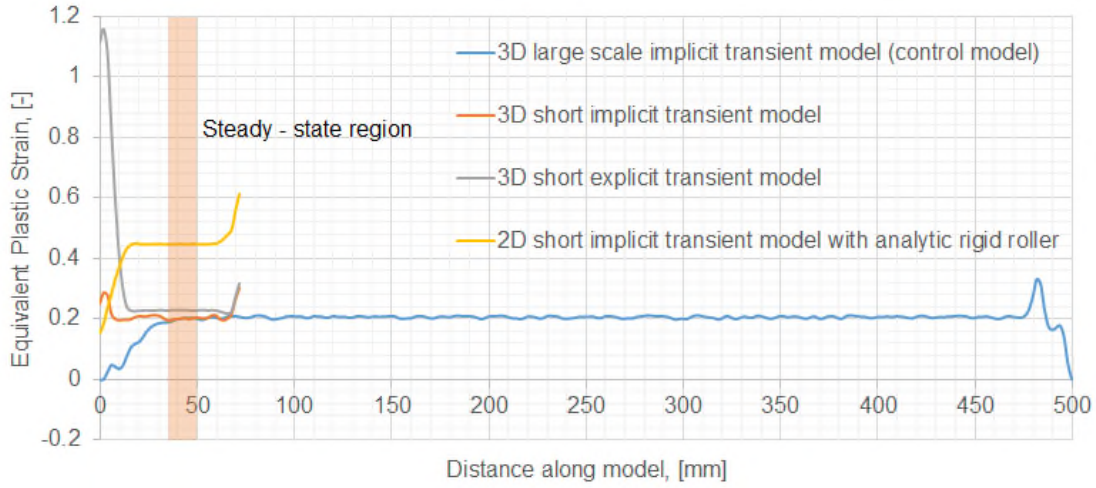

Figure 4-5 Equivalent plastic strain obtained along centreline on the top of the WAAM wall.

In the developed efficient models, the rolling load was maintained by applying a constant roller displacement (1.674 mm) in the vertical direction. The applied displacement was equivalent to a rolling load of 50 kN (25 kN for the half model due to symmetry). The rolling load was verified by examining the reaction force on the pivot of the roller (Figure 4-6) and by comparing contact pressure during rolling on the surface of the WAAM wall (Figure 4-7). Similar distribution and magnitude of contact pressure was obtained in all the models.

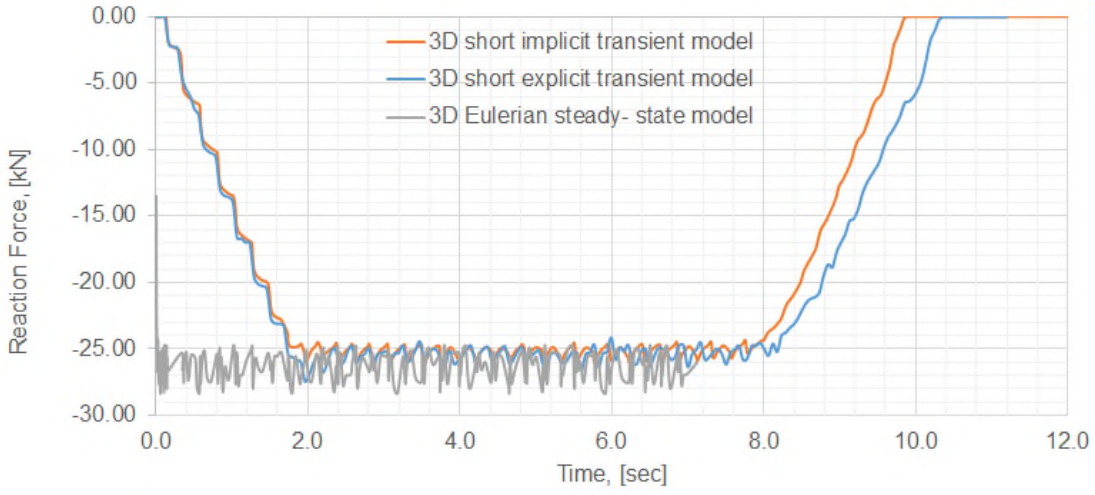

Figure 4-6 Reaction forces obtained at the rotation point of the rollers (note that only half of the WAAM component was considered in the models).

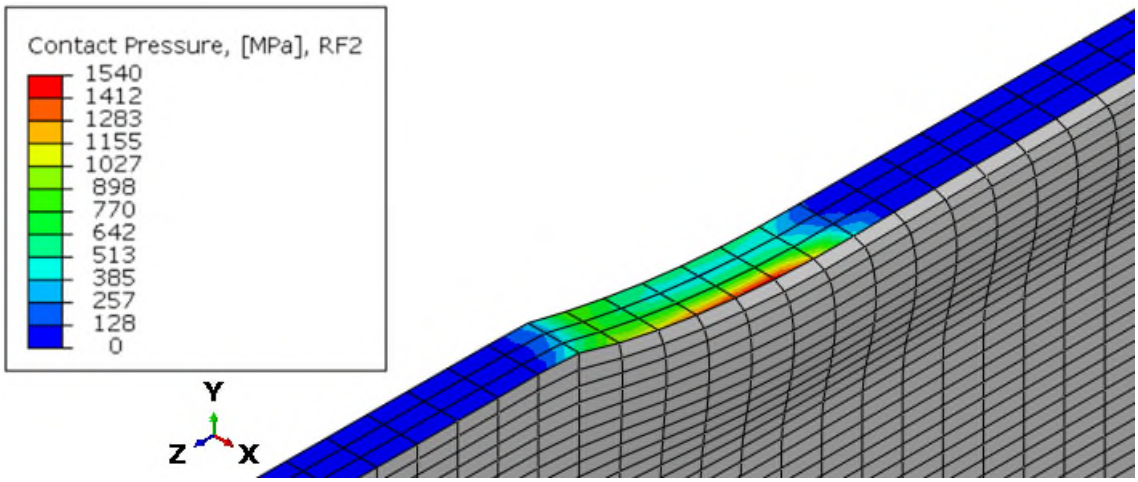

Figure 4-7 Contact pressure during rolling in 3D short implicit transient model.

4.3.3 Solution accuracy

The accuracy of the efficient models was examined through comparison with the large scale implicit transient model, which was based on the actual dimensions and rolling process of the WAAM component built in the previous experiment [35] and hence used here as the control model. Figure 4-8 presents longitudinal RS distributions on the inspection planes for different rolling models.

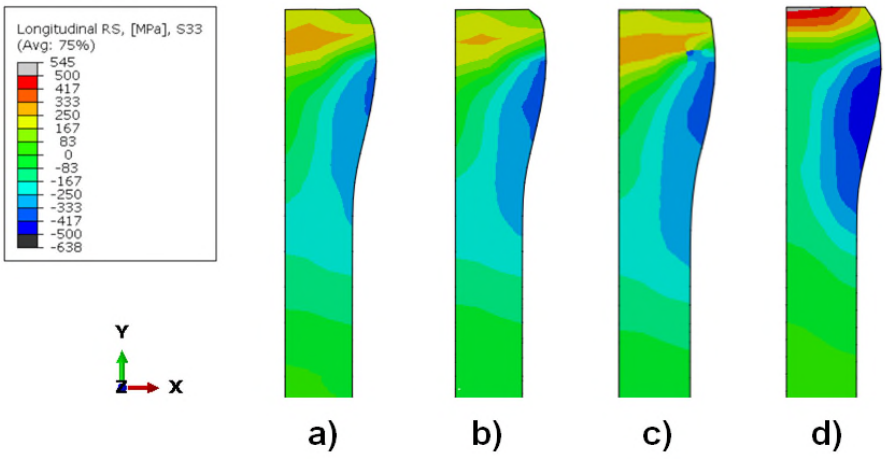

Figure 4-8 Longitudinal residual stress (RS) distribution on the inspection plane: a) large scale implicit transient model (control model), b) short implicit transient model, c) short explicit transient model, d) Eulerian steady-state model.

All models predicted tensile RS with a magnitude up to 582 MPa underneath the rolled surface and compressive RS with a magnitude up to 545 MPa underneath

the tension zone. The peak of the compressive RS shifted towards the outer surface of the wall (opposite to the symmetry plane). The short implicit transient model predicted the most accurate RS distribution compared to the control model. The short explicit transient model and the Eulerian steady-state model predicted larger regions under tensile RS, and the Eulerian model predicted larger magnitudes of both tensile and compressive RS.

Figure 4-9 shows the longitudinal PS distributions on the inspection planes for different rolling models. All models, except the Eulerian model, predicted concentrated tensile PS immediately under the rolled surface, while the Eulerian model predicted the highest tensile PS further underneath the rolled surface, which was concentrated on the side surface of the wall. The models predicted compressive PS in regions relatively far from the rolled surface. The longitudinal PS distribution predicted by the short implicit transient model was in best agreement with that predicted by the control model.

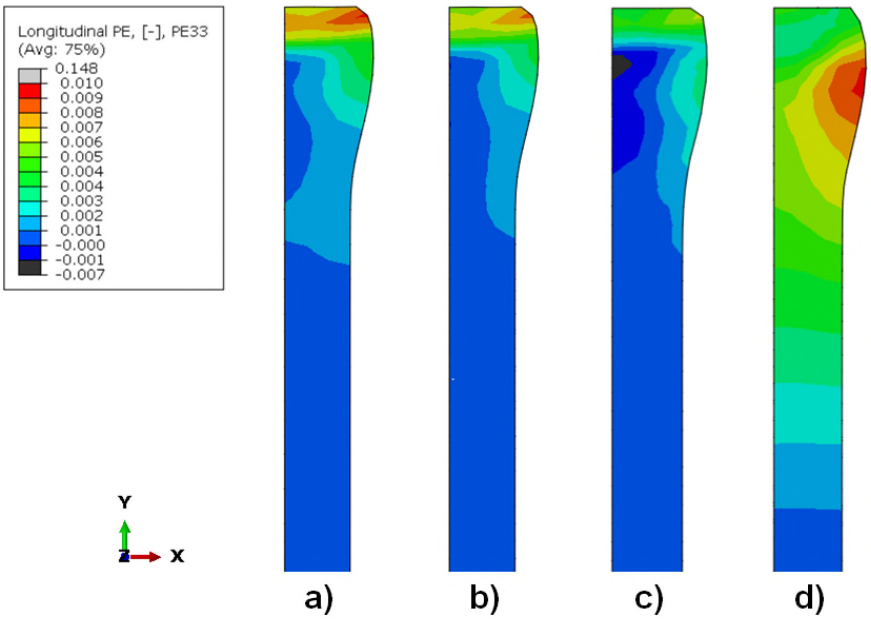

Figure 4-9 Longitudinal plastic strain (PS) distribution on the inspection plane: a) large scale implicit transient model (control model), b) short implicit transient model, c) short explicit transient model, d) Eulerian steady-state model.

Figure 4-10 shows the normal PS distributions on the inspection planes for different rolling models. Compressive PS was dominant in the deformed region,

and the peak PS was located approximately 2.2 mm below the rolled surface and close to the symmetry plane. No considerable tensile PS was found in the wall. The predictions of normal PS by all the efficient models achieved similar agreement with that obtained by the control model.

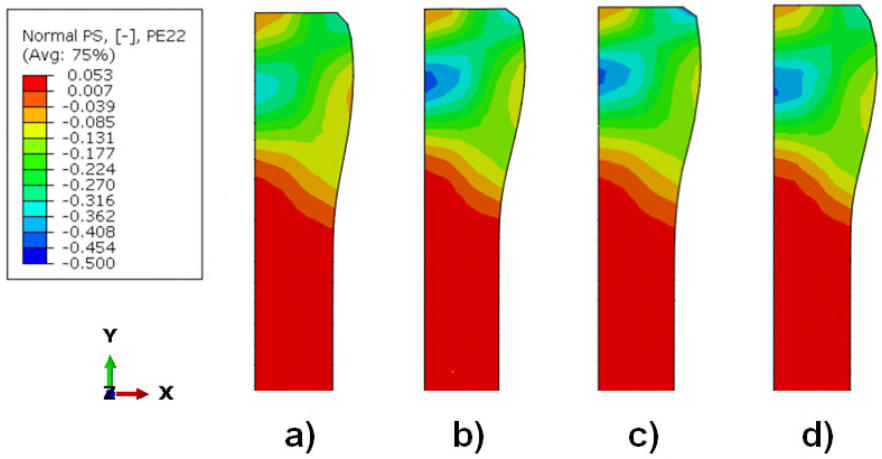

Figure 4-10 Normal PS distribution on the inspection plane: a) large scale implicit transient model (control model), b) short implicit transient model, c) short explicit transient model, d) Eulerian steady-state model.

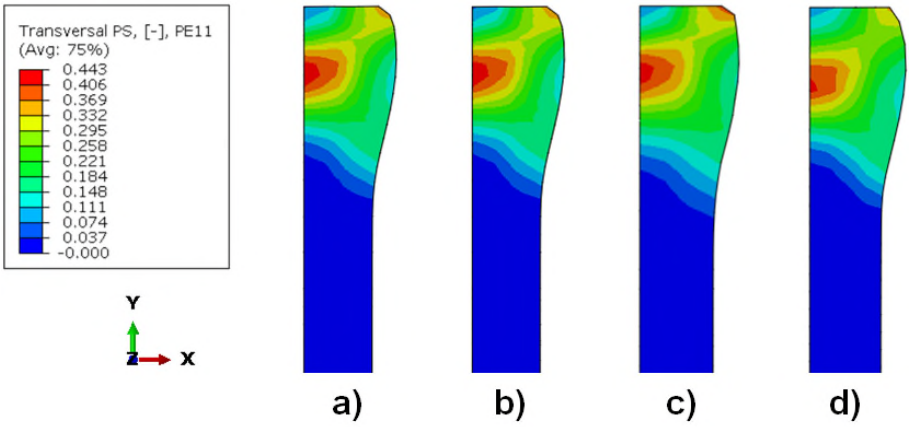

Figure 4-11 Transverse PS distribution on the inspection plane: a) large scale implicit transient model (control model), b) short implicit transient model, c) short explicit transient model, d) Eulerian steady-state model.

Figure 4-11 compares the transverse PS distributions predicted by different models. The predicted results were similar between all the models. In contrast to

the normal PS, the transverse PS was overwhelmingly tensile. The peak PS was located in the central portion of the deformed region.

Figure 4-12 compares the transverse displacement distributions predicted by different rolling models. There was an overall similarity between the results, while the displacement contour obtained by the Eulerian model was somewhat elongated in the vertical direction.

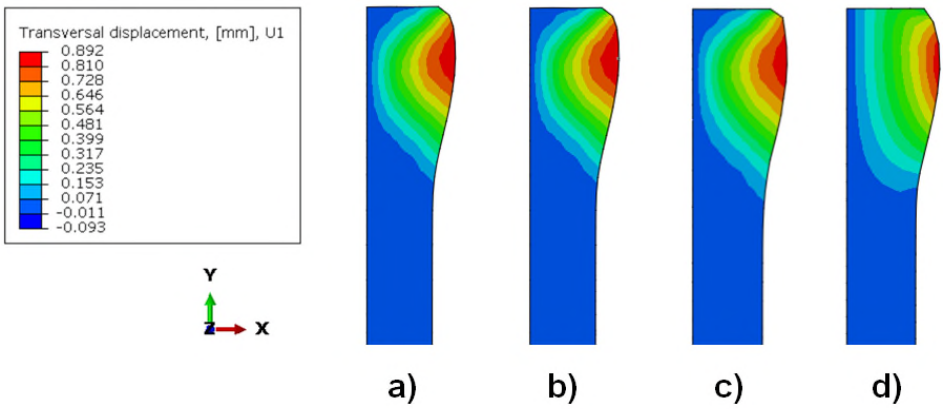

Figure 4-12 Transverse displacement distribution on the inspection plane: a) large scale implicit transient model (control model), b) short implicit transient model, c) short explicit transient model, d) Eulerian steady-state model.

4.3.4 2D vs. 3D rolling models

Figure 4-13 and Figure 4-14 compare the longitudinal PS and RS distributions, respectively, as obtained from the 3D large scale model (control model) and the 2D short transient models with elastic roller and analytic rigid roller. The 2D models captured the longitudinal tensile PS distribution in the region near the substrate, but they overestimated the tensile PS magnitude in the region close to the rolled surface. Nevertheless, the 2D modelling results for the longitudinal tensile RS distribution near the rolled surface were consistent with the prediction by the 3D control model. However, there was marked discrepancy in the compressive RS distribution near the substrate between the predictions by the 2D and 3D models. Figure 4-13 and Figure 4-14 also demonstrate a minor effect of elastic deformation of the roller on the predicted longitudinal PS and RS distributions under steady-state rolling.

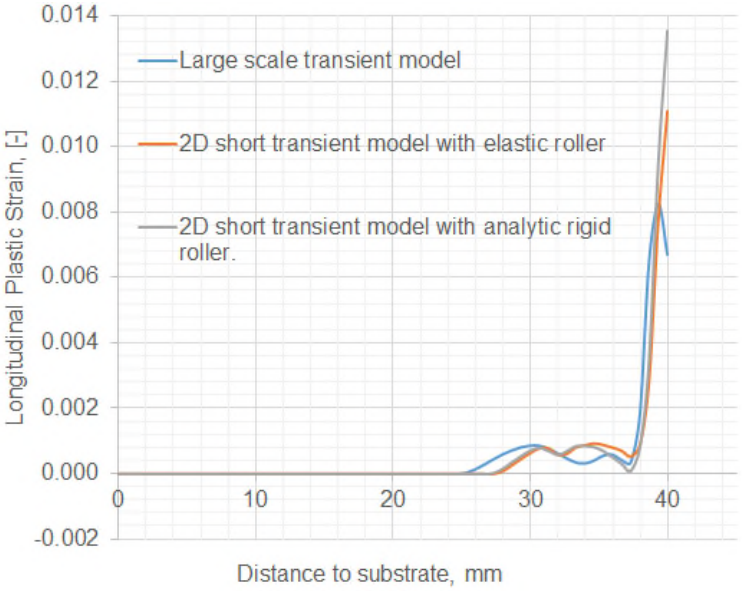

Figure 4-13 Longitudinal PS distributions on inspection planes.

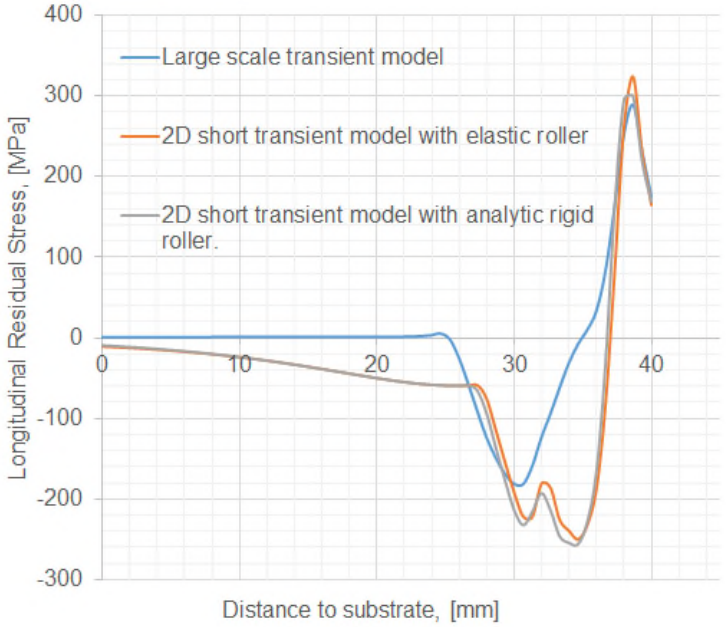

Figure 4-14 Longitudinal RS distributions on inspection planes.

Figure 4-15 confirms such a minor effect on the longitudinal RS when the full-field stress distributions are compared. The minor effect of the elastic deformation of the roller found here was consistent with the findings of Abbaszadeh et al. [34] using a 3D rolling model. However, it should be noted that a typical rolling load of

50 kN for WAAM was used in this study; the difference in results between elastic and rigid roller models could be considerable at significantly larger rolling loads.

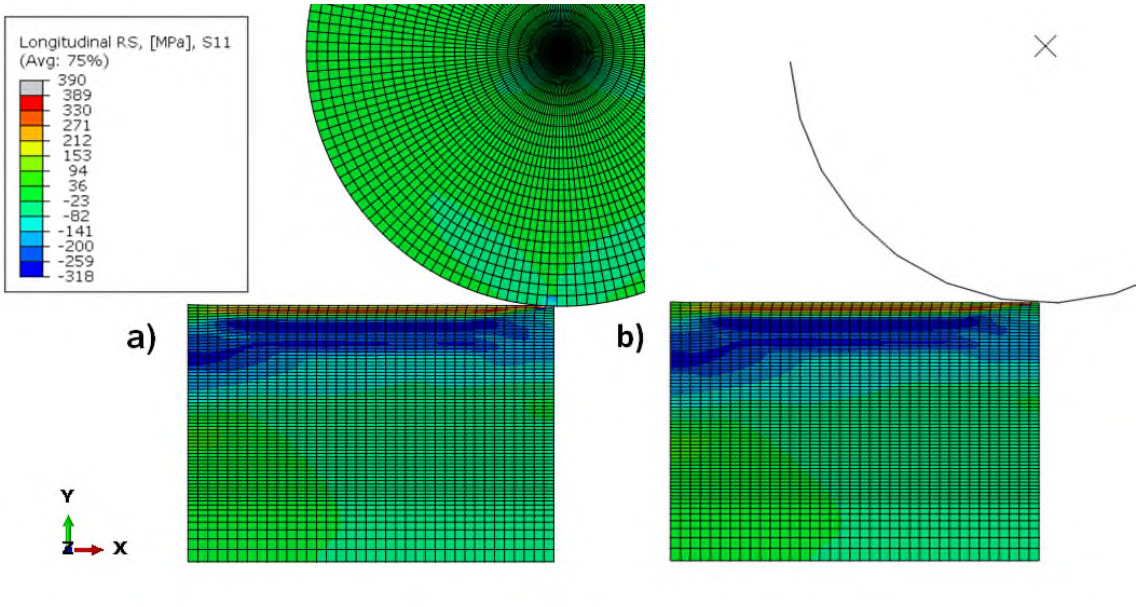

Figure 4-15 Longitudinal RS predicted by 2D short implicit transient models with a) elastic roller and b) analytic rigid roller.

The use of an elastic roller in the 2D model doubled the number of nodes involved in the analysis and increased the wall clock time by 48% (Table 4-2 Comparison of computational efficiency between different models.). Given the minor difference in results between the elastic and rigid roller models, it can be confirmed that the analytic rigid roller in the rolling model allowed significant computational savings with almost equivalent accuracy of predicted results.

4.4 Discussion

4.4.1 Computational efficiency

The highest computational efficiency was achieved by the 2D short implicit transient model with an analytic rigid roller, thanks to the dramatic computational saving by using fewer nodes (2623 nodes) with reduced degrees of freedom. The 2D model with an elastic roller comprised twice the number of nodes (6391) and demonstrated 48.6% lower efficiency compared to the 2D model with an analytic rigid roller. Besides the number of nodes and degrees of freedom, the solution method also affects the computational efficiency. The short explicit and implicit

transient models comprise an identical number of nodes, but the explicit analysis model demonstrated slightly lower efficiency than the implicit analysis model. This was mainly because the explicit solver was more computationally expensive than the implicit solver for problems involving contact with rigid bodies [54]. The uncertainty in efficacy of mass scaling techniques for explicit analysis also affected the computational efficiency. It was interesting to see that although the Eulerian steady-state model used a large number of nodes (32007), it still demonstrated high computational efficiency, similar to the short explicit transient model, with almost three times fewer nodes used (12064). Such a computational saving can be attributed to the steady-state detection option in the Eulerian model, which halted the analysis after rolling along a distance equivalent to 11.6% the modelled wall length. However, the steady-state detection option in Abaqus requires consistent mesh topology in the rolling direction [48], and it does not support the use of multiple CPUs. For all the developed efficient models, the benefits brought by the attempt to further reduce the nodes through progressive meshing techniques were deemed to be limited.

4.4.2 Steady-state rolling and its implication in computational efficiency

The steady-state rolling is of major interest for analysis since it dominates the mechanical response of the WAAM component to the rolling. The efficient model is effective and acceptable if it can capture the steady-state rolling. It was demonstrated that all the efficient models developed here had sufficient wall length to obtain a stable and consistent solution for the steady-state rolling (Figure 4-5).

The computational efficiency of the 3D short explicit transient model could be increased further by reducing the wall length in the model, since the whole length was still considerably larger than the length of the region where steady-state rolling was established (Figure 4-5). Similarly, to further increase efficiency, the wall length in the 2D short implicit transient model could be reduced. For the Eulerian model, the application of less strict steady-state detection norms could reduce the time required to reach steady state and hence increase the efficiency

of the model. As the solution to the 3D short implicit transient model experienced appreciable fluctuation in the region under steady-state rolling, further reduction in wall length is not suggested due to concern about solution accuracy.

4.4.3 Solution accuracy

To assess the solution accuracy of the efficient models, the distributions of longitudinal RS and PS in three directions were compared to the solution of the large scale implicit transient model (control model).

The solution of the short implicit transient model was in best agreement with the solution of the control model (Figure 4-8, Figure 4-9, Figure 4-10, Figure 4-11, Figure 4-12). The short explicit transient model, Eulerian steady-state model and 2D plane stress model demonstrated different levels of discrepancy of the predicted results compared to the control model.

The overall consistent results of the rolling simulations by the short implicit transient model and the control model could be explained by the fact that the largely reduced length of the WAAM component considered in the rolling model did not significantly impair the accuracy of the model solution, as long as the steady-state was reached. Moreover, the same mesh topology and Abaqus Standard solver (implicit method) were used in both models. The slight discrepancy in the results could be attributed to the applied constraints on the Start and End boundaries in the short model, which could lead to enhanced stiffness in the rolling direction.

The solution accuracy of the short explicit transient model (Figure 4-8 and Figure 4-9) was impaired by the artificially increased density of the material, as a result of the mass scaling which was used to accelerate computation. The increased density could exacerbate the effect of inertial force which could violate the equilibrium state assumed in the rolling process. As found in a parametric study conducted in this research, using lower values of mass scaling factor made the short transient explicit model more accurate, but led to significantly lower efficiency compared to the short implicit transient model. This confirmed the findings of Harewood et al. [54] and Oliver et al. [55] that the implicit solver is

more accurate and less computationally expensive than the explicit solver for relatively simple contact problems with rigid bodies involved.

Nevertheless, an explicit analysis still has the potential to better handle complex contact problems and large deformations than an implicit analysis. Furthermore, the short explicit transient model reached steady state earlier than the short implicit transient model (Figure 4-5). This allowed further reduction of the wall length, and as a result, a considerable reduction of nodes used in the analysis could be achieved. From a numerical algorithm point of view, the explicit solution method was better suited to parallel computation than the implicit method.

The Eulerian model was less accurate than the short implicit and explicit models due to the unrealistic rolling process simulated in the Eulerian model. The control model simulated the actual rolling process in reality [3], in which the deformable wall remained steady and the roller moved along the wall, causing the free rotation of the roller due to friction between the roller and the wall. In contrast, in the Eulerian model, the torque was applied to the steady roller, and the wall material movement was caused by the rotation of the roller and the friction between the roller and the wall. The friction caused material to “stick” to the roller, and the applied torque drew the material underneath, which increased longitudinal tensile PS under the roller (3 mm below the rolled surface) as compared to the control model (Figure 4-9). As a result, larger tensile deformation and higher compressive longitudinal RS were generated in this region (Figure 4-8). More extensive stretching of material due to the applied torque occurred as well on the rolled surface, which caused longitudinal tensile RS (Figure 4-8). As the Eulerian model also employed an explicit solver, similar issues to the short explicit transient model could affect the solution accuracy of the Eulerian model.

The 2D plane stress model did not accurately represent a rolling process for the WAAM component in which the RS and PS were non-uniformly distributed in the through-thickness direction of the wall (Figure 4-13 and Figure 4-14). During the rolling, the normal and longitudinal strains were accommodated by the transverse strain [4]. Meanwhile, the isotropic friction restricted the longitudinal and transverse deformation under the roller. The 2D model could not capture these

complex 3D phenomena due to its plane-stress assumption. In fact, the out-of-plane stress played a considerable role in the final state of the longitudinal residual stress and strain. As the wall and substrate were not actually aligned within the same plane, the substrate effect could not be realistically represented in a 2D model. For a similar reason, a 2D plane strain model defined on the transverse section (e.g., y-z plane of the 3D model in Figure 4-2) is not suitable for accurate simulation of the rolling process. It assumes zero strain in the longitudinal/rolling direction, where large deformation was observed in the 3D models. Nevertheless, the 2D plane stress model was 86.5% more efficient than the short 3D models (Table 4-2). Considering the computational efficiency, the 2D model could be used for rough and fast estimation of major rolling parameters for analysis later refined using 3D models.

4.5 Conclusions

In the present study, the efficiency and prediction of four models of high pressure rolling for a WAAM deposited wall, including the 3D short implicit transient model, 3D short explicit transient model, 3D Eulerian steady-state model and 2D short implicit transient model, were evaluated. The computational efficiency and solution accuracy of these models were compared with a conventional large-scale transient model (control model). It was demonstrated that the developed efficient models allowed for the simulation of rolling on the last layer of the built wall, with a computational time of less than one hour, using a desktop computer. This will enable development of efficient models to simulate inter-layer rolling for WAAM components; such simulation is currently unpractical. Based on the results and analyses, following conclusions are made:

1. The efficiency of a rolling model depends largely on the number of nodes and degrees of freedom involved in the FEM analysis. Reduction of component length in the model can dramatically improve the computational efficiency without impairing solution accuracy, since steady-state rolling can be established within a region of short length.

2. The implicit analysis method is more accurate and efficient than the explicit analysis method for the short rolling models with analytic rigid rollers and relatively low rolling loads.
3. The solution of the 3D short implicit transient model is most accurate among the developed efficient models, as compared to the control model. The accuracy of the 3D short explicit transient model was impaired by the artificially assigned high density of material (mass scaling for acceleration of computation). Reduction of the mass scaling factor improved accuracy, but increased computational cost significantly. The 3D Eulerian steady-state model is less accurate due to unrealistic representation of the rolling process, and its efficiency is limited by the restriction that parallel computation is not supported when the steady-state detection feature is enabled using the selected version of Abaqus software.
4. The 2D implicit transient model cannot capture the 3D deformation mechanism during rolling, and hence it is least accurate in predicting the distributions of longitudinal residual stress and plastic strain. Nevertheless, the 2D transient model is much more efficient than the 3D models, and it could be used for a quick qualitative estimate of the mechanical response of the WAAM component to rolling.
5. Application of an elastic deformable roller instead of an analytic rigid roller in the 2D rolling model barely affected the solution, but significantly reduced computational efficiency.

4.6 References

1. Karayel E., Bozkurt Y. Additive manufacturing method and different welding applications. Journal of Materials Research and Technology. September 2020; 9(5): 11424–11438. Available at: DOI:10.1016/j.jmrt.2020.08.039

2. Yilmaz O., Ugla AA. Microstructure characterization of SS308LSi components manufactured by GTAW-based additive manufacturing: shaped metal deposition using pulsed current arc. The International Journal of Advanced Manufacturing Technology. March 2017; 89(1–4): 13–25. Available at: DOI:10.1007/s00170-016-9053-y

3. Colegrove PA., Coules HE., Fairman J., Martina F., Kashoob T., Mamash H., Cozzolino LD. Microstructure and residual stress improvement in wire and arc additively manufactured parts through high-pressure rolling. Journal of Materials Processing Technology. October 2013; 213(10): 1782–1791. Available at: DOI:10.1016/j.jmatprotec.2013.04.012

4. Martina F., Roy MJ., Szost BA., Terzi S., Colegrove PA., Williams SW., et al. Residual stress of as-deposited and rolled wire+arc additive manufacturing Ti–6Al–4V components. Materials Science and Technology. 21 September 2016; 32(14): 1439–1448. Available at: DOI:10.1080/02670836.2016.1142704

5. Asala G., Khan AK., Andersson J., Ojo OA. Microstructural Analyses of ATI 718Plus® Produced by Wire-ARC Additive Manufacturing Process. Metallurgical and Materials Transactions A. September 2017; 48(9): 4211–4228. Available at: DOI:10.1007/s11661-017-4162-2

6. Gu J., Ding J., Williams SW., Gu H., Ma P., Zhai Y. The effect of inter-layer cold working and post-deposition heat treatment on porosity in additively manufactured aluminum alloys. Journal of Materials Processing Technology. April 2016; 230: 26–34. Available at: DOI:10.1016/j.jmatprotec.2015.11.006

7. Marinelli G., Martina F., Ganguly S., Williams S. Microstructure, hardness and mechanical properties of two different unalloyed tantalum wires deposited via wire + arc additive manufacture. International Journal of Refractory Metals and Hard Materials. September 2019; 83: 104974. Available at: DOI:10.1016/j.ijrmhm.2019.104974

8. Marinelli G., Martina F., Ganguly S., Williams S. Grain refinement in an unalloyed tantalum structure by combining Wire+Arc additive manufacturing and vertical cold rolling. Additive Manufacturing. March 2020; 32: 101009. Available at: DOI:10.1016/j.addma.2019.101009

9. Marinelli G., Martina F., Lewtas H., Hancock D., Mehraban S., Lavery N., et al. Microstructure and thermal properties of unalloyed tungsten deposited by Wire + Arc Additive Manufacture. Journal of Nuclear Materials. August 2019; 522: 45–53. Available at: DOI:10.1016/j.jnucmat.2019.04.049

10. Marinelli G., Martina F., Ganguly S., Williams S. Development of Wire + Arc additive manufacture for the production of large-scale unalloyed tungsten components. International Journal of Refractory Metals and Hard Materials. August 2019; 82: 329–335. Available at: DOI:10.1016/j.ijrmhm.2019.05.009

11. Welding Engineering and Laser Processing Centre of Cranfield University. Demo parts built for industry partners. WAAM. Available at: https://waammat.com/about/demo-parts (Accessed: 15 December 2020)

12. Williams SW., Martina F., Addison AC., Ding J., Pardal G., Colegrove P. Wire + Arc Additive Manufacturing. Materials Science and Technology. 2 May 2016; 32(7): 641–647. Available at: DOI:10.1179/1743284715Y.0000000073

13. Lockett H., Ding J., Williams S., Martina F. Design for Wire + Arc Additive Manufacture: design rules and build orientation selection. Journal of Engineering Design. 2 September 2017; 28(7–9): 568–598. Available at: DOI:10.1080/09544828.2017.1365826

14. Baufeld B., Biest OV der., Gault R. Additive manufacturing of Ti–6Al–4V components by shaped metal deposition: Microstructure and mechanical properties. Materials & Design. June 2010; 31: S106–S111. Available at: DOI:10.1016/j.matdes.2009.11.032

15. Clark D., Bache MR., Whittaker MT. Shaped metal deposition of a nickel alloy for aero engine applications. Journal of Materials Processing Technology. July 2008; 203(1–3): 439–448. Available at: DOI:10.1016/j.jmatprotec.2007.10.051

16. Wu B., Pan Z., Ding D., Cuiuri D., Li H., Xu J., et al. A review of the wire arc additive manufacturing of metals: properties, defects and quality improvement. Journal of Manufacturing Processes. October 2018; 35: 127–139. Available at: DOI:10.1016/j.jmapro.2018.08.001

17. Ding J., Colegrove P., Mehnen J., Williams S., Wang F., Almeida PS. A computationally efficient finite element model of wire and arc additive

manufacture. The International Journal of Advanced Manufacturing Technology. 2014; (70): 227–236. Available at: DOI:10.1007/s00170-013-5261-x

18. Ding J., Colegrove P., Mehnen J., Ganguly S., Sequeira Almeida PM., Wang F., Williams S. Thermo-mechanical analysis of wire and arc additive layer manufacturing process on large multi-layer parts. Computational Materials Science. July 2011; 50(12): S092702561100365X. Available at: DOI:10.1016/j.commatsci.2011.06.023

19. Szost BA., Terzi S., Martina F., Boisselier D., Prytuliak A., Pirling T., Hofmann M., Jarvis DJ. A comparative study of additive manufacturing techniques: Residual stress and microstructural analysis of CLAD and WAAM printed Ti-6Al-4V components. Materials and Design. 2016; 89: 559–567. Available at: DOI:10.1016/j.matdes.2015.09.115

20. Cordiano HV. Effect of Residual Stresses on the Low Cycle Fatigue Life of Large Scale Weldments in High Strength Steel. Journal of Engineering for Industry. 1 February 1970; 92(1): 86–92. Available at: DOI:10.1115/1.3427724

21. Webster GA., Ezeilo AN. Residual stress distributions and their influence on fatigue lifetimes. International Journal of Fatigue. 2001; 23: 375–383. Available at: DOI:10.1016/S0142-1123(01)00133-5

22. Dong P., Brust FW. Welding Residual Stresses and Effects on Fracture in Pressure Vessel and Piping Components: A Millennium Review and Beyond. Journal of Pressure Vessel Technology. 1 August 2000; 122(3): 329–338. Available at: DOI:10.1115/1.556189

23. Dong P. Residual stresses and distortions in welded structures: a perspective for engineering applications. Science and Technology of Welding and Joining. July 2005; 10(4): 389–398. Available at: DOI:10.1179/174329305X29465

24. Colegrove PA., Martina F., Roy MJ., Szost BA., Terzi S., Williams SW., Withers PJ., Jarvis D. High pressure interpass rolling of wire + arc additively

manufactured titanium components. Advanced Materials Research. August 2014; 996: 694–700. Available at: DOI:10.4028/www.scientific.net/AMR.996.694

25. McAndrew AR., Alvarez Rosales M., Colegrove PA., Hönnige JR., Ho A., Fayolle R., et al. Interpass rolling of Ti-6Al-4V wire + arc additively manufactured features for microstructural refinement. Additive Manufacturing. May 2018; 21: 340–349. Available at: DOI:10.1016/j.addma.2018.03.006

26. Hönnige JR., Colegrove PA., Ahmad B., Fitzpatrick ME., Ganguly S., Lee TL., et al. Residual stress and texture control in Ti-6Al-4V wire + arc additively manufactured intersections by stress relief and rolling. Materials & Design. July 2018; 150: 193–205. Available at: DOI:10.1016/j.matdes.2018.03.065

27. F. Martina Investigation of Methods to Manipulate Geometry, Microstructure and Mechanical Properties in Titanium Large Scale Wire + Arc Additive Manufacturing,. Cranfield University; 2014.

28. Colegrove PA., Donoghue J., Martina F., Gu J., Prangnell P., Hönnige J. Application of bulk deformation methods for microstructural and material property improvement and residual stress and distortion control in additively manufactured components. Scripta Materialia. July 2017; 135: 111–118. Available at: DOI:10.1016/j.scriptamat.2016.10.031

29. Martina F., Colegrove PA., Williams SW., Meyer J. Microstructure of Interpass Rolled Wire + Arc Additive Manufacturing Ti-6Al-4V Components. Metallurgical and Materials Transactions A. December 2015; 46(12): 6103–6118. Available at: DOI:10.1007/s11661-015-3172-1

30. Hönnige JR., Colegrove PA., Ganguly S., Eimer E., Kabra S., Williams S. Control of residual stress and distortion in aluminium wire + arc additive manufacture with rolling. Additive Manufacturing. August 2018; 22: 775–783. Available at: DOI:10.1016/j.addma.2018.06.015

31. Lee CH., Kobayashi S. New Solutions to Rigid-Plastic Deformation Problems Using a Matrix Method. Journal of Engineering for Industry. 1 August 1973; 95(3): 865–873. Available at: DOI:10.1115/1.3438238

32. Hwang SM., Kobayashi S. Preform design in plane-strain rolling by the finite-element method. International Journal of Machine Tool Design and Research. January 1984; 24(4): 253–266. Available at: DOI:10.1016/0020-7357(84)90060-X

33. Cozzolino LD., Coules HE., Colegrove PA., Wen S. Investigation of post-weld rolling methods to reduce residual stress and distortion. Journal of Materials Processing Technology. September 2017; 247: 243–256. Available at: DOI:10.1016/j.jmatprotec.2017.04.018

34. Abbaszadeh M., Hönnige JR., Martina F., Neto L., Kashaev N., Colegrove P., et al. Numerical Investigation of the Effect of Rolling on the Localized Stress and Strain Induction for Wire + Arc Additive Manufactured Structures. Journal of Materials Engineering and Performance. August 2019; 28(8): 4931–4942. Available at: DOI:10.1007/s11665-019-04249-y

35. Kashoob, T. The effects of direct rolling on the residual stress, distortion and geometry of ALM welded structures using thermo-mechanical models. MSc Thesis. Cranfield University; 2011.

36. Röttger K. Walzen hartgedrehter Oberflächen. PhD Thesis. Aachen: RWTH; 2003.

37. Yen YC., Sartkulvanich P., Altan T. Finite Element Modeling of Roller Burnishing Process. CIRP Annals. 2005; 54(1): 237–240. Available at: DOI:10.1016/S0007-8506(07)60092-4

38. Balland P., Tabourot L., Degre F., Moreau V. An investigation of the mechanics of roller burnishing through finite element simulation and experiments. International Journal of Machine Tools and Manufacture. February 2013; 65: 29–36. Available at: DOI:10.1016/j.ijmachtools.2012.09.002

39. Manouchehrifar, A., Alasvand, K. Finite Element Simulation of Deep Rolling and Evaluate the Influence of Parameters on Residual Stress Recent Researches in Applied Mechanics. WSEAS Press, Athens. : 121–127.

40. Beghini M., Bertini L., Monelli BD., Santus C., Bandini M. Experimental parameter sensitivity analysis of residual stresses induced by deep rolling on 7075-T6 aluminium alloy. Surface and Coatings Technology. September 2014; 254: 175–186. Available at: DOI:10.1016/j.surfcoat.2014.06.008

41. Hassani-Gangaraj SM., Carboni M., Guagliano M. Finite element approach toward an advanced understanding of deep rolling induced residual stresses, and an application to railway axles. Materials & Design. October 2015; 83: 689–703. Available at: DOI:10.1016/j.matdes.2015.06.026

42. Trauth D., Klocke F., Mattfeld P., Klink A. Time-efficient Prediction of the Surface Layer State after Deep Rolling using Similarity Mechanics Approach. Procedia CIRP. 2013; 9: 29–34. Available at: DOI:10.1016/j.procir.2013.06.163

43. Perenda J., Trajkovski J., Žerovnik A., Prebil I. Residual stresses after deep rolling of a torsion bar made from high strength steel. Journal of Materials Processing Technology. April 2015; 218: 89–98. Available at: DOI:10.1016/j.jmatprotec.2014.11.042

44. Mehner T., Bauer A., Härtel S., Awiszus B., Lampke T. Residual-stress evolution of cold-rolled DC04 steel sheets for different initial stress states. Finite Elements in Analysis and Design. May 2018; 144: 76–83. Available at: DOI:10.1016/j.finel.2017.11.006

45. Lan J., Feng S., Hua L. The residual stress of the cold rolled bearing race. Procedia Engineering. 2017; 207: 1254–1259. Available at: DOI:10.1016/j.proeng.2017.10.879

46. Pan R., Pirling T., Zheng J., Lin J., Davies CM. Quantification of thermal residual stresses relaxation in AA7xxx aluminium alloy through cold rolling. Journal of Materials Processing Technology. February 2019; 264: 454–468. Available at: DOI:10.1016/j.jmatprotec.2018.09.034

47. Coules HE., Horne GCM., Kabra S., Colegrove P., Smith DJ. Three-dimensional mapping of the residual stress field in a locally rolled aluminium alloy

specimen. Journal of Manufacturing Processes. April 2017; 26: 240–251. Available at: DOI:10.1016/j.jmapro.2017.02.010

48. Abaqus FEA Software. Version 6.14 - 4. User manual; Theory Guide.

49. Bijak-Żochowski M., Marek P. Residual stress in some elasto-plastic problems of rolling contact with friction. International Journal of Mechanical Sciences. January 1997; 39(1): 15–32. Available at: DOI:10.1016/0020-7403(96)00018-5

50. Rodríguez A., López de Lacalle LN., Celaya A., Lamikiz A., Albizuri J. Surface improvement of shafts by the deep ball-burnishing technique. Surface and Coatings Technology. February 2012; 206(11–12): 2817–2824. Available at: DOI:10.1016/j.surfcoat.2011.11.045

51. Balland P., Tabourot L., Degre F., Moreau V. Mechanics of the burnishing process. Precision Engineering. January 2013; 37(1): 129–134. Available at: DOI:10.1016/j.precisioneng.2012.07.008

52. Abaqus FEA Software. Version 6.14 - 4. User manual; Example Problems Guide.

53. Wang M., Yang H., Sun Z., Guo L., Ou X. Dynamic explicit FE modeling of hot ring rolling process. Transactions of Nonferrous Metals Society of China. December 2006; 16(6): 1274–1280. Available at: DOI:10.1016/S1003-6326(07)60006-5

54. Harewood FJ., McHugh PE. Comparison of the implicit and explicit finite element methods using crystal plasticity. Computational Materials Science. April 2007; 39(2): 481–494. Available at: DOI:10.1016/j.commatsci.2006.08.002

55. Oliver J., Huespe AE., Cante JC. An implicit/explicit integration scheme to increase computability of non-linear material and contact/friction problems. Computer Methods in Applied Mechanics and Engineering. April 2008; 197(21–24): 1865–1889. Available at: DOI:10.1016/j.cma.2007.11.027

56. Chin, J.Y., Lee, S.W., Paik, S.H. The effects of numerical result and computing time due to mass scaling in rolling analysis. 8th International LS-DYNA Users Conference. pp. 33–38.

57. Maniatty AM., Dawson PR., Weber GG. An Eulerian elasto-viscoplastic formulation for steady-state forming processes. International Journal of Mechanical Sciences. January 1991; 33(5): 361–377. Available at: DOI:10.1016/0020-7403(91)90075-E

58. Synka J., Kainz A. A novel mixed Eulerian–Lagrangian finite-element method for steady-state hot rolling processes. International Journal of Mechanical Sciences. December 2003; 45(12): 2043–2060. Available at: DOI:10.1016/j.ijmecsci.2003.12.008

59. Vetyukov Yu., Gruber PG., Krommer M., Gerstmayr J., Gafur I., Winter G. Mixed Eulerian-Lagrangian description in materials processing: deformation of a metal sheet in a rolling mill: Mixed Eulerian-Lagrangian description in materials processing: deformation of a metal sheet in a rolling mill. International Journal for Numerical Methods in Engineering. 9 March 2017; 109(10): 1371–1390. Available at: DOI:10.1002/nme.5314

60. Michaleris, P., DeBiccari, A. Prediction of welding distortion. Welding Journal. 76(4): 172–181.

5 Efficient determination and evaluation of steady-state thermal-mechanical variables generated by wire arc additive manufacturing and high pressure rolling

This chapter is based on the following publication:

Gornyakov V., Sun Y., Ding J., Williams S. Efficient determination and evaluation of steady-state thermal-mechanical variables generated by wire arc additive manufacturing and high pressure rolling. Submitted to Modelling and Simulation in Materials Science and Engineering (Manuscript ID: MSMSE-105517) for Publication.

For accurate simulation of a multilayer rolling process, the residual stresses and plastic strains caused by WAAM deposition cycles should be included in the model. This chapter presents the development and validation of efficient modelling method for simulation of WAAM and rolling using short efficient models, as well as the subsequent transfer of steady-state solution to the long model to determine residual stress and distortion in large-scale WAAM parts before and after clamps removal.

Abstract: Wire arc additive manufacturing (WAAM) of large component is susceptible to residual stress and distortion, which are detrimental but can be mitigated through rolling the component. In this study, an efficient modelling method is developed to simulate both WAAM and rolling, and this method can also be applied to other manufacturing processes to determine steady-state variables. For a clamped wall component, the computationally efficient reduced-size WAAM and rolling models (i.e., short models) can obtain steady-state solutions equivalent to those obtained by conventional full-size models. For the short models, the undesirable effect of reducing the length of modelled component is counteracted by imposing additional longitudinal constraint as proper to specific processes. The steady-state solution obtained by the short model is then mapped to a long model for analysis of residual stress and distortion after clamps removal. The WAAM model predictions of temperature, residual stress and distortion are in good agreement with experimental measurements.

For the steady-state WAAM region, compressive longitudinal plastic strain is formed uniformly in the wall, and the influential factors and implications of the plastic strain are analysed. The high pressure rolling on the WAAM-deposited wall introduces tensile plastic strain that compensates for the compressive plastic strain caused by WAAM deposition, thereby mitigating the tensile residual stress in the clamped wall and alleviating the bending distortion after clamps removal. This study demonstrates an efficient approach for modelling large-scale manufacturing and provides insights into the steady-state strains and stresses generated by WAAM and rolling.

Keywords: large-scale additive manufacturing; cold working; residual stress; distortion; plastic strain; simulation.

5.1 Introduction

Wire Arc Additive Manufacturing (WAAM) is an emerging variant of Additive Manufacturing (AM) technology, which can build medium- to large-scale fully-dense complex components with functional structural integrity [1–3]. WAAM with high deposition rate, which can be 9.5 kg/h for martensitic stainless steel [4] and most practically, 1-4 kg/h for aluminium and steel [1], provides rapid and economical route to large-scale AM. Using WAAM processes, large components were built from steel [5], titanium alloy [6], nickel superalloy [7], aluminium alloy [8], tantalum [10, 11], tungsten [11,12], etc., and functionally graded structures were also printed using refractory metals [13]. The modular design of WAAM process utilises standard welding equipment and wire consumables, and hence allows low build-up and operational cost [1,3,14]. Moreover, a range of cold working can be integrated in WAAM systems. For instance, high pressure rolling was recently combined with WAAM to introduce some beneficial effects, such as mitigation of distortion and residual stress [15], microstructural refinement or modification [5,16], elimination of porosity [17,18] and improvement of mechanical properties [19,20]. Despite the experimental evidence of the benefits brought by rolling, the underlying mechanisms responsible for such benefits are complex and need to be understood. Unfortunately, experimental measurements

are limited and difficult to provide adequate information for establishing the understanding. Therefore, modelling is crucial for gaining insights.

WAAM-built components are susceptible to residual stress (RS) and distortion [5,6], which are major challenges that hinder the wider applications of WAAM in industry. RS arises from the process-induced plastic strain (PS), among other incompatible deformation, as generated during the thermal cycles caused by WAAM deposition. Distortion usually occurs when the RS is partially released after the removal of clamps on the WAAM-built component, while it can also occur during the WAAM process due to the deformation induced by temperature changes. RS can lead to early fatigue failure, stress corrosion cracking and brittle fracture [21–24], while excessive distortion is detrimental to the process stability and geometrical precision. Therefore, determination and mitigation of RS and distortion is one of the main aims in WAAM research.

Thermal-mechanical Finite Element Analysis (FEA) models prove a robust numerical tool to determine RS and distortion in both powder-based AM [25–27] and WAAM [28–37]. However, the thermal-mechanical models are strongly nonlinear, and require fine meshes and small time increments to obtain accurate solution, meaning that the computational time can be too long to be practical for analysis of large WAAM-built components. As reported by Ding et al. [37], a 3D transient thermal-mechanical model for a 20-layer 500 mm long WAAM-deposited wall took 75 hours to obtain a solution using High-Performance Computing (HPC) facility. Such long computational time of conventional FEA model may not be acceptable for industrial WAAM components which can be several meters long. Thus, an efficient modelling approach is needed.

Several efficient FEA modelling techniques have been developed in the allied fields of welding, powder-based AM and WAAM. A straightforward approach to reduce computational time is the use of graded mesh or adaptive meshing to reduce the number of the nodes (and hence the degrees of freedom) in the thermal-mechanical model [28–31,36,37]. The efficiency gained through this approach is compromised by the effort/time spent in meshing and the spatial resolution required for the analysis. Another approach is the simplification of 3D

problems into 2D problems (reduction of the degrees of freedom). Camilleri et al. [38,39] and Fachinotti et al. [40] used a 2D transient thermal model to predict the temperature distribution in a section transverse to the welding direction. However, a 2D thermal model does not consider longitudinal heat flow, which is usually significant during WAAM deposition. An Eulerian model is efficient to obtain steady-state temperature field. Zhang et al. [41], Wang et al. [42] and Ding et al. [37] created Eulerian steady-state models where heat source remained stationary and was attached to Eulerian reference frame, while material flowed through the finite element mesh. The Eulerian model can be two-orders of magnitude faster than the conventional Lagrangian model, but its implementation for mechanical analysis is often sophisticated due to complicated mathematical formulation required [41,43]. For efficient mechanical analysis, Michaleris and DeBicarry [44,45] developed a PS-based method to predict distortion in large-scale welded thin-walled structures. The method is a variant of inherent strain method, which is based on elastic analysis using the sum of nonelastic strains as inherent strain, as originally proposed by Ueda et al. [46,47] for welding analysis. Recently, Chen et al. [48] implemented inherent strain method for multilayer deposition by direct metal laser sintering AM. However, some limitations of the inherent strain method have been identified for powder-based AM processes when small-scale thermal-elastic-plastic model is used to determine the inherent strain [49,50].

The FEA-based determination and evaluation of RS and distortion becomes more challenging when WAAM is combined with rolling. The rolling simulation for large components is also computationally demanding. It was shown that conventional FEA simulation of single-pass rolling in a 456 mm long weld took 95.3 hours using HPC facility [51]. For efficient modelling of high pressure rolling, Gornyakov et al. [52] (Chapter 4) demonstrated that a 3D implicit analysis model with reduced component length predicted steady-state RS and PS equivalent to the solution of a conventional full-size model, but the computational time was significantly reduced. Gornyakov et al. [52] (Chapter 4) also examined a number of other efficient modelling techniques for rolling, including explicit analysis, Eulerian steady-state model and 2D simulation, and they found that the short model using implicit solution algorithm is the best option for rolling simulation when both

efficiency and accuracy are required. However, Gornyakov et al. [52] (Chapter 4) did not investigate the effects of longitudinal constraint on the predictions by the short model, nor the transfer of short model solution to the full-size component for further analysis.

Most of previous research focused on the development of efficient modelling methods for individual manufacturing processes, such as WAAM [30,37] and rolling Chapter 4 and Ref. [52]. It still needs a general approach to enable efficient modelling of the combined process of WAAM and rolling. As steady state exists for both WAAM and rolling, it is hypothesised that steady-state variables such as strains and stresses, which are of major interest for most analyses, can be obtained using a technique in the same framework. Therefore, this study is aimed to develop an efficient modelling approach applicable to both WAAM and rolling, thereby gaining insights into the mechanism of rolling-enabled mitigation of WAAM deposition RS and distortion. The computational efficiency is enhanced through reducing component length in the model. To compensate for the length reduction, proper longitudinal constraint is imposed in the short model to obtain the steady-state strains and stresses. Then the steady-state solution is mapped into a full-size long model to carry out mechanical analysis for the whole component after removal of clamps. In particular, the process-induced PS distribution is investigated, which is the origin of RS and affects the distortion.

5.2 Modelling and verification/validation methods

5.2.1 Efficient method to simulate steady state of WAAM and rolling

Previous research showed that the WAAM [30,37] and rolling processes (Chapter 4 and Ref. [52]) operating in clamped walls can attain a steady-state within a short distance along the travelling direction of arc and roller (i.e., longitudinal direction), within which the PS and RS are almost constant. This means that a short transient model with reduced component length can be used to obtain the steady-state variables and save computational time. However, the steady-state solution obtained by the short model cannot be used for analysis of the effects of clamps removal on final RS and distortion, for which a full-size long model is needed,

since the self-constraint associated with the final state is dependent on the actual length of the component without external constraint.

Figure 5-1 shows the efficient method proposed here to determine the steady-state physical variables of WAAM and rolling, as well as the final RS field and distortion in the component. Firstly, a short model is generated to determine the steady-state solution. For the WAAM and rolling processes considered in this study, a component length of 72 mm was found to be sufficient to attain the steady-state. Secondly, the steady-state solution of the short model is mapped to a long mechanical model (the full length of the component is 500 mm for the studied WAAM and rolling). The solution slice obtained from the steady-state region in the short model is repeatedly in space mapped to the long mechanical model using a solution mapping technique (5.2.2 Solution mapping technique). The initial shape of the component in the mapped long model depends on the displacement solution of the short model. Thirdly, the final RS and distortion after removal of clamps are obtained using the long mechanical model.

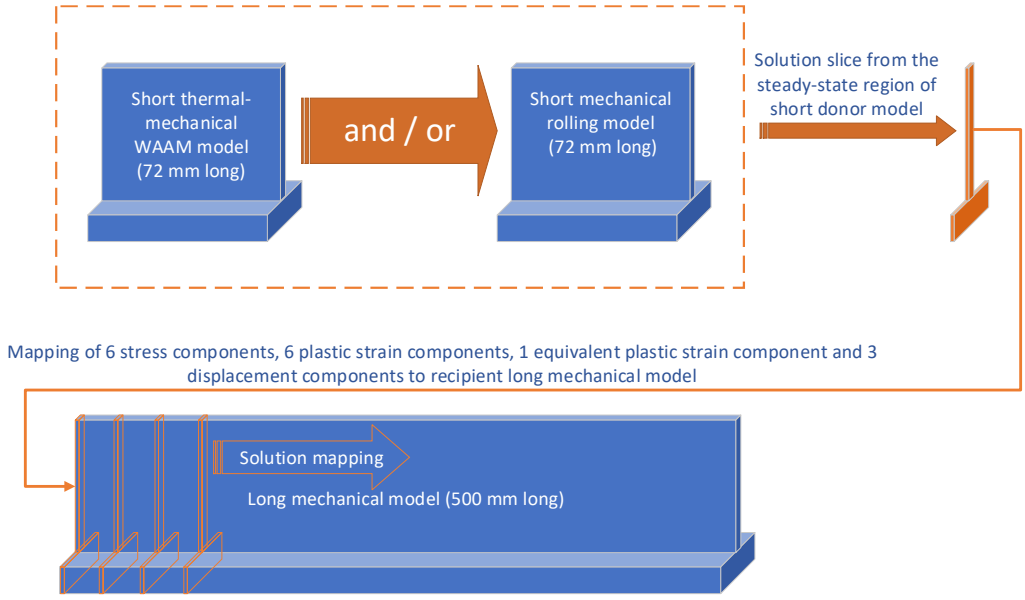

Figure 5-1 Schematic diagram of the proposed efficient method for determining steady-state thermal-mechanical variables using short models of WAAM and rolling, followed by mapping solution to long model for further analysis.

5.2.2 Solution mapping technique

Abaqus FEA software was used for the WAAM and rolling simulations. A solution mapping technique was developed to transfer the solution from the short mechanical model to the long mechanical model, while the standard functions of Abaqus software do not support the transfer of equivalent solution between models with different lengths.

The Abaqus keyword of *INITIAL CONDITIONS was used to define the initial state of the long model using external text files, which contain a list of elements with predefined initial parameters. Element numbers were assigned in a controlled manner during meshing, except in the substrate where the transition from fine mesh to coarse mesh is complicated and the mesh topology is not identical in the longitudinal direction (Figure 5-2 and Figure 5-3). The six components of stress tensor, six components of PS tensor and the equivalent PS were extracted from the solution slice perpendicular to the longitudinal direction in the steady-state region of the short mechanical model (donor). A Python script was developed to generate the initial conditions, in which the extracted solution slice was assigned sequentially in space to the corresponding elements of each transverse section of the long mechanical model (recipient). For the substrate with complicated mesh topology, average values of stress and PS were obtained from the short model and predefined to the long model. This simplification was necessary for the substrate since the controlled node numbering was not conducted in this region, and thus the distribution of mapped parameters is assumed to be uniform in this region of the recipient model. The Abaqus Keywords of *INITIAL CONDITIONS STRESS, PLASTIC STRAIN and HARDENING were added to the recipient model. A calculation of stress rebalancing was carried out in the recipient model with the predefined initial conditions and clamps, followed by the prediction of mechanical response to the removal of the clamps. It should be mentioned that the displacement solution was not mapped to the long WAAM mechanical model because negligible distortion was predicted by the short WAAM mechanical model under clamped condition, while displacement mapping was performed to the long rolling model because considerable deformation occurred in the short rolling model.

5.2.3 WAAM model and validation method

The proposed modelling method was applied to WAAM deposition of a mild steel (S355) wall (Figure 5-2). The validation of the WAAM model was based on previous experiments by Ding et al. [34,37] and Colegrove et al. [5], and the details of the experiments can be found in the references. A short multilayer model was used for thermal-mechanical analysis of WAAM deposition. The transient temperature field was predicted by a short thermal model and then the thermal solution was transferred to a short mechanical model. Only half of the wall and substrate was considered in the model due to symmetry.

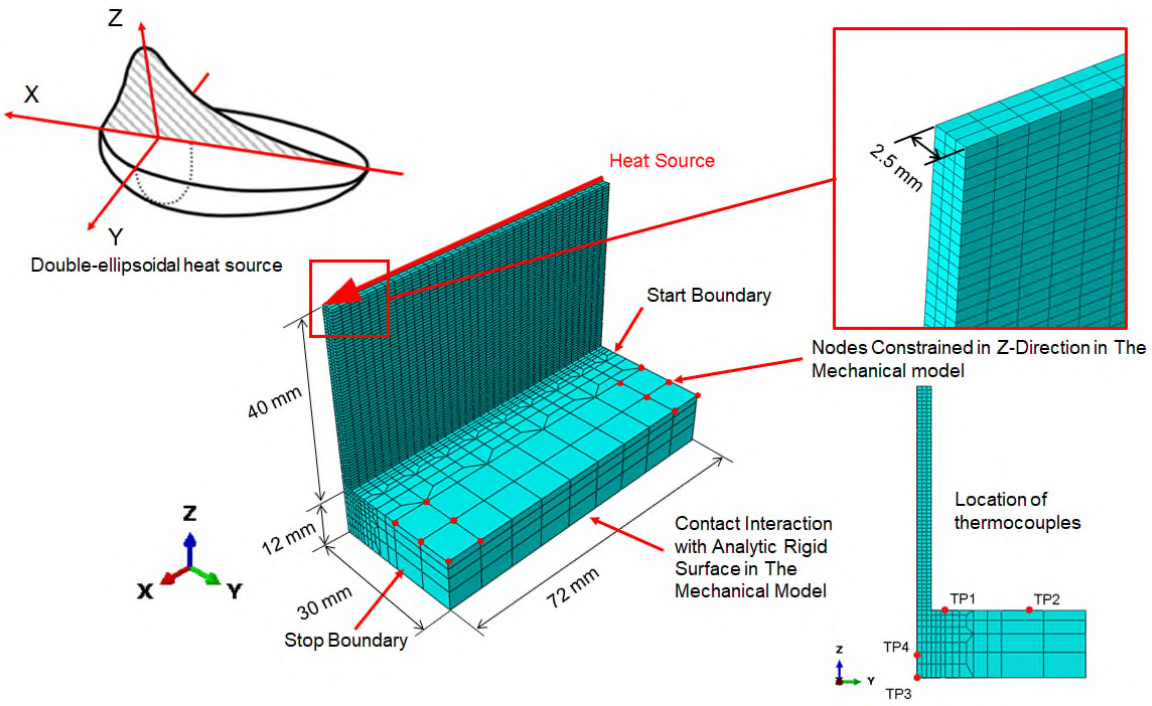

Figure 5-2 Short transient thermal-mechanical model of 20-layer WAAM-deposited wall with reduced length. The schematic of double-ellipsoidal heat source and the locations of thermocouples in the cross-section are also shown.

In the short thermal model, double ellipsoidal moving heat source was employed and implemented using Abaqus user defined subroutine DFLUX. The heat source parameters were adopted from Ref. [37]. Simplified element “birth” technique was used to simulate the deposition of a whole layer each time. Ding et al. [30] found

that the activation of the whole layer each time, instead of only activating the elements within the heat source radii, barely affects the solution accuracy.

WAAM associated with steep thermal gradients, which significantly influence heat conduction process in deposited components. Temperature dependent material properties required for accurate simulation of heat conduction phenomenon. Temperature dependent material properties reported in Ref. [44] were used in thermal model (Table 5-1). To account phase transformation, the specific heat was reduced at temperature 723 °C and above [34]. Latent heat of material melting was simulated with energy value 270 kJ/kg in range of temperatures 1450 – 1500 °C (solidus and liquidus temperatures accordingly) [44]. The thermal conductivity at temperatures higher than the melting point (1500 °C) was artificially increased to somewhat reflect the convective heat transfer in the molten pool.

Table 5-1 Temperature dependent thermal conductivity and specific heat adopted from Ref. [44].

Temperature (°C)	Thermal conductivity (W/m °C)	Specific heat (J/Kg °C)
20	52	480
100	51	507
200	48	532
300	44	574
400	43	624
500	39	703
600	35.6	788
700	32	870
723	28	798
850	26	679
900	26.4	658
1250	30	666
1450	30	666
1500	120	670
2000	120	670

Eight-node linear heat transfer brick elements (Abaqus designation DC3D8) were used in the thermal model. The mesh density gradually changed from being fine in the deposited wall (element size was 2 mm × 0.833 mm × 0.667 mm) to being coarse in the substrate (element size was 8 mm × 7.5 mm × 1.765 mm). The coefficient of convection and the emissivity of radiation for all free surfaces were 5.7 $W \cdot m^{-2} \cdot K^{-1}$ and 0.2, respectively. Values of coefficients were adopted from Ref. [34,44]. Conductive heat loss due to the water-cooled backing plate was simulated by imposing convection with a coefficient of 300 $W \cdot m^{-2} \cdot K^{-1}$ on the bottom of the substrate. Value of coefficient was found during numerical trials and chosen as the best matching with experimental results [34].

The mechanical model has the same dimensions and mesh topology as the thermal model. The element type was 3D stress eight-node linear brick with reduced integration (Abaqus designation C3D8R). WAAM thermal gradients cause uneven expansion and contraction of material, which in conjunction with material softening at high temperatures responsible for formation of uneven PS in deposited components. Yield stress has significant influence of RS and distortion during welding simulations [53]. Accurate simulation of PS and RS formation during WAAM required use of temperature dependent material properties. Solid state phase transformation was not considered, because for mild steel it does not play a significant role in residual stress [54]. Two sets of Yield strength material properties were used for the substrate and deposited wall, respectively [44] (Table 5-2 and Table 5-3). It should be mentioned that Colegrove et al. [5] found that the peak longitudinal RS near the interface between the substrate and deposit reached 600 MPa. This finding suggests that the actual value of yield strength of WAAM deposited wall could be larger than the 450 MPa for mild steel at 20 °C reported in Ref. [44]. In the present model, the values of mild-steel yield strength as suggested by Ref. [44] were increased by 50 MPa for the wall deposit at the temperature range of 20 – 500 °C to reflect the actual yield strength inferred from the experiments on the WAAM-built component.

Table 5-2 Temperature dependent Poisson's ratio and thermal expansion coefficient adopted from Ref. [44].

Temp. [°C]	Poisson's ratio	Temp. [°C]	Thermal expansion coefficient [1/°C]
20	0.29	20	1.20E-05
200	0.295	1000	1.50E-05
400	0.3	1500	1.50E-05
600	0.32		
800	0.35		
1000	0.39		
1500	0.39		

Table 5-3 Temperature dependent Young's modulus and yield strength of filler metal and base metal adopted from Ref. [44].

Temp. (°C)	Young's Modulus [GPa]	Yield Strength [MPa]			
		Deposit	Deposit (εp = 0.01)	Substrate	Substrate (εp = 0.01)
20	206	500	570	350	420
100	203	500	570	330	400
200	201	470	550	305	380
300	200	440	500	270	350
400	165	370	420	230	290
500	100	310	350	180	230
600	60	170	215	125	160
700	40	60	100	60	100
800	30	50	80	60	60
900	20	50	50	60	60
1000	10	50	50	60	60
1500	10	50	50	60	60

A surface-to-surface contact interaction was specified between the bottom of the substrate and an analytic rigid shell simulating the backing plate. Six nodes in each corner of the top surface of the substrate were constrained in the vertical direction in order to simulate the clamps (Figure 5-2).

The short model with reduced component length has lower resistance to longitudinal deformation compared to the actual deposited wall. For this reason, additional longitudinal constraint was applied to the short model and the influence of different constraint conditions on predicted PS and RS are investigated. Three types of longitudinal constraint were considered in the short model, i.e., free ends, constrained ends and full constraint. For the free-ends condition, there is no additional longitudinal constraint imposed on the two end-surfaces of the shortened wall component; for the constrained-ends condition, the longitudinal displacements of the nodes on the two end-surfaces corresponding to the start and stop boundaries are constrained; for the full-constraint condition, all the nodes in the meshed wall component are constrained from longitudinal motion.

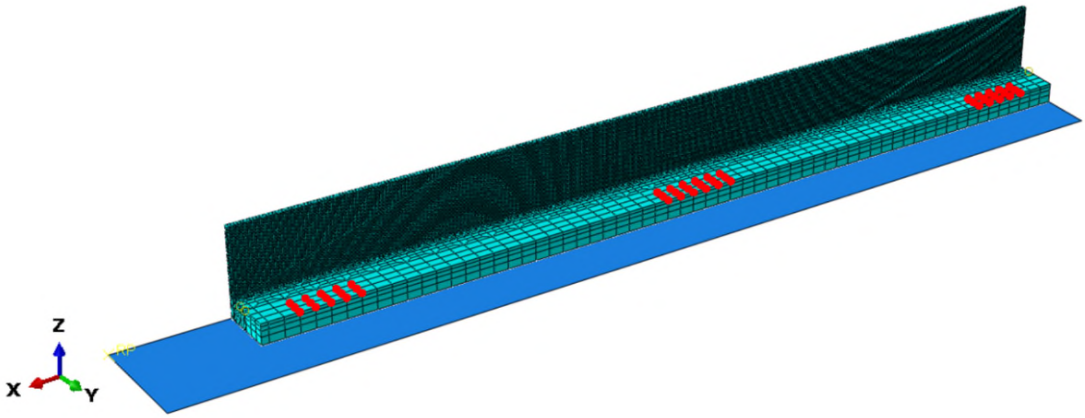

Figure 5-3 Mapped long mechanical model to simulate the removal of clamps (the constrained nodes are indicated in red).

In the long mechanical model, all dimensions were set to be the same as those in the experiment [37], and elasto-plastic properties identical to the short model were used. The steady-state PS and RS that were predicted by the short model were mapped to the long model using the solution mapping technique (5.2.2 Solution mapping technique). In addition, the longitudinal constraint used in the short model was removed in the long model. The backing-plate support to the built component was simulated through surface-to-surface contact interaction between the substrate bottom and an analytic rigid shell. The clamps were simulated through fixing the selected nodes on the top surface of the substrate (Figure 5-3). During the mechanical analysis using the long model, stress

balancing was first established and then the clamps were removed to obtain the final state.

5.2.4 Rolling model and verification method

The efficient modelling method (Sections 5.2.1 and 5.2.2) was also applied to high pressure rolling on a wall component with identical geometry to the WAAM-deposited component, as shown in Figure 5-4. The rolling simulation considered two scenarios. In the first scenario, the rolling was performed on the component with a stress-free initial condition, i.e., pure rolling analysis. In the second scenario, the WAAM and rolling processes were combined, and the WAAM-induced PS and RS were defined as the initial condition for the rolling simulation.

The setup of the short rolling model was detailed in Chapter 4. Only key information is repeated here for brevity. The temperature was assumed to be room temperature and kept constant when rolling was simulated as an individual process. When rolling was combined with WAAM, the rolling was simulated on the top surface of the WAAM deposited wall after cooling, i.e., post-build rolling simulation (inter-layer rolling simulation will be reported separately in Chapter 7). The flat roller was modelled as a rigid shell. The assumption of rigid roller is beneficial to computational efficiency without impairing solution accuracy Chapter 4 and Ref. [52]. For pure rolling simulation, the substrate and wall were modelled as a deformable body with material properties adopted from Ref. [44] for mild steel S355. A vertical rolling load of 50 kN was imposed to the wall through controlling the penetration of the roller and a friction coefficient of 0.3 was assumed for the contact between the roller surface and the top surface of the wall. All nodes on the bottom surface of the substrate were fixed to represent the clamps during rolling. Similar to the short WAAM model, different longitudinal constraint conditions (i.e., free ends, constrained ends and full constraint) were considered in the short rolling model to investigate the sensitivity of the predicted results to the assumed longitudinal constraint.

To verify the efficacy of the short model, a conventional full-size transient rolling model (500 mm long) was also developed Chapter 4 and Ref. [52]. The PS and RS distributions predicted by the short model are compared with those predicted

by the full-size model for the steady state of rolling, such that the accuracy of the short model to predict steady-state PS and RS can be verified.

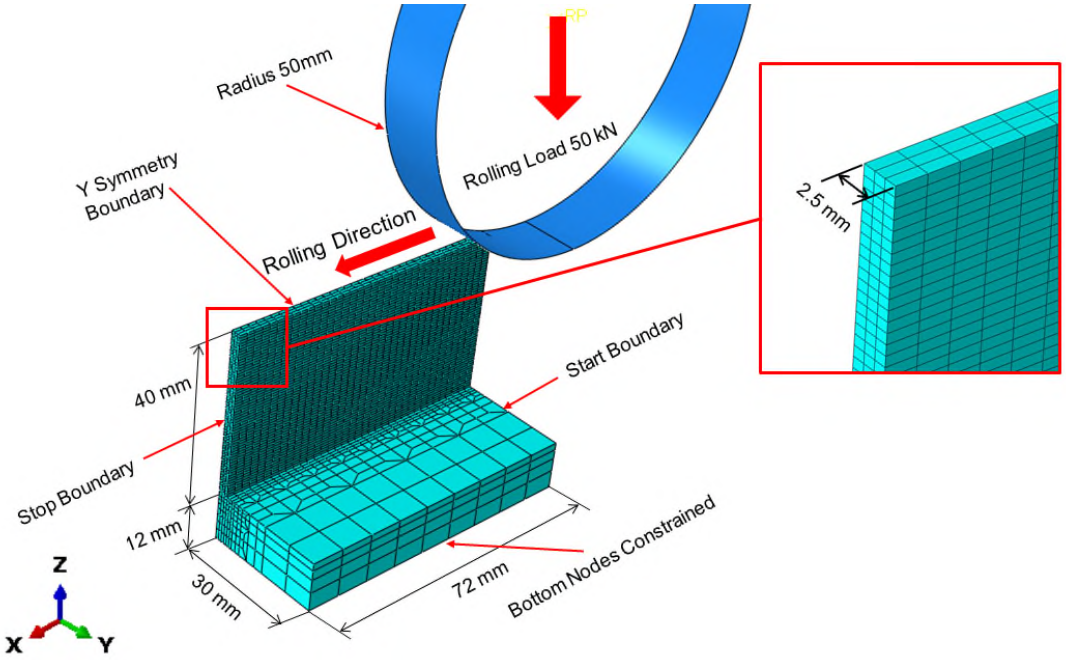

Figure 5-4 Short rolling model [52] for a wall component with identical geometry to the WAAM-deposited component (Figure 5-2).

Finally, the steady-state solution of the short model was also transferred to a long mechanical model using the solution mapping technique (Section 5.2.2), similar to the WAAM model (Figure 5-3). The mapped long model was then employed for the analysis of RS and distortion in the rolled wall after removal of clamps.

5.2.5 WAAM + rolling model

A sequential coupling approach was used to model the combination of WAAM and rolling. The solution to the mechanical model of the WAAM deposition was used as the initial condition for the rolling model, and thereby the post-build rolling was simulated. The WAAM + rolling model is aimed to reveal the mechanism of the rolling-enabled mitigation of the RS and distortion in the WAAM deposited wall component. The combination of WAAM and rolling was simulated for the identical wall component modelled in Sections 5.2.3 and 5.2.4.

5.3 Results and discussion

5.3.1 Computational efficiency

The computational efficiency of the developed modelling method is evaluated through comparison of computational time between the efficient model and conventional full-size model. The WAAM and rolling simulations were implemented using four processors in a grid computer system at Cranfield University. Table 5-4 presents the comparison between the conventional full-size transient WAAM model developed by Ding et al. [37] and the efficient WAAM model developed in this study. Using the efficient model, the computational time can be reduced by 76.1% and 97.8% for thermal and mechanical analyses, respectively, and a 83% reduction in total computational time was achieved. For rolling simulation, 95.9% less computational time was consumed by the efficient model in comparison with the conventional full-size model (Table 5-5). Therefore, it can be concluded that the developed modelling method can significantly enhance the efficiency of both WAAM and rolling simulations.

Table 5-4 Computational time comparison between the conventional full-size WAAM model and the efficient WAAM model developed in this study.

	Computational time of thermal model for WAAM	Computational time of mechanical model for WAAM	Total computational time
Conventional full-size WAAM model [37]	51 h, 24 min	24 h, 1 min	75 h, 25 min
Efficient WAAM model	12 h, 18 min	26 min – Short model 5 min – Long model	12 h, 49 min
Time saving	76.1%	97.8%	83.0%

Table 5-5 Computational time comparison between the conventional full-size rolling model and the efficient rolling model developed in this study.

	Computational time for rolling	Computational time of mapped long mechanical model	Total computational time
Conventional full-size rolling model Chapter 4 and Ref. [52]	17 h, 47 min	N/A	17 h, 47 min
Efficient rolling model	37 min Chapter 4 and Ref. [52] (short model)	7 min	44 min
Time saving	96.5%	N/A	95.9%

The saving of the computational time is mainly attributed to the reduction of the number of nodes in the model and the less process time involved in the simulation. The short model consists of approximately 12000 nodes, while the number of nodes is approximately 82000 for the conventional full-size model. As the short models considered only 14.4% length of the actual component, it means that the travel time of the heat source or roller over the component length in the short models is only 14.4% of the travel time for the full-size component. Unlike the conventional full-size transient model, the mapped long mechanical model used here took only several minutes to obtain the solution, because it did not simulate the WAAM and rolling processes but instead only calculated the RS and distortion after removal of clamps, which was much less computationally expensive.

5.3.2 WAAM deposition

5.3.2.1 Thermal analysis using short model

The accuracy of the thermal solution obtained by the short WAAM model is verified through comparing the predicted transient temperatures with the experimental measurements using thermocouples [37]. The locations of the thermocouples (TP1-TP4) used in the experiments are shown in the cross-section of the WAAM thermal model (Figure 5-2).

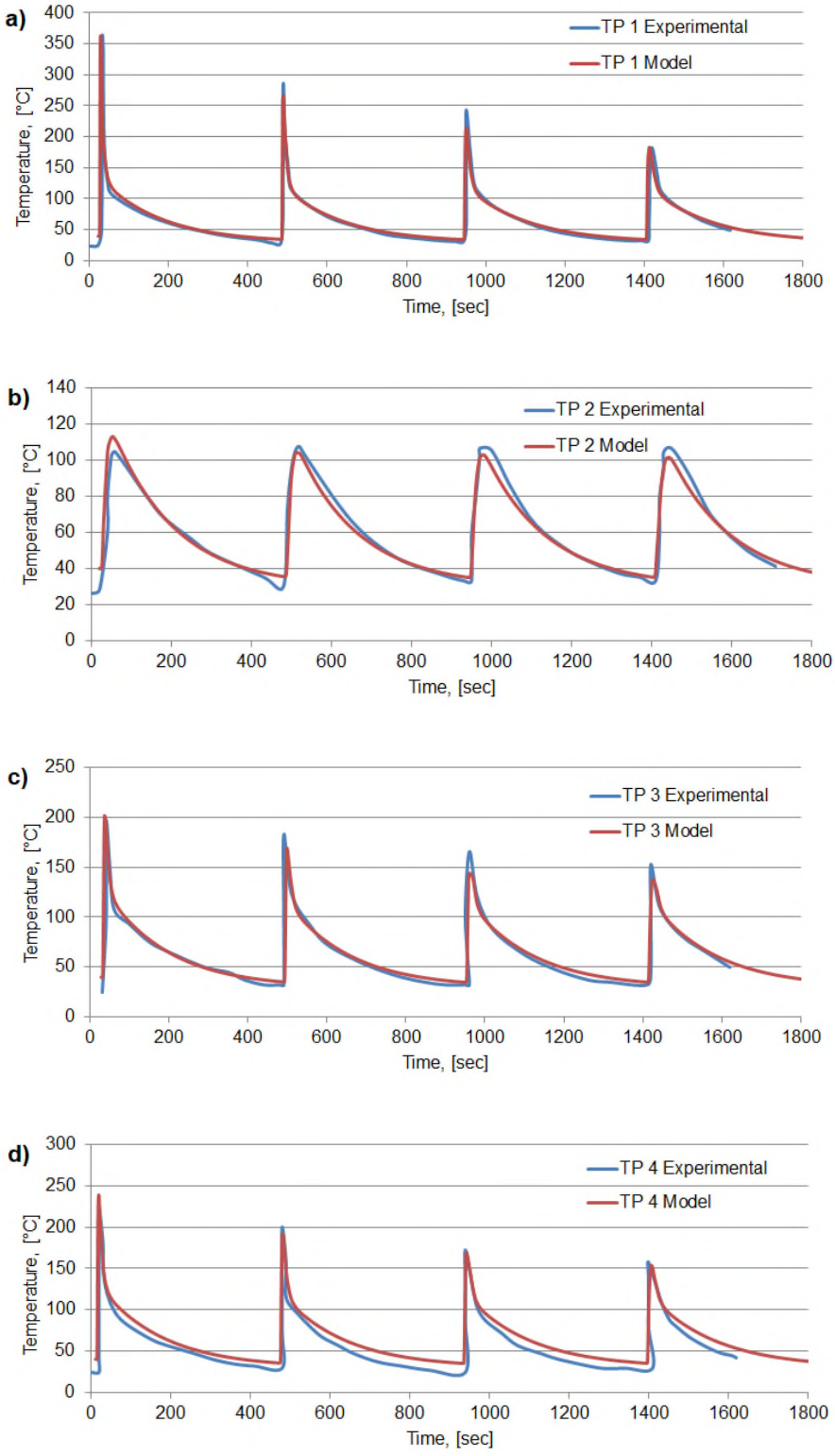

Figure 5-5 Temperature histories predicted by the short thermal WAAM model at the thermocouple locations: a) TP1, b) TP2, c) TP3 and d) TP4 (see Figure 5-2 for locations). The experimental measurements by Ding [34] are also included for comparison.

Figure 5-5 shows the comparison of the temperature histories at the thermocouple locations. It should be noted that only the temperature data for the first four layers are presented, and in the model the TP2 is not located at any element node, so the interpolated temperature is used. Good agreement is evident, which means that the reduced length of the short model does not impair the accuracy of the thermal solution.

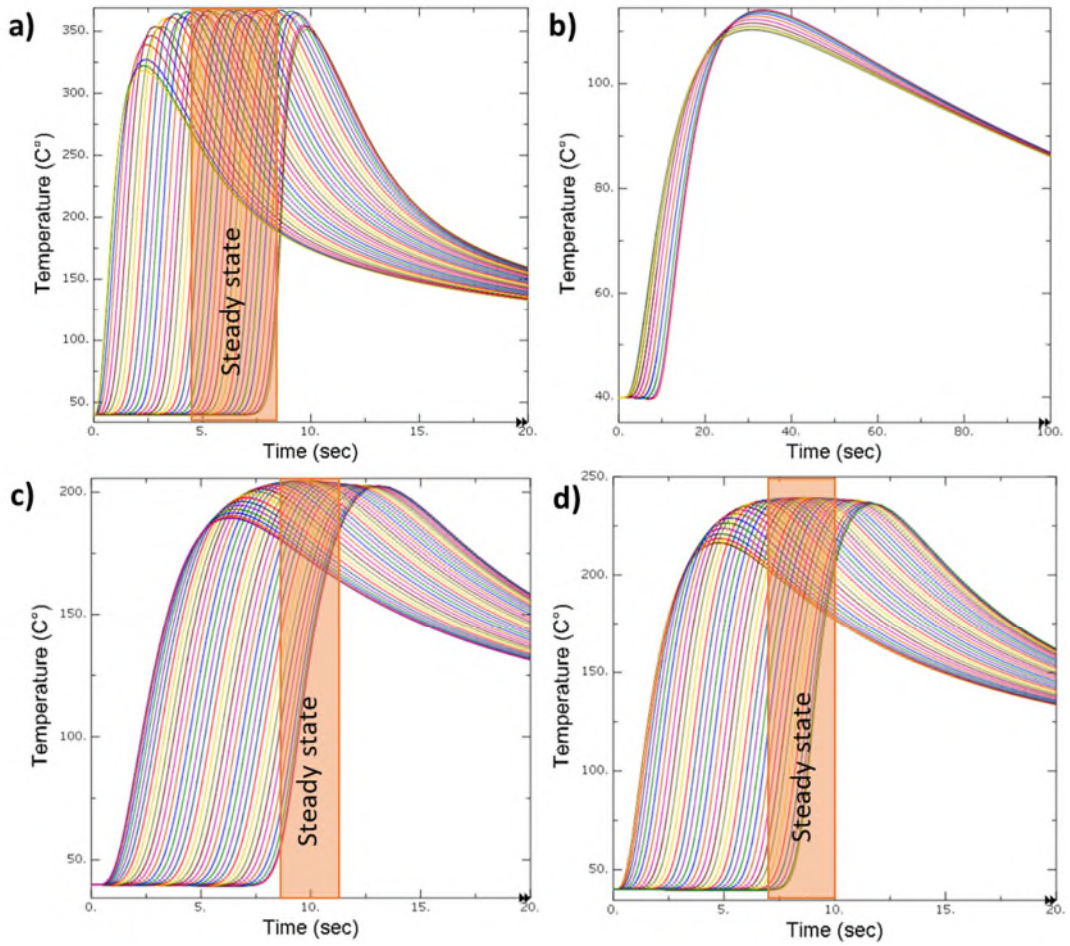

Figure 5-6 Predicted temperature histories at different longitudinal locations (i.e., different X coordinates) which are coincident with a) TP1, b) TP2, c) TP3 and d) TP4 in the YZ plane (see Figure 5-2 for locations of TP1-TP4). Note that the peak temperatures corresponding to steady-state of the WAAM deposition are highlighted.

To demonstrate the steady state of the temperature field during WAAM deposition, the temperature histories at different longitudinal locations are compared in Figure 5-6. These inspected locations share the Y and Z coordinates

with the thermocouple locations (TP1-TP4), but have different X coordinates. We denote these locations using the thermocouple labels (TP1-TP4). The longitudinal location closest to the WAAM start boundary experienced temperature rise first, but its peak temperature is lowest. The highest peak temperature was attained at the locations where the temperature started to rise after 2.5 – 3.5 seconds, corresponding to a distance of 21 – 29 mm to the WAAM start boundary. For the TP1, TP3 and TP4 locations, the highest peak temperatures remain constant within a period of time, indicating the time-independence of the peak temperature and the attainment of the steady state. For the TP2 locations in the substrate far from the deposited wall (fewer data are available due to the coarse mesh adopted at these locations, see Figure 5-2), the heating and cooling are much slower, and a constant peak temperature cannot be conclusively distinguished. However, the far-field temperatures with low peaks do not contribute to the generation of RS after cooling [30]. The temperature results confirmed that the steady-state solution of near-field temperatures, which are critical to the RS development during WAAM deposition [30], can be obtained using the short thermal model.

5.3.2.2 Mechanical analysis using short model

The PS and RS distributions in the WAAM component are analysed using the short mechanical model. The net thermal deformation after WAAM deposition is negligible since the temperatures in the initial, inter-layer and final states are all approximately same as room temperature (Figure 5-5). Therefore, the process-induced PS is the main origin of the RS and hence it is important to accurately predict the PS.

Prior to beginning of deposition, PS considered 0 in the substrate and in the first activated layer. Following layer-by-layer deposition induced even compressive PS in the WAAM wall and below the wall in the substrate. To reveal the mechanism of the longitudinal PS formation, the variations of both the PS and temperature with time are correlated during the deposition of the layer 10. Figure 5-7 shows the temperature profile and longitudinal PS in the middle of the layer 10 when the heat source was passing.

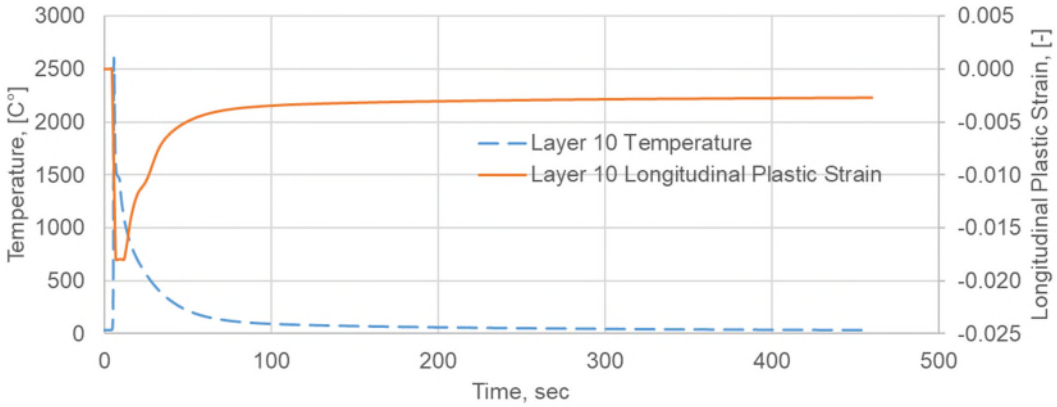

Figure 5-7 Temperature profile and longitudinal PS variation in the middle of the layer 10 during the deposition of layer 10.

When the heat source approached to the inspected point, the heating caused thermal expansion of the material but the expansion was constrained by colder material in front and behind of the heat source. Consequently, compressive stress was generated and the material was yielded at the compressive state due to the low yielding strength at the high temperature. After the heat source passed the inspected point, the cooling caused thermal shrinkage of affected material. The compressive PS reached maximum at the peak temperature and then reduced due to the counteracting of the tensile PS developed during cooling. Similar evolution of PS occurred during deposition of all layers.

Figure 5-8 shows the predicted longitudinal PS distributions in the steady-state region after the deposition of the twenty layers in the clamped condition. The results for different longitudinal constraint conditions adopted in the short model are compared. The prediction by the full-size mechanical model [30,37] is used as a reference to evaluate the accuracy of the steady-state solution of the short model. The PS is compressive and approximately uniform (ranging from -0.2% to -0.3%) in the deposited wall. The substrate region immediately underneath the wall experienced less plastic deformation and the PS ranges from -0.02% to -0.2%, while the substrate region far from the wall did not experience any plastic deformation. The short model with full longitudinal constraint best captured the PS profiles, while the short models with free ends and constrained ends

overestimated the compressive PS in the wall, and it appears that the less the longitudinal constraint, the more significant the overestimate.

Figure 5-9 shows the 3D distributions of the PS predicted by the full-size model [30,37] and the short model with full longitudinal constraint. According to the full-size model, the predicted PS distribution is approximately uniform over the majority of the interior region (i.e., steady-state region), except some slight deviation near the clamps (three clamps on each side of the substrate). However, the compressive PS near the wall ends (free from longitudinal constraint in the full-size model) are significantly higher than that in the steady-state region, and this feature is consistent with the effect of longitudinal constraint on PS, as revealed by the short model (Figure 5-8 b-c). In contrast, the short model with full longitudinal constraint completely avoided the wall end effect and thus is reliable to obtain the steady-state solution.

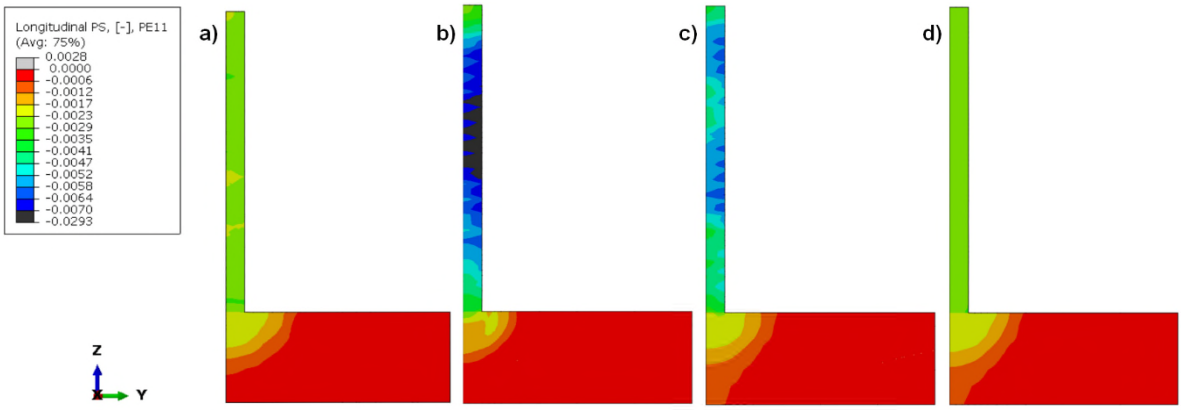

Figure 5-8 Cross-sectional distributions of longitudinal PS in the steady-state region for the WAAM: a) full-size mechanical model [34], b) short mechanical model with free ends, c) short mechanical model with constrained ends, d) short mechanical model with full longitudinal constraint.

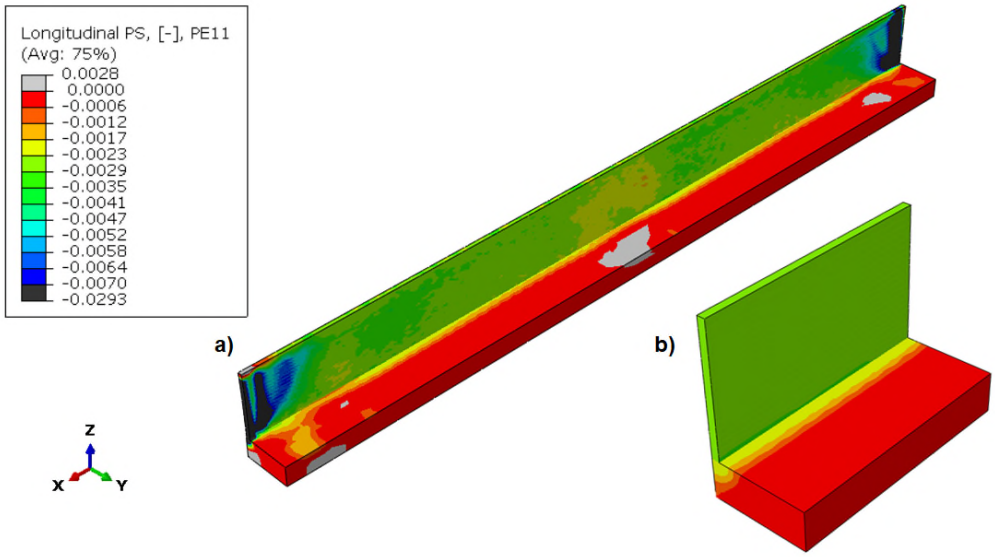

Figure 5-9 3D distributions of the longitudinal PS for the WAAM: a) full-size mechanical model [34], b) short mechanical model with full longitudinal constraint.

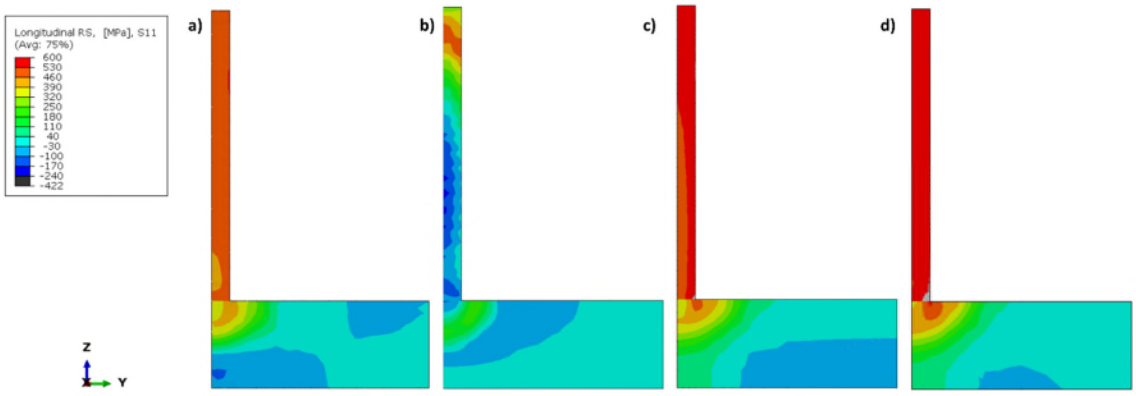

Figure 5-10 Cross-sectional distributions of longitudinal RS in the steady-state regions for the WAAM: a) full-size mechanical model [34], b) short mechanical model with free ends, c) short mechanical model with constrained ends, d) short mechanical model with full longitudinal constraint.

Figure 5-10 shows the predicted longitudinal RS distributions in the steady-state region. The full-size model [30,37] predicted tensile RS in both the wall and the substrate region immediately below the wall (Figure 5-10 a), while counterbalancing compressive longitudinal RS formed in the bottom and side regions of the substrate. The RS distribution predicted by the short model with free ends is markedly different from that predicted by the full-size model (Figure 5-10 a and b), mainly due to the large difference in PS distribution (Figure 5-8 a

and b). The RS predictions by the short models with constrained ends and full longitudinal constraint are both similar to the prediction by the full-size model [30,37], although the short model with constrained ends overestimated the PS in the wall (Figure 5-8 c).

5.3.2.3 Mechanical analysis using mapped long model

The steady-state solution of the short mechanical model with full longitudinal constraint was mapped to the long mechanical model. The efficacy of the mapping (Sections 5.2.1, 5.2.2 and 5.2.3) is demonstrated in Figure 5-10d and Figure 5-11a, which show that the longitudinal RS distributions in the steady-state region are similar between the short model (donor) and the long model (recipient). The slight discrepancy in steady-state RS can be attributed to the limitation of the solution mapping technique (Section 5.2.2) and the differences in longitudinal constraint condition and clamps locations between the short and long models (Figure 5-2 and Figure 5-3). The mapped long model also captured the nonuniform RS distributions near the two free ends of the full-size component. After removal of clamps, the tensile RS in the wall reduces significantly and even converts to compression on the top surface of the wall (Figure 5-11 b). Upward bending distortion was generated due to the partial relaxation of the original tensile RS in the wall, and the deformation was essentially elastic as no additional PS was generated. It should be mentioned that additional simulation of removal of clamps using the short model did not capture the bending distortion, indicative of the necessity of the long model.

Figure 5-12 presents the through-height line profiles of the longitudinal RS distribution in the steady-state region. Under the clamped condition, the mapped long model predicted uniform tensile RS of 500 MPa in the whole wall, which rapidly reduces to 300 MPa in the substrate, since the substrate has lower yield strength, larger cross-sectional area and smaller compressive PS (Figure 5-8). The tensile RS in the wall dropped significantly after removal of clamps, and the final RS exhibits an approximately linear distribution. The RS prediction and measurements agree well, indicative of good accuracy of the mapped long mechanical model.

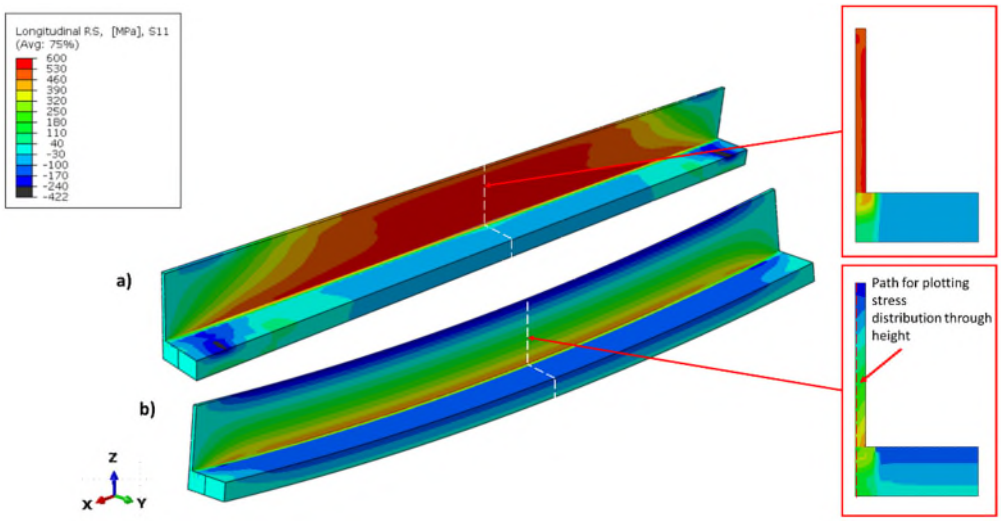

Figure 5-11 Longitudinal RS distributions predicted by the mapped long mechanical model for the WAAM: a) before clamps removal, b) after clamps removal (a deformation scale factor of 5 is used to improve visibility of distortion). The RS distributions in the middle-length section are also shown.

In order to further assess the solution accuracy, the predicted distortion after clamps removal was compared to the experimental measurement [34,37] for a four-layer WAAM deposited wall (Figure 5-13). The maximum out-of-plane distortion measured by Ding et al. [34,37] was 3.4 mm, while the mapped long model predicted distortion of 3.1 mm. The prediction error is 8.8% and such a small discrepancy could be attributed to the idealisation of the clamps (nodal displacements are fixed at clamping locations in the model).

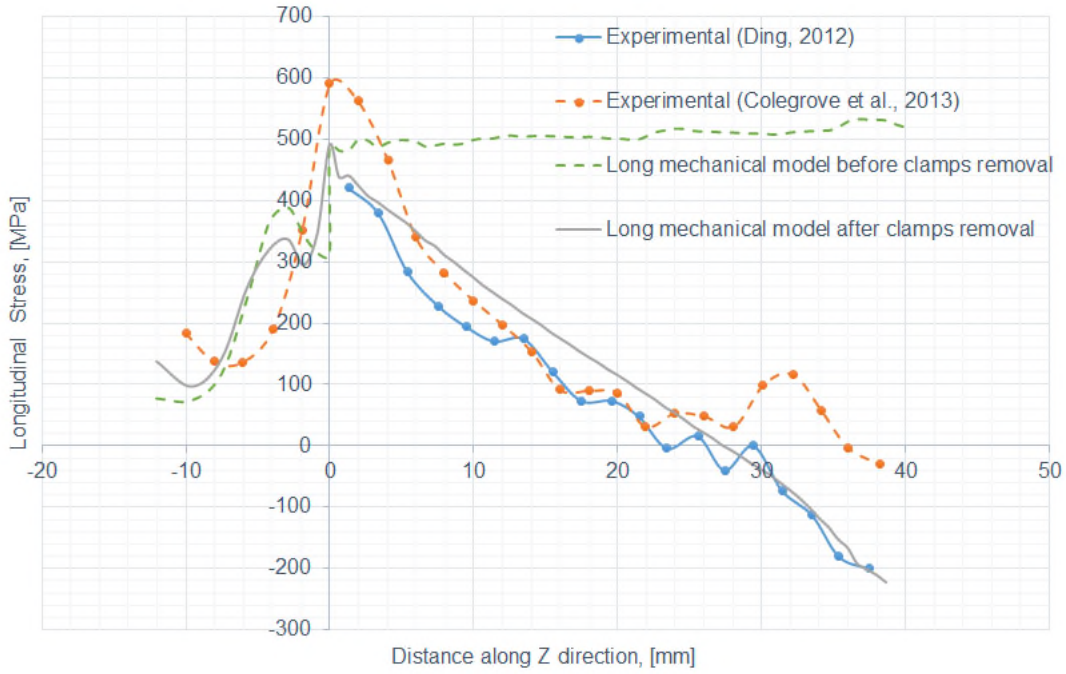

Figure 5-12 Longitudinal RS distributions along the Z-direction (through wall height, see Figure 5-11b for the path of the line plots) in the mapped long mechanical model before and after clamps removal for the WAAM component. The experimental measurements by Ding et al. [34] and Colegrove et al. [5] are also included, which were conducted using neutron diffraction after clamps removal.

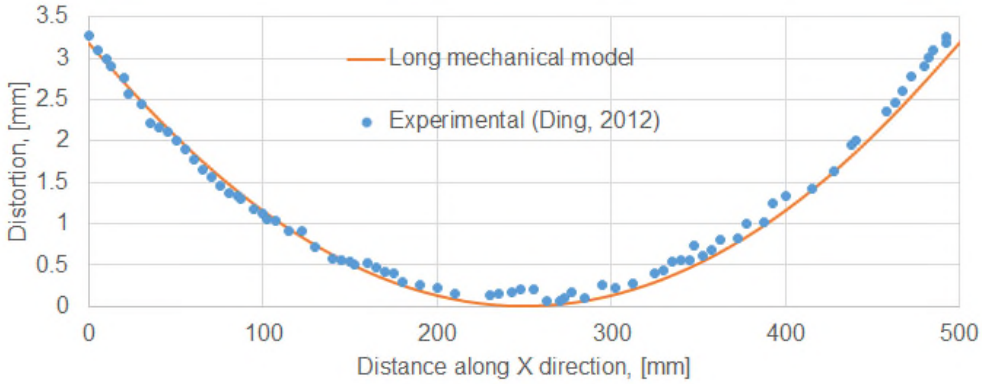

Figure 5-13 Verification of out-of-plane distortion predicted by the mapped long mechanical model after clamps removal. Note that the experimental measurement by Ding [34] using a 3D laser scanner was based on a four-layer deposited wall, and the WAAM model was adapted accordingly.

5.3.3 High pressure rolling

5.3.3.1 Mechanical analysis using short model

Pure rolling analysis is presented in this section. The PS and RS distributions predicted by the short model for the clamped wall component have been reported in Chapter 4. Here, the analysis is focused on the effects of different longitudinal constraint conditions on the results, as well as the RS redistribution due to removal of clamps. It should be noted that the steady-state of rolling is identified in the region where the equivalent PS is uniformly distributed in the longitudinal direction and it has been confirmed that the short model has captured the steady state Chapter 4 and Ref. [52].

Figure 5-14 shows the longitudinal PS distributions in the steady-state region of the rolled wall. The wall height was reduced after the rolling by the flat roller. The region near the roller expanded laterally. It is clearly seen that the longitudinal constraint has pronounced effect on the PS results. The conventional full-size model predicted tensile PS near the rolled top surface. The short model with constrained ends predicted most accurate PS distribution relative to the solution by the full-size model, while the short model with free ends overestimated the PS and the short model with full longitudinal constraint underestimated the PS. The PS has significant implication in the RS generated after rolling, as revealed in the following.

Figure 5-15 shows the longitudinal RS distributions in the steady-state region of the rolled wall. In consistence with the PS distributions, the solution of the short model with constrained ends achieved best agreement with the solution of the full-size model. The RS is tensile underneath the rolled surface, and it is compressive underneath the tension zone and near the wall side. Both the short models with free ends and full longitudinal constraint underestimated the RS.

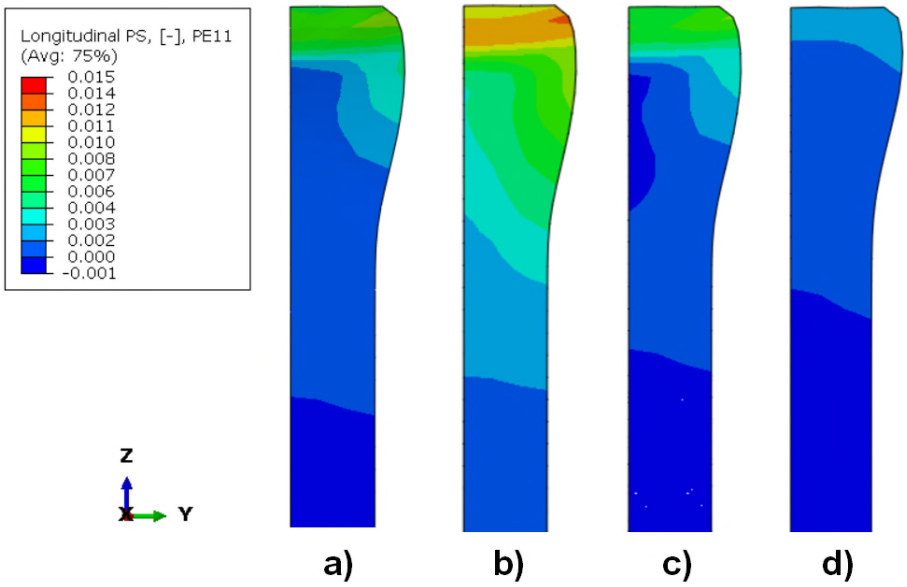

Figure 5-14 Comparison of predicted longitudinal PS distributions in the steady-state region of high pressure rolling: a) conventional full-size model [52], b) short model with free ends, c) short model with constrained ends [52], d) short model with full longitudinal constraint.

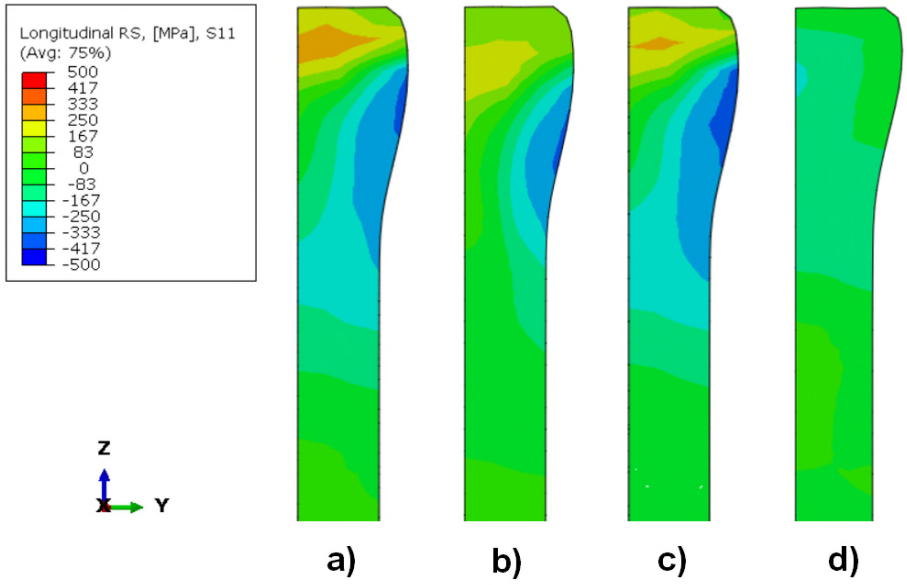

Figure 5-15 Comparison of predicted longitudinal RS distributions in the steady-state region of high pressure rolling: a) conventional full-size model [52], b) short model with free ends, c) short model with constrained ends [52], d) short model with full longitudinal constraint.

5.3.3.2 Mechanical analysis using mapped long model

Figure 5-16 shows the longitudinal RS distributions predicted by the mapped long mechanical model for the rolling. The RS distribution in the steady-state region is almost unchanged after the solution mapping from the short model with constrained ends (Figure 5-15c and Figure 5-16a). The removal of clamps results in expansion of tension zone underneath the rolled surface and shrinkage of compression zone underneath the tension zone. However, the effect of clamps removal on the overall RS distribution in the rolled wall is marginal (Figure 5-16), unlike the significant effect for the WAAM (Figure 5-11). Moreover, no discernible distortion of the rolled wall was generated after clamps removal (Figure 5-16), in contrast to the bending distortion for the WAAM (Figure 5-11).

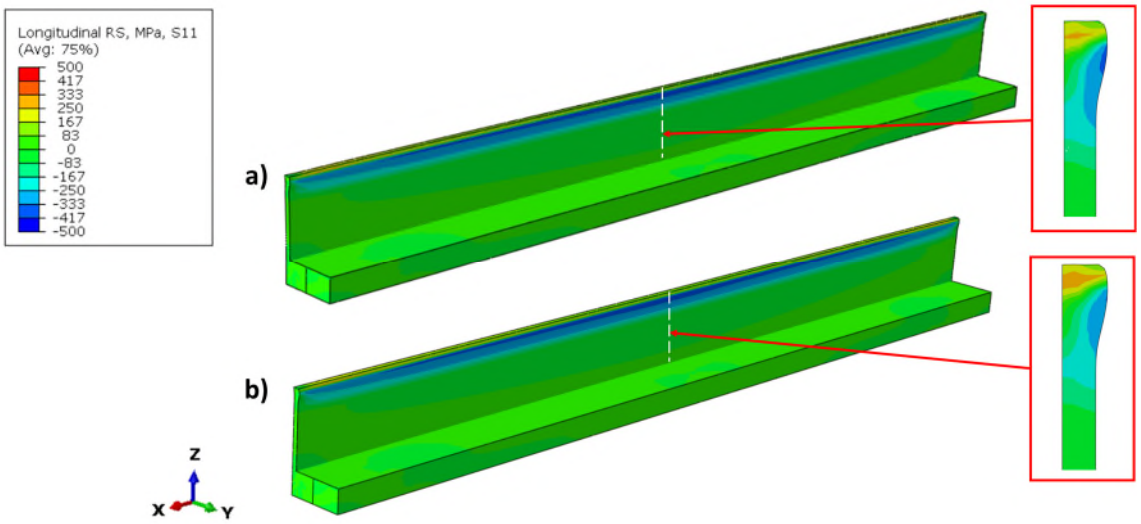

Figure 5-16 Longitudinal RS distributions predicted by the mapped long mechanical model for the high pressure rolling: a) before clamps removal, b) after clamps removal (a deformation scale factor of 5 is used to improve visibility of distortion). The RS distributions in the middle-length section are also shown.

5.3.4 Combination of WAAM and rolling

The results of the WAAM + rolling model are presented in this section. Figure 5-17 shows the longitudinal PS distributions in the steady-state region. After WAAM deposition, compressive PS is dominant in the wall (Figure 5-17a). The rolling gave rise to tensile PS and hence the compressive PS caused by WAAM deposition was reduced after rolling (Figure 5-17b). Given the 50 kN rolling load

used, significant tensile PS was generated near the rolled surface (Figure 5-17b), which is similar to the tensile PS solely caused by rolling (Figure 5-14c). This means that the PS induced by the rolling overwhelms the PS induced by the WAAM deposition. However, when the rolling load is reduced, it is anticipated that the rolling-induced PS will also decrease and then it will have less impact on the WAAM-induced PS. It is interesting to see that the removal of clamps does not affect the PS distribution, indicative of the elastic nature of the material response (Figure 5-17 c and d).

Figure 5-18 shows the longitudinal RS distributions in the steady-state region. It is clearly seen from Figure 5-18a and Figure 5-18b that the post-build rolling reduces the tensile RS in the WAAM-deposited wall, while the RS in the substrate is less affected, due to the distance from the substrate to the rolled surface. The mitigation of WAAM deposition RS by rolling can be attributed to the effect of rolling on PS, i.e., rolling introduces tensile PS and reduces the compressive PS in the WAAM-deposited wall (Figure 5-18). Interestingly, the RS in the wall is similar between the combined WAAM-rolling (Figure 5-18c) and the individual rolling (Figure 5-16a). This means that the rolling dominates the final RS in the wall for the given rolling load of 50 kN (Figure 5-4). The removal of clamps results in slight decrease of tensile RS in both wall and substrate (Figure 5-18d).

Figure 5-19 shows the 3D distributions of the longitudinal RS in the wall component, which are similar between the clamped and unclamped conditions. In addition, there is no significant distortion found after removal of clamps. This is because the WAAM deposition RS in the clamped condition has been largely mitigated by rolling and then no much RS was relaxed during clamps removal to generate distortion.

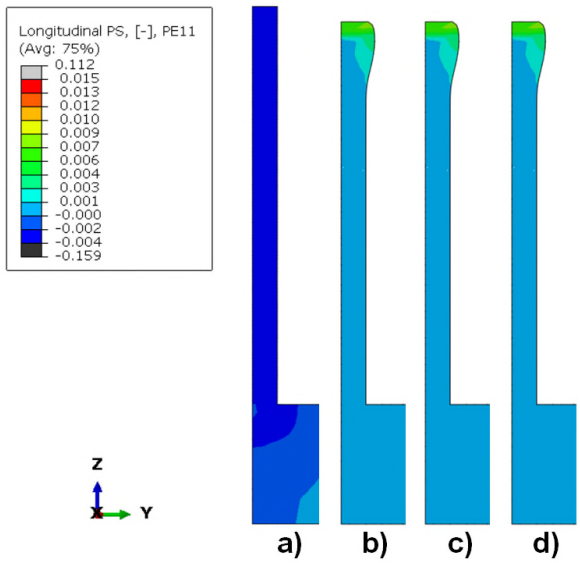

Figure 5-17 Predictions of longitudinal PS distributions in steady-state region: a) short WAAM model with clamps, b) short WAAM + rolling model with clamps (WAAM model result is used as initial condition), c) mapped long model with clamps, d) mapped long model after clamps removal.

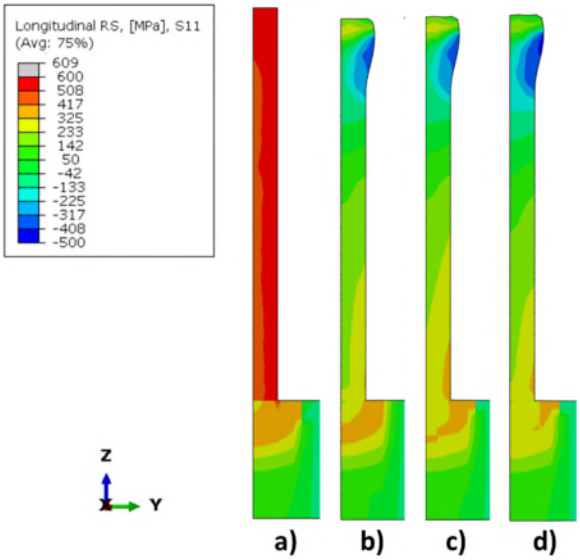

Figure 5-18 Predictions of longitudinal RS distributions in steady-state region: a) short WAAM model with clamps, b) short WAAM + rolling model with clamps (WAAM model result is used as initial condition), c) mapped long model with clamps, d) mapped long model after clamps removal.

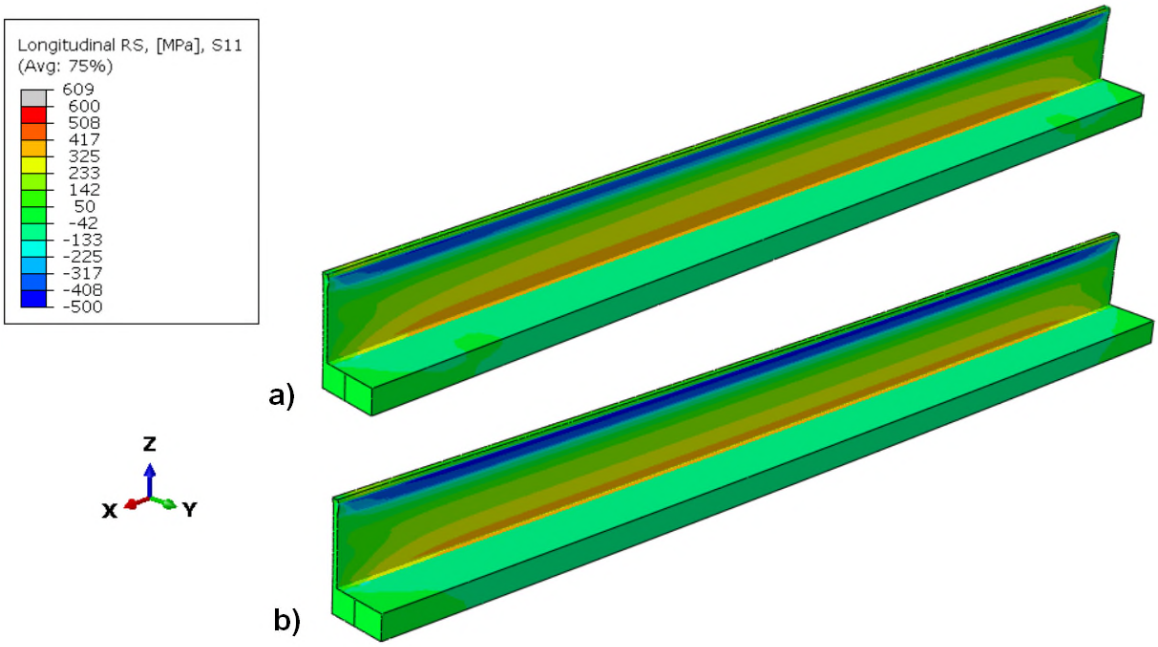

Figure 5-19 3D distributions of longitudinal RS predicted by the mapped long mechanical model for the combined process of WAAM and rolling: a) before clamps removal, b) after clamps removal (a deformation scale factor of 5 is used to improve visibility of distortion).

5.3.5 Generalisation and limitation

This study has demonstrated that the developed modelling method (Sections 5.2.1 and 5.2.2) is efficient to simulate both WAAM and rolling (Sections 5.3.1-5.3.4), which enables analyses and understanding of individual WAAM/rolling and combined WAAM-rolling processes for large components encountered in practice. This efficient modelling method could also be applied to other manufacturing processes (e.g., welding and machining), as long as steady-state exists.

There are three key considerations in this efficient modelling method.

First, a proper length for the shortened component should be used in the short model. The attainment of steady-state has been verified for both WAAM (Figure 5-8) and rolling, Chapter 4 and Ref. [52]. The gain of higher efficiency through further reducing the model length is marginal. The advantage of the short 3D model over 2D model lies in the fact that the physical mechanisms involved in the

manufacturing processes are essentially 3D and the short 3D model is able to capture these mechanisms but the 2D model is not. For instance, accurate prediction of transient temperature field during WAAM deposition relies on the formulation of heat source and heat transfer, of which both exhibit 3D characteristics. It has been also demonstrated that a 2D rolling model has limited predictive capability and accuracy, Chapter 4 and Ref. [52]. Nevertheless, a 2D mechanical model (e.g., plane strain model) could be used for the WAAM deposition based on the transient temperature field predicted by the short 3D thermal model. Such an attempt can potentially further reduce the computational time, although the short 3D mechanical model is already efficient (Table 5-4). Given a full longitudinal constraint used in the short WAAM model, a plane strain condition assumed in a 2D mechanical model is valid in such a case, but the modelling can be complicated due to transferring solution between 3D thermal model and 2D mechanical model [55]. On the other hand, plane strain condition is not acceptable when WAAM is combined with rolling.

Second, proper longitudinal constraint should be imposed to the short mechanical model. It is interesting to see that, given identical component length, to obtain accurate steady-state solution, full longitudinal constraint is needed for the short WAAM model (Figure 5-8 and Figure 5-10), while longitudinal constraint is only needed on the two end-surfaces of the wall component for the short rolling model (Figure 5-14 and Figure 5-15). This difference can be attributed to the distinctive mechanisms for plastic flow during WAAM and rolling processes. For the studied WAAM process, the PS is generated primarily due to internal constraint of isotropic thermal deformation upon localised heating/cooling and it occurs mainly at high temperatures when the yield strength is low; a full longitudinal constraint does not change the deformation mode and is representative in the steady-state WAAM region of the studied long component. The constrained-ends condition does not provide sufficient longitudinal constraint in the steady-state region of the short WAAM model (Figure 5-8c). However, if the actual length of the component (Figure 5-4) is shorter, the additional longitudinal constraint needed in the short model could be lower. For the studied rolling process, the PS results from the vertical penetration of roller at room temperature and assuming full longitudinal

constraint adds unphysical resistance to the roller penetration and thus is not representative in the steady-state rolling region. Therefore, it is crucial to impose proper longitudinal constraint in the short model in order to obtain accurate steady-state solution, and the added constraint being equivalent to that for full length is dependent on specific processes and components that are modelled.

Third, a long mechanical model representative for the actual component geometry, with the steady-state solution mapped from the short model as initial condition, is needed for the analysis of final state after clamps removal. However, the computational time for the mapped long model is much less than the conventional full-size WAAM or rolling model (Table 5-4 and

Table 5-5), which is particularly beneficial to the computational efficiency. This benefit is realised because the computationally expensive WAAM and rolling simulations are conducted using the short model, while only the effects of clamps removal are analysed by the mapped long model.

The main drawbacks of the developed efficient modelling approach include: (1) the mapping of steady-state solution requires same mesh topology of the component along the longitudinal direction; (2) the mechanical response in the regions corresponding to the unsteady-state WAAM deposition or rolling at the two ends of the modelled component are not captured. These drawbacks do not impair the accuracy of the steady-state solutions obtained by the WAAM and rolling models (Sections 5.3.2 and 5.3.3).

Another limitation of the efficient modelling method is that the short mechanical model is applicable only when the component is clamped during the WAAM deposition and rolling. A full-size mechanical model is still needed to capture the in-process distortion when the component is not effectively clamped or intentionally allowed to move in certain directions. In such a case, the inherent strain method can be used as an efficient solution to the in-process distortion. Nevertheless, the short model still can be used to estimate the inherent strain for such an analysis.

5.4 Concluding remarks

An efficient modelling method is developed to determine temperature, plastic strain, residual stress and distortion in large-scale additive manufacturing. In this method, a short model is used to obtain steady-state solution for a clamped component and then the solution is mapped to a long model for analysis of final RS and distortion after removal of clamps. This method has been applied to simulate WAAM, rolling and their combination for a wall component, and it can potentially be used as a general method for other manufacturing processes, as long as steady state exists. The following conclusions are drawn:

1. Computational time of WAAM and rolling simulations can be significantly reduced using the developed efficient modelling method. The high

efficiency is gained through reducing the component length and process time considered in the simulation to obtain steady-state solution. The enhanced efficiency is essential for simulation of WAAM + rolling process.

2. The short models for WAAM and rolling can obtain steady-state solutions equivalent to those obtained by conventional full-size models, as long as proper additional constraint is imposed. A full longitudinal constraint is needed for the short WAAM model, while only the two ends of the shortened component need to be constrained for the short rolling model.
3. For the WAAM deposition, the predictions of temperature, residual stress and distortion are in good agreement with experimental measurements. Within the steady-state region, uniform compressive longitudinal plastic strain is generated in the wall, which is responsible for the tensile longitudinal residual stress under the clamped condition. For the rolling process, tensile longitudinal plastic strain is generated and concentrated near the top surface rolled by the flat roller, where both tensile and compressive longitudinal residual stresses arise. The removal of clamps does not cause considerable distortion after rolling.
4. For the combined WAAM-rolling process, the rolling can effectively mitigate the tensile residual stress in the WAAM-deposited wall under clamped condition, because the rolling introduces tensile plastic strain that counteracts the compressive plastic strain generated by the WAAM deposition. The rolling-enabled mitigation of residual stress in the clamped wall implies that, the WAAM bending distortion caused by the stress relief after clamps removal can be effectively alleviated by the rolling.
5. The short mechanical model assumes that the component is fully clamped during WAAM deposition, and hence it cannot capture in-process distortion, which may occur if the component is not effectively clamped. Nevertheless, the steady-state solution mapping technique enables the estimate of distortion due to removal of clamps in the long mechanical model.

5.5 References

1. Williams SW., Martina F., Addison AC., Ding J., Pardal G., Colegrove P. Wire + Arc Additive Manufacturing. Materials Science and Technology. 2 May 2016; 32(7): 641–647. Available at: DOI:10.1179/1743284715Y.0000000073

2. Ding D., Pan Z., Cuiuri D., Li H. Wire-feed additive manufacturing of metal components: technologies, developments and future interests. The International Journal of Advanced Manufacturing Technology. October 2015; 81(1–4): 465–481. Available at: DOI:10.1007/s00170-015-7077-3

3. Lockett H., Ding J., Williams S., Martina F. Design for Wire + Arc Additive Manufacture: design rules and build orientation selection. Journal of Engineering Design. 2 September 2017; 28(7–9): 568–598. Available at: DOI:10.1080/09544828.2017.1365826

4. Martina F., Ding J., Williams S., Caballero A., Pardal G., Quintino L. Tandem metal inert gas process for high productivity wire arc additive manufacturing in stainless steel. Additive Manufacturing. January 2019; 25: 545–550. Available at: DOI:10.1016/j.addma.2018.11.022

5. Colegrove PA., Coules HE., Fairman J., Martina F., Kashoob T., Mamash H., et al. Microstructure and residual stress improvement in wire and arc additively manufactured parts through high-pressure rolling. Journal of Materials Processing Technology. October 2013; 213(10): 1782–1791. Available at: DOI:10.1016/j.jmatprotec.2013.04.012

6. Martina F., Roy MJ., Szost BA., Terzi S., Colegrove PA., Williams SW., et al. Residual stress of as-deposited and rolled wire+arc additive manufacturing Ti–6Al–4V components. Materials Science and Technology. 21 September 2016; 32(14): 1439–1448. Available at: DOI:10.1080/02670836.2016.1142704

7. Asala G., Khan AK., Andersson J., Ojo OA. Microstructural Analyses of ATI 718Plus® Produced by Wire-ARC Additive Manufacturing Process. Metallurgical and Materials Transactions A. September 2017; 48(9): 4211–4228. Available at: DOI:10.1007/s11661-017-4162-2

8. Gu J., Ding J., Williams SW., Gu H., Ma P., Zhai Y. The effect of inter-layer cold working and post-deposition heat treatment on porosity in additively manufactured aluminum alloys. Journal of Materials Processing Technology. April 2016; 230: 26–34. Available at: DOI:10.1016/j.jmatprotec.2015.11.006

9. Marinelli G., Martina F., Ganguly S., Williams S. Microstructure, hardness and mechanical properties of two different unalloyed tantalum wires deposited via wire + arc additive manufacture. International Journal of Refractory Metals and Hard Materials. September 2019; 83: 104974. Available at: DOI:10.1016/j.ijrmhm.2019.104974

10. Marinelli G., Martina F., Ganguly S., Williams S. Grain refinement in an unalloyed tantalum structure by combining Wire+Arc additive manufacturing and vertical cold rolling. Additive Manufacturing. March 2020; 32: 101009. Available at: DOI:10.1016/j.addma.2019.101009

11. Marinelli G., Martina F., Lewtas H., Hancock D., Mehraban S., Lavery N., Lavery N., Ganguly S., Williams S. Microstructure and thermal properties of unalloyed tungsten deposited by wire + arc additive manufacture. Journal of Nuclear Materials. August 2019; 522: 45–53. Available at: DOI:10.1016/j.jnucmat.2019.04.049

12. Marinelli G., Martina F., Ganguly S., Williams S. Development of Wire + Arc additive manufacture for the production of large-scale unalloyed tungsten components. International Journal of Refractory Metals and Hard Materials. August 2019; 82: 329–335. Available at: DOI:10.1016/j.ijrmhm.2019.05.009

13. Marinelli G., Martina F., Lewtas H., Hancock D., Ganguly S., Williams S. Functionally graded structures of refractory metals by wire arc additive manufacturing. Science and Technology of Welding and Joining. 4 July 2019; 24(5): 495–503. Available at: DOI:10.1080/13621718.2019.1586162

14. Clark D., Bache MR., Whittaker MT. Shaped metal deposition of a nickel alloy for aero engine applications. Journal of Materials Processing Technology. July 2008; 203(1–3): 439–448. Available at: DOI:10.1016/j.jmatprotec.2007.10.051

15. Colegrove P., Ikeagu C., Thistlethwaite A., Williams S., Nagy T., Suder W., Steuwer A., Pirling T. Welding process impact on residual stress and distortion. Science and Technology of Welding and Joining. November 2009; 14(8): 717–725. Available at: DOI:10.1179/136217109X406938

16. Martina F., Colegrove PA., Williams SW., Meyer J. Microstructure of Interpass Rolled Wire + Arc Additive Manufacturing Ti-6Al-4V Components. Metallurgical and Materials Transactions A. December 2015; 46(12): 6103–6118. Available at: DOI:10.1007/s11661-015-3172-1

17. Gu J., Ding J., Williams SW., Gu H., Ma P., Zhai Y. The effect of inter-layer cold working and post-deposition heat treatment on porosity in additively manufactured aluminum alloys. Journal of Materials Processing Technology. April 2016; 230: 26–34. Available at: DOI:10.1016/j.jmatprotec.2015.11.006

18. Hönnige JR., Colegrove PA., Ganguly S., Eimer E., Kabra S., Williams S. Control of residual stress and distortion in aluminium wire + arc additive manufacture with rolling. Additive Manufacturing. August 2018; 22: 775–783. Available at: DOI:10.1016/j.addma.2018.06.015

19. Colegrove PA., Donoghue J., Martina F., Gu J., Prangnell P., Hönnige J. Application of bulk deformation methods for microstructural and material property improvement and residual stress and distortion control in additively manufactured components. Scripta Materialia. July 2017; 135: 111–118. Available at: DOI:10.1016/j.scriptamat.2016.10.031

20. Martina F. Investigation of methods to manipulate geometry, microstructure and mechanical properties in titanium large scale wire + arc additive manufacturing. Thesis for: Doctor of Philosophy. Cranfield University; 2014.

21. Cordiano HV. Effect of Residual Stresses on the Low Cycle Fatigue Life of Large Scale Weldments in High Strength Steel. Journal of Engineering for Industry. 1 February 1970; 92(1): 86–92. Available at: DOI:10.1115/1.3427724

22. Webster GA., Ezeilo AN. Residual stress distributions and their influence on fatigue lifetimes. International Journal of Fatigue. 2001; 23: 375–383. Available at: DOI:10.1016/S0142-1123(01)00133-5

23. Dong P., Brust FW. Welding residual stresses and effects on fracture in pressure vessel and piping components: A Millennium review and beyond. Journal of Pressure Vessel Technology. 1 August 2000; 122(3): 329–338. Available at: DOI:10.1115/1.556189

24. Dong P. Residual stresses and distortions in welded structures: a perspective for engineering applications. Science and Technology of Welding and Joining. July 2005; 10(4): 389–398. Available at: DOI:10.1179/174329305X29465

25. Denlinger ER., Michaleris P. Effect of stress relaxation on distortion in additive manufacturing process modeling. Additive Manufacturing. October 2016; 12: 51–59. Available at: DOI:10.1016/j.addma.2016.06.011

26. Biegler M., Marko A., Graf B., Rethmeier M. Finite element analysis of in-situ distortion and bulging for an arbitrarily curved additive manufacturing directed energy deposition geometry. Additive Manufacturing. December 2018; 24: 264–272. Available at: DOI:10.1016/j.addma.2018.10.006

27. Denlinger ER., Gouge M., Irwin J., Michaleris P. Thermomechanical model development and in situ experimental validation of the Laser Powder-Bed Fusion process. Additive Manufacturing. August 2017; 16: 73–80. Available at: DOI:10.1016/j.addma.2017.05.001

28. Zhao H., Zhang G., Yin Z., Wu L. A 3D dynamic analysis of thermal behavior during single-pass multi-layer weld-based rapid prototyping. Journal of Materials Processing Technology. March 2011; 211(3): 488–495. Available at: DOI:10.1016/j.jmatprotec.2010.11.002

29. Xiong J., Lei Y., Li R. Finite element analysis and experimental validation of thermal behavior for thin-walled parts in GMAW-based additive manufacturing with various substrate preheating temperatures. Applied Thermal Engineering.

November 2017; 126: 43–52. Available at: DOI:10.1016/j.applthermaleng.2017.07.168

30. Ding J., Colegrove P., Mehnen J., Williams S., Wang F., Almeida PS. A computationally efficient finite element model of wire and arc additive manufacture. Int J Adv Manuf Technol. 2014; (70): 227–236. Available at: DOI:10.1007/s00170-013-5261-x

31. Montevecchi F., Venturini G., Grossi N., Scippa A., Campatelli G. Finite Element mesh coarsening for effective distortion prediction in Wire Arc Additive Manufacturing. Additive Manufacturing. December 2017; 18: 145–155. Available at: DOI:10.1016/j.addma.2017.10.010

32. Chiumenti M., Cervera M., Salmi A., Agelet de Saracibar C., Dialami N., Matsui K. Finite element modeling of multi-pass welding and shaped metal deposition processes. Computer Methods in Applied Mechanics and Engineering. August 2010; 199(37–40): 2343–2359. Available at: DOI:10.1016/j.cma.2010.02.018

33. Montevecchi F., Venturini G., Scippa A., Campatelli G. Finite Element Modelling of Wire-arc-additive-manufacturing Process. Procedia CIRP. 2016; 55: 109–114. Available at: DOI:10.1016/j.procir.2016.08.024

34. Ding J. Thermo-mechanical analysis of wire and arc additive manufacturing process. PhD Thesis. Cranfield University; 2012.

35. Graf M., Hälsig A., Höfer K., Awiszus B., Mayr P. Thermo-mechanical modelling of wire-arc additive manufacturing (WAAM) of semi-finished products. Metals. 1 December 2018; 8(12): 1009. Available at: DOI:10.3390/met8121009

36. Anca A., Fachinotti VD., Escobar-Palafox G., Cardona A. Computational modelling of shaped metal deposition. International Journal for Numerical Methods in Engineering. 7 January 2011; 85(1): 84–106. Available at: DOI:10.1002/nme.2959

37. Ding J., Colegrove P., Mehnen J., Ganguly S., Sequeira Almeida PM., Wang F., Williams S. Thermo-mechanical analysis of wire and arc additive layer

manufacturing process on large multi-layer parts. Computational Materials Science. July 2011; 50(12): S092702561100365X. Available at: DOI:10.1016/j.commatsci.2011.06.023

38. Camilleri D., Comlekci T., Gray TGF. Computational prediction of out-of-plane welding distortion and experimental investigation. The Journal of Strain Analysis for Engineering Design. February 2005; 40(2): 161–176. Available at: DOI:10.1243/030932405X7809

39. Camilleri D., Mollicone P., Gray TGF. Computational methods and experimental validation of welding distortion models. Proceedings of the Institution of Mechanical Engineers, Part L: Journal of Materials: Design and Applications. October 2007; 221(4): 235–249. Available at: DOI:10.1243/14644207JMDA148

40. Fachinotti VD., Cardona A., Baufeld B., Van der Biest O. Finite-element modelling of heat transfer in shaped metal deposition and experimental validation. Acta Materialia. November 2012; 60(19): 6621–6630. Available at: DOI:10.1016/j.actamat.2012.08.031

41. Zhang L., Michaleris P. Investigation of Lagrangian and Eulerian finite element methods for modeling the laser forming process. Finite Elements in Analysis and Design. February 2004; 40(4): 383–405. Available at: DOI:10.1016/S0168-874X(03)00069-6

42. Wang S., Goldak J., Zhou J., Tchernov S., Downey D. Simulation on the thermal cycle of a welding process by space–time convection–diffusion finite element analysis. International Journal of Thermal Sciences. May 2009; 48(5): 936–947. Available at: DOI:10.1016/j.ijthermalsci.2008.07.007

43. Shanghvi JY., Michaleris P. Thermo-elasto-plastic finite element analysis of quasi-state processes in Eulerian reference frames. International Journal for Numerical Methods in Engineering. 10 March 2002; 53(7): 1533–1556. Available at: DOI:10.1002/nme.345

44. Michaleris, P., DeBiccari, A. Prediction of welding distortion. Welding Journal. 1997; 76: 172–181.

45. Michaleris P., Zhang L., Bhide SR., Marugabandhu P. Evaluation of 2D, 3D and applied plastic strain methods for predicting buckling welding distortion and residual stress. Science and Technology of Welding and Joining. November 2006; 11(6): 707–716. Available at: DOI:10.1179/174329306X147724

46. Ueda Y., Murakawa H. Applications of computer and numerical analysis techniques in welding research. Materials & Design. June 1985; 6(3): 103–111. Available at: DOI:10.1016/0261-3069(85)90052-4

47. Ueda Y., Kim YC., Yuan MG. A predicting method of welding residual stress using source of residual stress. QUARTERLY JOURNAL OF THE JAPAN WELDING SOCIETY. 1988; 6(1): 59–64. Available at: DOI:10.2207/qjjws.6.59

48. Chen Q., Liang X., Hayduke D., Liu J., Cheng L., Oskin J., et al. An inherent strain based multiscale modeling framework for simulating part-scale residual deformation for direct metal laser sintering. Additive Manufacturing. August 2019; 28: 406–418. Available at: DOI:10.1016/j.addma.2019.05.021

49. Bugatti M., Semeraro Q. Limitations of the inherent strain method in simulating powder bed fusion processes. Additive Manufacturing. October 2018; 23: 329–346. Available at: DOI:10.1016/j.addma.2018.05.041

50. Liang X., Chen Q., Cheng L., Hayduke D., To AC. Modified inherent strain method for efficient prediction of residual deformation in direct metal laser sintered components. Computational Mechanics. December 2019; 64(6): 1719–1733. Available at: DOI:10.1007/s00466-019-01748-6

51. Cozzolino LD., Coules HE., Colegrove PA., Wen S. Investigation of post-weld rolling methods to reduce residual stress and distortion. Journal of Materials Processing Technology. September 2017; 247: 243–256. Available at: DOI:10.1016/j.jmatprotec.2017.04.018

52. Gornyakov V., Sun Y., Ding J., Williams S. Computationally Efficient Models of High Pressure Rolling for Wire Arc Additively Manufactured

Components. Applied Sciences. 4 January 2021; 11(1): 402. Available at: DOI:10.3390/app11010402

53. Zhu XK., Chao YJ. Effects of temperature-dependent material properties on welding simulation. Computers & Structures. 1 May 2002; 80(11): 967–976. Available at: DOI:10.1016/S0045-7949(02)00040-8

54. Deng D. FEM prediction of welding residual stress and distortion in carbon steel considering phase transformation effects. Materials & Design. February 2009; 30(2): 359–366. Available at: DOI:10.1016/j.matdes.2008.04.052

55. Ni J., Wang X., Gong J., Abdel Wahab M. Thermal, metallurgical and mechanical analysis of circumferentially multi-pass welded P92 steel pipes. International Journal of Pressure Vessels and Piping. August 2018; 165: 164–175. Available at: DOI:10.1016/j.ijpvp.2018.06.009

6 Understanding and designing post-build rolling for mitigation of residual stress and distortion in wire arc additively manufactured components

This chapter is based on the following publication:

Gornyakov V., Ding J., Sun Y., Williams S., Understanding and designing post-build rolling for mitigation of residual stress and distortion in wire arc additively manufactured components. Submitted to Materials & Design in Elsevier (Manuscript ID: JMADE-D-21-02630) for Publication.

As it was found in Cranfield University [1], post-build rolling can reduce distortion with an efficacy comparable to inter-layer rolling in WAAM produced components. In the literature the effect of the rolling parameters and roller design on final residual stress (RS) and plastic strain (PS) distribution was presented, but the mechanism of the influence was not revealed. The influence of the friction coefficient on RS and PS during post-build rolling of WAAM parts with slotted roller was not investigated either.

This Chapter presents a numerical study on the influence of the main process variables associated with post-build rolling on the mechanical response of the WAAM wall, and the considered variables include roller geometry, rolling load and friction coefficient. The efficacy of roller design and rolling loads in mitigating tensile RS is compared between different analysis cases, and thereby recommendations are provided for implementation of optimal post-build rolling. The computationally efficient short implicit transient model, as described in Chapter 4, is used for the rolling simulations. In the long model, the initial conditions (RS and PS distributions), as caused by the thermal deposition process, are transferred from the results of the simulation of the short mechanical multilayer model using the Solution Mapping Technique (Chapter 5).

Abstract: Post-build rolling is envisioned to be more efficient and convenient to implement, as compared to inter-layer rolling, for mitigation of residual stress (RS) and distortion in metallic components built by wire arc additive manufacturing (WAAM). In this study, based on numerical simulations that considered both

WAAM deposition and post-build rolling, the mechanisms of rolling-enabled mitigation of RS and distortion in a WAAM-built steel wall have been revealed. The influences of the process configurations, such as roller design (flat, profiled and slotted rollers), rolling load (25-75 kN) and roller-to-wall friction coefficient (0-0.8) on the distributions of PS and RS were investigated. It was found that for all the designed rollers, higher rolling load increased the rolling-induced tensile PS, and consequently led to more extensive mitigation of the WAAM-generated tensile RS. The slotted roller at all investigated rolling loads was most effective to introduce tensile PS to counteract the compressive PS generated by the WAAM deposition, and thereby to reduce the tensile longitudinal RS and the final distortion after removal of clamps. The simulations also demonstrated that the friction coefficient significantly affected the longitudinal tensile PS and RS when the slotted roller was used in the rolling. However, the efficacy of the flat/profiled roller is insensitive to friction coefficient. This study could underpin the development of an optimal post-build rolling process for efficient mitigation of RS and distortion in WAAM components.

Keywords: wire + arc additive manufacturing; cold working; residual stress; plastic deformation; roller design; rolling load

6.1 Introduction

Wire Arc Additive Manufacturing (WAAM) is a modern near-net-shape manufacturing technology, which has gained increasing popularity in aerospace, automotive, military, and petroleum industries. WAAM allows building of components with various dimensions, from relatively simple walls [1] and cylindrical structures [2], to complex parts with variable thickness of deposits [2]. Parts with medium geometric resolution and surface quality [3] have been built using steel [1,4], aluminium alloy [5], titanium alloy [6], nickel superalloy [7], tantalum [8] and tungsten [9]. This new technology is based on sequential deposition of metallic layers with a wire consumable, an arc heat source, a robotic manipulator, and a precise computer control. The standard robotic equipment, heat sources and wire consumables, which are widely available in the market, reduce build-up and operational cost of WAAM [10–13]. Design flexibility,

reduced manufacturing time and low buy-to-fly ratio [10] make the WAAM process attractive for small batch manufacturing.

One of the main challenges in applying WAAM process for building large-scale structures is to control and reduce RS and distortion. RS arises from “mismatch” between different regions of the deposit upon uneven heating and cooling [14]. RS may cause build distortion as well as stress corrosion cracking and brittle fractures [15–18], which can all lead to major failure of WAAM parts. Heat treatment is an effective method to eliminate RS [19], which normally works through evenly heating the component, thereby reducing yield strength and relaxing RS gradually. However, this method is expensive and difficult to apply for large components, and it could adversely affect mechanical properties.

High pressure rolling has been developed as a versatile and cheap technique for reducing RS in welds [20]. Rolling induces tensile PS in the weld, and as a result, the compressive PS generated during the welding process is compensated for, and hence the tensile RS is relaxed. The first research on such a RS mitigation method was conducted in Russia by Kurkin et al. [21,22]. Post-weld rolling was found effective to reduce RS even in thick joints [23,24] and the effectiveness is proportional to the rolling load [20].

In the last decade high pressure rolling has been also widely implemented for controlling RS and distortion in WAAM. Colegrove et al. [1] reported reduction of RS and distortion in WAAM steel components after both inter-layer and post-build rolling with profiled (i.e., roller with radiused groove) and slotted rollers. The results demonstrated a trend that as the rolling load increases (from 25 kN to 75 kN), the final distortion decreases. The slotted roller was found to be more effective in reducing RS and distortion, as it introduces lateral restraint to the wall during rolling and promotes larger deformation in longitudinal direction. Interestingly, the distortion of the post-build rolled sample is comparable to that of the inter-layer rolled sample.

Colegrove et al. [25] and Martina et al. [6] investigated inter-layer rolling with flat and profiled rollers on WAAM Ti-6Al-4V components. For both rollers, the distortion decreased with the increase of the rolling load. However, the distortion

cannot be completely eliminated, similar to the observation in WAAM steel components [1]. This is partially due to the absence of side restraint during the rolling of the WAAM wall, which causes significant deformation in the transverse direction. For complicated structures, Hönnige et al. [26] investigated the effect of inter-layer rolling on intersections with “inverted” roller (i.e., roller with convex profile), and reported that although this roller can improve the microstructure, it does not affect RS distributions at the intersections, presumably because the thermal influence of WAAM deposition dominated over the rolling [26].

Most of the reported high-pressure rolling experiments for WAAM components were conducted between each layer (i.e., inter-layer rolling), which is time consuming and costly. Fortunately, as suggested by Colegrove et al. [1], the post-build rolling (i.e., rolling of a last layer only) can provide a similar efficacy as the inter-layer rolling for distortion reduction, with much less time and cost, while the efficacy of post-build rolling for residual stress mitigation has not been examined in experiments.

Finite Element Analysis (FEA) has been proved a robust method for studying WAAM and rolling processes [33,34], which can significantly reduce experimental effort. The influence of rolling load and friction coefficient on RS distribution during post-build rolling have been studied numerically by Cozzolino [28] for conventional welds and by Abbaszadeh et al. [29] for WAAM. Tangestani et al. [30] investigated the effect of the roller design on the longitudinal RS distribution in post-build rolled WAAM components. It was found that the increase in the rolling load/depth led to a greater depth of compressive longitudinal RS. Comparing to other rollers, the slotted roller can induce a larger magnitude of longitudinal RS with a greater depth. The surface depth curvature of the roller has a minor effect on the longitudinal RS distribution. Tangestani et al. [30] also demonstrated that the variation of the friction coefficient between the roller and the wall marginally affected RS and PS distributions at relatively low rolling loads.

However, neither of the rolling models by Abbaszadeh et al. [29] or Tangestani et al. [30] considered the initial PS generated by WAAM, which can affect strain hardening of the material during rolling. The influence of post-build rolling on the

WAAM-generated PS distribution and the mechanism of PS formation were not reported in the literature, while PS distribution plays a key role in RS formation during rolling. Although the effects of the rolling parameters and roller design on RS distribution were demonstrated in the literature, the RS mitigation mechanism and the RS redistribution after removal of clamps were not revealed. For the slotted roller, the friction effect has not been investigated either. Therefore, the aim of this research is to fill the aforementioned knowledge gap and to investigate the influences of the main process parameters of the post-build rolling on the mechanical response of the WAAM deposited wall. The considered process-related variables include roller geometry, rolling load and friction coefficient, and the mechanical variables under investigation are PS, RS and distortion.

6.2 Materials and methods

6.2.1 Materials and experiments

The WAAM deposition and post-build rolling to be modelled are consistent with previous experiments [1]. A structural steel plate (grade S355JR-AR) with a thickness of 12 mm was used as the substrate (see chemical compositions in Table 6-1). Cold Metal Transfer process was used with Lincoln Electric SupraMIG G3Si1/ER70S-6 wire (⌀ 0.8 mm, see chemical compositions in Table 6-1). A 490 mm long linear wall was built with a layer width of 5 mm and a layer height of 2 mm, and the deposition parameters are listed in

Table 6-2. The rolling loads ranged from 25 kN to 75 kN. Six clamps were applied during WAAM deposition and rolling, and the clamps were removed after manufacture.

Table 6-1 The chemical compositions of the substrate plate and the filler wire.

C, %	Mn, %	Si, %	P, %	S, %	N, %	Nb, %	Cu, %	Fe, %
The substrate steel grade S355JR-AR								
0.24	1.60	0.55	0.045	0.045	0.009	0.003–0.100		Balance
The filler wire Lincoln Electric SupraMIG G3Si1/ER70S-6								

0.08	1.50	0.92	⩽0.040	⩽0.035			0.16	Balance

Table 6-2 WAAM deposition parameters.

Wire feed speed, m/min	Travel speed, mm/s	Heat input, J/mm	Assumed efficiency
10	8.33	269.5	0.9

6.2.2 Thermal-mechanical model of WAAM deposition

General purpose FEA software Abaqus was employed for the numerical simulations in this study. To obtain the PS and RS distributions caused by the WAAM deposition, an efficient thermal-mechanical model was used Chapter 5 and [31]. Firstly, the temperature field was predicted using a short multilayer thermal model with a calibrated double-ellipsoidal heat source. Then the temperature histories were transferred to a short multilayer mechanical model, from which the PS and RS evolution during the deposition was calculated. The solution mapping method described in Chapter 5 and Ref. [31] (Figure 6-1) was used to transfer the PS and RS distributions obtained by the WAAM model to the short post-build rolling model as the initial conditions, and to transfer the steady-state solution of the short model to full-size long model for determining final state after removal of clamps. This method is applicable to both WAAM and rolling, Chapter 5 and Ref. [31].

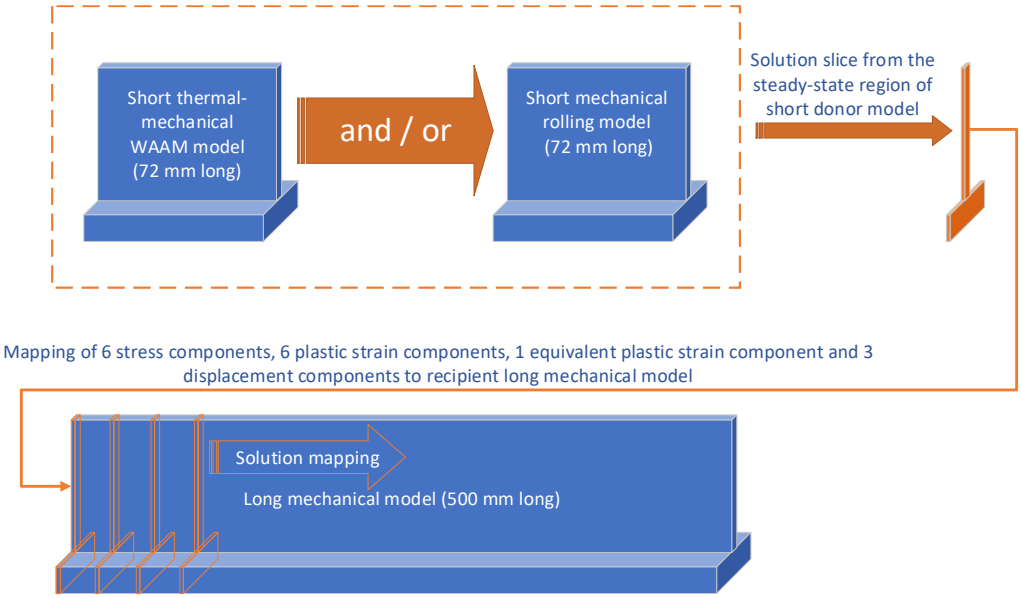

Figure 6-1 Mapping method to transfer steady-state solution between different models [31].

6.2.3 Post-build rolling model

Three sets of rolling models were developed to carry out parametric sensitivity analysis and furthermore to identify the RS and distortion mitigation mechanisms. In Set 1 models the effects of different rolling variables were studied for the flat roller without consideration of the WAAM process. The Set 2 models studied the effects of the friction coefficient on the PS and RS distributions for a given rolling load. Three different rollers, including flat, profiled, and slotted rollers, as shown in Figure 6-2, were investigated. The Set 3 models focused on the investigation into the effects of rolling load and roller design on the PS and RS distributions. It should be noted that, the Set 1 models simulated the rolling alone, while the Set 2 and Set 4 models incorporated the PS and RS predicted by the thermal-mechanical WAAM model as the initial condition. Table 6-3 summarises the different variables used in the rolling models. For Set 2 models, four friction coefficients were considered, μ = 0; 0.1; 0.5; 0.8. A friction coefficient of 0.1 is recommended in the literature to simulate the lubricated contact between the roller and component [32–35], while the coefficient is assumed to be 0.5 for simulating the unlubricated steel-to-steel contact [27,36] and steel-to-aluminium

contact [37,38]. For Set 3 models, it was assumed that μ = 0.1, as in the experiments lubricant was applied between the wall and the slotted roller [1].

Table 6-3 Rolling process variables considered in different sets of models.

	Roller Design	Rolling Load, F (kN)	Friction Coefficient, μ (-)	WAAM Deposition Before Rolling
Set 1 #	Flat	25, 50, 75	0.5	Not included
Set 2	Flat	50	0, 0.1, 0.5, 0.8	Included
	Profiled	50	0, 0.1, 0.5, 0.8	Included
	Slotted	50	0, 0.1, 0.5, 0.8	Included
Set 3	Flat	25, 50, 75	0.1	Included
	Profiled	25, 50, 75	0.1	Included
	Slotted	25, 50, 75	0.1	Included

These models are used to investigate the influence of the rolling alone on the material response.

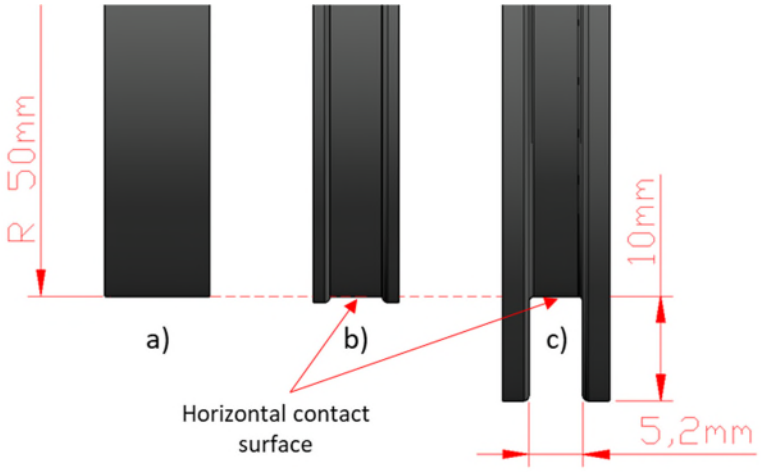

Figure 6-2 Design of the flat a), profiled b) and slotted c) rollers.

Computationally efficient 3D short implicit transient model (Chapter 4 and Ref. [39]) was used in the numerical analysis. The thermal-mechanical model of WAAM deposition provides the initial condition for the rolling models (Sets 2 and 3) and the details of the WAAM model can be found in a previous Chapter 5 and paper by the same authors [31]. The rolling model consists of two components: the analytic rigid roller and the deformable WAAM wall bonded to the substrate

(Figure 6-3 a). In the models with the flat and profiled rollers, the WAAM wall length is 72 mm, while for the slotted roller, it is 144 mm because the slotted roller requires a longer distance to reach a steady-state. As demonstrated in Chapter 4 and Ref. [39], the deformable WAAM wall has sufficient length to reach steady-state rolling for the model to obtain an accurate and consistent solution. Further increase in wall length will not change the distribution of steady-state PS and RS.

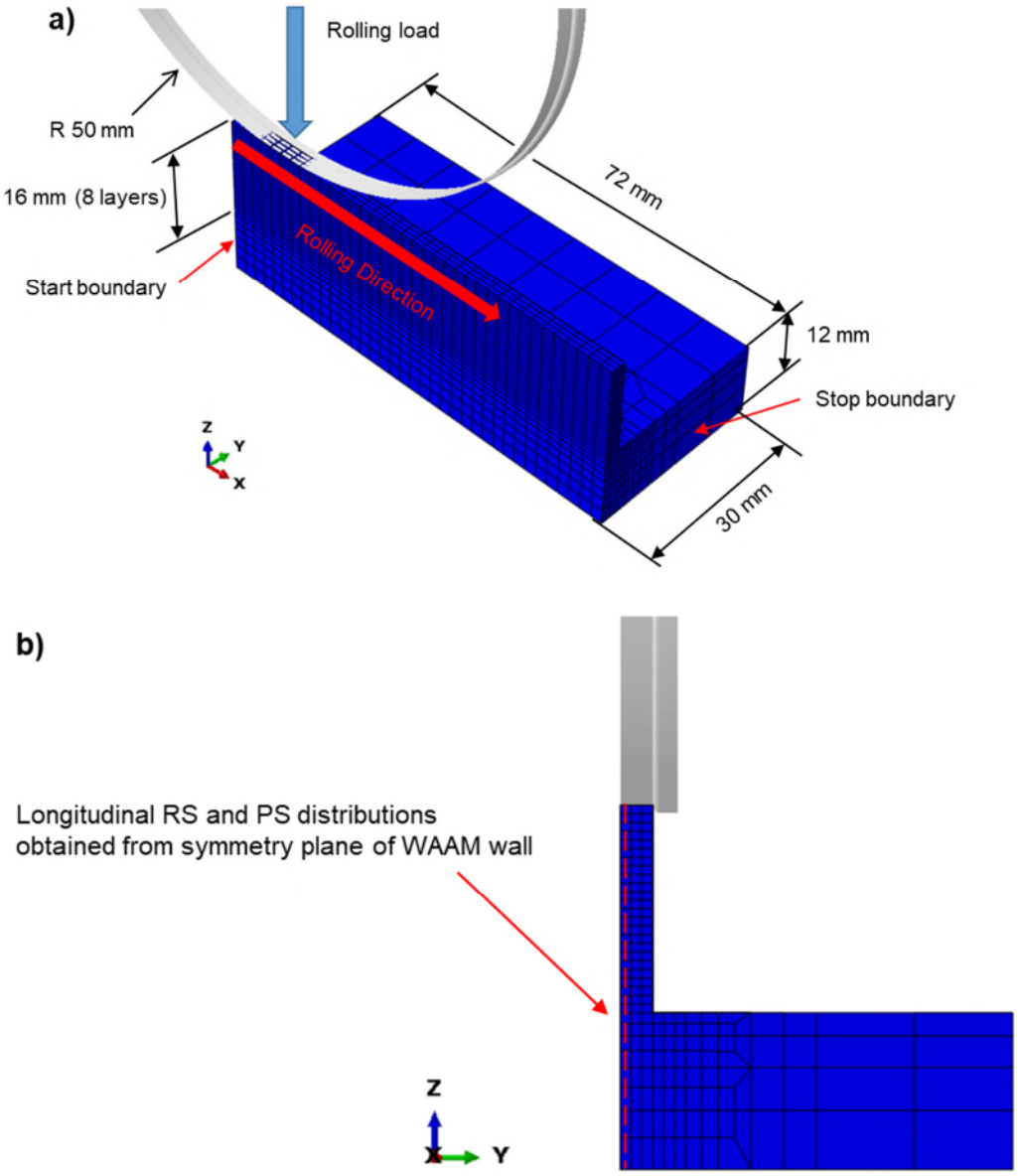

Figure 6-3 Post-build rolling model for WAAM built wall using profiled roller: a) model dimensions, b) inspection plane. Note that only half component is considered due to symmetry.

The solution mapping technique (Section 5.2.2) was used to transfer initial WAAM RS and PS distributions to the post-build rolling models. Post-build rolling models simulated only rolling process without inclusion of thermal effects related to WAAM deposition. Due to this, the elastic-plastic properties of mild steel for ambient temperature were used for the wall and substrate, as reported by Thompson et al. [40] (Table 6-4).

Table 6-4 The elastic-plastic material properties from Ref [40] for ambient temperature.

Young's modulus [GPa]	Poisson's ratio	Plastic strain	Yield stress deposit, [MPa]	Yield stress substrate, [MPa]
202	0.3	0	440	390
		0.04	550	500
		0.12	615	565
		0.51	676	626

For simplification, it was assumed that the material properties are isotropic and not influenced by the microstructural changes caused by the thermal cycles and rolling. A yield strength value of 502 MPa was found in the certificate of ER70-S6 welding wire, which was used during experiments [1]. Colegrove et al.'s experiments [1] showed that the longitudinal tensile RS reached 600 MPa on the border between the WAAM deposit and substrate. For mild steel, the magnitude of RS is usually equal to the yield strength [41,42]. These findings suggested that the actual yield strength of the WAAM deposit could be higher than the reported 390 MPa at 20 C° [40]. Therefore, the yield strength of the deposit at room temperature was increased by 50 MPa in the rolling model compared to Thompson et al.'s data [40]. Material properties of the substrate were not altered and equivalent to those suggested by Thompson et al. [40].

The rolling model comprises two analysis steps: loading step and rolling step. In the loading step, the roller was gradually lowered via vertical load control until having pressed the top surface of the wall with the prescribed rolling load. The compressive loading location is 10 mm away from the Start boundary (Figure 6-3a). During the rolling step, the roller was moved along the wall with the prescribed rolling load and at a horizontal speed of 3 mm s^{-1}. It should be noted that no torque was applied to the roller. The rolling was terminated 10 mm away from the Stop Boundary (Figure 6-3a). The distance of 10 mm was chosen to prevent plastic collapse in the vertical direction at the edge of the wall due to rolling load.

Surface-to-surface contact interaction with friction (penalty formulation) was specified between the roller and the wall surface, and the friction force drove the rotation of the roller in the rolling step. To simulate the clamping of the WAAM component to the worktable during the rolling process, the bottom of the substrate was constrained in all directions, which is similar to the method adopted by Abbaszadeh et al. [29]. To avoid the unrealistic longitudinal deformation due to reduced length in the short model, the Start and Stop boundaries of the model were constrained for nodal movement in X direction (i.e., longitudinal rolling direction), Chapter 5 and Ref. [31].

The 3D 8-node linear brick elements (Abaqus designation C3D8R) were used in the mechanical model. A coarse mesh (element dimensions: 8 mm × 7.5 mm × 1.765 mm) was used for the substrate, while a fine mesh (element dimensions: 2 mm × 0.833 mm × 0.667 mm) was used for the deposited wall subject to large deformation under rolling. A mesh sensitivity analysis was carried out to ensure that the results of the simulation are independent of the mesh density.

6.2.4 Long mechanical model

To determine the final PS and RS distributions and the distortion of the 500 mm long post-build rolled WAAM wall after removing the constraints/clamps, the solution mapping method (Chapter 5 and Ref. [31]) was employed, Figure 6-1. The solution slice from the steady-state region of the short post-build rolling model was spatially repeatedly mapped to the long mechanical model. The long

model has the same cross-section, material properties and mesh density as the short model, but the length of the WAAM wall in the long model is 500 mm, which is consistent with previous experiments [1].

6.2.5 Inspection planes

Detailed analysis was performed for an inspection plane located 48 mm away from the Start Boundary of the 72 mm long WAAM wall rolled by the flat/profiled roller and 86 mm away for the 144 mm long wall rolled by the slotted roller, as shown in Figure 6-3b. This is the region where the rolling reached the steady state (Chapter 4 and Ref. [39]). For the short models, all the inspections were performed for the simulations under the clamped condition. In the 500 mm long mechanical model the inspection data was collected in the mid-length plane, under both clamped and unclamped conditions.

6.2.6 Model solution time

A high-performance computer with four nodes was used for the computation. The maximum wall-clock time to obtain the solution of the 72 mm long WAAM wall model with the flat roller was 13 min 40 sec, while the 144 mm long wall model with the slotted roller took 1 hour 13 min. The wall-clock time to solve the long mechanical model was 6 min 43 sec. Much more computational time is expected if a full-size model is used for the WAAM deposition and rolling simulations (Chapters 4 and 5, Ref. [31,39]).

6.3 Results and discussion

Figure 6-4 and Figure 6-5 show the PS and RS distributions, respectively, after the WAAM deposition and the rolling with the flat, profiled and slotted rollers at a rolling load of 50 kN. The thermal cycles during the WAAM deposition caused significant compressive longitudinal PS, which is approximately -0.003 in the wall and -0.002 in the substrate immediately underneath the wall. The rolling induced tensile PS in the wall and reduced the magnitude of compressive PS in the substrate below the wall. The slotted roller induced larger magnitude of tensile PS in the wall and it less markedly reduced the wall height comparing to the flat and profiled rollers. Longitudinal tensile RS in the wall (474 – 594 MPa), as

caused by the thermal deposition cycles, was converted to compressive RS in the core of the wall by the rolling. The magnitude of the tensile RS in the substrate below the wall was also reduced by the rolling. Tensile RS remained in the region under the rolled surface. Compared to the flat and profiled rollers, the slotted roller converted the tensile RS to compressive RS in more extensive region further away from the rolled surface.

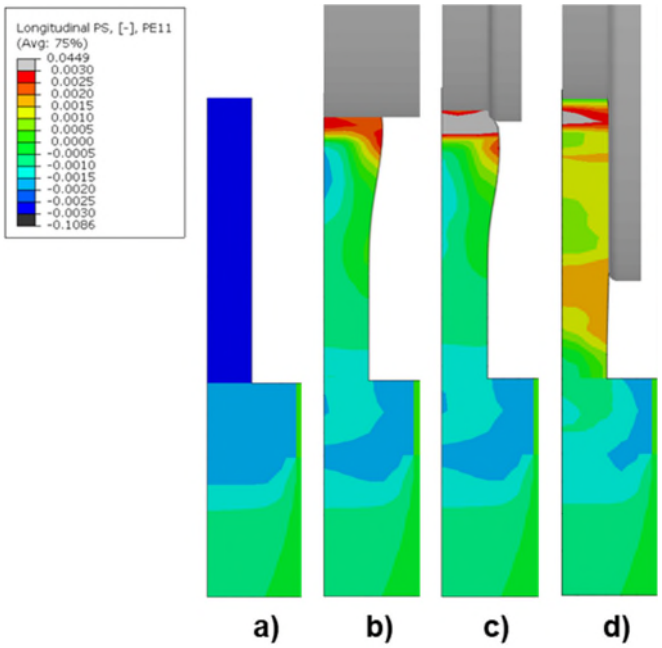

Figure 6-4 Longitudinal PS distributions: a) after WAAM deposition, and after rolling with b) flat roller, c) profiled roller and d) slotted roller at F = 50 kN and μ = 0.1.

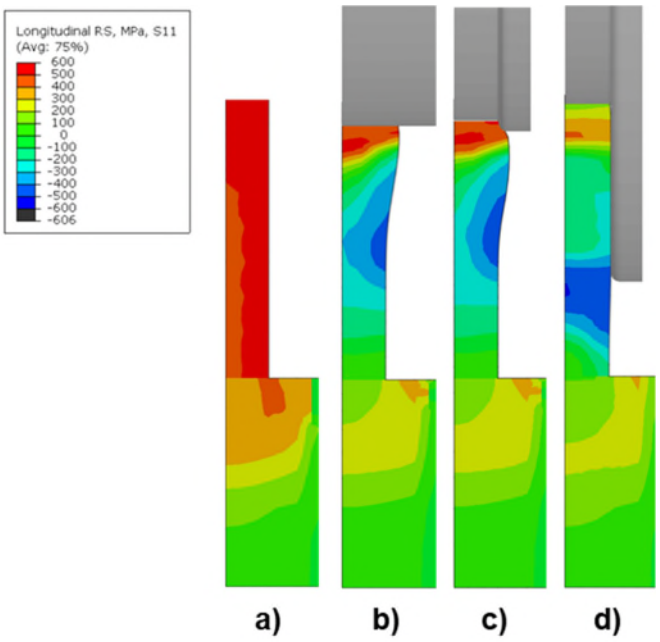

Figure 6-5 Longitudinal RS distributions: a) after WAAM deposition, and after rolling with b) flat roller, c) profiled roller and d) slotted roller at F = 50 kN and μ = 0.1.

6.3.1 Model Set 1

6.3.1.1 Longitudinal PS formation during rolling

The mechanism of the PS generation in the wall during rolling with the flat roller is revealed in Figure 6-6. To isolate the rolling effect, the initial conditions were assumed stress-free without considering WAAM deposition. During the loading step the vertical compressive plastic deformation under the roller was accompanied by the transverse and longitudinal tensile plastic deformation. Three plastically deformed zones can be identified under the roller (Figure 6-6). Zone 1 and Zone 3 were deformed in compression and Zone 2 was in tension. During the rolling step, the material in front of the roller experienced compressive plastic deformation (Zone 1), while the material behind the roller experienced tensile plastic deformation (Zone 2), which is due to the longitudinal stretching effect of the rolling (i.e., vertical compression caused longitudinal elongation). The material in Zone 2 deformed with an angle to the rolled surface, because of the resultant force arising from the vertical rolling load and the horizonal moving traction (Figure 6-7). At the end of the rolling step, for the majority region of the

wall, the influence of compression Zones 1 and 3 was overwhelmed by the influence of tension Zone 2.

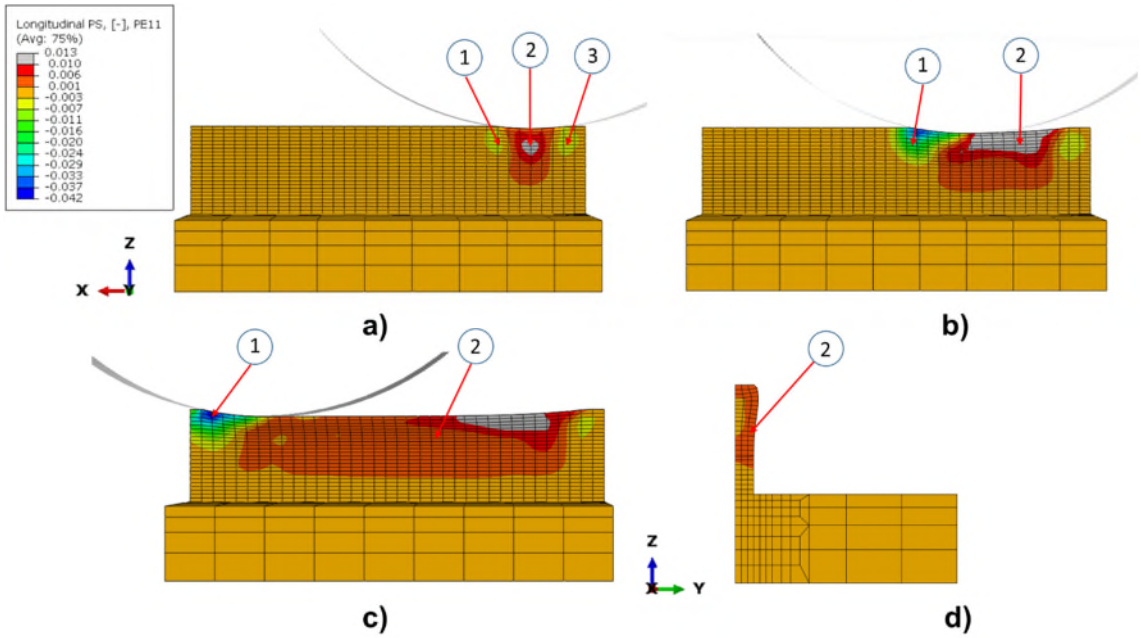

Figure 6-6 Longitudinal PS generation during rolling with the flat roller (F = 50 kN and μ = 0.5): a) at the end of the initial establishment of contact, b) at the beginning of the roller motion, c) at the end of the rolling step, and d) in the final rolling state on the transverse section. Note that in this analysis case the wall is assumed to be free from any strain and stress before rolling.

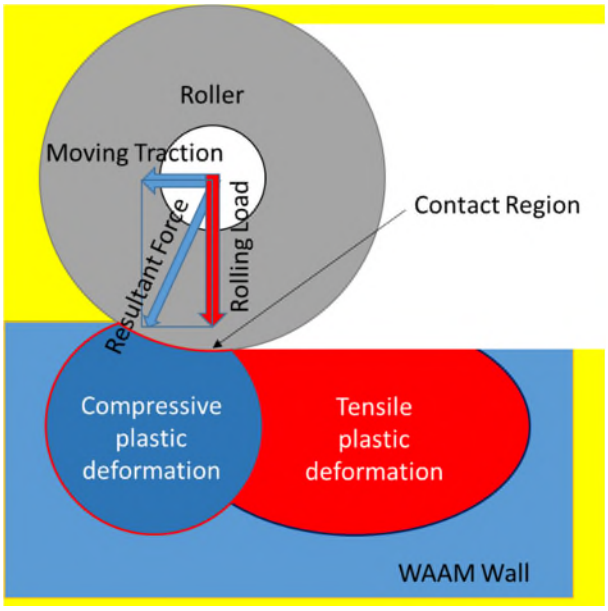

Figure 6-7 Schematic of resultant force during rolling with flat roller. The longitudinal plastic deformation zones are also shown.

6.3.1.2 Longitudinal stress evolution during rolling

The mechanism of the longitudinal RS caused by the rolling with the flat roller can be revealed in Figure 6-8. The plastic deformation induced by the rolling was constrained by the underlying material and then caused elastic straining between the unevenly deformed regions of the wall, resulting in the formation of RS. Four zones are defined to characterise the longitudinal stress evolution during the rolling process, i.e., Zone 1 in front of the roller below the wall surface, Zone 2 at the contact surface between the roller and wall, Zone 3 beneath the roller in the core of the wall and Zone 4 behind the roller at the rolled surface. In the end of the loading step (Figure 6-8a), plastic deformation developed under the roller, giving rise to compressive stress in Zones 1, 2 and 3. During the rolling step, the compression zones (Zones 1, 2 and 3) followed the motion of the roller and extended gradually. A tensile RS zone (Zone 4) developed due to the nonuniform distribution of plastic deformation (Figure 6-6), and as a result tensile elastic deformation (stretching) of material occurred behind the roller.

In the final state after the rolling, compressive RS is distributed in the core of the wall, while tensile RS is distributed around the rolled surface. The compressive plastic deformation zone concentrated near the stop boundary (Figure 6-6) is the main driving source of the tensile RS at the rolled surface. Similar tensile RS was also obtained experimentally in WAAM parts [6] and found in previous rolling simulations for conventional welds [28].

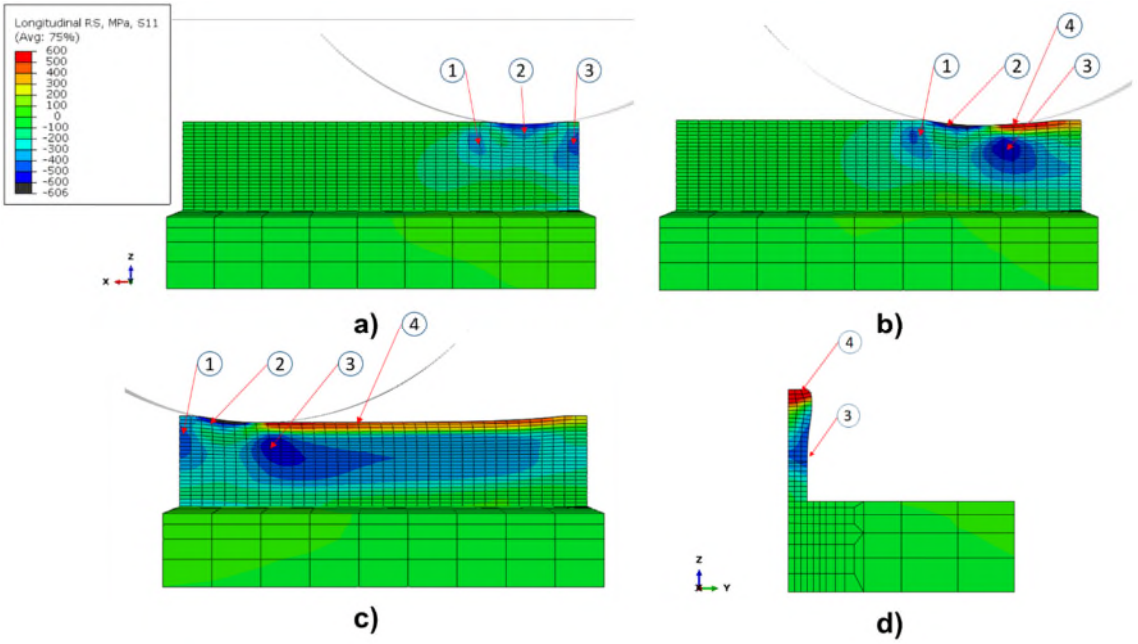

Figure 6-8 Longitudinal stress evolution during rolling with flat roller (F = 50 kN and μ = 0.5): a) at the end of the initial establishment of contact, b) at the beginning of the roller motion, c) at the end of the rolling step, d) in the final rolling state on the transverse section. Note that in this analysis case the wall and substrate are assumed free from any strain and stress before rolling.

6.3.2 Model Set 2

6.3.2.1 Influence of friction coefficient

6.3.2.1.1 Longitudinal plastic strain

Figure 6-9 shows the influence of the friction coefficient (between the wall and the roller) on PS distributions in the WAAM deposited wall after rolling with the flat, profiled and slotted rollers. Larger friction coefficient mainly caused increase of tensile PS under the rolled surface and such an effect is most marked for the slotted roller. As a stronger friction enhanced the adherence of the wall material to the surface of the roller, a greater tensile deformation was generated on the rolled surface. The constraint effect of the friction can explain the peak tensile deformation 1-2 mm below the rolled surface. This effect limited the deformation of the contact surface, but caused greater deformation underneath. Similar phenomenon has also been found in previous studies of rolling on single layer

deposit [28], cylindrical samples [43], as well as weld seams [23,27] and WAAM wall [44].

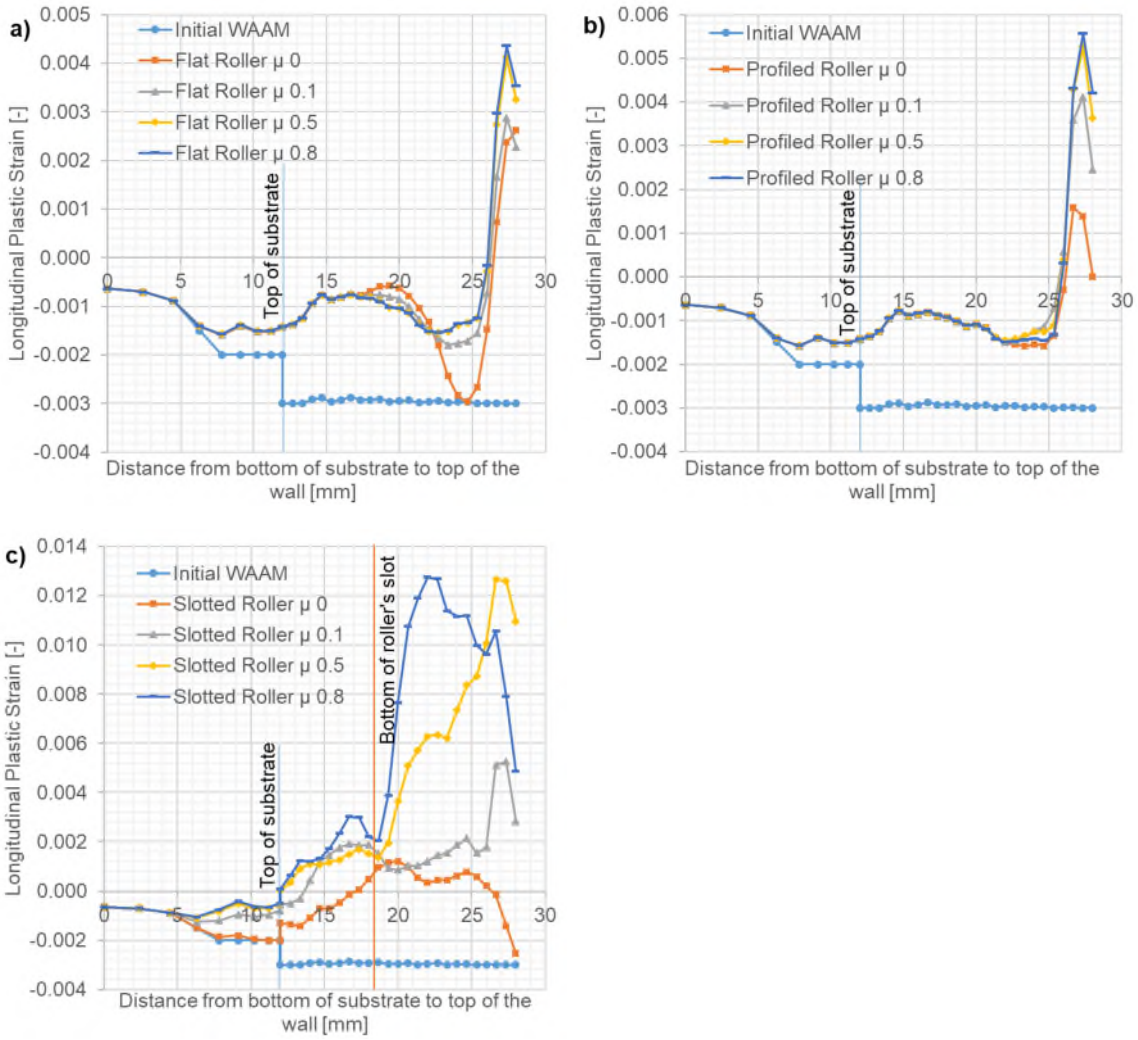

Figure 6-9 Influence of friction coefficient on longitudinal PS in the WAAM built component after rolling: a) flat roller, b) profiled roller, and c) slotted roller (F = 50 kN).

For the slotted roller, the compressive PS associated with the WAAM deposition was converted to tensile PS in the entire wall and the magnitude of compressive PS in the substrate was significantly reduced (Figure 6-9c). With the increase of friction coefficient, the rolling-induced tensile PS increased, and more material was affected through the depth of the wall. Friction also promoted deeper penetration of the slotted roller (Figure 6-10), resulting in greater longitudinal tensile deformation. However, in the flat and profiled rollers models, the change of friction coefficient only caused small variation of the penetration. The additional

friction between the side wall surface and the slot surface is responsible for the deeper penetration of the slotted roller. The lateral deformation of the wall during rolling increased the contact area, and the material adhered to the slot surface helped the roller plunge deeper into the wall. The larger the friction coefficient, the more significant the aforementioned effect.

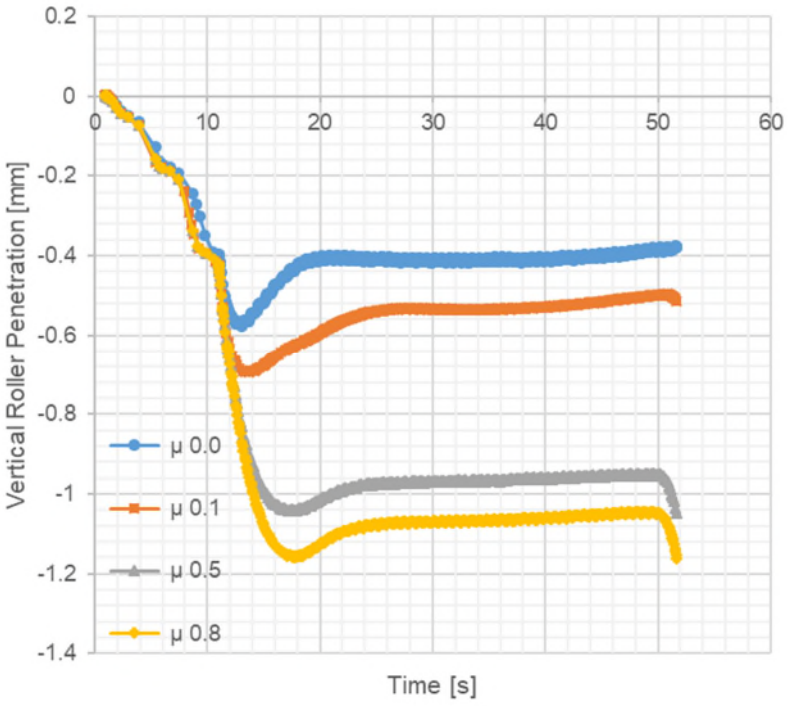

Figure 6-10 Vertical penetration of slotted roller for different friction coefficients (F = 50 kN).

6.3.2.1.2 Longitudinal residual stress

Figure 6-11 demonstrates the influence of friction coefficient on longitudinal RS distributions in the WAAM component rolled with flat, profiled and slotted rollers. Friction coefficient is found to have a significant impact on the longitudinal RS distributions when using a slotted roller. The slotted roller with μ ≥ 0.5 converted the WAAM tensile RS to compressive RS in the whole wall. The main reason for this is the deeper penetration of the slotted roller to the wall at larger friction coefficients (Figure 6-10). The increased penetration and the constraint of transverse deformation by the slot surface promoted larger longitudinal tensile deformation (Figure 6-9c) and compressive RS (Figure 6-11). The compressive RS in the component can improve fatigue performance [45,46], while tensile RS

has detrimental effects [46]. However, the friction effect on RS is insignificant for the flat and profiled rollers (Figure 6-11 a and b). It is also interesting to find that the horizontal reaction force of the flat and profiled rollers is insensitive to the friction coefficient and for F = 50 kN the force fluctuated in the range of 5-6 kN with friction coefficients of 0 and 0.8, implying that the horizontal resistance is mainly due to the indentation step created by the flat/profiled roller (Figure 6-7) rather than the friction force.

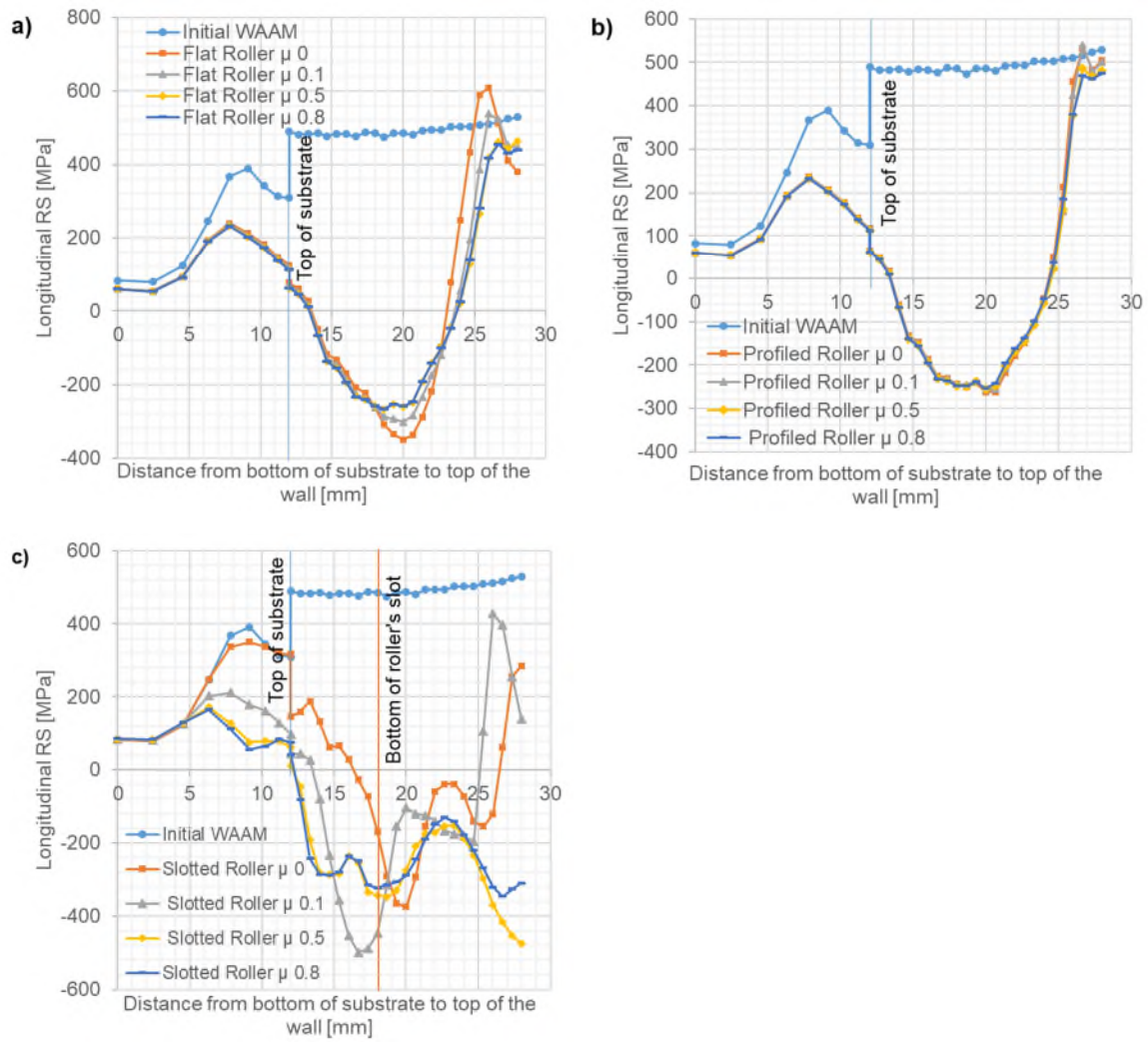

Figure 6-11 Influence of friction coefficient on longitudinal RS distributions in the WAAM built component after rolling with: a) flat roller, b) profiled roller and c) slotted roller (F = 50 kN).

The present modelling results imply that rolling using a slotted roller with μ > 0.5 could significantly improve the effectiveness of the rolling. However, in practice

rolling using a slotted roller without application of lubricant was unsuccessful, since the slotted roller was stuck in the WAAM wall due to insufficient horizontal moving traction capacity. The simulation confirmed that for the slotted roller at F = 50 kN, the predicted horizontal reaction force on the pivot of the roller increased from 5.74 kN to 11 kN when the friction coefficient increased from 0.1 to 0.8. Practical implementation of the unlubricated post-build rolling with slotted roller should be tested using a rolling rig with larger moving traction capacity.

6.3.3 Model Set 3

6.3.3.1 Influence of rolling load

6.3.3.1.1 Longitudinal plastic strain

The effects of the rolling load on the compressive longitudinal PS in the WAAM component for the flat, profiled and slotted rollers models are presented in Figure 6-12 and Figure 6-13. The compressive PS generated by the WAAM deposition can be significantly reduced by the rolling even with a relatively low rolling load of 25 kN. When a higher rolling load was used, the compressive PS in the wall transformed into tensile PS, and more significant plastic deformation occurred underneath the rolled surface.

With increase of the rolling load, the flat and profiled rollers models demonstrated a similar response. After rolling at F = 25 kN, the compressive PS reduced in the wall, as shown in Figure 6-13 a), b). As the rolling load increased to 50 kN, the compressive PS in the substrate reduced as well and converted to tensile PS underneath the rolled surface. When the rolling load further increased to 75 kN, the compressive PS was further reduced in the wall and substrate, and the tensile PS under the rolled surface significantly increased. The peak PS is found to be 2 mm under the rolled surface, which can be enhanced by the friction as explained in the Section 6.3.2.1. Similar effect is also found for the slotted roller, except that the rolling with the slotted roller is more effective to reduce compressive PS and promote tensile PS in the wall.

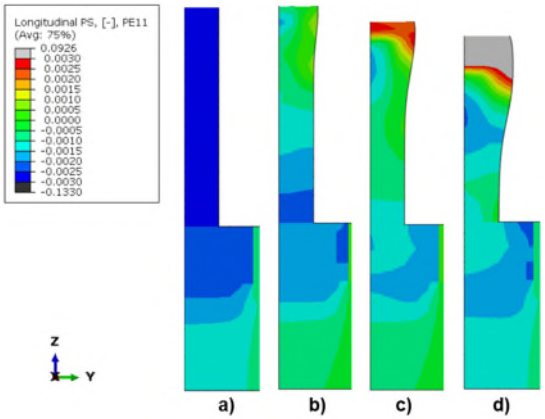

Figure 6-12 Contour maps of longitudinal PS distributions in WAAM component: a) after deposition, and after rolling with flat roller at rolling loads of b) 25 kN, c) 50 kN and d) 75 kN (μ = 0.1).

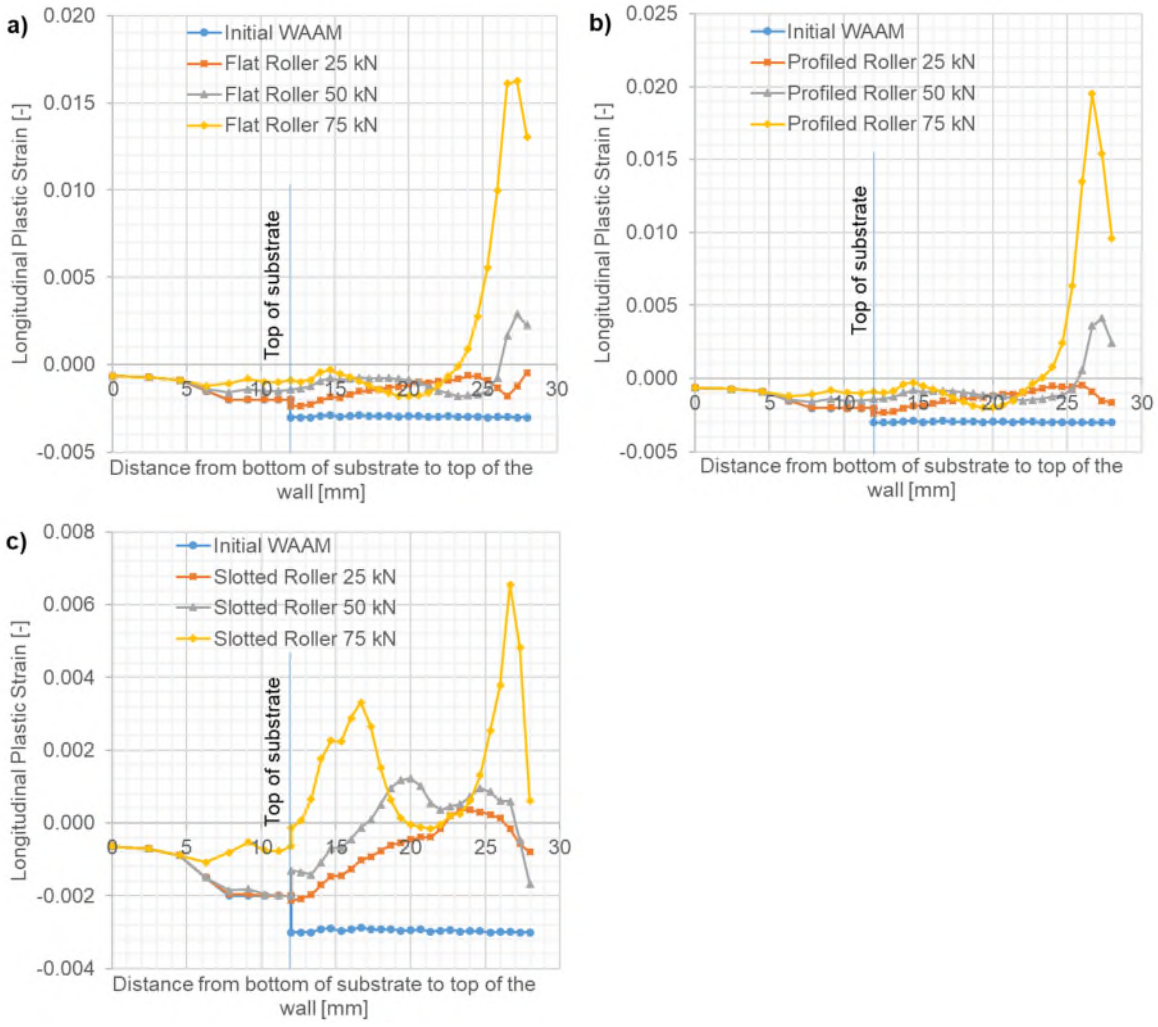

Figure 6-13 Influence of rolling load on longitudinal PS in the WAAM component after rolling: a) flat roller, b) profiled roller, and c) slotted roller (μ = 0.1).

6.3.3.1.2 Longitudinal residual stress

The effects of rolling on the longitudinal tensile RS induced by WAAM deposition for different rolling loads are presented in Figure 6-14 and Figure 6-15. The efficacy of the rolling to mitigate the WAAM deposition RS is enhanced by increasing the rolling loads for all the rollers. The tensile RS caused by the WAAM deposition was converted to compressive RS in the central region of the wall, while the tensile RS near/in the substrate was reduced. With increase of rolling load, the peak of compressive RS increased and moved to a greater distance away from the rolled surface. This response can be explained by the greater effect of the compression Zone 3 (Figure 6-8), which became larger and moved deeper due to the higher rolling load. In the flat and profiled rollers models, a higher rolling load caused an increase of tensile RS immediately under the rolled surface. It is also interesting to see that the rolling dominated the final RS and eliminated the feature of the WAAM deposition RS in the wall when the rolling load reached 75 kN.

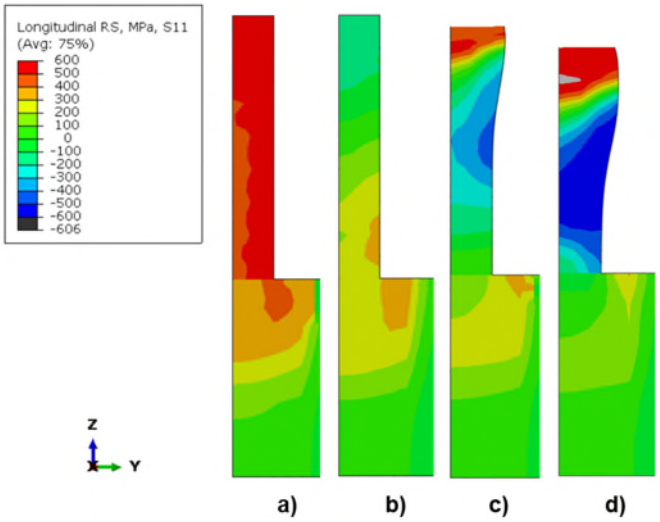

Figure 6-14 Contour maps of longitudinal RS distributions in WAAM component a) after deposition, and after rolling with flat roller at rolling loads of b) 25 kN, c) 50 kN and d) 75 kN (μ = 0.1).

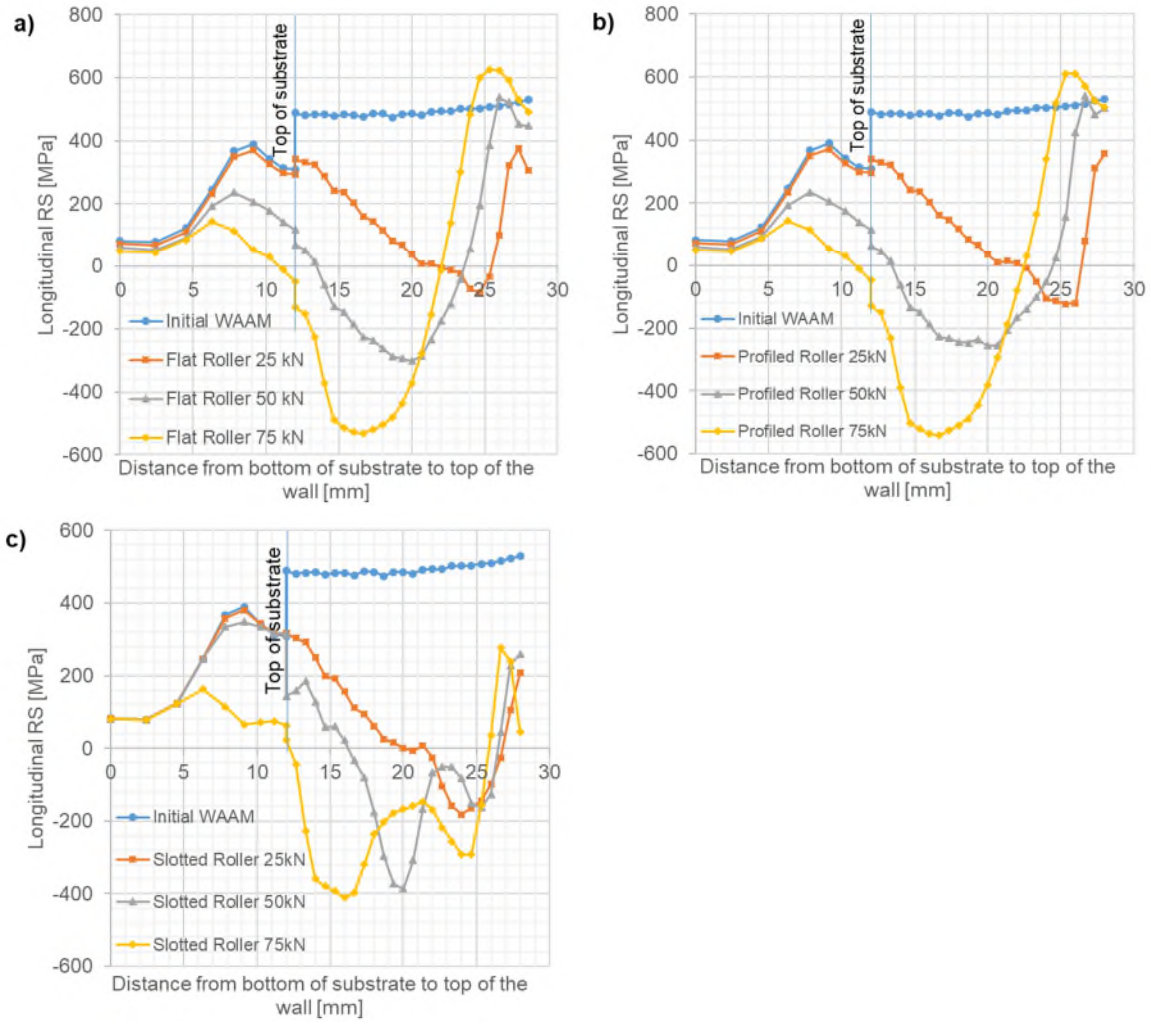

Figure 6-15 Influence of rolling load on the longitudinal RS in the WAAM component after rolling a) flat roller, b) profiled roller, and c) slotted roller (μ = 0.1).

In general, all the rolling models showed that as the rolling load increased, the tensile RS mitigation efficacy was enhanced, and the converted compressive RS covered more extensive region in the wall. However, an excessive rolling load could face practical difficulty regarding machine capacity and it may not be always beneficial to reduce distortion (Section 6.3.4).

6.3.3.2 Influence of roller design

6.3.3.2.1 Longitudinal plastic strain

The effects of rolling on the WAAM-induced longitudinal compressive PS for different rollers are presented in Figure 6-16. The flat and profiled rollers models demonstrated similar predictions for all tested loads, despite that the profiled

roller induced slightly larger longitudinal PS near the rolled surface, as compared to the flat roller. This difference arises because the lateral constraint provided by the edge of the profiled roller is larger than that solely provided by the friction for the flat roller, and hence the transverse deformation on the rolled surface can be more significantly constrained by the profiled roller.

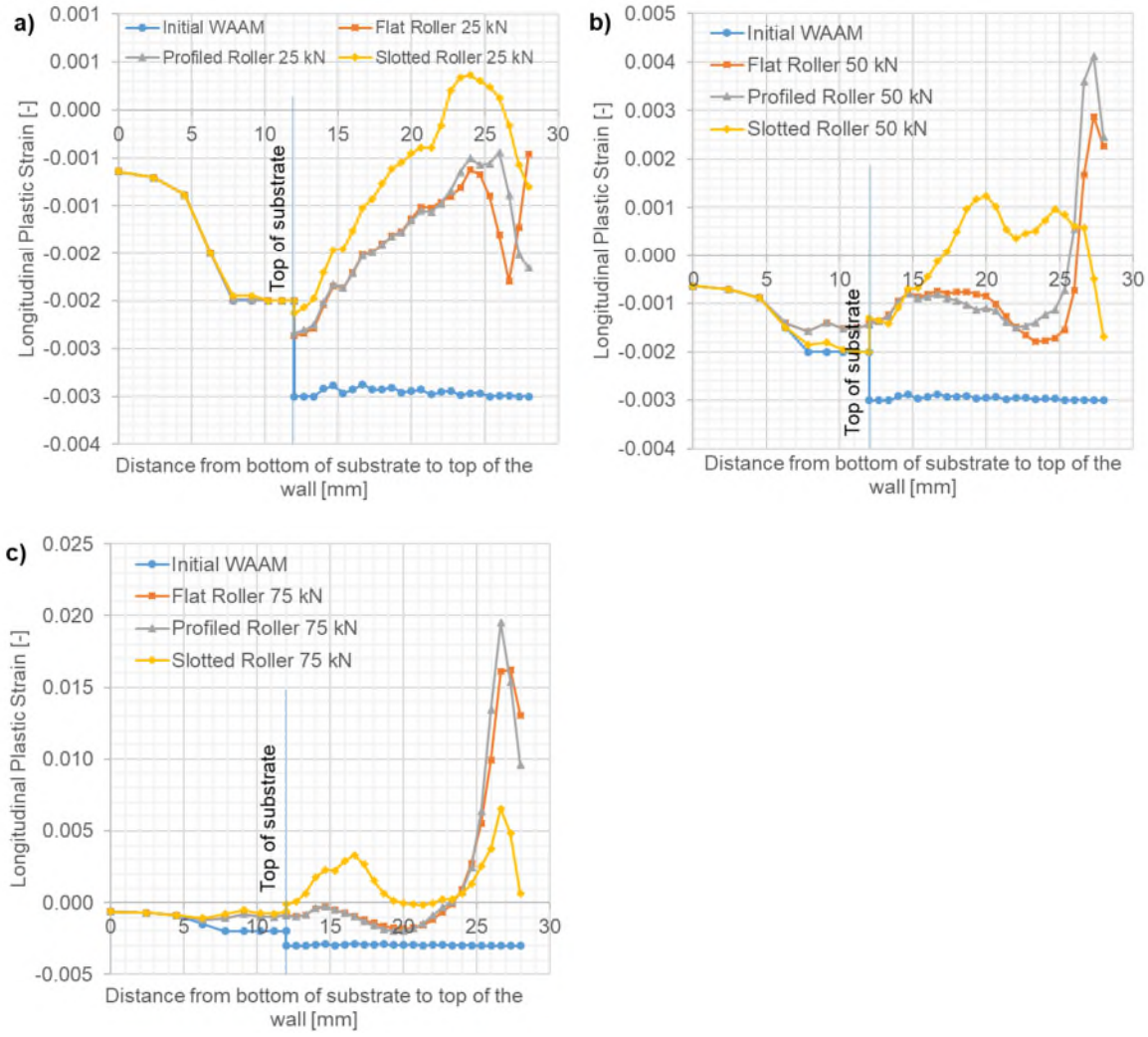

Figure 6-16 Influence of roller design on mitigation of the compressive longitudinal PS caused by WAAM deposition. The rolling loads are a) 25 kN, b) 50 kN and c) 75 kN (μ = 0.1).

Similar behaviour was also observed in experiments by Martina et al. [6], who measured the average engineering strain induced by the profiled roller and found it was larger in the normal direction than in the transverse direction. But for the flat roller the transverse strain is larger than the normal strain. However, the flat

and profiled rollers models predicted a similar PS distribution in the aforementioned region when the friction coefficient was 0.5 and higher, as shown in Figure 6-9 a and b.

Compared with the flat and profiled rollers, for all rolling loads the slotted roller converted compressive PS to tensile PS in a larger region in the wall centre. This is due to the more extensive constraining effect of the slot surface, which prevented the transverse deformation and promoted the longitudinal deformation. In contrast, the flat and profiled rollers produced greater magnitude of tensile PS in the region that is 3 to 5 mm below the rolled surface.

6.3.3.2.2 Longitudinal residual stress

Figure 6-17 shows the influence of roller design on the longitudinal tensile RS generated by the WAAM deposition. The predicted RS distributions are compared between rolling with the flat, profiled and slotted rollers. Under all the considered rolling loads, the flat and profiled rollers demonstrated similar RS distributions with minor difference in the region immediately below the rolled surface. In contrast, the slotted roller reduced the WAAM tensile RS more effectively and led to relatively uniform compressive RS distribution in the core of the wall at F = 75 kN. The main reason for such a stress feature is that the slot surface constrained the transverse deformation and meanwhile promoted the longitudinal deformation. For F = 75 kN, the lower magnitude of RS after rolling can be explained by the larger tensile plastic deformation having occurred in this region (Figure 6-16 c).

The design of roller has a great impact on the final PS and RS after rolling and thus influences the effectiveness of the post-build rolling. At all investigated rolling loads, compared to the flat and profiled rollers, the slotted roller induced a larger magnitude of compressive PS and the compression region is deeper in the wall. As a result, the reduction in tensile RS was found in a larger volume of material in the WAAM wall. Based on the results of this study, it is recommended that post-build rolling with a slotted roller should be developed further for minimising RS in steel WAAM structures.

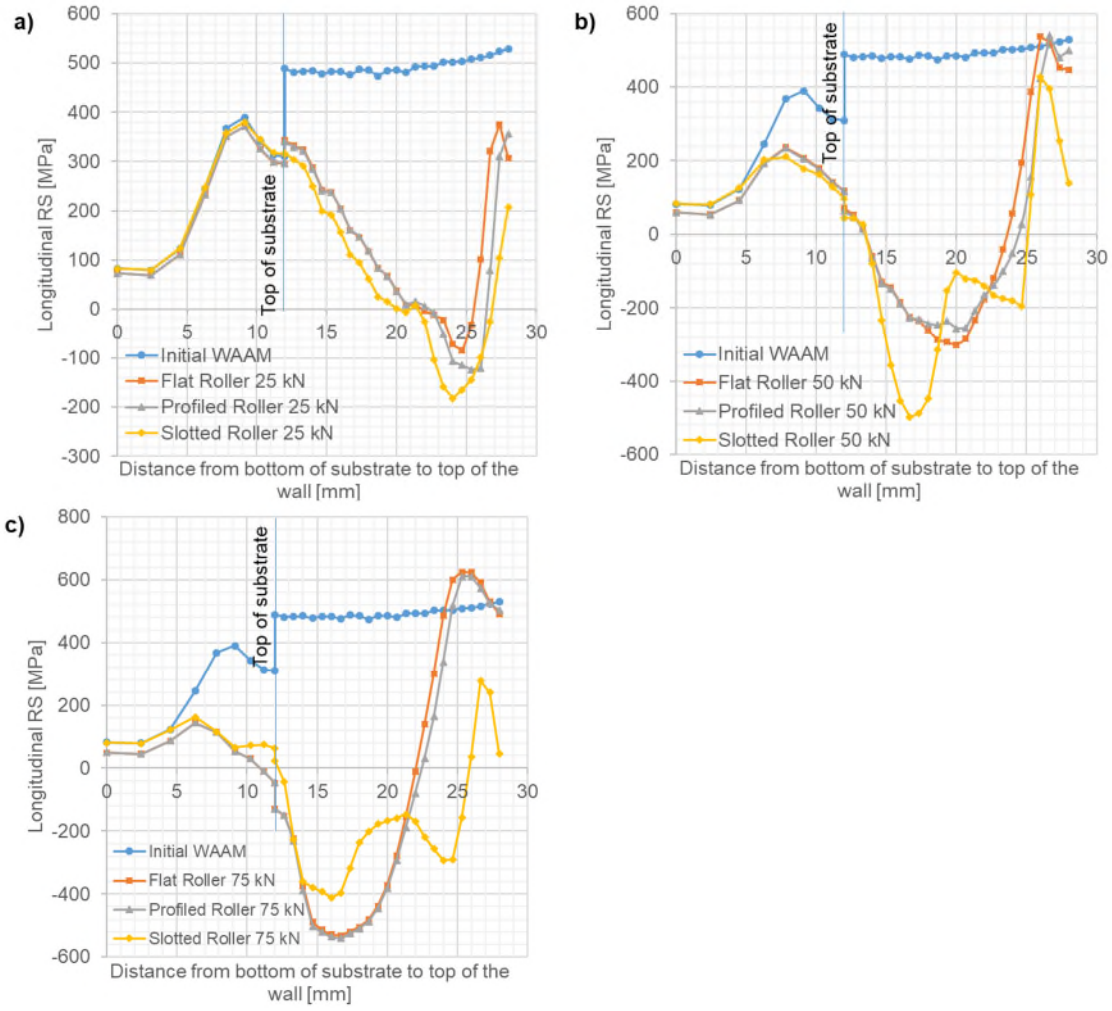

Figure 6-17 Influence of roller design on mitigation of the tensile longitudinal RS caused by WAAM deposition. The rolling loads are a) 25 kN, b) 50 kN, and c) 75 kN (μ = 0.1).

Unfortunately, measurements of RS in post-build rolled WAAM parts using the designed rollers and rolling loads considered here were not found in the literature. Thus, the simulation results were compared to the RS measured in the WAAM parts inter-layer rolled with profiled and slotted rollers at the rolling load of 50 kN [1]. Significant difference in RS is found between the measurements after inter-layer rolling and the predictions by post-build rolling models.

During inter-layer rolling with profiled and slotted rollers, a significant reduction of longitudinal tensile RS was observed at the border between the WAAM wall and the substrate [1]. However, after the inter-layer rolling the RS in the wall was still

mainly tensile, except slight compressive RS appearing near the rolled surface. [1]. Conversely, at the same rolling load (F = 50 kN) the post-build rolling models with flat, profiled and slotted rollers predicted compressive RS in the core of the WAAM wall and high tensile RS under the rolled surface,

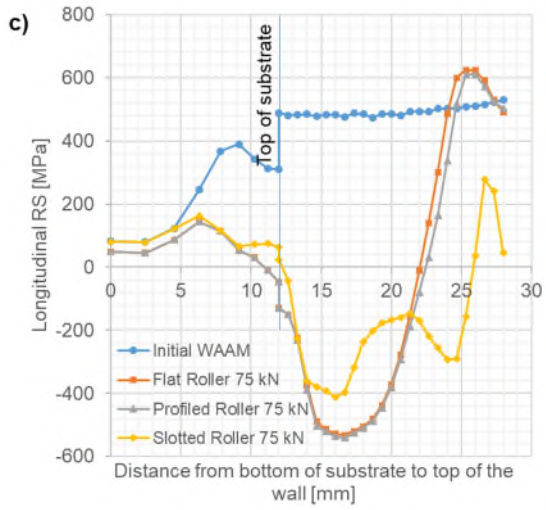

Figure 6-17 b). The distinctive distribution of the measured RS after inter-layer rolling could be attributed to the interaction of rolling with cyclic formation of RS during WAAM deposition [14], which reduced the effectiveness of rolling to mitigate tensile RS. In addition, it should be mentioned that the RS measurements were performed after removal of clamps in the experiments [1], while the post-build rolling models predicted RS in the clamped condition (Figure 6-17). Nevertheless, for the post-build rolling the difference between RSs predicted under clamped condition and after clamps removal is insignificant, and minor RS redistribution occurred after clamps removal, refer to Section 6.3.4.

6.3.4 PS and RS distributions and distortion in large-scale post-build rolled WAAM component

To investigate the PS and RS distributions and distortion in the large-scale WAAM component, the steady-state solution slice from the short rolling model with the flat roller was transferred to the long mechanical model using the solution mapping method (Chapter 5 and Ref. [31]), Figure 6-1. Figure 6-18 shows the RS distribution and deformed configuration in the rolled full-length WAAM component before and after clamps removal. Two narrow tensile zones are formed on the

top and bottom of the wall, between which there is a wide compression zone. The distortion is barely seen, implying that the rolled wall is free from distortion issue.

Figure 6-19 presents the effect of the post-build rolling on the WAAM-induced longitudinal RS distribution along the wall height, as predicted by the long mechanical model before and after clamps removal. High tensile RS in the as-built WAAM wall was balanced by the reaction force at the clamps. The removal of clamps caused significant redistribution of tensile RS in the wall and the nearby substrate. As the wall shrank, the tensile RS relaxed and reduced markedly, and even converted to compressive RS at the top of the wall. The clamps removal in the WAAM + post-build rolling model caused minor redistribution of longitudinal RS. The RS distribution remained virtually the same as that before clamps removal. This can be attributed to the relatively low height of the WAAM deposited wall studied here and the dominant influence of rolling on RS at the 50 kN rolling load. As the tensile RS in the wall was already largely mitigated by the rolling under the clamped condition, the total reaction force at the clamps is reduced from —37.083 kN after WAAM deposition to —2.09 kN after the rolling with the flat roller ($F = 50$ kN, $\mu = 0.1$). When the clamps were removed, the equilibrium between the tensile and compressive RSs reached shortly with minor redistribution of RS. As a result, the net bending moment was close to zero and the WAAM wall with substrate remained virtually undistorted (

Figure 6-20).

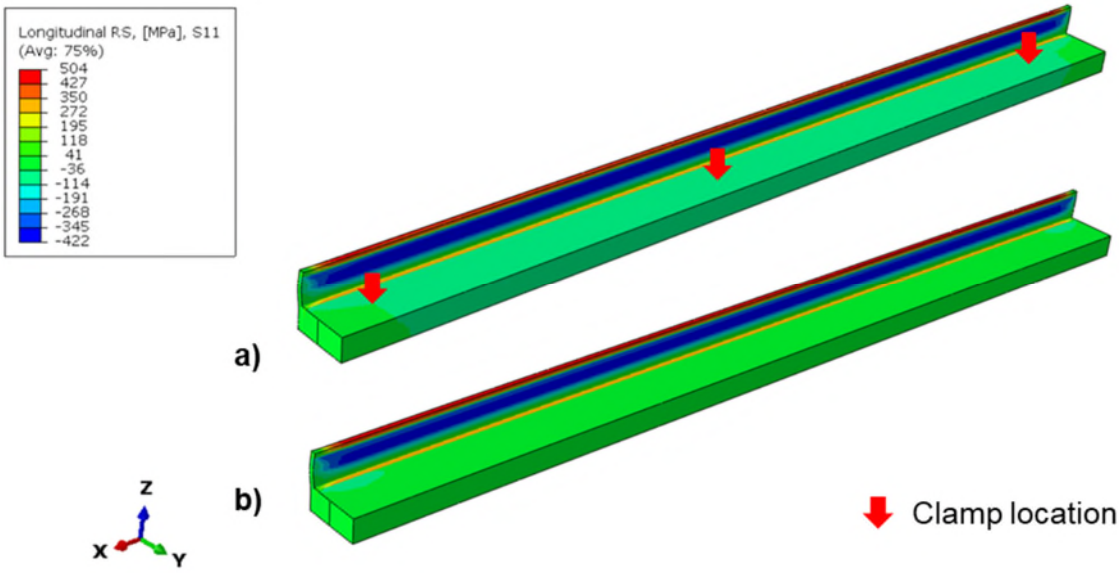

Figure 6-18 Longitudinal RS distribution and deformed configuration of 500 mm long post-build rolled WAAM component a) before and b) after removal of clamps (a deformation scale factor of 25 is used to aid visualisation). Note that the steady-state solution was mapped from the short model with the flat roller. Red arrows indicate locations of clamps.

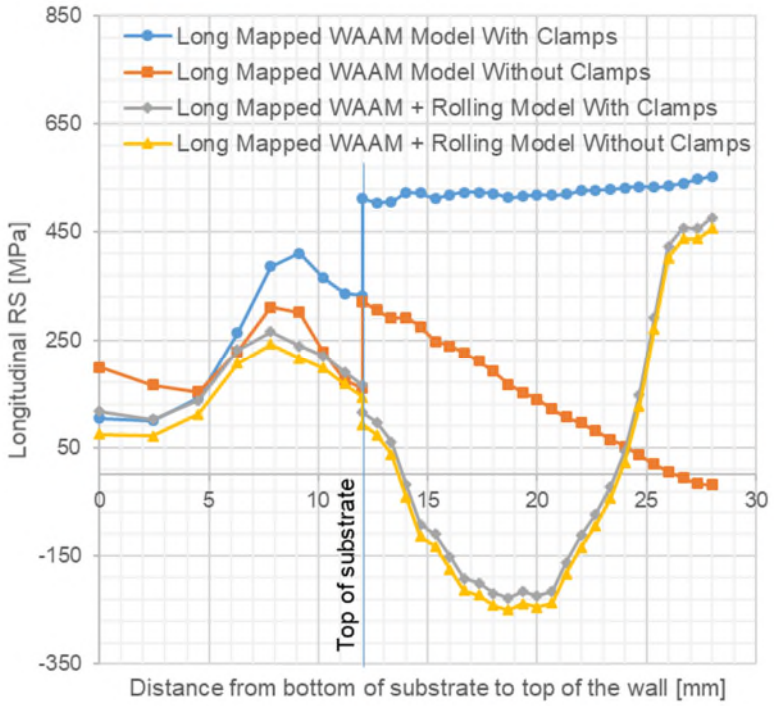

Figure 6-19 Influence of the post-build rolling using the flat roller on the WAAM deposition RS obtained by the long mechanical model before and after clamps removal (F = 50 kN and μ = 0.1).

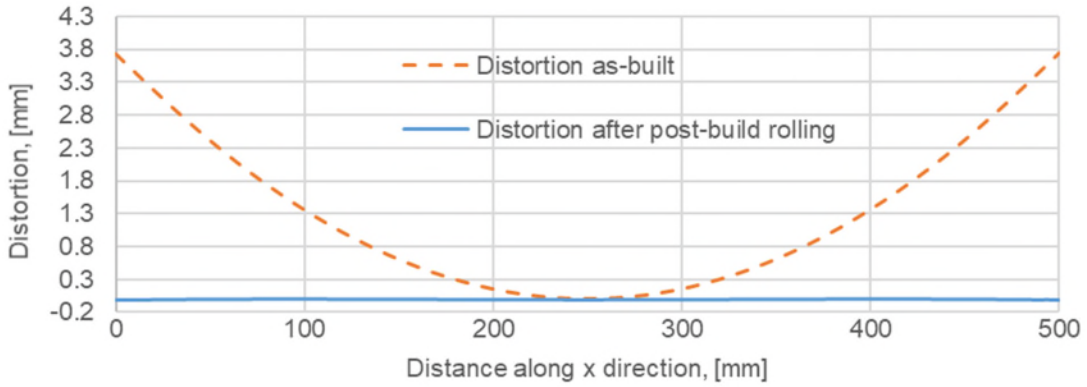

Figure 6-20 Comparison of vertical distortion in as-built and post-build rolled full-length WAAM component after removal of clamps (flat roller, F = 50 kN and μ = 0.1).

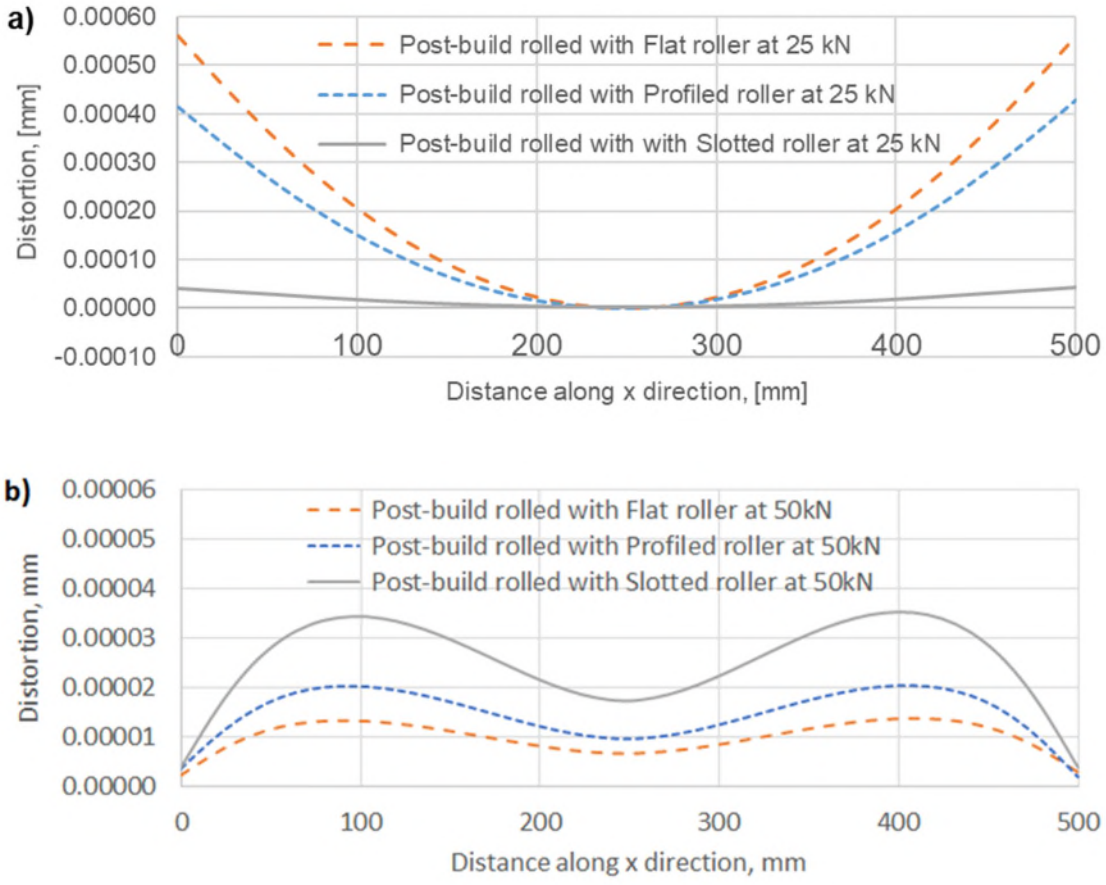

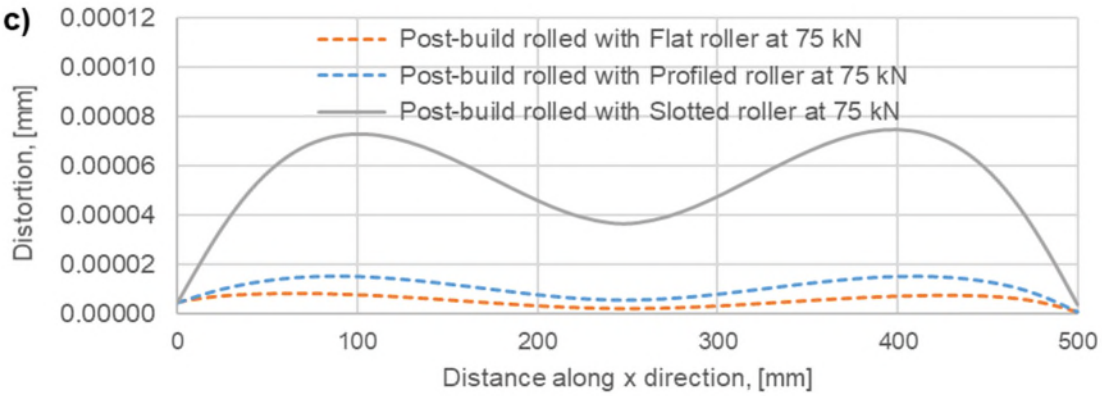

Figure 6-21 Comparison of distortion in long WAAM components after post-build rolling with flat, profiled and slotted rollers at rolling loads of a) 25 kN, b) 50 kN, and c) 75 kN (μ = 0.1).

Figure 6-21 shows the comparison of vertical distortion after clamps removal in the long WAAM component rolled with flat, profiled and slotted rollers at rolling loads from 25 kN to 75 kN. In general, the post-build rolling virtually eliminated the distortion caused by thermal deposition process with all types of investigated rollers and at all rolling loads. The predicted distortion varies from 560 μm for flat roller at F = 25 kN to 0.00768 μm for flat roller at F = 75 kN. The flat and profiled rollers are less effective to reduce distortion than the slotted roller for all rolling loads considered. However, the slotted roller could cause greater inverse distortion when the rolling loads increased from 25 kN to 75 kN. This is because excessive material was affected by the compressive RS in the WAAM wall during the rolling by the slotted roller.

Given the efficacy of the post-build rolling in mitigation of distortion, the practical implementation of post-build rolling has wide potentials to achieve the required reduction of distortion with slotted roller at lower rolling load or with flat and profiled rollers at higher rolling loads.

6.3.5 Effect of initial WAAM deposition conditions on PS and RS distributions at various rolling loads

Figure 6-22 shows the comparison of PS and RS distributions predicted by the flat roller model at various rolling loads with and without consideration of WAAM thermal deposition conditions. The initial thermal deposition condition plays an important role in the prediction of PS distribution regardless of rolling load. The models without initial conditions underpredicted the compressive PS in the final state. In contrary, the effect of WAAM deposition on the RS prediction depends on the rolling load. At relatively low rolling load (25 kN) the model without initial condition underpredicted the tensile RSs that are 7 mm below the rolled surface and in the substrate. With increase of rolling load to 50 kN, the discrepancy between the RSs predicted by the models with and without initial thermal deposition conditions reduced, and at the rolling load of 75 kN, minor difference was found, which can be attributed to the dominant influence of the high pressure rolling over thermal deposition on the final RS. However, all the rolling models without initial conditions underpredicted tensile RS in the substrate.

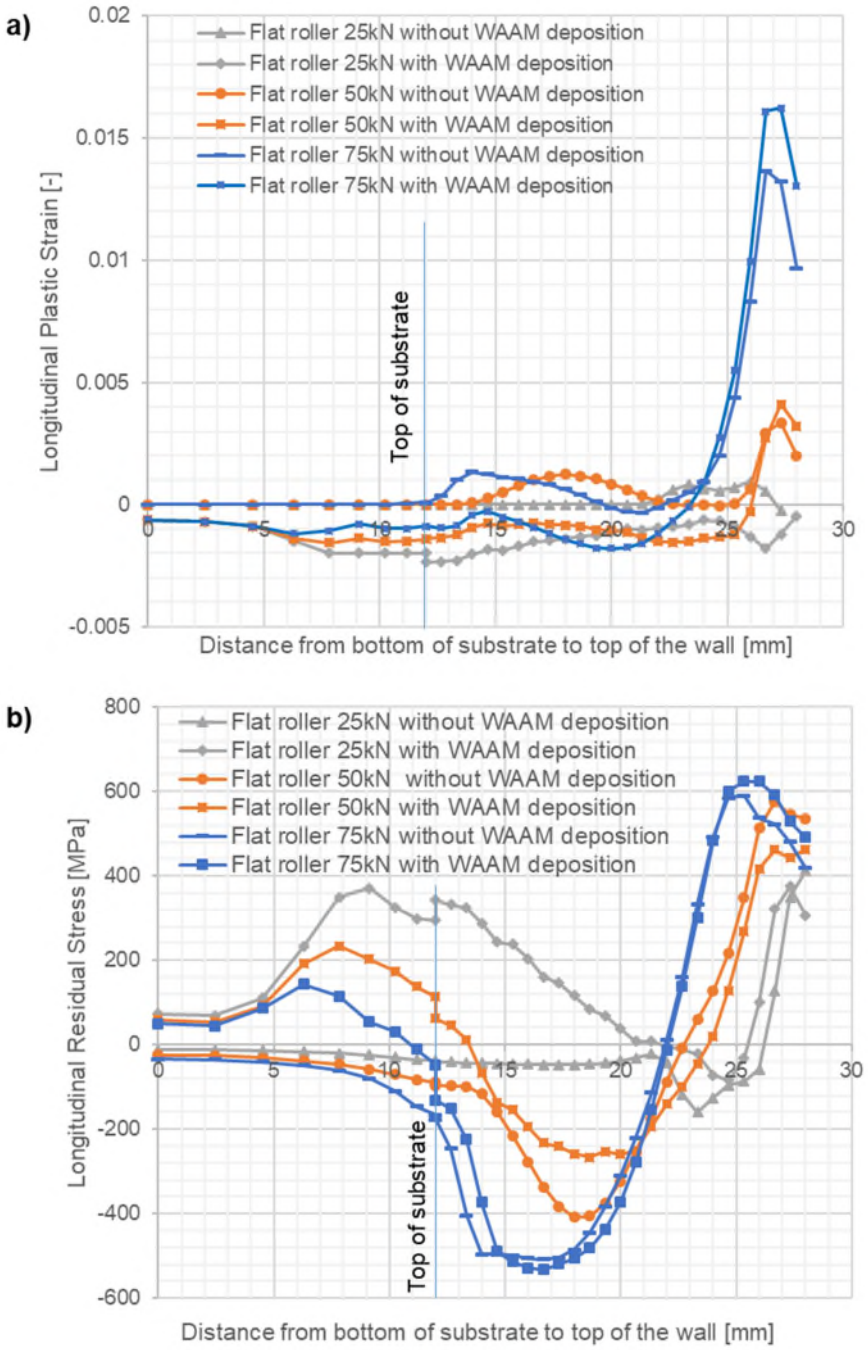

Figure 6-22 Comparison in a) PS and b) RS predictions between flat roller models with and without consideration of the WAAM deposition before rolling simulation (μ = 0.5).

These findings partially coincide with the result of the numerical study by Abbaszadeh et al. [29], who found that at rolling loads larger than 20 kN the difference between the RS distributions in the wall, as predicted by the models

with and without initial conditions (i.e., initial RS), tends to be negligible. However, Abbaszadeh et al. [29] did not consider the initial PS in their rolling model and claimed that the initially specified RS does not affect distribution of final PS. By contrast, the current study demonstrated the importance of considering the initial thermal PS in the rolling model to examine the effect of rolling on final PS.

6.3.6 Limitations of post-build rolling for RS and distortion mitigation in WAAM components

It should be noted that post-build rolling for mitigation of RS and distortion in WAAM components has the following limitations. First, the rolling may not be effective for RS mitigation in WAAM walls taller than the wall studied here. Second, the rise of the rolling load to increase process effectiveness for the tall wall could cause excessive deformation or even plastic collapse of the wall. Third, the produced RS profile at higher rolling loads could be unfavourable in terms of fatigue performance of the component (i.e., large region affected by high tensile RS at the rolled surface, as shown in Figure 6-5 and Figure 6-14, can have detrimental effect [46]). Nevertheless, properly designed post-build rolling could be an efficient alternative to the time consuming and complicated inter-layer rolling. Optimisation of inter-layer rolling through WAAM + rolling simulations could also be an interesting topic for future work.

6.4 Conclusions

The present modelling study investigated post-build rolling as an efficient method for mitigation of RS and distortion in a WAAM-built steel wall component. The influences of the roller design (flat, profiled and slotted rollers), roller-to-wall friction coefficient (0-0.8) and rolling loads (25-75 kN) on WAAM-generated PS and RS distributions were examined. The following conclusions are drawn:

1. Post-build rolling can introduce adequate tensile PS for the wall considered here with relatively small height, thereby counteracting the longitudinal compressive PS and tensile RS caused by the WAAM deposition. For a taller wall, it is anticipated that higher rolling load is required to achieve the similar effectiveness.

2. Post-build rolling was found effective to eliminate distortion in the WAAM component at all investigated rolling loads and for all types of rollers. Slotted roller was most effective at a rolling load of 25 kN, but it generated inverse distortion (small magnitude) at rolling loads of 50 kN and 75 kN, due to excessive compressive RS induced by the rolling. With increase of rolling load the distortion reduced for the flat and profiled rollers, but the magnitude of inverse distortion increased for the slotted roller.
3. Post-build rolling with highest rolling load (75 kN) considered here most effectively mitigated RS. With all types of investigated rollers, larger volume of material deformed with tensile PS when increasing the rolling load, and the WAAM-generated tensile RS converted to compressive RS extending deeper in the core of the wall.
4. For all the rolling loads investigated (25 kN to 75 kN), the slotted roller induced longitudinal tensile PS of larger magnitude and it reduced the tensile RS in the wall more effectively, as compared to the flat and profiled rollers.
5. The efficacy of the flat and profiled rollers is insensitive to the roller-to-wall friction coefficient. In contrast, an increase of friction coefficient drastically increased the efficacy of the slotted roller, which has additional slot surface subject to friction. The additional friction is helpful for the slotted roller to penetrate deeper and induce more extensive tensile PS in the wall, but it also increases the horizonal motion resistance.
6. From modelling considerations, the flat roller with a friction coefficient of 0.5 and higher value can be used to represent the profiled roller. The initial conditions accounting for the WAAM deposition PS and RS play significant roles in the determination of final PS and RS in the rolling models at relatively low rolling loads. At high rolling loads, the rolling dominates the final RS and hence the initial condition has less impact.

6.5 References

1. Colegrove PA., Coules HE., Fairman J., Martina F., Kashoob T., Mamash H., Cozzolino LD. Microstructure and residual stress improvement in wire and arc

additively manufactured parts through high-pressure rolling. Journal of Materials Processing Technology. October 2013; 213(10): 1782–1791. Available at: DOI:10.1016/j.jmatprotec.2013.04.012

2. Welding Engineering and Laser Processing Centre of Cranfield University. Demo parts built for industry partners. WAAM. Available at: https://waammat.com/about/demo-parts (Accessed: 15 December 2020)

3. Karayel E., Bozkurt Y. Additive manufacturing method and different welding applications. Journal of Materials Research and Technology. September 2020; 9(5): 11424–11438. Available at: DOI:10.1016/j.jmrt.2020.08.039

4. Yilmaz O., Ugla AA. Microstructure characterization of SS308LSi components manufactured by GTAW-based additive manufacturing: shaped metal deposition using pulsed current arc. The International Journal of Advanced Manufacturing Technology. March 2017; 89(1–4): 13–25. Available at: DOI:10.1007/s00170-016-9053-y

5. Gu J., Ding J., Williams SW., Gu H., Ma P., Zhai Y. The effect of inter-layer cold working and post-deposition heat treatment on porosity in additively manufactured aluminum alloys. Journal of Materials Processing Technology. April 2016; 230: 26–34. Available at: DOI:10.1016/j.jmatprotec.2015.11.006

6. Martina F., Roy MJ., Szost BA., Terzi S., Colegrove PA., Williams SW., Meyer J., Hofmann M. Residual stress of as-deposited and rolled wire+arc additive manufacturing Ti–6Al–4V components. Materials Science and Technology. 21 September 2016; 32(14): 1439–1448. Available at: DOI:10.1080/02670836.2016.1142704

7. Asala G., Khan AK., Andersson J., Ojo OA. Microstructural analyses of ATI 718Plus® produced by wire-arc additive manufacturing process. Metallurgical and Materials Transactions A. September 2017; 48(9): 4211–4228. Available at: DOI:10.1007/s11661-017-4162-2

8. Marinelli G., Martina F., Ganguly S., Williams S. Grain refinement in an unalloyed tantalum structure by combining Wire+Arc additive manufacturing and

vertical cold rolling. Additive Manufacturing. March 2020; 32: 101009. Available at: DOI:10.1016/j.addma.2019.101009

9. Marinelli G., Martina F., Ganguly S., Williams S. Development of Wire + Arc additive manufacture for the production of large-scale unalloyed tungsten components. International Journal of Refractory Metals and Hard Materials. August 2019; 82: 329–335. Available at: DOI:10.1016/j.ijrmhm.2019.05.009

10. Williams SW., Martina F., Addison AC., Ding J., Pardal G., Colegrove P. Wire + arc additive manufacturing. Materials Science and Technology. 2 May 2016; 32(7): 641–647. Available at: DOI:10.1179/1743284715Y.0000000073

11. Lockett H., Ding J., Williams S., Martina F. Design for Wire + Arc Additive Manufacture: design rules and build orientation selection. Journal of Engineering Design. 2 September 2017; 28(7–9): 568–598. Available at: DOI:10.1080/09544828.2017.1365826

12. Baufeld B., Biest OV der., Gault R. Additive manufacturing of Ti–6Al–4V components by shaped metal deposition: Microstructure and mechanical properties. Materials & Design. June 2010; 31: S106–S111. Available at: DOI:10.1016/j.matdes.2009.11.032

13. Clark D., Bache MR., Whittaker MT. Shaped metal deposition of a nickel alloy for aero engine applications. Journal of Materials Processing Technology. July 2008; 203(1–3): 439–448. Available at: DOI:10.1016/j.jmatprotec.2007.10.051

14. Ding J., Colegrove P., Mehnen J., Williams S., Wang F., Almeida PS. A computationally efficient finite element model of wire and arc additive manufacture. Int J Adv Manuf Technol. 2014; (70): 227–236. Available at: DOI:10.1007/s00170-013-5261-x

15. Cordiano HV. Effect of residual stresses on the low cycle fatigue life of large scale weldments in high strength steel. Journal of Engineering for Industry. 1 February 1970; 92(1): 86–92. Available at: DOI:10.1115/1.3427724

16. Webster GA., Ezeilo AN. Residual stress distributions and their influence on fatigue lifetimes. International Journal of Fatigue. 2001; 23: 375–383. Available at: DOI:10.1016/S0142-1123(01)00133-5

17. Dong P., Brust FW. Welding Residual Stresses and Effects on Fracture in Pressure Vessel and Piping Components: A Millennium Review and Beyond. Journal of Pressure Vessel Technology. 1 August 2000; 122(3): 329–338. Available at: DOI:10.1115/1.556189

18. Dong P. Residual stresses and distortions in welded structures: a perspective for engineering applications. Science and Technology of Welding and Joining. July 2005; 10(4): 389–398. Available at: DOI:10.1179/174329305X29465

19. Cho JR., Lee BY., Moon YH., Van Tyne CJ. Investigation of residual stress and post weld heat treatment of multi-pass welds by finite element method and experiments. Journal of Materials Processing Technology. November 2004; 155–156: 1690–1695. Available at: DOI:10.1016/j.jmatprotec.2004.04.325

20. Altenkirch J., Steuwer A., Withers PJ., Williams SW., Poad M., Wen SW. Residual stress engineering in friction stir welds by roller tensioning. Science and Technology of Welding and Joining. February 2009; 14(2): 185–192. Available at: DOI:10.1179/136217108X388624

21. Kurkin SA., Anufriev VI., Milekhin ES. Improving the mechanical properties of welded joints in the AMg6 alloy by plastic deformation during arc welding. Svarochnoe Proizvodstvo. 1980; (27): 20–24.

22. Kurkin SA., Anufriev VI. Preventing distortion of welded thin-walled members of AlMg6 and 1201 aluminum alloys by rolling the weld with a roller behind the welding arc. Svarochnoe Proizvodstvo. 1984; (31): 52–55.

23. Coules HE., Colegrove P., Cozzolino LD., Wen SW., Kelleher JF. High pressure rolling of low carbon steel weld seams: Part 2 – Roller geometry and residual stress. Science and Technology of Welding and Joining. January 2013; 18(1): 84–90. Available at: DOI:10.1179/1362171812Y.0000000080

24. Sule J., Ganguly S., Coules H., Pirling T. Application of local mechanical tensioning and laser processing to refine microstructure and modify residual stress state of a multi-pass 304L austenitic steels welds. Journal of Manufacturing Processes. April 2015; 18: 141–150. Available at: DOI:10.1016/j.jmapro.2015.03.003

25. Colegrove PA., Martina F., Roy MJ., Szost BA., Terzi S., Williams SW., Withers PJ., Jarvis D. High pressure interpass rolling of wire + arc additively Manufactured titanium components. Advanced Materials Research. August 2014; 996: 694–700. Available at: DOI:10.4028/www.scientific.net/AMR.996.694

26. Hönnige JR., Colegrove PA., Ahmad B., Fitzpatrick ME., Ganguly S., Lee TL., et al. Residual stress and texture control in Ti-6Al-4V wire + arc additively manufactured intersections by stress relief and rolling. Materials & Design. July 2018; 150: 193–205. Available at: DOI:10.1016/j.matdes.2018.03.065

27. Cozzolino LD., Coules HE., Colegrove PA., Wen S. Investigation of post-weld rolling methods to reduce residual stress and distortion. Journal of Materials Processing Technology. September 2017; 247: 243–256. Available at: DOI:10.1016/j.jmatprotec.2017.04.018

28. L. D. Cozzolino Finite element analysis of localised rolling to reduce residual stress and distortion. PhD Thesis. Cranfield University; 2013.

29. Abbaszadeh M., Hönnige JR., Martina F., Neto L., Kashaev N., Colegrove P., Williams S., Klusemann B. Numerical investigation of the effect of rolling on the localized stress and strain induction for wire + arc additive manufactured structures. Journal of Materials Engineering and Performance. August 2019; 28(8): 4931–4942. Available at: DOI:10.1007/s11665-019-04249-y

30. Tangestani R., Farrahi GH., Shishegar M., Aghchehkandi BP., Ganguly S., Mehmanparast A. Effects of vertical and pinch rolling on residual stress distributions in wire and arc additively manufactured components. Journal of Materials Engineering and Performance. April 2020; 29(4): 2073–2084. Available at: DOI:10.1007/s11665-020-04767-0

31. Gornyakov V., Sun Y., Ding J., Williams S. Efficient determination and evaluation of steady-state thermal-mechanical variables generated by wire arc additive manufacturing and high pressure rolling. Accepted for publication in Modelling and Simulation in Materials Science and Engineering (Manuscript ID: MSMSE-105517.R2).

32. Perenda J., Trajkovski J., Žerovnik A., Prebil I. Residual stresses after deep rolling of a torsion bar made from high strength steel. Journal of Materials Processing Technology. April 2015; 218: 89–98. Available at: DOI:10.1016/j.jmatprotec.2014.11.042

33. Lan J., Feng S., Hua L. The residual stress of the cold rolled bearing race. Procedia Engineering. 2017; 207: 1254–1259. Available at: DOI:10.1016/j.proeng.2017.10.879

34. Pan R., Pirling T., Zheng J., Lin J., Davies CM. Quantification of thermal residual stresses relaxation in AA7xxx aluminium alloy through cold rolling. Journal of Materials Processing Technology. February 2019; 264: 454–468. Available at: DOI:10.1016/j.jmatprotec.2018.09.034

35. Stolarski TA., Tobe S. Rolling Contacts: Stolarski/Rolling Contacts. Chichester, UK: John Wiley & Sons, Ltd; 2000. Available at: DOI:10.1002/9781118903001 (Accessed: 23 April 2020)

36. Coules HE., Horne GCM., Kabra S., Colegrove P., Smith DJ. Three-dimensional mapping of the residual stress field in a locally rolled aluminium alloy specimen. Journal of Manufacturing Processes. April 2017; 26: 240–251. Available at: DOI:10.1016/j.jmapro.2017.02.010

37. Hutchings IM., Shipway P. Tribology: friction and wear of engineering materials. 2017.

38. Marks LS. Marks' standard handbook for mechanical engineers. Eleventh editon, [90. anniversary edition]. Avallone EA, Baumeister T, Sadegh AM (eds.) New York: McGraw-Hill; 2007.

39. Gornyakov V., Sun Y., Ding J., Williams S. Computationally Efficient Models of High Pressure Rolling for Wire Arc Additively Manufactured Components. Applied Sciences. 4 January 2021; 11(1): 402. Available at: DOI:10.3390/app11010402

40. Thompson M.A., Fresini M., DosSantos J., Hedgegard J., Richardson I.M. Improving the competitiveness of the European steel fabrication industry using synchronised tandem wire welding technology [Technical]. SYNFAB; 2005. Report No.: 3.

41. Colegrove P., Ikeagu C., Thistlethwaite A., Williams S., Nagy T., Suder W., Steuwer A., Pirling T. Welding process impact on residual stress and distortion. Science and Technology of Welding and Joining. November 2009; 14(8): 717–725. Available at: DOI:10.1179/136217109X406938

42. Woo W., An GB., Kingston EJ., DeWald AT., Smith DJ., Hill MR. Through-thickness distributions of residual stresses in two extreme heat-input thick welds: A neutron diffraction, contour method and deep hole drilling study. Acta Materialia. June 2013; 61(10): 3564–3574. Available at: DOI:10.1016/j.actamat.2013.02.034

43. Cook, M., Larke, E. C. Resistance of copper and copper alloys to homogeneous deformation in compression. J.Inst.Met. January 1945; 71: 371–390.

44. McAndrew AR., Alvarez Rosales M., Colegrove PA., Hönnige JR., Ho A., Fayolle R., Eyitayo K., Stan I., Sukrongpang P., Crochemore A., Pinter Z. Interpass rolling of Ti-6Al-4V wire + arc additively manufactured features for microstructural refinement. Additive Manufacturing. May 2018; 21: 340–349. Available at: DOI:10.1016/j.addma.2018.03.006

45. Hassani-Gangaraj SM., Carboni M., Guagliano M. Finite element approach toward an advanced understanding of deep rolling induced residual stresses, and an application to railway axles. Materials & Design. October 2015; 83: 689–703. Available at: DOI:10.1016/j.matdes.2015.06.026

46. McClung RC. A literature survey on the stability and significance of residual stresses during fatigue. Fatigue & Fracture of Engineering Materials and Structures. March 2007; 30(3): 173–205. Available at: DOI:10.1111/j.1460-2695.2007.01102.x

7 Modelling and optimising hybrid process of WAAM + rolling

This chapter is based on the following publication:

Gornyakov V., Sun Y., Ding J., Williams S., Modelling and optimising hybrid process of wire arc additive manufacturing and high pressure rolling. To be submitted soon to Additive Manufacturing in Elsevier (Manuscript ID: TBA) for Publication.

At Cranfield University, many experiments have confirmed that high-pressure inter-layer rolling can reduce residual stress and distortion in WAAM components. However, the proposed in-process rolling technique is inefficient and requires optimisation to reduce manufacturing time. The mechanism of residual stress and distortion mitigation was not revealed from experiments due to difficulty in obtaining sufficient information, while numerical models for simulation of WAAM deposition and inter-layer rolling were not reported mainly due to high computational cost. This chapter presents the newly developed efficient models of WAAM deposition and inter-layer rolling. With the aid of the models a better understanding of the mechanism has been established. Furthermore, several rolling strategies and roller designs are examined to improve rolling efficiency.

Abstract: High-pressure inter-layer (IL) rolling is effective to mitigate residual stress (RS) and distortion in large scale components built by Wire Arc Additive Manufacturing (WAAM). Many experiments have confirmed the benefits of a hybrid process of WAAM and rolling, but few modelling studies have been attempted to understand the mechanism and optimise the process, owing to the challenges associated with enormous computational cost and complicated coupling between WAAM and rolling. For the first time, in this study efficient coupled WAAM and rolling models have been developed for a steel wall that was deposited using WAAM and IL rolled using both flat and slotted rollers. The predicted RS distributions and deformed configurations are in good agreement with previous experiments. Cyclic re-formation of tensile RS was found during WAAM deposition in the clamped condition. The deposition and rolling exhibit

certain depth of influence on deposited layers in the wall, i.e., the influence depth is characterised by the number of underlying layers where plastic deformation is induced by the arc or by the roller. During the WAAM deposition and IL rolling with the flat roller, the deposition had larger depth of influence than the rolling, and hence the rolling only reduced the re-formation rate of WAAM tensile RS. The IL rolling with the slotted roller had much larger depth of influence than the IL rolling with the flat roller, thereby significantly mitigating the WAAM tensile RS. Furthermore, the slotted roller is more effective in mitigation of the final distortion due to the relaxation of WAAM tensile RS after removal of clamps. To reduce the additional time incurred by rolling in the hybrid process, stacked-layers and post-build rolling was also simulated. It was found that the stacked-4-layer and stacked-10-layer rolling achieved similar mitigation effectiveness but higher manufacture efficiency compared to the IL rolling. However, post-build rolling only mitigated the tensile RS in the upper half of the wall due to its insufficient influence depth relative to the wall height. Therefore, the slotted roller operating on stacked layers is recommended for an optimal hybrid process of WAAM and rolling.

Keywords: WAAM; inter-layer rolling; residual stress; distortion; optimisation

7.1 Introduction

Wire arc additive manufacturing (WAAM) is gaining popularity for small batch manufacturing of medium- to large-scale components in aerospace, automotive, military and energy industries [1–4]. WAAM relies on the sequential deposition of layers in open air or in a controlled chamber using a wire consumable, an electric arc aided with shielding gas, and a manipulator such as a robotic arm or gantry machine under precise control of computer system. A wide variety of wire feedstock is available in the market for WAAM depositing complex components made from steel [5], aluminium [6], titanium alloys [7], tungsten [8], tantalum [9], nickel superalloys [10] and functionally graded materials [11]. WAAM is well suited for industrial applications [12–16] thanks to its high deposition rate (up to 10 kg/h for steel), reduced manufacturing time, enhanced design flexibility, low buy-to-fly ratio, and low operational and build-up cost associated with welding

and robotic equipment. In addition, WAAM is more environmentally friendly than other powder-based Additive Manufacturing (AM) processes [17].

The arc heat source utilised in WAAM causes local heating and uneven thermal expansion in the deposit and surrounding material. Consequently, local plastic deformation occurs as the material is susceptible to yielding at high temperatures. During cooling, the deposited hot material tends to shrink, but the surrounding colder material constrains the thermal shrinkage. The mismatch in the process-induced permanent deformation accumulated between different regions gives rise to residual stress (RS) [18]. Distortion and RS are the main technical challenges facing WAAM for wider applications in the industry [5]. Excessive distortion causes process instability and makes the WAAM component unsuitable for assembly or service, whilst RS can significantly degrade fatigue performance, induce brittle fracture and reduce the corrosion resistance of the built component [19–22].

Several techniques have been proposed to mitigate RS and distortion during deposition of WAAM components, such as in-process rolling [5], induction assisted WAAM process [23], symmetrical printing, back-to-back building, and combining deposition of shorter layers [13]. In addition, optimisation of process parameters and development of optimal tool path could also reduce RS and distortion in WAAM [24,25].

High-pressure rolling has been extensively studied in experiments by researchers at Cranfield University for reducing RS and distortion in WAAM [5,7,26–28]. Colegrove et al. [5] proposed the application of inter-layer rolling for mitigation of RS and distortion in steel WAAM components, and both profiled roller (i.e., roller with concave contact surface) and slotted roller were used in their research. They investigated several rolling strategies, including inter-layer rolling, rolling every four deposited layers and rolling only on the last deposited layer (i.e., post-build rolling). They found that rolling can reduce the peak tensile RS at the interface between the wall and substrate and mitigate final distortion. Interestingly, the slotted roller was found more effective in reduction of RS and distortion.

Martina et al. [7] and Colegrove et al. [28] reported a significant reduction of RS and distortion in inter-layer rolled Ti-Al-6V WAAM components. Application of “inverted” roller (roller with convex profile) to Ti-6Al-4V WAAM intersections was studied by Hönnige et al. [27]. However, inter-layer rolling did not affect RS distribution in the intersection, presumably because the inherent thermal deposition cycle had a stronger influence than the in-process rolling had on the final RS state. Some experimental results also showed that rolling enabled microstructure refinement in inter-layer rolled WAAM components [5,28–31].

Despite the advantages found in experiments as mentioned above, inter-layer rolling of WAAM still faces several practical challenges. For instance, the rolling of each layer takes significant time, and in previous experiments, the rolling commenced only when the deposit cooled below 50 °C [5]. In addition, the slotted roller required application of lubricant before rolling of each layer, followed by degreasing [5]. All these operations remarkably increased manufacturing time. Process optimisation is hence needed to improve manufacturing efficiency, which requires a thorough understanding of the mechanisms of RS and distortion mitigation.

The finite element method (FEM) was successfully applied for the simulation of rolling [32,33], which helps obtain valuable information to understand the mechanism while minimising experimental time and cost. Unfortunately, the modelling of inter-layer rolling for WAAM components has not been reported in the literature. One main challenge faced here is the high computational cost of a rolling model coupled with WAAM deposition. For example, to obtain a solution for single-pass high-pressure rolling simulation in a 456 mm long component took up to 95 hours using High-Performance Computing (HPC) facility [34]. In real engineering scenario, WAAM built components can be several meters long and can comprise a large number of deposited layers, meaning that inter-layer rolling simulation could take weeks to complete for just one analysis case. To overcome the computational challenge, recently Gornyakov et al. [35] developed efficient modelling based on reduced-size steady-state rolling models [35] and thermal-mechanical solution mapping technique [36], presented in Chapters 4 and 5.

For simulation of post-build rolling, Gornyakov et al. [37] (Chapter 6) investigated the formation of plastic strain (PS) and RS in both unrolled and rolled states for a WAAM deposited wall and thereby elucidated the mechanism of WAAM RS and distortion mitigation by the post-build rolling (Chapter 6). Abbaszadeh et al. [38] and Tangestani et al. [39] studied the influences of roller design, rolling load and other process parameters on RS and PS distribution. These studies on post-build rolling could be helpful for gaining insights, but inter-layer rolling exhibits a more complicated cyclic PS and RS formation mechanism caused by alternating deposition and rolling.

The present study is aimed to reveal the mechanism for mitigating RS and distortion by inter-layer rolling of a WAAM deposited wall and to optimise the rolling strategy for large-scale AM. The hybrid process of WAAM and rolling is simulated using an efficient coupled model. Different roller designs and rolling strategies are examined and evaluated to improve the effectiveness and efficiency of rolling for WAAM components.

7.2 Materials and methods

7.2.1 Experiments

The WAAM component studied here was deposited and inter-layer rolled in a previous experiment [5]. Twenty layers with dimensions of 490 mm x 5 mm x 2 mm for each layer were deposited to build a wall with the aid of a Cold Metal Transfer (CMT) process using 0.8 mm Lincoln Electric SupraMIG G3Si1/ER70S-6 wire. Mild steel (grade S355JR-AR) plate with dimensions of 500 mm x 60 mm x 12 mm was used as the substrate. The CMT deposition was carried out with a travel speed of 500 mm/min, a wire feed speed of 10 m/min, a contact tip-to-workpiece distance of 13 mm (the torch was perpendicular to the workpiece). The shielding gas was Ar 80% /CO2 20% with a flow rate of 20 l/min. Six clamps were used to restrain the substrate during the WAAM deposition. Inter-layer rolling was conducted by controlling the vertical load and moving the roller without application of torque. The sketch of the equipment used for the WAAM deposition and rolling, as well as clamps locations, are presented in Figure 7-1.

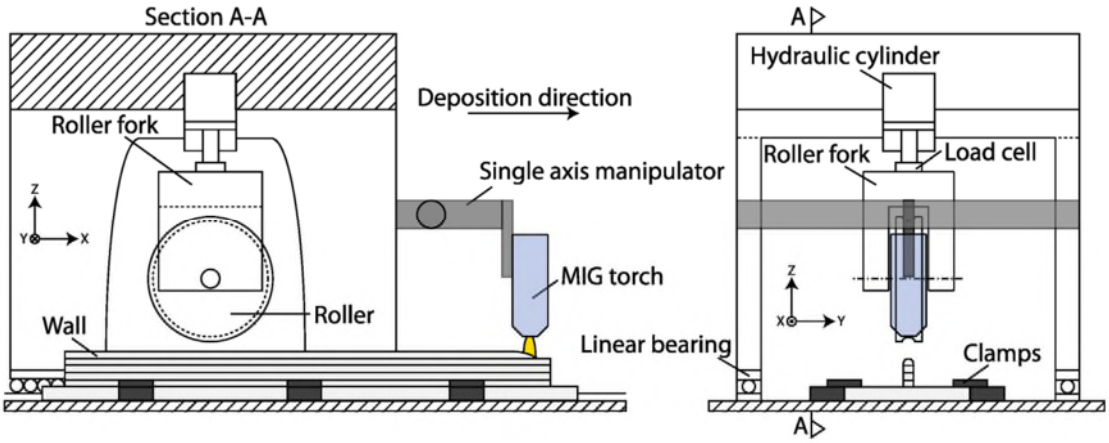

Figure 7-1 Schematic representation of equipment for WAAM deposition and rolling [5].

Both profiled and slotted rollers were used, and the inter-layer rolling commenced when the deposit cooled down to 50 °C. For the slotted roller, the rolling was not started until the deposited wall reached a height larger than the depth of the slot of the roller, which was the height of six layers. A lubricant was applied to the deposited wall before each run of rolling with the slotted roller, which was then degreased before depositing a new layer on the rolled deposit. The neutron diffraction method was employed to measure the RS after clamps were removed from the substrate. The out-of-plane distortion was measured along the bottom line of the substrate after removal of clamps. Details of the experiments can be found in Ref. [5].

7.2.2 Short thermal model of WAAM deposition

A short thermal multi-layer model was used to obtain the steady-state solution of the transient temperature field during WAAM deposition [36] (the paper is part of the outcome of this PhD research) (Figure 7-2). Refer to Chapter 5. The length of the modelled component was reduced to 72 mm to increase computational efficiency. This length is sufficient for the WAAM process to reach a steady-state and the short model predicts a temperature field consistent with the full-length thermal model [36]. Goldak's double-ellipsoidal heat source model was used to represent the power input [40] and the heat source parameters were adopted from Ref. [41]. The addition of material was simulated by sequential activation of

the whole layer for each deposition. The thermal model has been validated against temperature measurements using thermocouples (Chapter 5 and Ref. [36]).

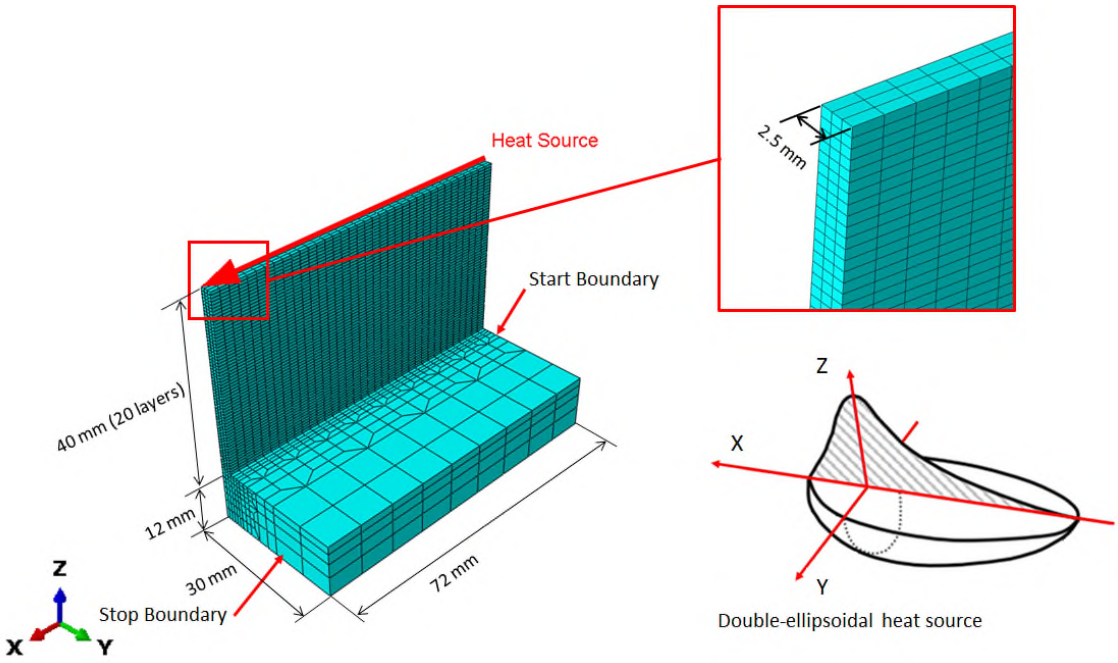

Figure 7-2 Short multi-layer thermal model for the WAAM process (only half part is modelled due to symmetry).

7.2.3 Short mechanical model of multi-layer deposition and rolling

7.2.3.1 Overview of the models

Figure 7-3 presents the short mechanical model of multi-layer deposition and rolling of WAAM component with reduce length of 72 mm. As demonstrated in Ref. [35,36] and in Chapters 4 and 5, the short mechanical model significantly reduced computational cost without impairing the accuracy of the steady-state solution and the adopted length is sufficient to achieve a steady state for WAAM deposition and rolling. In the WAAM model, the PS and RS were generated due to the mechanical response to the thermal expansion and contraction of the material, and all nodes of the WAAM model were assumed to be constrained in the longitudinal direction during the deposition step to counteract the underestimated constraint as a result of the reduced component length [36], and the longitudinal constraint was relaxed except the end surfaces during the rolling

step. The mechanical model of WAAM deposition was validated against the experimental results of RS and distortion [36] (the paper is part of the outcome of this PhD research). The details of the mechanical model for WAAM deposition can be found in Ref. [36]. Refer to Chapter 5.

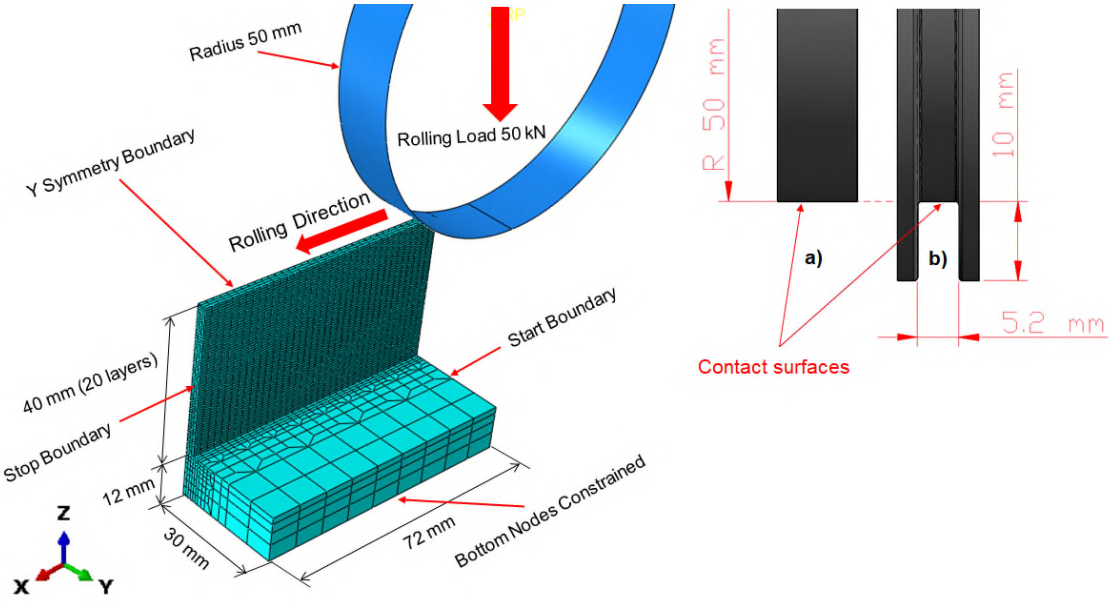

Figure 7-3 Left: short mechanical model of multi-layer WAAM deposition and rolling (only half part is modelled due to symmetry); Right: design of a) flat and b) slotted rollers.

An accurate simulation of the clamps is necessary for the prediction of RS distribution and distortion [5]. Due to the incomplete length of the short model, a simplified clamping simulation was implemented. All nodes at the bottom of the substrate were constrained against movement in all directions.

General purpose FEM software Abaqus was employed for the simulations. The mechanical models were meshed using 9036 C3D8R 8-node linear brick elements and the mesh density was same as the thermal model. Graded meshing technique was used, i.e., the element dimensions vary from being relatively small in the wall (2 mm x 0.833 mm x 0.667 mm) to being relatively large (8 mm x 7.5 mm x 1.765 mm) in the substrate. A sensitivity analysis showed that an increase of the mesh density in the rolling contact region does not affect the solution.

7.2.3.2 Coupling between WAAM deposition and rolling

In previous models of post-build rolling (Chapter 6 and Ref. [37] (the paper is part of the outcome of this PhD research)), the simulations of WAAM deposition and rolling were not fully coupled, i.e., the rolling model used WAAM model prediction as initial condition, while the WAAM model was independent of the rolling model. Such an approach is beneficial for computational efficiency. For the inter-layer rolling studied here, both uncoupled and coupled rolling models were developed and compared to examine the effects of coupling on the prediction accuracy and on the potential decoupling simplification to save computational cost. The coupling, in the context of this research, means that for each layer the solution of the rolling model is dependent on the solution of the WAAM deposition model, and vice versa. In the uncoupled model, the RS and PS distributions, as predicted by the short mechanical model of the WAAM deposition (Chapter 5 and Ref. [36]), were transferred to the short multi-layer rolling model, using the solution mapping technique (Chapter 5 and Ref. [36]), but the rolling model solution was not incorporated in the WAAM deposition model and thus the deposition model was independent of the rolling model. Both the uncoupled and coupled models consist of the following simulation steps for each layer: new layer activation, thermal deposition cycle, roller placement, roller indentation and rolling.

7.2.3.3 Roller design and assumptions

Design of flat and slotted rollers is presented in Figure 7-3. The roller was simplified as an analytic rigid shell. For the given rolling load, the application of deformable elastic roller does not affect the solution in 3D [38] and 2D [35] models, Chapter 4. The flat roller in the model was used to represent the profiled roller in the experiment [5] to improve computational efficiency. Previous studies [37] (the paper is part of the outcome of this PhD research) demonstrated that a flat roller model with a roller-to-wall friction coefficient no less than 0.5 predicted RS and PS distributions similar to those predicted by a profiled roller model, refer to Chapter 6. Although the profiled and slotted rollers used in the experiment [5] had radiused contact surfaces, the contact surfaces are assumed to be flat in the models. Application of a radiused roller would require a finer mesh in the contact

region, which will drastically increase computational cost. According to Abbaszadeh et al. [38] and Tangestani et al. [39], the variation of roller radius (or roller curvature depth) only minorly affected PS and RS distributions in the WAAM wall.

7.2.3.4 Rolling simulation and contact interaction

Penetration of the roller to the wall during the rolling step was simulated through controlling displacement; the reduced length in the short model was insufficient for simulation of transitional processes taking place during load-controlled analysis. To reach the prescribed rolling load, values of displacement for each layer were found iteratively. The rolling load was defined as the normal reaction force on the pivot of the roller. Moving reaction force was caused by the translational movement of the roller along the wall. The roller rotated freely due to friction between the roller and the wall. Node-to-surface contact interaction was specified between the flat roller surface and the top surface of each layer. A friction coefficient of 0.5 was assumed in the model with the flat roller, which is typical for an unlubricated contact with steel, as suggested by Cozzolino et al. [34] and Coules et al. [42]. In the model with the slotted roller, the contact surfaces include the roller surface, and the side and top surfaces of the wall. A friction coefficient of 0.1 for lubricated contact was used to simulate the friction effects for the slotted roller, which was also adopted in previous studies [43–46].

7.2.3.5 Material properties

Layer by layer thermal solution produced by coupled WAAM model used to generate initial PS and RS distribution in short mechanical multilayer deposition and rolling model. RS formed as a response of the material on the thermal expansion/contraction and plastic yielding of material at high temperatures restricted by boundary conditions. Steep thermal gradients produced by WAAM model requires temperature-dependent material properties for accurate simulation of WAAM RS and PS. Temperature-dependent elastic-plastic properties of S355 mild steel were adopted from the dataset reported by Thompson et al. [47] (

Table 7-1, Table 7-2,

Table 7-3 and Table 7-4).

Table 7-1 Temperature-dependent thermal expansion coefficient [47].

Temp. (°C)	Thermal expansion coefficient (1/°C)	Temp. (°C)	Thermal expansion coefficient (1/°C)
20	1.22E-05	800	1.14E-05
100	1.22E-05	850	1.17E-05
200	1.27E-05	900	1.21E-05
300	1.35E-05	1000	1.27E-05
400	1.41E-05	1100	1.33E-05
480	1.33E-05	1200	1.39E-05
540	1.20E-05	1300	1.45E-05
600	1.11E-05	1400	1.50E-05
700	1.07E-05		

Table 7-2 Temperature-dependent Young's Modulus and Poisson's ratio [47].

Temp. [°C]	Young's Modulus [GPa]	Poisson's ratio
25	202	0.3
90	200	0.31
150	198	0.32
300	197	0.35
450	136	0.375
600	65	0.4
700	40	0.42
750	35	0.43
900	20	0.46

1050	10	0.48
1200	10	0.48
1350	10	0.48

Table 7-3 Temperature and plastic strain dependent yield stress of deposit [47].

Temp. [°C]	Plastic strain	Yield stress deposit, [MPa]	Temp. [°C]	Plastic strain	Yield stress deposit, [MPa]
20	0	440	600	0	250
20	0.04	550	600	0.02	310
20	0.12	615	600	0.11	360
20	0.51	676	600	0.55	440
200	0	355	700	0	90
200	0.03	488	700	0.04	170
200	0.29	675	700	0.21	250
200	0.54	740	700	0.56	305
400	0	405	800	0	50
400	0.02	530	800	0.09	82
400	0.06	580	800	0.58	135
400	0.55	640	950	0	86
500	0	360	1100	0	70
500	0.02	432	1200	0	40
500	0.1	500	1300	0	18
500	0.55	575	1400	0	10

Two sets of Yield stress material properties were used for the wall deposit (Table 7-3) and the substrate (Table 7-4), respectively. The yield strength of the deposit, as suggested by Thompson et al. [47], is relatively low (390 MPa), while according to the material certificate of the consumed ER70-S6 wire [5], the minimum yield strength is greater than 502 MPa. In most cases the magnitude of tensile RS reached the yield strength of the material [48]. Colegrove et al. [5] measured a

tensile longitudinal RS of 600 MPa at the interface between the WAAM wall and the substrate. Therefore, to obtain more realistic simulation results, the yield strength of the modelled wall deposit was increased by 50 MPa at the temperature of 20 °C, relative to the material data reported by Thompson et al. [47]. Annealing effect of layer-by-layer WAAM deposition on PS in underlaid layers simulated by the relaxation of the PS history at temperatures above 950 °C. No strain hardening occurred above this temperature.

Table 7-4 Temperature and plastic strain dependent yield stress of substrate [47].

Temp. [°C]	Plastic strain	Yield stress substrate, [MPa]	Temp. [°C]	Plastic strain	Yield stress substrate, [MPa]
20	0	390	600	0	250
20	0.04	500	600	0.02	310
20	0.12	565	600	0.11	360
20	0.51	626	600	0.55	440
200	0	355	700	0	90
200	0.03	488	700	0.04	170
200	0.29	675	700	0.21	250
200	0.54	740	700	0.56	305
400	0	405	800	0	50
400	0.02	530	800	0.09	82
400	0.06	580	800	0.58	135
400	0.55	640	950	0	86
500	0	360	1100	0	70
500	0.02	432	1200	0	40
500	0.1	500	1300	0	18
500	0.55	575	1400	0	10

7.2.3.6 Category of models and rolling strategy

The models were divided into two sets (Table 7-5). The models in Set 1 were used for validation and investigation of PS and RS evolution during WAAM deposition and inter-layer rolling. The models in Set 2 were used for optimisation of the rolling strategy.

Table 7-5 Short mechanical models of multi-layer WAAM deposition and rolling

<table>
<tr><td></td><td>Roller shape</td><td>Rolling strategy</td><td>Purpose</td></tr>
<tr><td rowspan="3">Set 1</td><td>Flat roller for uncoupled WAAM deposition and rolling model #</td><td rowspan="3">Inter-layer (IL)</td><td rowspan="3">Model validation and process investigation</td></tr>
<tr><td>Flat roller</td></tr>
<tr><td>Slotted roller</td></tr>
<tr><td rowspan="6">Set 2</td><td>Flat roller</td><td rowspan="2">Every 4 deposited layers – (Stacked 4L)</td><td rowspan="6">Optimisation of rolling strategy</td></tr>
<tr><td>Slotted roller</td></tr>
<tr><td>Flat roller</td><td rowspan="2">Every 10 deposited layers – (Stacked 10L)</td></tr>
<tr><td>Slotted roller</td></tr>
<tr><td>Flat roller</td><td rowspan="2">Post-build – (PB)</td></tr>
<tr><td>Slotted roller</td></tr>
</table>

Except for this model, all other models are fully coupled between WAAM deposition and rolling.

7.2.4 Long mechanical model

The short mechanical model of WAAM deposition and rolling cannot predict the RS distribution and distortion in the full-length WAAM component after removal of clamps. To overcome this limitation, a long mechanical model was used to investigate the response of large WAAM component to the clamps removal.

The long mechanical model has the same mesh density, material properties and dimensions as the short mechanical model (except the full length of 500 mm being consistent with the experiment [5]). The long mechanical model allowed the simulation of the clamping and boundary conditions equivalent to the experiment [5]. The steady-state solution mapping technique (Chapter 5 and Ref. [36]) was used to transfer the RS and PS solution from the short mechanical model of

WAAM deposition and rolling to the long mechanical model. The long mechanical model is described in greater detail in Chapter 5 and Ref. [36].

7.2.5 Computational efficiency

HPC facility was employed to obtain the solution of the 20-layer WAAM deposition and rolling models. The short model with the flat roller took 8 hours 37 min of wall clock time to complete the computation using 16 CPUs. The short model with the slotted roller needed 14 hours 35 min. Conventional single-layer rolling simulation for a 500 mm long WAAM component took 4 hours 26 min to obtain the solution [35]. As a simulation of 20-layer rolling on a 500 mm long WAAM component would take 20 times longer than the single-layer rolling model, it can be estimated that the short mechanical model of the WAAM deposition and inter-layer rolling is 89% more efficient than the conventional full-size rolling model. The long mechanical model with steady-state solution mapped from the short model is highly efficient and the computational time was 6 min 43 sec using 2 CPUs.

7.2.6 Inspection plane and validation approach

The inspection plane in the short inter-layer rolling model is located 48 mm away from the start boundary in the longitudinal direction. This is the region where the model reached a steady-state. For the long model the inspection plane is in the mid-length of the component. Longitudinal RS and PS distributions were obtained along the vertical path in the symmetry plane of the WAAM wall (Figure 7-4).

To validate the inter-layer rolling model, the predicted longitudinal RS distribution and wall dimension in the inspection plane were compared to experimental measurement by Colegrove et al. [5]. The magnitude of distortion was also compared between the prediction and the measurement [5].

7.3 Results

7.3.1 Key features of predicted RS and distortion

7.3.1.1 Short mechanical models of WAAM deposition and inter-layer rolling

Figure 7-4 shows contour maps of longitudinal RS distributions after the WAAM deposition without rolling and the WAAM deposition + IL rolling with flat and slotted rollers. In the clamped condition, the WAAM deposition generated evenly distributed tensile RS in the wall and the substrate immediately underneath the wall. Counterbalancing compressive RS of lower magnitude formed in the remaining region of the substrate. Most significant longitudinal RS (609 MPa) was generated on the border between the wall and substrate. The IL rolling with the flat roller significantly reduced the magnitude of tensile RS in the wall and the substrate (RS: 232 - 169 MPa), and formed a compressive RS region 2 mm below the last rolled layer (RS: —337 MPa). The IL rolling with the slotted roller substantially reduced the magnitude of tensile RS in the wall (RS: 138 - −56 MPa) and generated a more extensive region with compressive RS (−324 MPa) under the rolled surface.

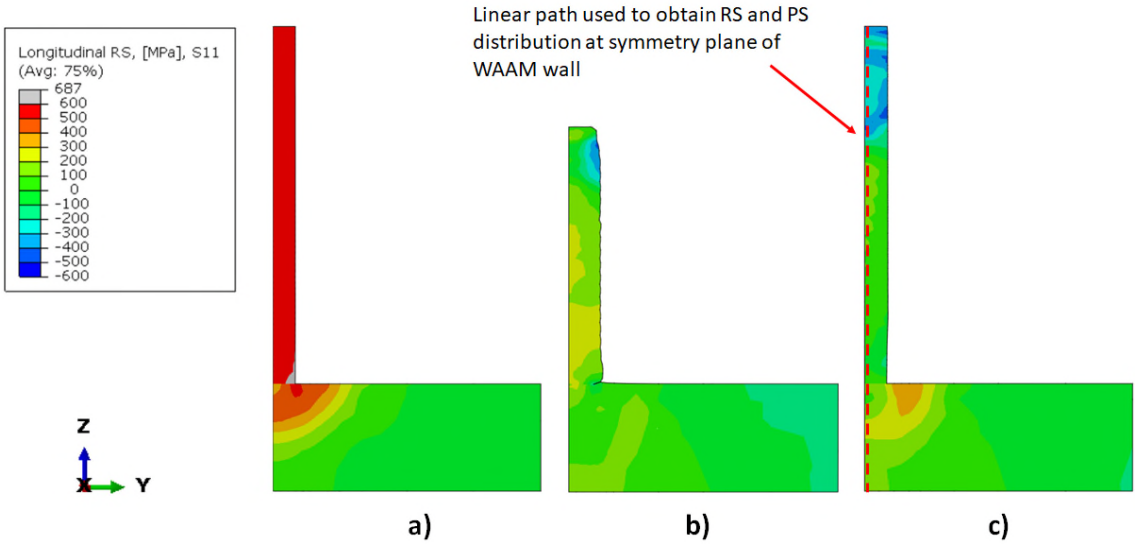

Figure 7-4 Longitudinal RS distribution in WAAM deposited wall under the clamped condition: a) after WAAM without rolling, b) after IL rolling with the flat roller, and c) after IL rolling with the slotted roller.

7.3.1.2 Long mechanical model

Figure 7-5 and Figure 7-6 show the 3D distributions of RS and the deformed configuration in the long mechanical models before and after removal of clamps, respectively. After steady-state solution was mapped, the absence of the longitudinal constraints in the long model caused the magnitude of RS to reduce at the two ends of the WAAM wall (Figure 7-5a). After clamps removal, a relaxation of tensile RS in the wall caused the component to bend upwards (concave upwards), Figure 7-6a). The magnitude of tensile RS (20 - 206 MPa) reduced largely in the wall, as compared to the RS in the clamped condition (600 MPa), and it even converted to compressive RS (−200 MPa) at the top of the wall, but the tensile RS (488 MPa) remained high on the border between the wall and the substrate.

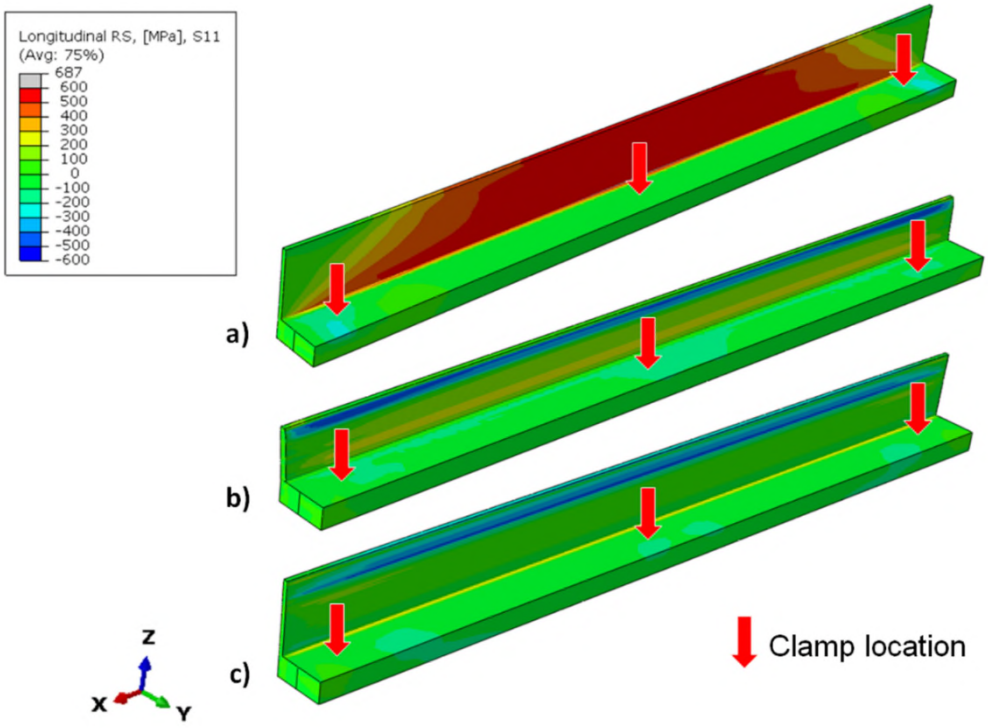

Figure 7-5 Longitudinal RS distributions and deformed configurations before clamps removal: a) WAAM without rolling, b) WAAM + IL rolling with the flat roller, c) WAAM + IL rolling with the slotted roller (a deformation scale factor of 5 is used to aid visualisation).

For the WAAM + IL rolling model with the flat and slotted rollers, a minor redistribution of longitudinal RS occurred in the long model under the clamped condition, after the steady-state solution was mapped from the short model, Figure 7-5 b) and c). For the IL rolling with the flat roller, the clamps removal caused the component to slightly bend upwards and the compressive RS in the region under the rolled surface increased in magnitude (from – 328 to – 494 MPa), Figure 7-6 b). In contrary, the component that was IL rolled with the slotted roller slightly bent downwards. As a result, the magnitude of compressive RS under the rolled surface reduced (from −470 to −370 MPa) (Figure 7-6 c).

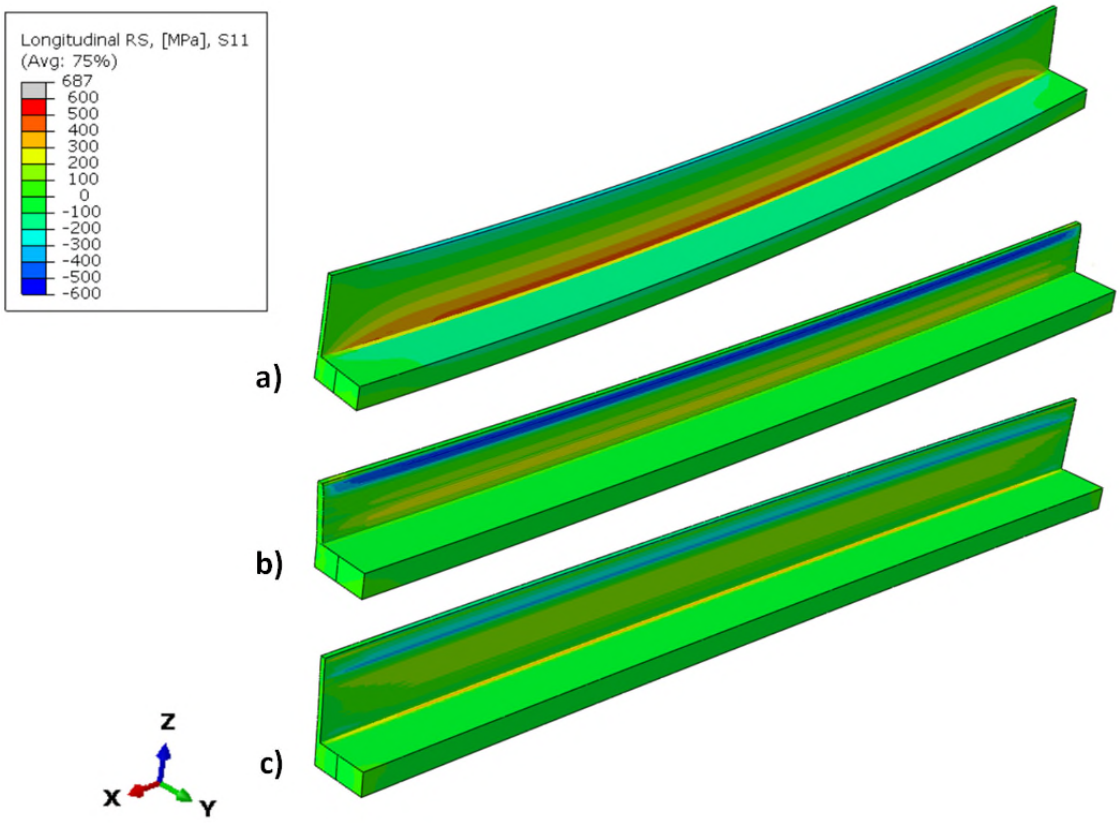

Figure 7-6 Longitudinal RS distributions and deformed configurations after clamps removal: a) WAAM without rolling, b) WAAM + IL rolling with the flat roller, c) WAAM + IL rolling with the slotted roller (a deformation scale factor of 5 is used to aid visualisation).

7.3.2 Comparison with experimental results

Figure 7-7 a) shows a comparison of the longitudinal RS obtained from the long mechanical models after clamps removal, of which the steady-state solution was mapped from the coupled and uncoupled short WAAM + IL rolling models. The predictions are compared with experimental measurements [5]. The final RS distribution predicted by the coupled model is in overall good agreement with the experimental measurement. However, discrepancy was observed between the prediction and measurement in the region within a distance of 10 mm to the top of the wall. The mapped coupled model predicted compressive RS in this region, while tensile RS was obtained experimentally. The long mechanical model associated with the uncoupled short model significantly underpredicted the final RS, as compared to the experimental data. This indicates that a coupling model is essential for the simulation of the inter-layer rolling.

Figure 7-7b shows the longitudinal RS distribution predicted by the long mechanical model associated with the coupled model using the slotted roller, which is also compared to the experimental measurement [5]. The long model demonstrated a good correlation in the region from 10 to 28 mm through the wall height. However, the model underpredicted RS in the wall closer to the substrate and predicted local peaks of compressive and tensile RS near the top of the wall, while such peaks were not observed in experimental measurements [5].

The discrepancy between the prediction and measurement (Figure 7-7) could be partially attributed to the limitations of the neutron diffraction measurement technique [49]. It is well known that neutron diffraction measurement is sensitive to microstructure and its resolution is limited to the gauge volume adopted. Martina et al. [7] using the contour method obtained in the top layers of Ti-6Al-4V WAAM + IL rolled component RS distribution similar to predicted by model, Figure 7-7b. Given the complexity of the hybrid process, the accuracy of the model is deemed sufficient for the purpose of this study.

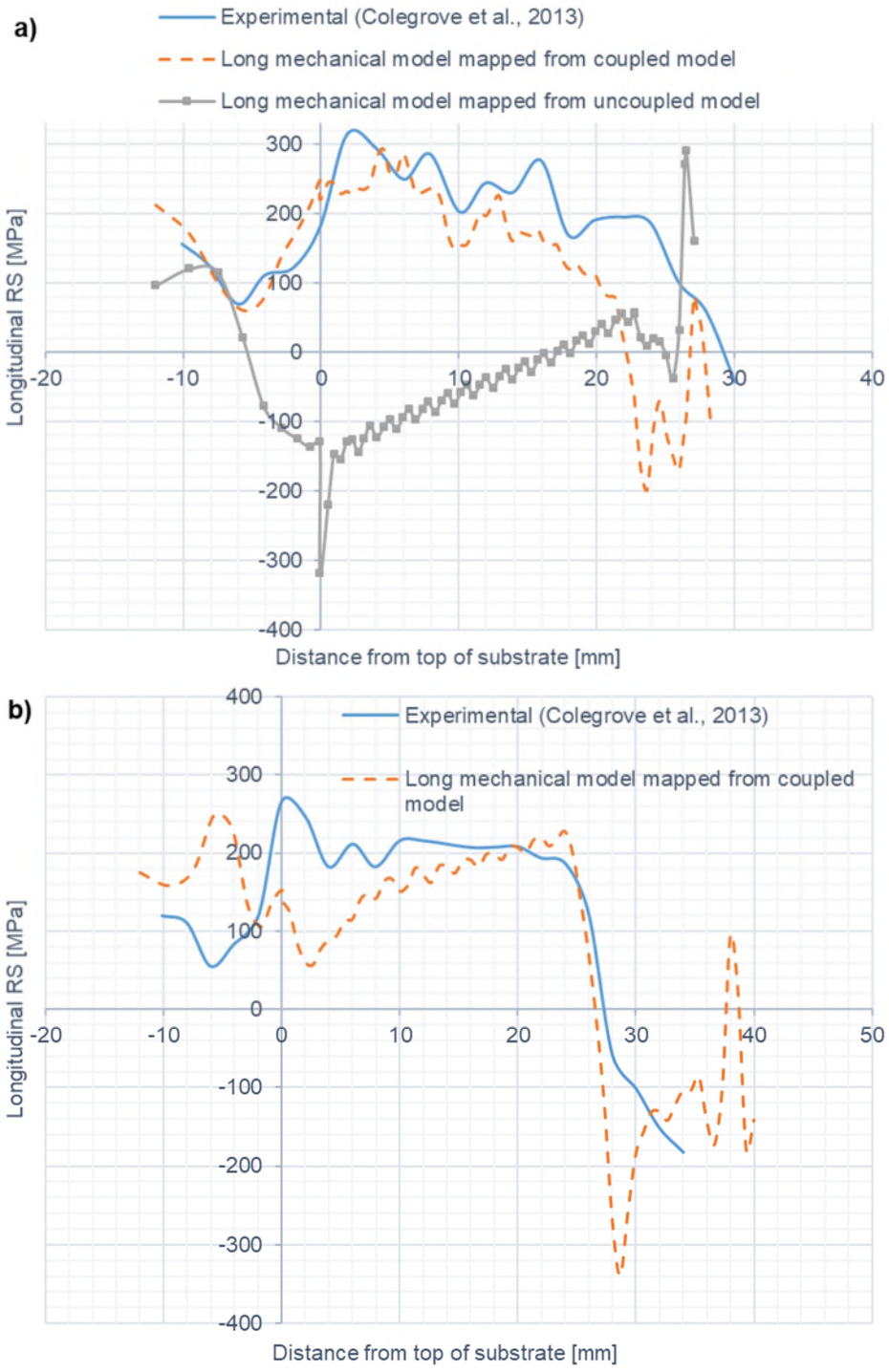

Figure 7-7 Longitudinal RS distributions predicted by the long mechanical models after clamps removal, as compared to experimental measurements [5]. The flat roller a) and slotted roller b) were used in the rolling simulations, and the long model was based on the steady-state solution mapped from the short WAAM + IL rolling model.

Figure 7-8 shows the deformed configurations of the wall on the cross-section. The predictions of the width and height of the rolled wall by the short IL rolling models are in good agreement with the observation in the macrographs [5]. The discrepancy between the predicted and measured widths of the rolled wall is 2.7 % and 0 % for the rolling with the flat roller and the slotted roller, respectively.

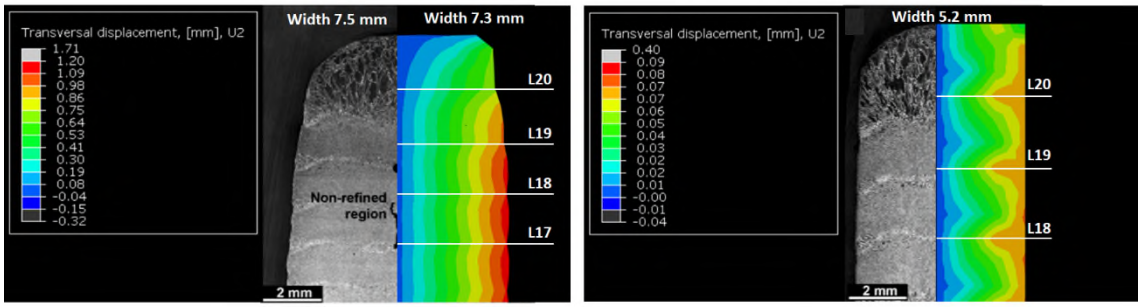

Figure 7-8 Comparison of the predicted configurations of the rolled wall with experimental observations in macrograph [5]: a) rolled with profiled roller in the experiment and flat roller in simulation, and b) rolled with slotted roller in both experiment and simulation. The predicted wall width and transversal displacement after rolling are also shown.

The predictions of rolled wall height also agree well with the experiments [5]. For the flat roller model, the predicted height is 28.48 mm, while the measured height is 28.0 ± 0.2 mm. The IL rolling with the slotted roller barely changed the wall height compared to the as-built condition. The height of the rolled wall is 39.8 mm predicted by the model, while it is 40 mm found experimentally.

Figure 7-9 shows the distortion predicted by the mapped long mechanical model after removal of clamps. In the experiment [1], only the magnitude of the distortion was measured; hence, the experimental measurement is not included in Figure 7-9. The long mechanical model underpredicted the magnitude of the distortion. For instance, the maximum out-of-plane distortion predicted by the long mechanical model in the as-built condition is 2.4 mm, compared to 6.7 mm in the measurement [1]. The maximum distortion predicted by the WAAM + IL model with the flat roller is 0.78 mm, while it is 2.6 mm found experimentally. For the slotted roller, a downward distortion of – 0.27 mm was predicted, while the

experiment showed an upward distortion of 1.2 mm. Despite the discrepancy in the magnitude of the distortion (potential causes of the discrepancy are discussed in Section 7.4.4), the IL rolling model correctly captured the trend observed in the experiment, i.e., the rolling reduced the WAAM distortion, and the slotted roller was more effective than the flat roller.

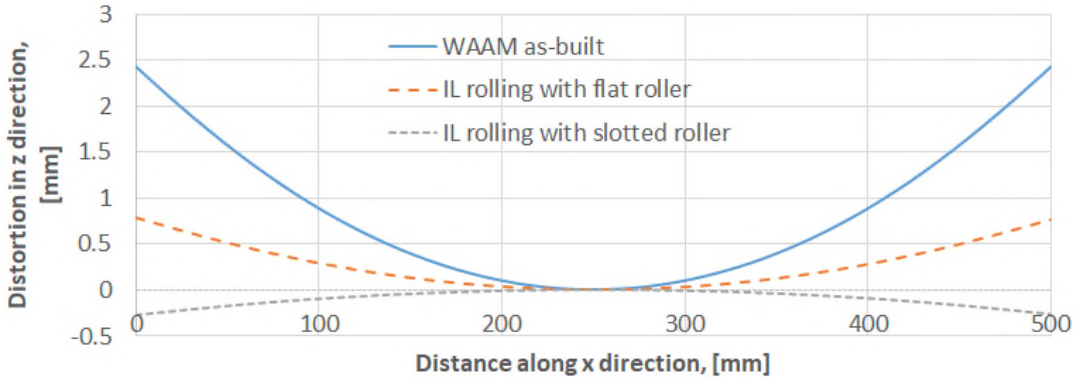

Figure 7-9 Predicted distortion of the WAAM component after removal of clamps in as-built condition without rolling, after IL rolling with the flat roller and after IL rolling with the slotted roller.

7.3.3 Stress and PS evolution during WAAM deposition and inter-layer rolling

Figure 7-10, Figure 7-11 and Figure 7-12 show the concurrent evolution of temperature, longitudinal stress and PS in layer 6 during the hybrid process of the WAAM deposition of layers 6-14 and the IL rolling with the flat roller. The layer 6 was selected for inspection since it is representative and subject to the minimal influence of the constraint caused by the substrate on the evolution of the inspected stress and PS in the WAAM wall.

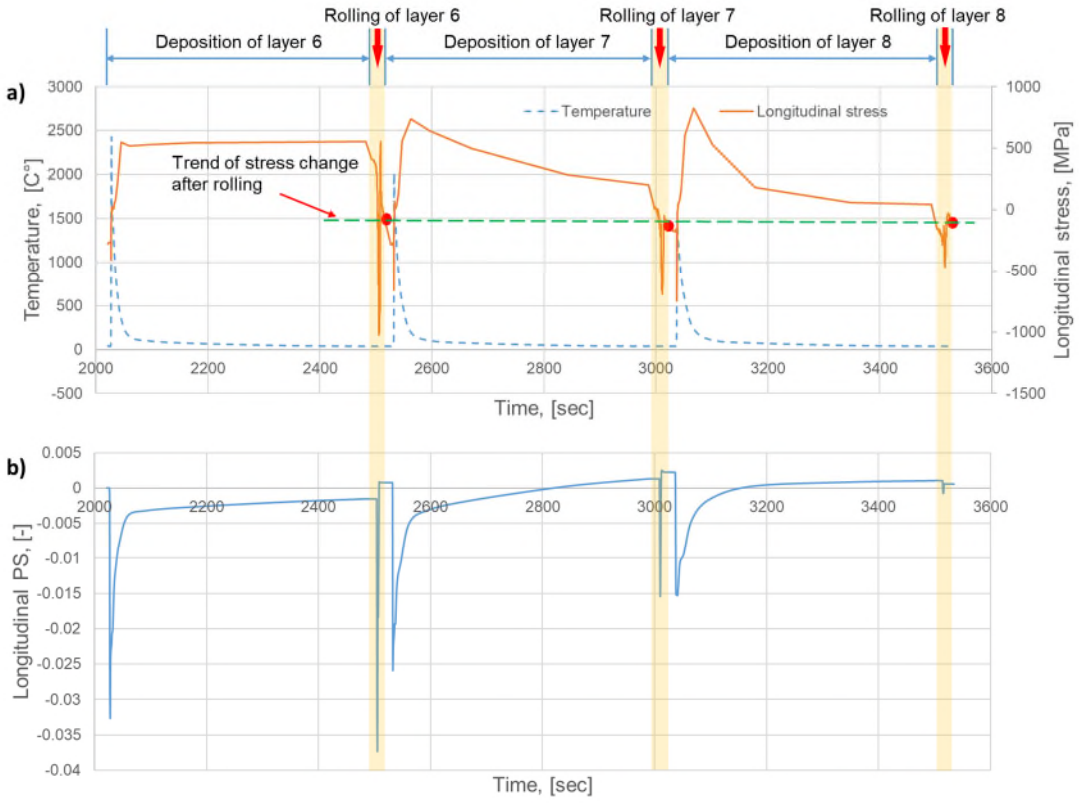

Figure 7-10 Concurrent evolution of temperature and longitudinal stress a), and longitudinal PS b), in layer 6 during WAAM deposition of layers 6-8 and IL rolling with the flat roller. The data were collected at the top of layer 6 in the inspection plane and the rolling phases are highlighted in the yellow shaded areas.

It is clearly seen from Figure 7-10 that tensile RS (550 MPa) formed in layer 6 after the layer was deposited, which accompanied the generation of compressive PS in the deposit. The subsequent rolling of layer 6 induced tensile PS and compressive RS (−280 MPa), and overall, the stress magnitude was lowered by the rolling. Figure 7-11 and Figure 7-12 show that the alternating deposition and rolling of layers 8-14 led to cyclic tensile stress re-formation and reduction in layer 6, which was caused by the WAAM deposition and rolling, respectively. As the peak temperature in layer 6 dropped from 2422 °C to 400 °C, the deposition of the layer 13 and subsequent layers did not further generate PS in layer 6. In other words, the subsequent alteration of stress became fully elastic. Similarly, the response of layer 6 to the IL rolling also became elastic after layer 09 was rolled, earlier than the termination of the deposition effect.

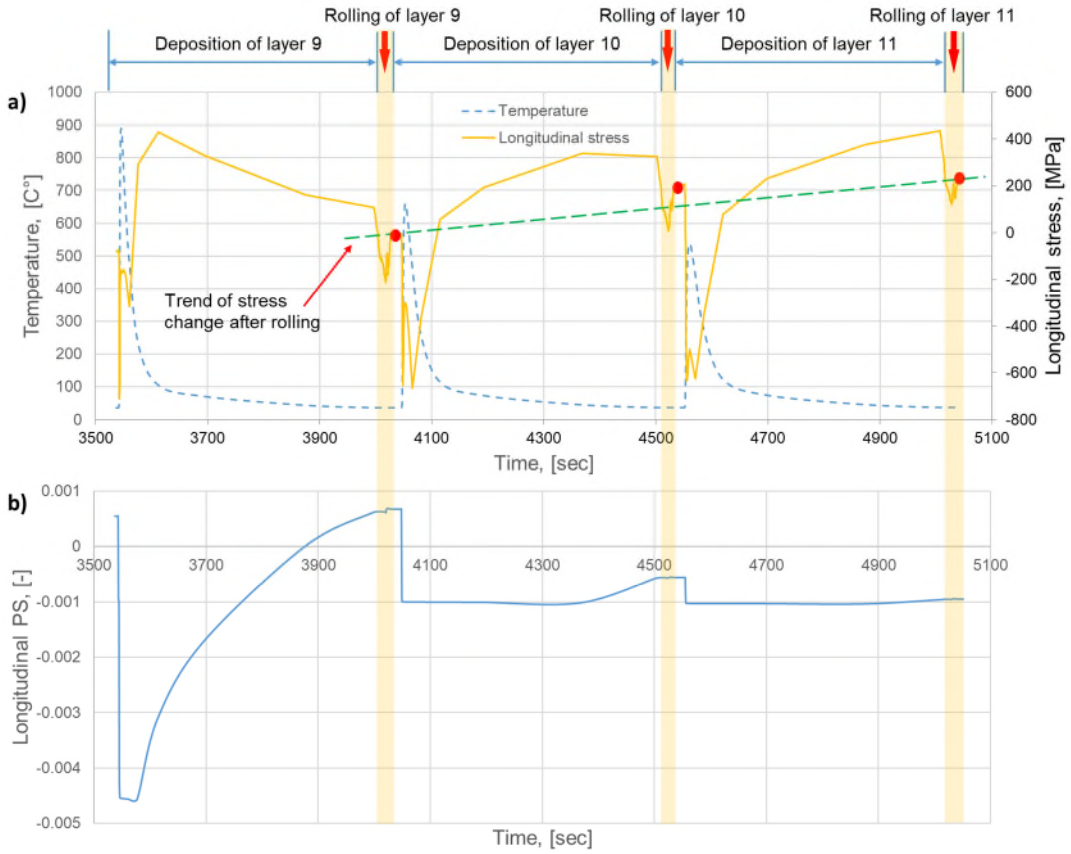

Figure 7-11 Concurrent evolution of temperature and longitudinal stress a), and longitudinal PS b), in layer 6 during WAAM deposition of layers 9-11 and IL rolling with the flat roller. The data were collected at the top of layer 6 in the inspection plane and the rolling phases are highlighted in the yellow shaded areas.

A trend in the change of the RS magnitude after each run of rolling is identified from Figure 7-10, Figure 7-11 and Figure 7-12 (refer to green dashed line for the trend). The magnitude of RS in layer 6 gradually increased after rolling of the layers 9-11. During rolling of layers 12-14, the magnitude of RS in layer 6 remained steady. Thanks to IL rolling with the flat roller, the initially formed tensile RS in layer 6, reduced from 550 MPa to 200 MPa.

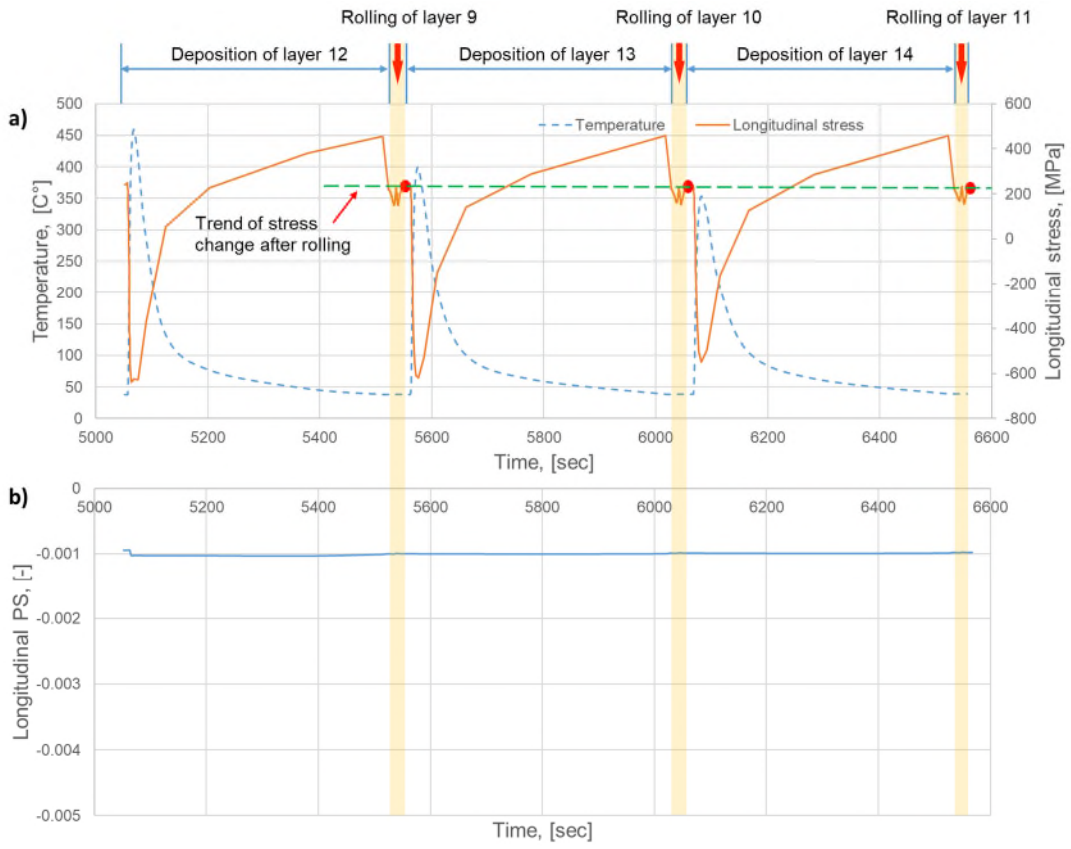

Figure 7-12 Concurrent evolution of temperature and longitudinal stress a), and longitudinal PS b), in layer 6 during WAAM deposition of layers 12-14 and IL rolling with the flat roller. The data were collected at the top of layer 6 in the inspection plane and the rolling phases are highlighted in the yellow shaded areas.

A similar evolution of longitudinal stress and PS in layer 6 was also found during the hybrid process of the WAAM deposition of layers 6-13 and the IL rolling with the slotted roller (Figure 7-13). The WAAM deposition and rolling processes caused alternating plastic flow in layer 6 during layer-by-layer deposition and rolling of layers 6-13. However, thanks to the rolling with the slotted roller, tensile RS in layer 6 was reduced from 500 MPa to −29 MPa.

Moreover, the IL rolling with the slotted roller was more effective to mitigate the WAAM RS than flat roller. The IL rolling with the slotted roller caused plastic flow in layer 6 during rolling of layers 6-13, while the IL rolling with the flat roller virtually did not affect PS in layer 6 during rolling of layer 10 and the subsequent layers.

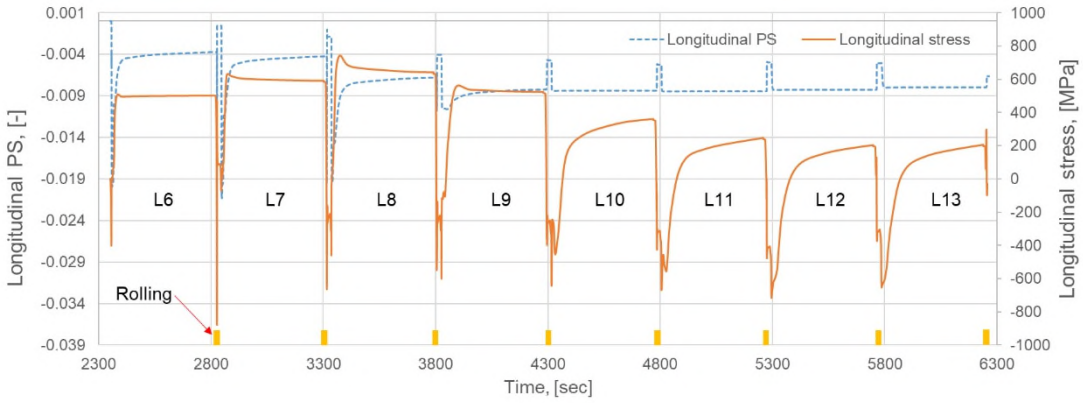

Figure 7-13 Concurrent evolution of longitudinal PS and stress in layer 6 during WAAM deposition of layers 6-13 and IL rolling with the slotted roller. The data were collected at the top of layer 6 in the inspection plane and the rolling phases are highlighted in the yellow shaded areas.

7.3.4 Comparison between different rolling strategies

To examine the potential improvement of manufacturing efficiency through reducing rolling runs, additional simulations were performed for rolling after WAAM deposition of several layers. Figure 7-14 compares the predicted longitudinal RS distributions after WAAM deposition without rolling, WAAM deposition plus IL rolling, stacked-layers rolling and post build (PB) rolling using the flat roller. These results were obtained from the inspection planes in the short mechanical models of multi-layer deposition and rolling.

The stacked 4L and 10L rolling strategies led to RS magnitude similar to IL rolling, and the effectiveness of mitigating WAAM deposition RS is also similar. The stacked 10L rolling generated local peaks of tensile RS in the middle of the wall and in the substrate. The PB rolling reduced the magnitude of WAAM deposition RS at the top of the wall. However, compared with the in-process rolling strategies, after the PB rolling more significant tensile RS remained in lower half of the wall and in the substrate immediately underneath the wall. It was also found that the more runs of rolling, the lower height of the rolled wall (Table 7-6).

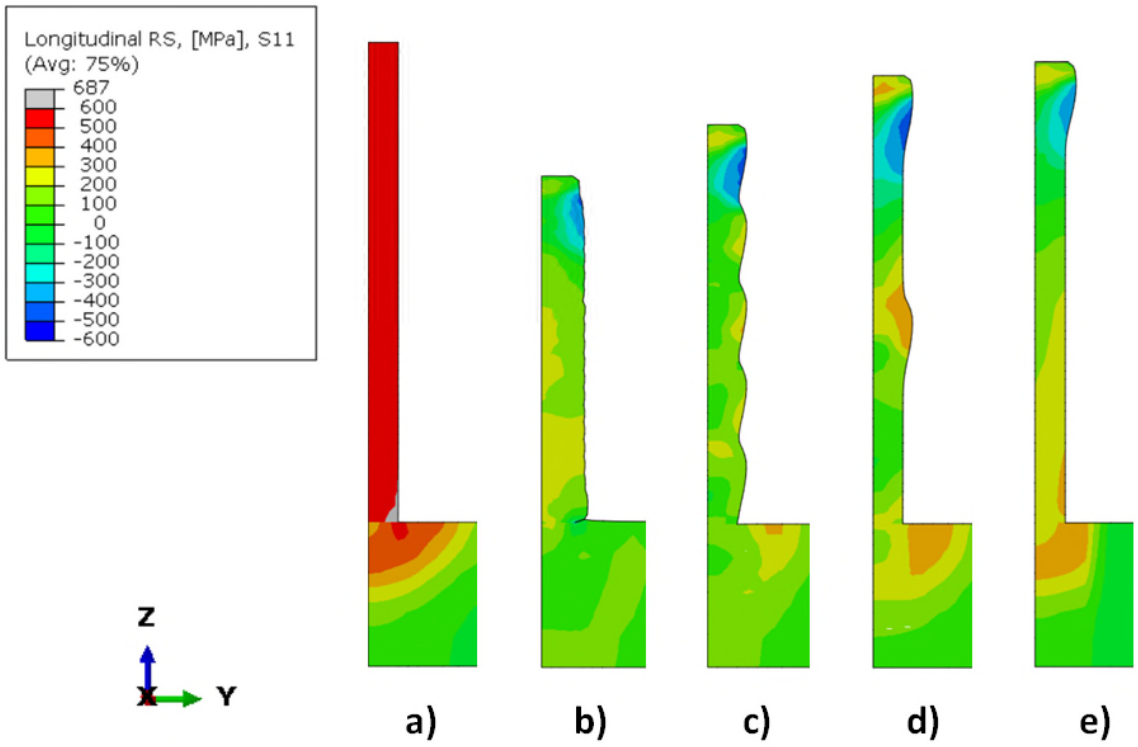

Figure 7-14 Comparison of longitudinal RS distributions in clamped condition: a) WAAM deposition without rolling, b) WAAM deposition + IL rolling, c) WAAM deposition + stacked 4L rolling, d) WAAM deposition + stacked 10L rolling, e) WAAM deposition + PB rolling. The flat roller was used in the rolling simulations.

Table 7-6 Wall height after WAAM deposition and rolling with the flat roller.

Rolling strategy	WAAM without rolling	WAAM + IL	WAAM + stacked 4L	WAAM + stacked 10L	WAAM + PB
Rolling runs	0	20	5	2	1
Height of the wall [mm]	40	28.48	33.49	37.36	38.36

Figure 7-15 compares longitudinal RS distributions in the inspection plane between WAAM without rolling, WAAM + IL rolling, WAAM + stacked-layers rolling and WAAM + PB rolling when the slotted roller was used in the rolling. All examined rolling strategies were found effective to mitigate the tensile RS in the WAAM deposited wall. The rolling with the slotted roller produced a more extensive compressive RS region than the flat roller (Figure 7-14). Only a minor

difference is seen when comparing the RS distributions in the IL and stacked 4L rolled WAAM walls. The stacked 10L rolling generated RS distribution overall similar to the IL rolling, but it gave rise to a peak of tensile RS (470 MPa) in the middle of the wall. After the PB rolling, the wall region close to the substrate remained being subjected to pronounced tensile RS (388 MPa). The height of the rolled wall changes marginally with increasing the number of rolling runs (Table 7-7).

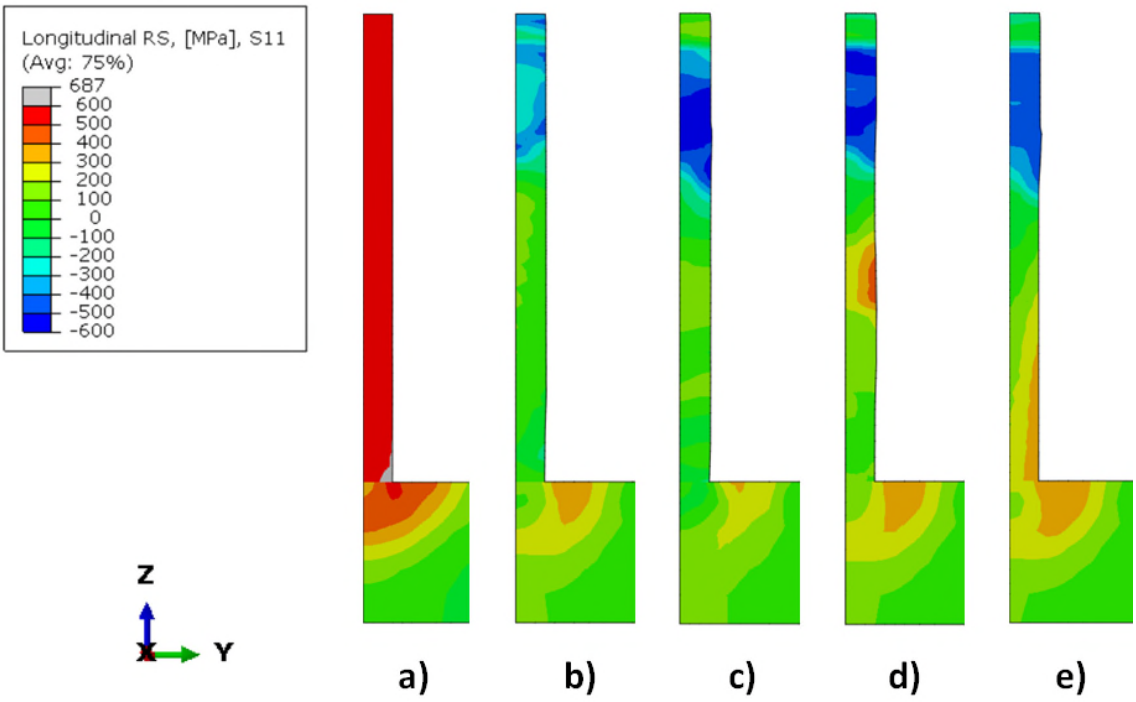

Figure 7-15 Comparison of longitudinal RS distributions in clamped condition: a) WAAM deposition without rolling, b) WAAM deposition + IL rolling, c) WAAM deposition + stacked 4L rolling, d) WAAM deposition + stacked 10L rolling, e) WAAM deposition + PB rolling. The slotted roller was used in the rolling simulations.

Table 7-7 Wall height after WAAM deposition and rolling with the slotted roller.

Rolling strategy	WAAM without rolling	WAAM + IL	WAAM + stacked 4L	WAAM + stacked 10L	WAAM + PB
Rolling runs	0	20	5	2	1
Height of the wall [mm]	40	39.84	39.64	39.32	39.63

7.4 Discussion

7.4.1 RS and distortion

7.4.1.1 Multi-layer deposition and rolling in clamped condition

The 50 kN IL rolling with the flat and slotted rollers effectively mitigated the longitudinal RS in the WAAM deposited wall under clamped condition (Figure 7-4). The RS mitigation can be attributed to the rolling-induced change in PS distribution. Figure 7-16 and Figure 7-17 show PS distributions after WAAM without rolling, WAAM + IL, WAAM + stacked 4L, WAAM + stacked 10L and WAAM + PB rolling with the flat and slotted rollers. The rolling induced tensile PS, which overall reduced or eliminated the WAAM-induced compressive PS and affected the RS distributions after the applied different rolling patterns.

As shown in Figure 7-14 and Figure 7-15, compared to the flat roller, the slotted roller produced smaller tensile RS in the lower part of the wall and larger compressive RS in the upper part of the wall. This difference can be attributed to the ability of the slotted roller to induce larger tensile PS in the wall (Figure 7-16 and Figure 7-17). The constraining effect of the slot sides on the wall eliminates transversal deformation and promotes longitudinal deformation during the rolling. This finding is in agreement with previous experimental [5] and numerical studies presented in Chapter 6 and Ref. Gornyakov et al. [37]. Conversely, the flat roller produced larger transversal deformation (Figure 7-8).

The RS distribution produced by the IL rolling with the slotted roller is more beneficial for the WAAM component than that produced by the IL rolling with the flat roller. The lower magnitude of tensile RS in the wall leads to lower distortion

after removal of clamps (Figure 7-9). Furthermore, the larger compressive RS near the top of the wall improves fatigue performance of the built component [50,51].

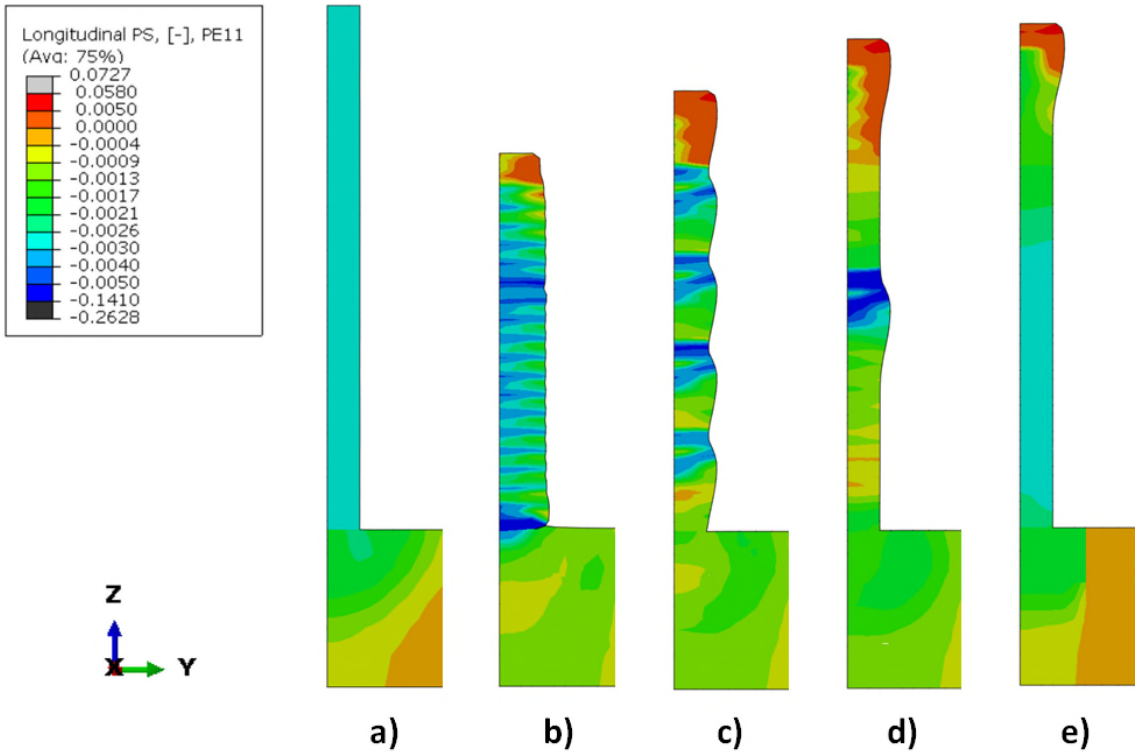

Figure 7-16 Comparison of longitudinal PS distributions in clamped condition: a) WAAM deposition without rolling, b) WAAM deposition + IL rolling, c) WAAM deposition + stacked 4L rolling, d) WAAM deposition + stacked 10L rolling, e) WAAM deposition + PB rolling. The flat roller was used in the rolling simulations.

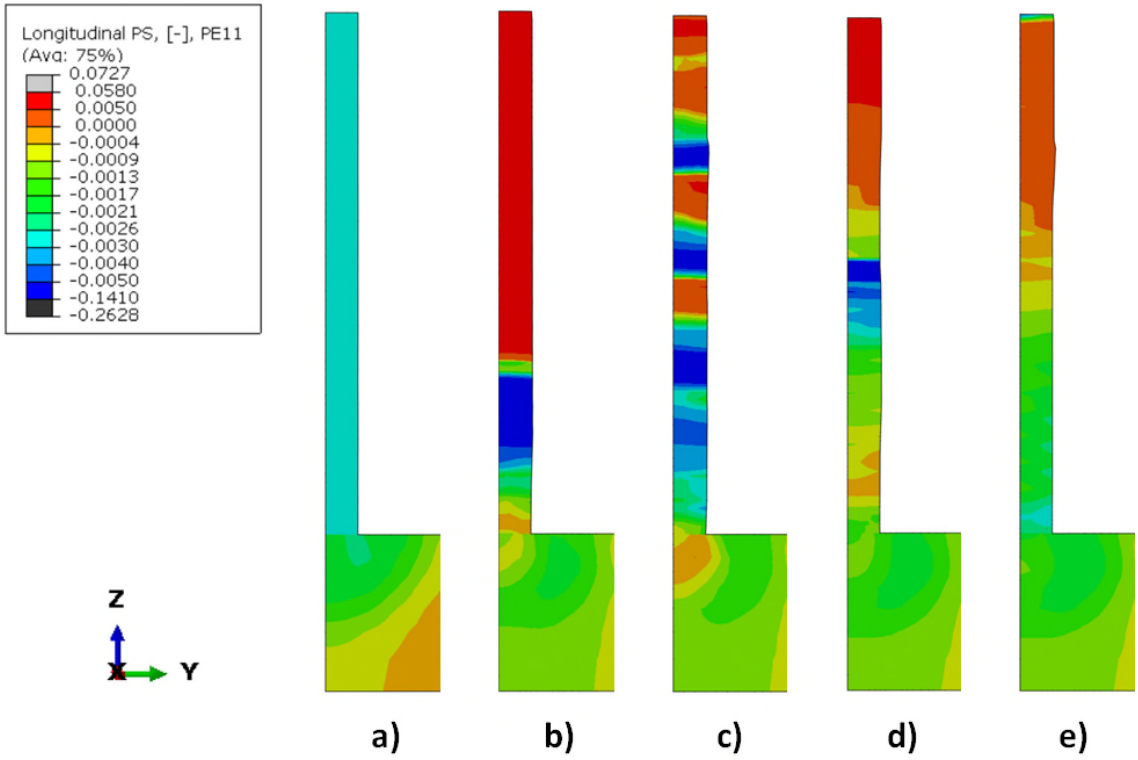

Figure 7-17 Comparison of longitudinal PS distributions in clamped condition: a) WAAM deposition without rolling, b) WAAM deposition + IL rolling, c) WAAM deposition + stacked 4L rolling, d) WAAM deposition + stacked 10L rolling, e) WAAM deposition + PB rolling. The slotted roller was used in the rolling simulations.

7.4.1.2 Deposited and rolled wall after removal of clamps

IL rolling with flat and slotted rollers reduced the distortion caused by the release of WAAM deposition RS after removing clamps (Figure 7-6). Large distortion of the as-built component was driven by large unbalanced longitudinal tensile RS in the wall under clamped condition, which created a net bending moment on the clamps. After removal of clamps, a significant redistribution of RS caused large bending distortion (Figure 7-6a). The IL rolling reduced tensile RS and induced compressive RS in the wall. This change in RS state significantly reduced the net bending moment exerted on the clamps than the as-built component. Indeed, much lower nodal forces at the clamping points were predicted by the IL rolled model under clamped condition, as compared to the model of WAAM deposition without rolling. The final RS state in the IL rolled component was close to balance

and a new equilibrium was reached shortly. A minor redistribution of RS occurred, resulting in a relatively small distortion (Figure 7-6 b and c, and Figure 7-9).

Interestingly, the IL rolling using the slotted roller caused the component to bend in the opposite direction compared to the IL rolling with the flat roller (Figure 7-6 and Figure 7-9). This is because of the larger magnitude and extent of tensile PS induced by the slotted roller compared to the flat roller (Figure 7-16b and Figure 7-17b). As a result, tensile RSs converted to compressive RSs in the larger region at the top of the wall (Figure 7-5c). Consequently, after clamps removal, compressive RS relaxed and caused the component to bend downwards (Figure 7-6 c and Figure 7-9).

7.4.2 Deformation mechanism during WAAM deposition and inter-layer rolling

Deposition and rolling have a certain depth of influence, i.e., the plastic deformation in underlying deposited layers of the wall was changed by the arc or by the roller, and the influence covered certain depth or number of layers. The process (deposition or rolling) with a larger depth and magnitude of influence dominates the final RS.

The RS formation during WAAM deposition is mainly driven by the accumulated plastic deformation at high temperatures. The mechanisms of WAAM RS formation have been explained in Ref. [18]. The deposition process induced compressive PS in layer 6 during the deposition of layers 6-12 (Figure 7-10, Figure 7-11 and Figure 7-12). During the deposition of layer 13 and subsequent layers, the peak temperature became insufficient (400 °C and lower) to initiate plastic deformation in layer 6 (Figure 7-12). Therefore, the distance equivalent to the height of 7 layers from the heat source can be considered as the depth of deposition influence for cyclic plasticity, below which the material solely undergoes elastic deformation during reheating.

Rolling alone can introduce tensile PS in the wall, which can counteract the WAAM-induced compressive PS for a hybrid process [37]. The tensile PS induced by the IL rolling with the flat roller also exhibits an influence depth. For

instance, the rolling-induced PS in the layer 6 reduced after new layers were deposited. The rolling after deposition of layer 10 virtually did not affect the PS in the layer 6, which means that only the 4 layers below the rolled surface were yielded by the IL rolling process (Figure 7-11 and Figure 7-12). Therefore, the distance over the height of 4 layers can be considered as the depth of rolling influence for cyclic plasticity, below which the material solely undergoes elastic deformation during rolling.

As the deposition influence depth is larger than the rolling influence depth for the flat roller, the compressive PS generated by WAAM still dominated over the tensile PS induced by the IL rolling (Figure 7-16b). Nevertheless, the rolling reduced the tensile RS, as the overall magnitude of compressive PS was lowered. For instance, the rolling of the newly deposited layer 6 converted the tensile RS to compressive RS (Figure 7-10). However, during deposition of subsequent layers, further re-formation of RS in layer 6 gradually converted the compressive RS back to tensile RS and increased the RS magnitude gradually. Considering the whole process, the IL rolling reduced the rate of tensile RS development driven by the multi-layer deposition after the rolling of the current deposited layer. Thereby, as a consequence of IL rolling, the final longitudinal RS in layer 6 reduced from 550 MPa to 200 MPa (Figure 7-10, Figure 7-11 and Figure 7-12).

In contrast, the IL rolling with the slotted roller demonstrated twice larger the influence depth than the rolling with the flat roller (Figure 7-13). This difference arises because the slotted roller imposes restriction in transversal direction and promotes longitudinal plastic deformation (Figure 7-17b). The WAAM deposition had comparable to the rolling process influence depth (8 layers), but lower than the rolling process magnitude of influence. Consequently, the rolling with the slotted roller more significantly influenced the underlying material than the WAAM deposition. Thus, the longitudinal RS in layer 6 reduced from 500 MPa to −29 MPa after the WAAM deposition and IL rolling with the slotted roller (Figure 7-13).

7.4.3 Optimisation of rolling strategy

The RS profiles produced by the stacked 4L and 10L rolling using the flat and slotted rollers were found similar to the IL rolling (Figure 7-14 and Figure 7-15). This can be attributed to the increased influence depth for the stacked-layers rolling compared to IL rolling (Figure 7-16).

Figure 7-18 shows the evolution of longitudinal PS in layer 6 during WAAM deposition and stacked 4L rolling with the flat roller. It was found that the PS was influenced with a depth of 7 layers below the rolled surface for the stacked 4L rolling, while for the IL rolling only 4 layers below the surface were influenced. On the other hand, the influence depth of deposition was 4 layers for the stacked 4L rolling (

Figure 7-18), compared to 7 layers for the IL rolling (Figure 7-12).

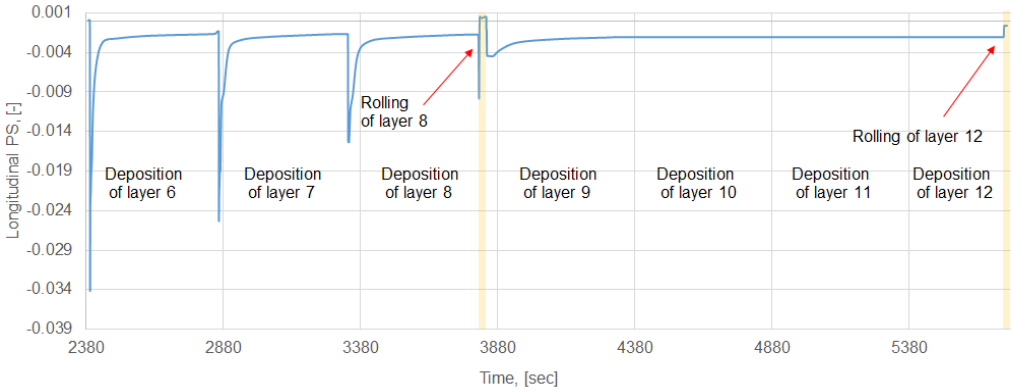

Figure 7-18 Evolution of longitudinal PS in layer 6 during WAAM deposition and stacked 4L rolling with flat roller. The rolling phases are highlighted in the yellow shaded areas.

During the IL rolling, the penetration of the flat roller was resisted by the strain hardened material in the previously deposited and rolled layers. The increase in the width of the rolled wall also enhances the resistance (Figure 7-14 b). By contrast, during the stacked 4L rolling, larger roller penetration was achieved at the identical rolling load due to the fewer strain hardening and less increase in wall width. As a result, the PS was influenced in deeper regions of the wall during the stacked 4L rolling, as compared to the IL rolling (Figure 7-16). Figure 7-19

illustrates the mechanism of the cyclic variation of longitudinal RS during WAAM + stacked 4L rolling with the flat roller. Deposition generated tensile RS in layers 1-4. As the rolling influence depth was 7 layers, the rolling of layer 4 reduced the longitudinal tensile RS in the layers 1-4 and in the substrate under the wall. As the deposition influence depth was 4 layers, deposition of layers 5-8 caused formation and re-formation of tensile RS in layers 2-8. Subsequent rolling of layer 8 reduced tensile RS in layers 2-8. Same variation of RS occurred during deposition of layers 9 – 12 and rolling of layer 12. After the final rolling of layer 20, tensile RS in all layers was reduced by the rolling.

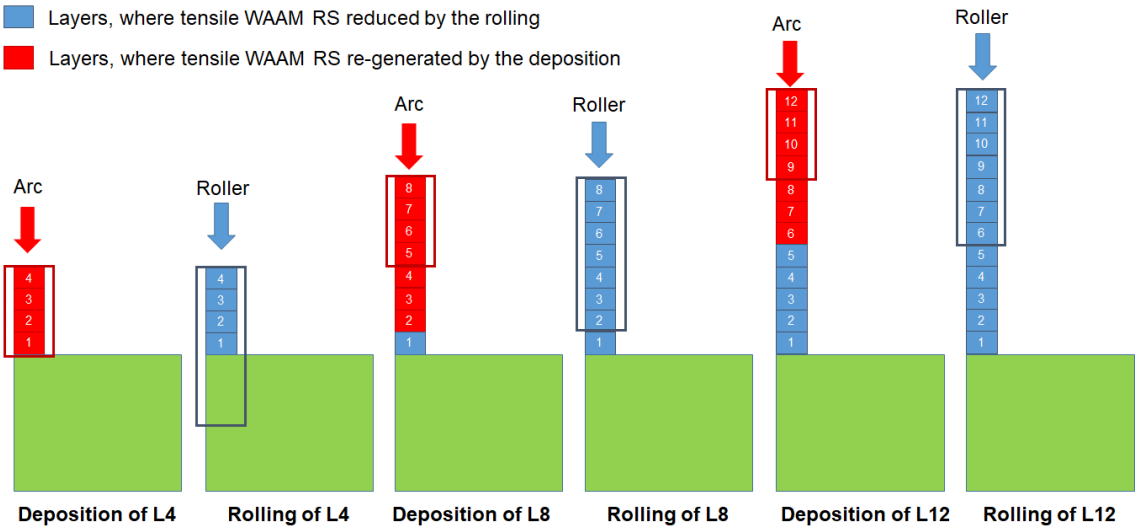

Figure 7-19 Schematic of cyclic variation of longitudinal RS during WAAM + stacked 4L rolling with the flat roller. The boxed blue and red layers are those influenced by rolling and WAAM deposition, respectively.

The schematic representation in Figure 7-19 captures the RS distributions shown in Figure 7-14c, where tensile RS in the whole wall reduced by the rolling process. The interaction between the stacked 4L rolling and WAAM deposition also determined the RS in the wall rolled using the slotted roller, but the RS distribution is distinctive due to the difference in the specific interaction associated with increased efficacy of the rolling process with the slotted roller, as compared to the flat roller rolling.

The stacked 10L rolling with both the flat and slotted rollers demonstrated a peak of tensile RS in the middle of the wall (Figure 7-14d and Figure 7-15d). This is

because the rolling of 2 layers only (L10 and L20) is insufficient to reduce compressive PS in the whole WAAM wall (Figure 7-16d and Figure 7-17d). Similarly, a large tensile RS region close to the substrate was observed in the PB rolled wall (Figure 7-14e and Figure 7-15e). In this case, the rolling of layer 20 only is inadequate to reduce the compressive PS (Figure 7-16e and Figure 7-17e) and tensile RS in the whole wall.

The stacked-layers and PB rolling with flat and slotted rollers have the prospect to improve manufacturing efficiency by reducing the number of rolled layers. However, using WAAM components built with stacked 10L rolling is not recommended with respect to fatigue sensitive applications. The high tensile RS in the middle of the wall can negatively affect the service life of the component [50,51]. The PB rolling can be efficiently employed for RS mitigation in relatively low height WAAM components (Chapter 6 and Ref. [37]). However, PB rolling with flat and slotted rollers at 50 kN rolling load appear insufficient to mitigate tensile RS in the whole 20 layers high WAAM component studied here. Despite the lower efficiency of the in-process rolling with the slotted roller (lubricant is needed before each rolling run), the rolling strategies based on the slotted roller reduced tensile RS in the whole wall to a greater degree and achieved lower distortion, as compared to the flat roller.

Another consideration for the evaluation is the reduction of WAAM wall height after rolling, which also influences manufacturing efficiency. Larger reduction in height requires more deposited layers to achieve a designed height of the wall. Rolling with the slotted roller is more beneficial because it caused marginal reduction in the wall height (Table 7-7), while rolling with the flat roller caused more marked height reduction (Table 7-6). In addition, the reduced wall surface irregularity of components built with the slotted roller minimises post-build machining (Figure 7-15).

Based on the previous evaluation with regard to both mitigation effectiveness and manufacturing efficiency, it is recommended that the stacked 4L rolling with the slotted roller is potentially an optimal process for future application.

7.4.4 Further improvement of model accuracy

The long mechanical models mapped from the short WAAM model and the short WAAM + IL rolling model underpredicted distortion after removal of clamps, mainly due to the limitations of the efficient modelling method (Chapter 5 and Ref. [36]). Due to the length reduction, the short mechanical models of WAAM deposition and IL rolling assumed rigid clamping through constraining all the nodal displacements on the substrate bottom. However, in the experimental setup by Colegrove et al. [5], six clamps were applied to small regions in the substrate, which are anticipated to exhibit considerable compliance. As a result, in-process distortion is expected to occur which cannot be captured by the short model under fully rigid clamping. The influence of the clamping system on final distortion was also discussed by Colegrove et al. [5].

The accuracy of distortion prediction can be improved by increasing the component length in the short mechanical model and using more realistic clamping simulation. A longer model will be able to capture the accumulation of in-process distortion accompanied by the movement of the substrate with the less rigid clamps. However, the computational efficiency will be reduced.

7.4.5 Limitations of the modelling approach

Proposed modelling approach has several limitations. The solution mapping technique do not account transient processes during deposition and rolling at the ends of the long WAAM parts, which usually occurred during experiments. RS and PS are assumed evenly distributed in deposition direction of the long WAAM part.

Despite the model predicted largest tensile RS at the border between the wall and the substrate, which often responsible for delamination/ tearing of produced wall from the substrate [52], models does not aim to predict in process failure of the WAAM parts observed during experiments.

Model cannot account defects induced during deposition, which could initiate crack growth during manufacturing and result in delamination/ tearing between layers or separation of the deposited wall from the substrate.

7.5 Conclusions

Efficient models for inter-layer rolling, stacked-layers rolling and post-build rolling were developed to investigate the rolling-enabled mitigation of residual stress and distortion in a WAAM deposited wall component. The models were validated using previous experimental data. The concurrent evolution of temperature, longitudinal stress and plastic strain during WAAM deposition and inter-layer rolling was revealed to understand the mechanism. Optimisation of the rolling strategy was also conducted to reduce manufacturing time without compromise of the mitigation effectiveness. The following conclusions are drawn:

1. The rolling frequency and the roller design affect the influence depth of WAAM deposition and rolling. The influence depth is manifested as the reaching depth of the plastic flow induced by the deposition or rolling of each layer. The larger the influence depth and the magnitude of induced PS, the more extensive the impact on the residual stress. The difference in influence depth is associated with histories of strain hardening and layer deformation, but the difference in magnitude related to the roller design. Such a difference affects the interaction between the deposition and rolling in the hybrid process, and the interaction determines the final residual stress and distortion in the WAAM-built component.
2. Cyclic re-formation of tensile stress occurred during WAAM deposition. The rolling with the flat roller had smaller influence depth compared to the deposition. Therefore, the inter-layer rolling with the flat roller only reduced the increase rate of the WAMM-generated tensile residual stress during the consecutive deposition of layers. Thanks to the lateral constraint of the slotted roller, the rolling with the slotted roller promoted longitudinal tensile plastic deformation and had greater influence on the underlying material than the deposition process. Consequently, the inter-layer rolling with the slotted roller significantly reduced the tensile residual stress, and it also produced compressive residual stress in a large region.

3. Stacked-layers rolling can be used as an alternative of inter-layer rolling to reduce the manufacturing time of the hybrid process. Stacked 4L and 10L rolling has larger influence depth, as compared to inter-layer rolling, thereby leading to longitudinal residual stress distributions similar to those produced by the inter-layer rolling but with much fewer runs of rolling. The stacked-layers rolling with slotted roller has higher effectiveness of stress mitigation and additional benefits such as minor reduction of the wall height, and hence it is potentially optimal for the hybrid process.
4. Post-build rolling has relatively large influence depth, but it is not as effective as the inter-layer and stacked-layers rolling to mitigate the residual stress and distortion in the WAAM wall studied here, since the influence depth only covers the upper half of the wall. Nevertheless, it could be efficiently applied to lower height WAAM components.
5. As the rolling mitigates the WAAM-generated tensile residual stress in the clamped component, the distortion due to the stress relaxation after removal of clamps is reduced by the rolling. The slotted roller is more effective in distortion mitigation since it can more significantly mitigate the WAAM residual stress.

7.6 References

1. Layer by layer Cost effective manufacturing of metal components Wire Arc Additive Manufacturing. Available at: http://fronius.com.tw/en/welding-technology/info-centre/magazine/2019/waam (Accessed: 23 February 2021)

2. Additive Manufacturing solutions. Vallourec have selected two technologies to improve the future of the metallic component value chain for the Oil & Gas market: Thermal spray and Wire Arc Additive Manufacturing (WAAM). Available at: https://solutions.vallourec.com/en/Oil-and-Gas/OCTG/Products/Additive-Manufacturing (Accessed: 23 February 2021)

3. Fletcher, J.M. The Future for WAAM. Additive Manufacturing AMazing. Available at: http://additivemanufacturing.com/2019/08/27/the-future-for-waam/ (Accessed: 23 February 2021)

4. Busachi, A., Kuepper, D., Brunelli, J., Heising, W., Moeller, C., Fisher, D., Watts, C., Drake, R. Modelling applications of additive manufacturing in defence support services: Introducing the AM - decision support system. Available at: https://www.google.com/url?sa=t&rct=j&q=&esrc=s&source=web&cd=&ved=2ahUKEwiH8JSqnc_zAhXIAWMBHcwRCj4QFnoECAIQAQ&url=https%3A%2F%2Fwww.sto.nato.int%2Fpublications%2FSTO%2520Meeting%2520Proceedings%2FSTO-MP-AVT-267%2FMP-AVT-267-03B.pdf&usg=AOvVaw2_l5Pw-ku7qxHFdvTNDV69 (Accessed: 16 October 2021)

5. Colegrove PA., Coules HE., Fairman J., Martina F., Kashoob T., Mamash H., Cozzolino LD. Microstructure and residual stress improvement in wire and arc additively manufactured parts through high-pressure rolling. Journal of Materials Processing Technology. October 2013; 213(10): 1782–1791. Available at: DOI:10.1016/j.jmatprotec.2013.04.012

6. Gu J., Ding J., Williams SW., Gu H., Ma P., Zhai Y. The effect of inter-layer cold working and post-deposition heat treatment on porosity in additively manufactured aluminum alloys. Journal of Materials Processing Technology. April 2016; 230: 26–34. Available at: DOI:10.1016/j.jmatprotec.2015.11.006

7. Martina F., Roy MJ., Szost BA., Terzi S., Colegrove PA., Williams SW., Meyer J., Hofmann M. Residual stress of as-deposited and rolled wire+arc additive manufacturing Ti–6Al–4V components. Materials Science and Technology. 21 September 2016; 32(14): 1439–1448. Available at: DOI:10.1080/02670836.2016.1142704

8. Marinelli G., Martina F., Ganguly S., Williams S. Development of Wire + Arc additive manufacture for the production of large-scale unalloyed tungsten components. International Journal of Refractory Metals and Hard Materials. August 2019; 82: 329–335. Available at: DOI:10.1016/j.ijrmhm.2019.05.009

9. Marinelli G., Martina F., Ganguly S., Williams S. Grain refinement in an unalloyed tantalum structure by combining Wire+Arc additive manufacturing and vertical cold rolling. Additive Manufacturing. March 2020; 32: 101009. Available at: DOI:10.1016/j.addma.2019.101009

10. Asala G., Khan AK., Andersson J., Ojo OA. Microstructural Analyses of ATI 718Plus® Produced by Wire-ARC Additive Manufacturing Process. Metallurgical and Materials Transactions A. September 2017; 48(9): 4211–4228. Available at: DOI:10.1007/s11661-017-4162-2

11. Shen C., Pan Z., Cuiuri D., Roberts J., Li H. Fabrication of Fe-FeAl Functionally Graded Material Using the Wire-Arc Additive Manufacturing Process. Metallurgical and Materials Transactions B. February 2016; 47(1): 763–772. Available at: DOI:10.1007/s11663-015-0509-5

12. Martina F., Ding J., Williams S., Caballero A., Pardal G., Quintino L. Tandem metal inert gas process for high productivity wire arc additive manufacturing in stainless steel. Additive Manufacturing. January 2019; 25: 545–550. Available at: DOI:10.1016/j.addma.2018.11.022

13. Williams SW., Martina F., Addison AC., Ding J., Pardal G., Colegrove P. Wire + Arc Additive Manufacturing. Materials Science and Technology. 2 May 2016; 32(7): 641–647. Available at: DOI:10.1179/1743284715Y.0000000073

14. Lockett H., Ding J., Williams S., Martina F. Design for Wire + Arc Additive Manufacture: design rules and build orientation selection. Journal of Engineering Design. 2 September 2017; 28(7–9): 568–598. Available at: DOI:10.1080/09544828.2017.1365826

15. Baufeld B., Biest OV der., Gault R. Additive manufacturing of Ti–6Al–4V components by shaped metal deposition: Microstructure and mechanical properties. Materials & Design. June 2010; 31: S106–S111. Available at: DOI:10.1016/j.matdes.2009.11.032

16. Clark D., Bache MR., Whittaker MT. Shaped metal deposition of a nickel alloy for aero engine applications. Journal of Materials Processing Technology. July 2008; 203(1–3): 439–448. Available at: DOI:10.1016/j.jmatprotec.2007.10.051

17. Wu B., Pan Z., Ding D., Cuiuri D., Li H., Xu J., Norrish J. A review of the wire arc additive manufacturing of metals: properties, defects and quality

improvement. Journal of Manufacturing Processes. October 2018; 35: 127–139. Available at: DOI:10.1016/j.jmapro.2018.08.001

18. Ding J., Colegrove P., Mehnen J., Williams S., Wang F., Almeida PS. A computationally efficient finite element model of wire and arc additive manufacture. Int J Adv Manuf Technol. 2014; (70): 227–236. Available at: DOI:10.1007/s00170-013-5261-x

19. Cordiano HV. Effect of Residual Stresses on the Low Cycle Fatigue Life of Large Scale Weldments in High Strength Steel. Journal of Engineering for Industry. 1 February 1970; 92(1): 86–92. Available at: DOI:10.1115/1.3427724

20. Webster GA., Ezeilo AN. Residual stress distributions and their influence on fatigue lifetimes. International Journal of Fatigue. 2001; 23: 375–383. Available at: DOI:10.1016/S0142-1123(01)00133-5

21. Dong P., Brust FW. Welding Residual Stresses and Effects on Fracture in Pressure Vessel and Piping Components: A Millennium Review and Beyond. Journal of Pressure Vessel Technology. 1 August 2000; 122(3): 329–338. Available at: DOI:10.1115/1.556189

22. Dong P. Residual stresses and distortions in welded structures: a perspective for engineering applications. Science and Technology of Welding and Joining. July 2005; 10(4): 389–398. Available at: DOI:10.1179/174329305X29465

23. Bai X., Zhang H., Wang G. Modeling of the moving induction heating used as secondary heat source in weld-based additive manufacturing. The International Journal of Advanced Manufacturing Technology. March 2015; 77(1–4): 717–727. Available at: DOI:10.1007/s00170-014-6475-2

24. Michel F., Lockett H., Ding J., Martina F., Marinelli G., Williams S. A modular path planning solution for Wire + Arc Additive Manufacturing. Robotics and Computer-Integrated Manufacturing. December 2019; 60: 1–11. Available at: DOI:10.1016/j.rcim.2019.05.009

25. Wang X., Wang A., Li Y. A sequential path-planning methodology for wire and arc additive manufacturing based on a water-pouring rule. The International Journal of Advanced Manufacturing Technology. August 2019; 103(9–12): 3813–3830. Available at: DOI:10.1007/s00170-019-03706-1

26. Hönnige JR., Colegrove PA., Ganguly S., Eimer E., Kabra S., Williams S. Control of residual stress and distortion in aluminium wire + arc additive manufacture with rolling. Additive Manufacturing. August 2018; 22: 775–783. Available at: DOI:10.1016/j.addma.2018.06.015

27. Hönnige JR., Colegrove PA., Ahmad B., Fitzpatrick ME., Ganguly S., Lee TL., et al. Residual stress and texture control in Ti-6Al-4V wire + arc additively manufactured intersections by stress relief and rolling. Materials & Design. July 2018; 150: 193–205. Available at: DOI:10.1016/j.matdes.2018.03.065

28. Colegrove PA., Martina F., Roy MJ., Szost BA., Terzi S., Williams SW., et al. High Pressure Interpass Rolling of Wire + Arc Additively Manufactured Titanium Components. Advanced Materials Research. August 2014; 996: 694–700. Available at: DOI:10.4028/www.scientific.net/AMR.996.694

29. Martina F., Colegrove PA., Williams SW., Meyer J. Microstructure of Interpass Rolled Wire + Arc Additive Manufacturing Ti-6Al-4V Components. Metallurgical and Materials Transactions A. December 2015; 46(12): 6103–6118. Available at: DOI:10.1007/s11661-015-3172-1

30. McAndrew AR., Alvarez Rosales M., Colegrove PA., Hönnige JR., Ho A., Fayolle R., et al. Interpass rolling of Ti-6Al-4V wire + arc additively manufactured features for microstructural refinement. Additive Manufacturing. May 2018; 21: 340–349. Available at: DOI:10.1016/j.addma.2018.03.006

31. Hönnige J., Seow CE., Ganguly S., Xu X., Cabeza S., Coules H., et al. Study of residual stress and microstructural evolution in as-deposited and inter-pass rolled wire plus arc additively manufactured Inconel 718 alloy after ageing treatment. Materials Science and Engineering: A. January 2021; 801: 140368. Available at: DOI:10.1016/j.msea.2020.140368

32. Hwang SM., Kobayashi S. Preform design in plane-strain rolling by the finite-element method. International Journal of Machine Tool Design and Research. January 1984; 24(4): 253–266. Available at: DOI:10.1016/0020-7357(84)90060-X

33. Lee CH., Kobayashi S. New Solutions to Rigid-Plastic Deformation Problems Using a Matrix Method. Journal of Engineering for Industry. 1 August 1973; 95(3): 865–873. Available at: DOI:10.1115/1.3438238

34. Cozzolino LD., Coules HE., Colegrove PA., Wen S. Investigation of post-weld rolling methods to reduce residual stress and distortion. Journal of Materials Processing Technology. September 2017; 247: 243–256. Available at: DOI:10.1016/j.jmatprotec.2017.04.018

35. Gornyakov V., Sun Y., Ding J., Williams S. Computationally Efficient Models of High Pressure Rolling for Wire Arc Additively Manufactured Components. Applied Sciences. 4 January 2021; 11(1): 402. Available at: DOI:10.3390/app11010402

36. Gornyakov V., Sun Y., Ding J., Williams S. Efficient determination and evaluation of steady-state thermal-mechanical variables generated by wire arc additive manufacturing and high pressure rolling. Accepted for publication in Modelling and Simulation in Materials Science and Engineering (Manuscript ID: MSMSE-105517.R2).

37. Gornyakov V., Ding J., Sun Y., Williams S., Understanding and designing post-build rolling for mitigation of residual stress and distortion in wire arc additively manufactured components. Submitted to Materials & Design in Elsevier (Manuscript ID: JMADE-D-21-02630) for Publication.

38. Abbaszadeh M., Hönnige JR., Martina F., Neto L., Kashaev N., Colegrove P., et al. Numerical Investigation of the Effect of Rolling on the Localized Stress and Strain Induction for Wire + Arc Additive Manufactured Structures. Journal of Materials Engineering and Performance. August 2019; 28(8): 4931–4942. Available at: DOI:10.1007/s11665-019-04249-y

39. Tangestani R., Farrahi GH., Shishegar M., Aghchehkandi BP., Ganguly S., Mehmanparast A. Effects of Vertical and Pinch Rolling on Residual Stress Distributions in Wire and Arc Additively Manufactured Components. Journal of Materials Engineering and Performance. April 2020; 29(4): 2073–2084. Available at: DOI:10.1007/s11665-020-04767-0

40. Goldak J., Chakravarti A., Bibby M. A new finite element model for welding heat sources. Metallurgical Transactions B. June 1984; 15(2): 299–305. Available at: DOI:10.1007/BF02667333

41. Ding J., Colegrove P., Mehnen J., Ganguly S., Sequeira Almeida PM., Wang F., et al. Thermo-mechanical analysis of Wire and Arc Additive Layer Manufacturing process on large multi-layer parts. Computational Materials Science. July 2011; : S092702561100365X. Available at: DOI:10.1016/j.commatsci.2011.06.023

42. Coules HE., Horne GCM., Kabra S., Colegrove P., Smith DJ. Three-dimensional mapping of the residual stress field in a locally rolled aluminium alloy specimen. Journal of Manufacturing Processes. April 2017; 26: 240–251. Available at: DOI:10.1016/j.jmapro.2017.02.010

43. Perenda J., Trajkovski J., Žerovnik A., Prebil I. Residual stresses after deep rolling of a torsion bar made from high strength steel. Journal of Materials Processing Technology. April 2015; 218: 89–98. Available at: DOI:10.1016/j.jmatprotec.2014.11.042

44. Lan J., Feng S., Hua L. The residual stress of the cold rolled bearing race. Procedia Engineering. 2017; 207: 1254–1259. Available at: DOI:10.1016/j.proeng.2017.10.879

45. Pan R., Pirling T., Zheng J., Lin J., Davies CM. Quantification of thermal residual stresses relaxation in AA7xxx aluminium alloy through cold rolling. Journal of Materials Processing Technology. February 2019; 264: 454–468. Available at: DOI:10.1016/j.jmatprotec.2018.09.034

46. Stolarski TA., Tobe S. Rolling Contacts: Stolarski/Rolling Contacts. Chichester, UK: John Wiley & Sons, Ltd; 2000. Available at: DOI:10.1002/9781118903001 (Accessed: 23 April 2020)

47. Thompson M.A., Fresini M., DosSantos J., Hedgegard J., Richardson I.M. Improving the competitiveness of the European steel fabrication industry using synchronised tandem wire welding technology [Technical]. SYNFAB; 2005. Report No.: 3.

48. Leggatt RH. Residual stresses in welded structures. International Journal of Pressure Vessels and Piping. March 2008; 85(3): 144–151. Available at: DOI:10.1016/j.ijpvp.2007.10.004

49. The Neutron Diffraction (ND) technique measures residual stresses deep within a material by detecting the diffractions of an incident neutron beam. Available at: https://www.veqter.co.uk/residual-stress-measurement/neutron-diffraction (Accessed: 13 March 2021)

50. McClung RC. A literature survey on the stability and significance of residual stresses during fatigue. Fatigue & Fracture of Engineering Materials and Structures. March 2007; 30(3): 173–205. Available at: DOI:10.1111/j.1460-2695.2007.01102.x

51. Hassani-Gangaraj SM., Carboni M., Guagliano M. Finite element approach toward an advanced understanding of deep rolling induced residual stresses, and an application to railway axles. Materials & Design. October 2015; 83: 689–703. Available at: DOI:10.1016/j.matdes.2015.06.026

52. Wu Q., Mukherjee T., Liu C., Lu J., DebRoy T. Residual stresses and distortion in the patterned printing of titanium and nickel alloys. Additive Manufacturing. October 2019; 29: 100808. Available at: DOI:10.1016/j.addma.2019.100808

8 Conclusions

8.1 Summary of research

8.1.1 Efficient modelling

Efficient rolling and WAAM models were developed as tools to support the study of post-build rolling (Chapter 6), inter-layer and stacked-layers rolling (Chapter 7). These models have shown a significant improvement in computational efficiency (Table 5-4 and

Table 5-5). In the first step of the research, different efficient modelling methods of rolling were evaluated in terms of accuracy and computational time (Chapter 4). The model with reduced component length demonstrated significantly improved computational efficiency than the conventional full-scale rolling model, due to the largely reduced number of nodes and reduced process time required for simulation. Importantly, the length of the deformable component was adequate to reach steady-state rolling. The short model has been proved to be capable of providing consistent and stable solutions comparable to the conventional large-scale rolling model.

Among other models, the reduced length 2D rolling model has the lowest number of nodes with reduced degrees of freedom, so the model required the lowest computational time. However, due to the plane-stress assumption the 2D model cannot predict plastic strain (PS) and residual stress (RS) distributions with the same accuracy as the 3D model because the rolling of WAAM parts is a complex 3D phenomenon.

The study demonstrated that the explicit analysis method is less efficient and less accurate than the implicit analysis method for the relatively simple contact problems with rigid bodies involved using comparable computational resources. The mass scaling technique reduced the computational cost of the 3D short explicit transient model via increasing the deformable component's density and, as a consequence, it increased the size of stable time increment. However, the increased density raised the influence of artificial inertia, which affected the accuracy of the solution. The steady-state detection feature, as implemented in the 3D Eulerian model, stopped analysis as soon as steady-state rolling was detected. Due to this, the model's cost was similar to other developed 3D rolling models, despite a triply larger number of nodes involved in FE analysis. Unfortunately, the accuracy of the predicted results was impaired by physically inaccurate representation of the rolling process. The 3D short implicit transient model is best among all the examined models, when both computational efficiency and solution accuracy is considered, and it can obtain steady-state

solution equivalent to the control model which simulates the rolling in the full-scale component.

In the second stage of the research, an efficient solution mapping technique was developed (Chapter 5). Using this technique, steady-state solution is taken from the clamped short efficient model, and then spatially sequentially mapped to the long mechanical model. The final RS, PS distribution and distortion are calculated from the long mechanical model so that the effect of clamping conditions can be taken into the consideration. Since short models are used for computing the steady-state thermal-mechanical behaviours of the WAAM and rolling process, significant time saving was achieved. The RS distribution and distortion predicted by the long WAAM mechanical model are in good agreement with the experimental measurements after removal of clamps.

The efficient modelling method is universal and can be applied to other manufacturing processes in which a steady state is present. However, the length of the short models should be properly considered to maintain a balance between the computational cost and the model's ability to reach a steady state. In addition, the definitions of the longitudinal constraints of the short model are crucial and is dependent on the process being simulated. For example, full longitudinal constraints are required for the short mechanical WAAM model, while only two ends of the component need to be restricted for the short rolling model. The reason is that different plastic flow mechanism occurs during WAAM deposition and rolling. Compressive plastic flow, caused by WAAM deposition, occurs due to the low yield strength of the material at high temperatures and full longitudinal constraints are more representative for the long component built in reality. However, full longitudinal constraints prevent the longitudinal deformation caused by the roller during rolling simulation, while constraining only the two ends of the deformable component is more realistic to compensate for the underestimated longitudinal stiffness due to the reduction of the component length in the short model.

8.1.2 Mechanism of RS mitigation by high-pressure rolling in WAAM parts under clamped condition

WAAM process induces an approximately uniform longitudinal compressive PS distribution in the deposited wall, which results in constant longitudinal tensile RS in the wall under clamped condition. After post-build rolling with flat and profiled rollers, large tensile PS occurred under the rolled surface, but compressive PS with reduced magnitude remained in the core of the wall. In the area where the compressive PS was reduced or converted to be tensile, the WAAM tensile RS decreased. The profiled and flat rollers exhibited a similar mechanism of PS generation in the WAAM wall at a friction coefficient of 0.5 or a higher value. The edge of the profiled roller constrained the lateral deformation on the rolled surface and promoted longitudinal deformation. Similarly, friction limited lateral deformation in the contact region with the flat roller and enhanced longitudinal deformation.

In contrast, the slot of the slotted roller virtually eliminated the lateral deformation during the rolling process. It produced much greater longitudinal deformation compared to the flat and profiled rollers. As a result, the slotted roller produced a lower tensile deformation under the rolled surface but induced a significantly larger tensile PS in the core of the wall and more effectively mitigated the tensile WAAM-induced RS. In addition, the friction between the roller slot and the side of the wall helped the roller plunge deeper into the wall, which also promoted longitudinal deformation.

However, the combination of WAAM deposition and inter-layer rolling exhibits more complex RS and PS formation mechanism. The multi-layer deposition process results in the cyclic formation of longitudinal tensile RS in the WAAM wall. This cyclic formation of RS occurred due to uneven compressive plastic deformation as long as peak temperatures were high enough to promote the plastic flow of the material. Nevertheless, as the number of deposited layers increased, the peak temperatures reduced, and further cyclic alteration of tensile RS occurred fully elastically. Inter-layer rolling with the flat roller induced tensile PS in the 4 layers below the rolled surface and mitigated WAAM tensile RS, but

the deposition of the subsequent layer promoted compressive deformation and re-formed tensile RS in the 7 layers below. Even through the WAAM deposition had more significant influence on underlaying material, still the IL rolling with the flat roller reduced the rate of tensile RS re-formation during WAAM deposition and as result mitigated tensile RS in the wall.

By contrast, the WAAM deposition and the rolling had similar depth of influence during WAAM + IL rolling with the slotted roller. However, due to the larger magnitude of the rolling process influence, WAAM tensile RS was mitigated to a greater degree than with the flat roller.

8.1.3 Influence of the high-pressure rolling on RS and distortion in large-scale WAAM parts after removal of clamps

The deformation of the WAAM parts after removing the clamps is caused by the redistribution/ relaxation of the large tensile RS in the wall, which causes the parts to bend upward. After removing the clamps in the rolled WAAM parts, new RS equilibrium can be reached shortly. A minor redistribution of RS occurred, resulting in relatively small distortion.

The walls that were inter-layer rolled with flat rollers showed little concave upward distortion. By contrast, the parts rolled with a slotted roller exhibited slight concave downward distortion. During rolling, the slotted roller induced a larger region of longitudinal compressive RS at the top of the WAAM wall than the flat roller. Relaxation of compressive RS in this large region after clamps removal caused expansion of the wall, which resulted in convex downward distortion. For post-build rolling, the distortions were reduced and the RS is mitigated in low height WAAM parts in a similar way.

The predicted RS distributions in the inter-layer rolled large-scale WAAM parts after clamps removal are in good agreement with the experimental results. However, the final distortions are underpredicted, mainly due to the incapability of the short models to capture the in-process distortion during inter-layer WAAM deposition and rolling. To improve the prediction accuracy, longer component and

more realistic simulation of clamping are needed in the short model, which, however, may significantly increase the computational cost.

8.1.4 Optimisation of the high-pressure rolling for WAAM parts

The manufacturing time of WAAM + rolling can be reduced by minimising the number of rolled layers (e.g. using stacked-layers rolling method). Rolling with the flat roller and the slotted rollers for every 4 deposited layers created a longitudinal RS distribution similar to inter-layer rolling. The rolling with the flat roller reduced tensile RS with more layers than the number of layers affected by the deposition process. At the end of WAAM deposition + stacked 4 layers rolling, the WAAM tensile RS in all deposited layers was reduced by the rolling process. The efficacy of the slotted roller to reduce tensile RS during stacked 4 layers rolling associated with increased magnitude of rolling process influence.

However, rolling every 10 deposited layers was not sufficient to mitigate RS in the whole WAAM wall, the region subjected to WAAM-induced tensile RS remained in the middle of the wall. Post-build rolling with flat and slotted rollers can replace inter-layer rolling for relatively low height WAAM components (<10 deposited layers). However, a single rolling run was insufficient to introduce required tensile PS and mitigate RS in 20 layers height WAAM wall.

In terms of the process optimisation, the slotted roller is preferable to the flat roller as it caused marginal height reduction of the wall. In addition, the reduced surface roughness of components produced with slotted roller requires less post-build machining. Also, rolling with the slotted roller reduced tensile RS in the whole wall to a greater degree than the other rollers.

The efficacy of the rolling process to mitigate WAAM tensile RS within greater depth can be improved. With the increase of rolling load at the flat, profiled, and slotted rollers larger amount of material is affected by the rolling process. Tensile plastic strain with greater magnitude can be induced in the wall, resulting in the mitigation of tensile WAAM RS further away from the rolled surface. The largest practical rolling loads provides the highest effectiveness of RS and distortion mitigation. However, it should be noted that the excessive rolling load could be

detrimental. On the one hand, as induced by the rolling, the compressive longitudinal RS could lead to inverse/convex deformation of parts after clamps removal. On the other hand, excessive rolling load could cause plastic collapse of tall wall.

An increase of friction coefficient between the roller and the wall suppressed tensile plastic deformation of the material on the contact surface but caused a larger tensile deformation in the wall's core. The friction coefficient had a significant impact on RS distribution produced by the slotted roller. With the increase of friction coefficient, a larger amount of material in the wall's core was affected by the compressive RS. However, this effect is insignificant for the flat and the profiled rollers. As demonstrated by the rolling models, applying rolling with a slotted roller without lubrication or increased friction could significantly improve the rolling effectiveness. However, in practice, rolling with the slotted roller without lubricant was unsuccessful since the slotted roller can be stuck on the WAAM wall, due to the increased resisting force and the insufficient horizontal moving traction.

8.2 Contribution to knowledge

The research gaps presented in Chapter 1 have been filled by this PhD project. Computationally efficient models were developed, and a modelling technique for determining steady-state solution and transferring solution between various length models was introduced. Post-build and inter-layer rolling processes for WAAM parts were investigated, and optimisation of the rolling strategy was conducted with recommendations made for future industrial applications. This study provided the following intellectual contribution to knowledge and demonstrated efficient models and methods for use by the scientific community:

1. A computationally efficient modelling method for rolling of WAAM components was developed and demonstrated. The increased efficiency was achieved by the reduction of the length of the deformable component and the saving of the time of the simulated event. The reduced length was sufficient to reach steady state and to obtain stable and consistent solutions equivalent to conventional long rolling models. A solution

mapping technique has been developed to transfer steady-state solution from short models to long models so as to investigate mechanical response to clamps removal. The method is universal and can be also applied to other manufacturing process where a steady state is present.

2. Based on the simulations, the mechanism about how the rolling process reduces the RS has been revealed and different rolling strategies were evaluated, including post-build rolling, inter-layer rolling and stacked-layers rolling.
3. The effects of different roller designs and rolling parameters on the reduction of RS have been investigated. Post-build rolling with flat, profiled and slotted rollers at the largest tested rolling loads induced tensile PS to a greater depth to promote relaxation of WAAM tensile RS in the larger region of the wall. At all investigated rolling loads, the slotted roller demonstrated the greatest efficacy to mitigate RS and distortion. The slotted roller with increased friction demonstrated improved mitigation effectiveness of the rolling process.
4. An optimised rolling strategy has been developed, which can be used to achieve the minimum rolling operations while maintaining the sufficient mitigation of RS and distortion. This is based on the understanding of the PS and RS evolution during the hybrid process of WAAM deposition and stacked-layers rolling.

8.3 Future work

More research in following directions can be extended in future work to further improve efficiency and accuracy of proposed models, allowing practical industrial application of developed models for numerical design of hybrid WAAM and rolling manufacturing techniques. WAAM process gaining popularity in aerospace industry for manufacturing of large cylindrical components like rocket fuel tanks. Proposed hybrid WAAM and rolling models can be efficiently applied for this type of problems. While, scientific community will obtain efficient tool for future research and optimisation of microstructure and mechanical properties of WAAM plus inter-layer rolled parts.

8.3.1 Exploration of short explicit transient rolling model

The short explicit transient rolling model demonstrated lower accuracy due to the artificially increased material density used to reduce computational cost (Chapter 4). However, an explicit analysis still has the potential to handle better complex contact problems and large deformations, better suited to parallel computation than an implicit analysis. Furthermore, the short explicit transient model reached a steady state faster than the short implicit transient models. This allowed further reduction of the deformable component length, resulting in a considerable decrease number of nodes involved in the analysis.

Subsequent development of the short explicit transient rolling model should be conducted. The short explicit rolling model can potentially improve the solution's accuracy and reduce the computational cost by further reducing the modelled component length, identifying the optimal artificial density of a material, and employing parallel computation with a larger number of CPU cores.

8.3.2 Improvement of distortion prediction accuracy

The short thermal-mechanical and rolling models assume rigid clamping of a deformable component during deposition and rolling processes (Chapter 5). The model's limitations mainly arise from this simplification. The model did not capture the accumulation of the deformation during the deposition and rolling process, which happened in the experiments. This leads to underprediction of the final distortion. Further development of the short thermal-mechanical models should be conducted to simulate non-fully rigid clamps and improve the distortion prediction accuracy.

8.3.3 Experimental measurements of RS for post-build rolled WAAM components

Measurements of RS in post-build rolled WAAM parts using the designed rollers and the rolling loads considered in the presented study (Chapter 6) were not found in the literature. Therefore, experimental measurements could be carried out for further validation of the post-build rolling models.

8.3.4 Experimental measurements of RS for stacked-layers rolled WAAM components

Significant manufacturing time saving can be achieved with the aid of stacked-layers rolling instead of inter-layer rolling for WAAM parts (Chapter 7). However, measurements of RS in stacked-layers rolled WAAM parts were not found in the literature. Therefore, further experimental work could be conducted to obtain such important information.